Structure, Dynamics and Association of Thermosensitive Core-Shell Particles

DISSERTATION

zur Erlangung des akademischen Grades ein es
Doktors der Naturwissenschaften
- Dr. rer. nat. -
der Fakultät Biologie, Chemie und Geowissenschaften
der Universität Bayreuth

vorgelegt von

Jérôme Crassous

geboren in Toulouse / Frankreich

Bayreuth, 2009

Die vorliegende Arbeit wurde an der Universität Bayreuth in der Zeit von Oktober 2004 bis Januar 2009 am Lehrstuhl für Physikalische Chemie I unter Betreuung von Herrn Prof. Dr. Matthias Ballauff angefertigt.

Vollständiger Abdruck der von der Fakultät für Biologie, Chemie und Geowissenschaften der Universität Bayreuth zur Erlangung des akademischen Grades Eines doktors der Naturwissenschaften genehmigten Dissertation.

Dissertation eingereicht am: 04.05.2009
Zulassung durch die Promotionskommission: 06.05.2009
Wissenschaftliches Kolloquium: 20.07.2009

Amtierender Dekan: Prof. Dr. Axel H. E. Müller

Prüfungsausschuss:
Prof. Dr. Matthias Ballauff (Erstgutachter)
Prof. Dr. Nuri Aksel (Zweitgutachter)
Prof. Dr. Andreas Fery
Prof. Dr. Jürgen Senker (Vorsitzender)

Dès qu'un enfant comprend quelque chose, il se produit en lui un mouvement admirable. S'il est délivré de la crainte et du respect, vous le voyez se lever, dessiner l'idée à grands gestes, et soudain rire de tout son coeur, comme au plus beau des jeux.

(Emile-Auguste Chartier, dit Alain)

A mes parents,

Acknowledgment

With the support of the following people I could finish this thesis successfully and would like to express my gratitude to all of them.

It's my great pleasure to thank Prof. Matthias Ballauff for giving the opportunity and freedom to do research in this interesting field under his supervision. His guidance and support were a great help to always improve the quality of my work. Thanks to him I realize what it is to be and behave as a researcher.

I thank Prof. Nuri Aksel and Dr. Lutz Heymann for the fruitful comments and discussions concerning my work and for sharing their experience in the field of the rheology.

I thank Prof. Matthias Fuchs and his coworkers Oliver Henrich and David Hajnal for the very fruitful collaboration in the field of the dynamic and the development of the theoritical model biased on the mode coupling theory. It was a great pleasure to work with such outstanding scientists. I would also like to thank Miriam Siebenbüger for her technical support and for the measurements she performed during her Diplomarbeit.

I am also thankful to Dr. Alexander Wittemann and Jochen Ring for the synthesis of the system I used during my Phd. I also want to thank Dr. Alexander Wittemann for his constructive suggestions and collaboration in the field of the colloidal association.

Dr. Markus Drechsler, Prof. Ishi Talmon and Marc Schrinner are gratefully acknowledged for their invaluable contribution and tireless enumerable attempts to get TEM and Cryo-TEM images as well as Benjamin Gößler for the SEM pictures.

I thank Prof. Norbert Willenbacher and Dr. Raphael Régisser for the common work on the piezoelectric axial vibrator, and in the same sense the group of Dr. Wolfgang Pechhold, Theresia Groß and Dr. Ludwig Kirschenmann for the conception of this instrument.

Florian Schwaiger and prof. Werner Köhler are acknowledged for the experiments their performed and their contribution in the laser controlled micro-aggregation presented herein.

I would like to thank Dr. John Bosco, Dr. Antonis Keralakis for the fruitful discussions and collaborations. I am particularly thankful to Pierre Millard for the number of ideas we developed together and for his expertise in the polymer chemistry, to Adriana Mihut for the constant support and the time she spent to provide AFM pictures from various of my projects, and to Christophe Rochette and to Sergiu Mihut for developing of the programs for the SAXS and CryoTEM analysis.

I thank Elisabeth Düngfelder for her bureaucratic work with a lot of patience and kindness, and Karlheinz Lautenbach for his availability and technical support.

Last but not the least; I express my gratitude to my family members and friends for their strong supports, and simply for having always believed in me.

Contents

1 Introduction

Gels composed of cross-linked poly(N-isopropylacrylamide) (PNIPAM) chains can undergo a phase transition as function of temperature in which the network shrinks in a continuous or discontinuous fashion. The volume transition in macroscopic networks has been studied extensively by T. Tanaka and others [1, 2]. A review on work done on these macroscopic systems was given some time ago by Shibayama [3]. Starting with early work by Tanaka [4], many groups have developed syntheses of colloidal thermosensitive network by e.g. emulsion polymerization. Two types of particles can be prepared: Either the particles consist totally of a PNIPAM-network [5–12] or the PNIPAM-network is polymerized onto a solid core [13–20]. A great number of possible applications have been discussed for these systems that include widely separate fields as e. g. protein adsorption [19, 20]. They have also been recently used as a template for the reduction of metal nanoparticles [21–23] for applications in catalysis [22, 23]. A comprehensive review on the applications was given by Lyon [24].

They present a versatile phase behavior: on one hand they can behave like hard sphere with a liquid-crystal transition below the critical temperature [7, 9, 25, 26]. On the other hand in the absence of electrostatic stabilization or in saturated salt concentrations the particles become attractive after the low critical solution temperature. This leads to a partially or totally reversible aggregation of the system in the dilute regime and to the gelation of the system for higher concentrations [27–30]. The fine tuning of their interparticular potential can also be used for the association with other particles [31, 32].

Recently, the thermosensitive core-shell particles have attracted renewed interest as model colloids, in particular for a comprehensive study of the structure, dynamics, and flow behavior of concentrated suspensions [33–41]. Fig. 1.1 displays the overall structure and the volume transition of these particles in a schematic fashion: Immersed in water the PNIPAM-shell of the particles will swell if the temperature is low. However, raising the temperature in the system beyond 32^{o}C leads to a volume transition in which the network in the shell shrinks by expelling water. Thus, the effective volume fraction ϕ_{eff} determining the hydrodynamic volume of the particles can be adjusted through the temperature in the system. Hence, dense suspensions can be achieved out of a rather dilute state by lowering the temperature.

Senff et al. were the first to present investigations of the rheology of such core-shell particles [34]. The advantages of these thermosensitive particles over the classical hard sphere particles used in previous investigations [42, 43] of the flow behavior are at hand: The dense suspension is generated in situ thus avoiding shear and mechanical deformation during preparation and filling into a rheometric device. Also, all previous history caused by shearing the suspension can simply be erased by raising the temperature and thus lowering the volume fraction again. The high volume fraction can then be adjusted again and a pristine sample being in full equilibrium at all length scales can be generated. Senff et al [34]. showed that these "reversibly inflatable spheres" can be used to study the

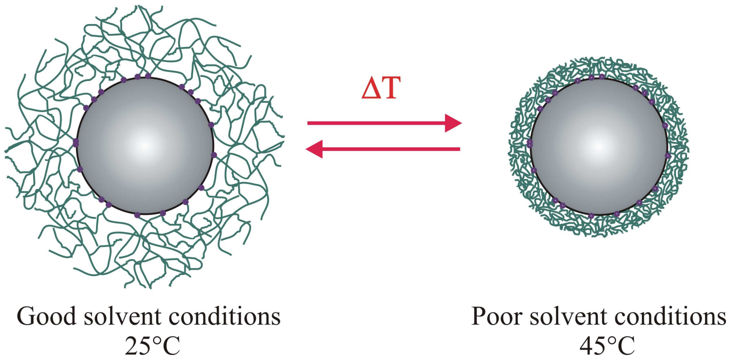

Figure 1.1: *Schematic representation of the volume transition in core-shell micronetworks: The polymer chains are affixed to the surface of the core.*

dependence of the viscosity η on the shear rate $\dot{\gamma}$. If the effective volume fraction of the particles is not too high, a *first Newtonian region* is observed if the shear rate $\dot{\gamma}$ is small. Here the viscosity η_0 of the suspension measured in this first Newtonian regime can be significantly larger than η_s the one of the pure solvent. At higher shear rates, the perturbation of the microstructure of the suspension by the advective forces can no longer be restored by the Brownian motion of the particles. Hence, significant *shear thinning* will result in which the reduced viscosity η/η_s is more and more lowered until one may speculate that a *second Newtonian region* is reached.

Recently, Senff's data [34] have been used to check the predictions of mode-coupling theory (MCT) [44, 45] for the flow behavior of concentrated suspensions [39, 40]. Good agreement was reached in this comparison employing schematic MCT models [39]. Hence, this comparison suggests that the thermosensitive particles shown in Fig. 1.1 present an excellent model system for the study of the dynamics of suspensions in the vicinity of the glass transition. However, no fully quantitative comparison of theory [44, 45] and experiment including a discussion of the fit parameters could not have been done before this work.

This work is dedicated to the study of this composite particles. The first part describes the characterization of the particles. Here we present the first study of thermosensitive core-shell particles and their volume transition (cf. Figure 1.1) by cryogenic transmission electron microscopy (cryo-TEM). The dependence on the degree of crosslinking and on the temperature has been first investigated. A new method was developed to quantitatively analyzed the TEM and CryoTEM images in order to access to the internal structure of colloids. The different observation are compared to data obtained by dynamic light scattering and small-angle X-ray scattering. The last part of the chapter focus on the colloidal crystallization of the particles.

The second part explores the dynamics of this system in the vicinity of the glass transition. For this purpose a new rheological set up is presented in the first section to measure the linear viscoelasticity of complex fluids on a bright frequency range. In the second chapter of this part, an interpretation of the dynamics of the colloidal core-shell dispersion in equilibrium and in flow biased on the mode coupling theory is developed.

The last part of the thesis investigates the field of the association. First the temperature controlled self-association of the system is put under scrutiny. Then the association of these composite microgels with gold nanoparticles will be discussed.

2 Characterization

2.1 Influence of the degree of crosslinking on the structure and swelling behavior of thermosensitive core-shell colloidal latexes.

2.1.1 Introduction

Environmentally sensitive microgels have attracted considerable interest due to their ability to swell and de-swell in response to external stimuli such as temperature, pH or light radiation [46–48]. A great number of possible applications have been discussed for these systems. A comprehensive review on the applications was given by Nayak and Lyon [24]. Microgels of poly(N-isopropylacrylamide) (PNIPAM) crosslinked by N,N'-methylenebisacrylamide (BIS) have been of particular interest. The temperature of the volume transition is located at 32°C in aqueous solution which makes them suitable candidates for possible medical applications such as controlled release systems [19, 20]. Other applications include e.g. the use of such systems as carriers for metallic nanoparticles in catalysis [22, 23].

The volume transition in macroscopic networks has been studied extensively by T. Tanaka and others [1–4]. A thermodynamic analysis of the transition can be done in terms of the classical Flory-Rehner theory [49–53]. Hence, the volume transtition in macroscopic gels seems to be rather well understood. For details the reader is deferred to the review of Shibayama [3]. Microgels with dimensions in the colloidal domain have been the subject of a large number of experimental studies in recent years. The investigations range from measurements of the macroscopic properties, such as turbidity [54, 55], high sensitive scanning microcalorimetry [55–57], rheology [7, 34], to experiments probing molecular interactions such as nuclear magnetic resonance [56, 58], light scattering [7, 13, 34, 49, 55, 56, 58, 59], small-angle X-ray and neutron scattering [17, 49, 59–64]. Compared to macroscopic gels, the degree of understanding of microgels is much less advanced, however.

This chapter is devoted to a comprehensive study of thermosensitive core-shell particles in aqueous solution. These particles have been synthesized by us [17, 63–65] and by others [13, 59]. They have been used as model system for the study of the flow behavior of concentrated suspensions [39, 40]. The results obtained so far provide an excellent test for the mode-coupling theory of the dynamics of dense colloidal systems [39, 40, 44, 45]. A further point commanding attention is the crystallization of these particles. Given the fact that the shell of these particles consist of a compressible network, this point is certainly in need of further elucidation and will be discussed in the chapter 2.3.

In this chapter we demonstrate that cryogenic transmission electron microscopy (Cryo-

Table 2.1: *Synthesis of the core particles.*

Styrol [g]	193.2
NiPAM [g]	10.5
SDS [g]	1.79
KPS [g]	0.39
H_2O [g]	706

TEM) was highly suited to study these core-shell particles in situ [22, 23, 65]. Cryo-TEM allows us to visualize the particles directly in the aqueous phase by shock-freezing of a suspension of the particles. The volume transition was for the first time directly made visible at different temperatures, including temperatures below and above room temperature, and can be compared to data obtained by small-angle X-ray scattering and dynamic light scattering. Moreover, the swelling of the network is modeled in terms of the Flory-Rehner theory. Special attention is paid to the interplay of the degree of crosslinking of the particles and the phase behavior at high volume fractions and will be discussed in the section crystallization.

2.1.2 Experimental

Synthesis and purification

The core-shell particles were synthesized in a two-step reaction as described in ref. [17]. The core particles were obtained by emulsion polymerization and used as seed for the radical polymerization of the cross-linked shell.

Chemical

N-isopropylacrylamide (NIPAM; Aldrich), N,N'-methylenebisacrylamide (BIS; Fluka), sodium dodecyl sulfate (SDS; Fluka), and potassium peroxodisulfate (KPS; Fluka) were used as received. Styrene (BASF) was washed with KOH solution and distilled prior to use. Water was purified using reverse osmosis (MilliRO; Millipore) and ion exchange (MilliQ; Millipore).

Core latex

Emulsion polymerization has been done using a 1-L flask equipped with a stirrer, a reflux condenser, and a thermometer. The recipe for the core latex is given in the following: SDS and NIPAM were dissolved in pure water with stirring and the solution is degassed by repeated evacuation under nitrogen atmosphere. After addition of styrene, the mixture is heated to 80^oC under an atmosphere of nitrogen. The initiator KPS dissolved in 15 mL of water is added while the mixture is stirred with 300 rpm. After 8 h the latex is cooled to room temperature and filtered through glass wool to remove traces of coagulum. Purification was done by dialysis of the latex against $2.5{\cdot}10^{-3}$ M KCl solution for approximately 3 weeks (Medicell, 12000-14000 *Dalton*). The masses of the different reactants are summarized in the table 2.1.

Core-shell latex

Table 2.2: *Synthesis of the core-shell Latices.*

Core-shell Latex (cross-linking $[mol.\%]$)	KS1 1.25	KS2 2.5	KS3 5	KS4 2.5
Core Latex $[wt.\%]$	20.1	18.9	21	19.5
Core Latex $[g]$	199.0	211.5	190.5	205.1
NiPA $[g]$	38.0	38.0	38.0	19.0
BIS $[g]$	0.6480	1.2959	2.5885	0.6470
KPS in 10 ml H_2O $[g]$	0.3834	0.3814	0.3812	0.3838
H_2O $[g]$	542.4	535.8	568.2	363.5
m_{PS}/m_{shell}	1.06	1.03	-	1.05

The seeded emulsion polymerization for the core-shell system under consideration here was done using 100 g of the core latex diluted with 320 g of deionized water together with 20 g of NIPAM and 1.43 g of BIS. No additional SDS was added in this step. After this stirred mixture has been heated to 80^oC, the reaction is started by the addition of 0.201 g of KPS (dissolved in 15 mL of water) and the entire mixture is allowed to stir for 4 h at this temperature. After cooling to room temperature the latex has been purified by exhaustive serum replacement against purified water (membrane: cellulose nitrate with a 0.10-μm pore width supplied by Schleicher and Schuell). The cells contain 750 ml. The purification was performed on circa 10 $wt.\%$ solution under 1, 2 bar nitrogen and used to concentrate the initial solutions and to adjust the salt concentration. The masses of the different reactants used for the synthesis of the different core-shell systems are summarized in the table 2.2.

Methods

Transmission electron microscopy

Samples for TEM were prepared by placing a drop of the 0.2 $wt.\%$ solution on a carbon-coated copper grid. After few seconds, excess solution was removed by blotting with filter paper. The cryo-TEM preparation was done on dilute samples (0.2 $wt.\%$). The sample was kept at room temperature and vitrified rapidly by the method described previously [66]. A few microliters of diluted emulsion were placed on a bare copper TEM grid (Plano, 600 mesh) held by the tweezers of the Controlled Environment Vitrification System (CEVS). The dimensions of the holes where the sample is absorbed and vitrified are $35 \times 35 \times 10$ μm. The excess liquid was removed with filter paper. Typically the film thickness where the particles are investigated ranges between 1 μm and the diameter of the particles ($\sim$100 nm). This sample was cryo-fixed by rapid immersing into liquid ethane cooled to -180^oC in a cryo-box (Carl Zeiss NTS GmbH). The specimen was inserted into a cryo-transfer holder (CT3500, Gatan, Munich, Germany) and transferred to a Zeiss EM922 EFTEM (Zeiss NTS GmbH, Oberkochen, Germany). Examinations were carried out at temperatures around -180^oC. The TEM was operated at an acceleration voltage of 200 kV. Zero-loss filtered images were taken under reduced dose conditions (<21000 e^-/nm^2) with an aperture $\alpha_0 = 10$ $mrad$ at a magnification of $16000X$. All images were recorded

Table 2.3: *Summary of the different parameters used for the normalization of the scattering intensity profile (see text for further details).*

Systems	c $[g/cm^3]$	$crosslinking$ $[mol.\%]$	$\frac{m_{core}}{m_{shell}}$	N/V $[nm^{-3}]$
Core	0.060	-	-	$9.62.10^{-8}$
KS1	0.032	1.25	1.19	$1.99.10^{-8}$
KS2	0.023	2.50	1.15	$2.79.10^{-8}$
KS3	0.035	5.00	1.04^1	$2.87.10^{-8}$

digitally by a bottom-mounted 16 bit CCD camera system (UltraScan 1000, Gatan). To avoid any saturation of the gray values all the measurements were taken with intensity below 15000, considering that the maximum value for a 16 bit camera is 2^{16}. Images have been processed with a digital imaging processing system (Digital Micrograph 3.9 for GMS 1.4, Gatan). The experiment at 45^oC were performed in an Oxford CT-3500 (now: Gatan, Pleasanton, CA) cryo-holder, and were examined in an FEI (The Netherlands) T12 G^2 dedicated cryogenic-temperature transmission electron microscope.

Dynamic light scattering

Dynamic light scattering (DLS) was done using a Peters ALV 5000 light scattering goniometer equipped with a He-Ne laser ($\lambda = 632.8$ nm). The temperature was controlled with an accuracy of 0.1^oC. The samples were highly diluted ($c = 2.5.10^{-3}$ $wt.\%$) to prevent multiple scattering and filtered through a 1.2 μm filter to remove dust. The salt concentration in KCl was set to 10^{-4} $mol.L^{-1}$ and 5.10^{-2} $mol.L^{-1}$. The measurements were performed at a scattering angle of 90^o for temperatures between 10 and 50 ^oC.

Small-angle X-Ray scattering

Small-angle X-Ray scattering experiments have been performed on both core and core-shell systems. Most of the SAXS measurements reported here have been performed at the ID2 beamline at the European Synchrotron Radiation Facility (ESRF, Grenoble, France). The diameter of the X-ray beam was 150 μm and the incident wave length equals to 0.1 nm. SAXS pattern were recorded with a two-dimensional camera located at a distance of 5 m from the sample within an evacuated flight tube. The background scattering has been subtracted from the data and corrections were made for spatial distortions and for the detector efficiency. The concentrations of the latices varies between 2 and 6 $wt.\%$ (see Table 2.3). For the latex concentrations used here we assume that the influence of interparticular interferences can be dismissed without problems and that the structure factor $S(q)$ is equal to 1 [17, 67].

In order to check the detector the same core solution has been measured on a modified Kratky camera for q between 0.03 and 4 nm^{-1}. The description of the camera and of the evaluation of the scattering is given elsewhere [17].

The density of the shell has been calculated considering the value of the density of the polystyrene core (1.0525 g/cm^3), the density of the core-shell for the KS2 at 25 ^oC (1.098 g/cm^3) and the mass ratio m_{PS}/m_{shell} determined gravimetrically (1.03) using the formula:

$$\varrho_{shell} = \frac{1-(m_{PS}/m_{shell})/(1+m_{PS}/m_{shell})}{\varrho^{-1}_{core-shell} - \varrho^{-1}_{core}(m_{PS}/m_{shell})/(1+m_{PS}/m_{shell})} \tag{2.1}$$

The shell density derives from this calculation is equal to 1.149 g/cm^3. The same calculation performed this time considering the density of the core particles (1.059 g/cm^3) and the mass ratio between the core particles and the shell polymerized in the second step of the polymerization m_{core}/m_{shell} (1.15) gives a value of 1.147 g/cm^3. The same calculation performed on the KS1 considering the density of the core-shell measured at 20^oC (1.098 g/cm^3) and the different mass-ratios ($m_{PS}/m_{shell} = 1.06$, $m_{core}/m_{shell} = 1.19$) gives respectively a density of 1.151 and 1.148 g/cm^3. The different results for the two systems obtained from the two calculations are in good agreement within the experimental error, which is mostly coming from the determination of the mass ratio by gravimetry. For the rest of the work the density for the PNIPAM and for the cross-linked shell will be considered equal to 1.149 g/cm^3. In this way the density value of the shell is slightly higher than the density of pure PNIPAM in water as determined by Shibayama and al. (1.140 g/cm^3) [1], which is natural considering the cross-linking of the system.

The electronic density has been calculated in $electrons/nm^3$ using the formula:

$$\varrho_e = \frac{N_A.\varrho.n_{e^-}}{M} \tag{2.2}$$

with ϱ the density of the system, M and n_{e^-} the molecular weight and the number of electrons per constituting molecules. From the density values the excess electronic density $\Delta\varrho_e$ of the cross-linked shell follows as 45.5 e^-/nm^3. The respective quantity of polystyrene is 7.5 e^-/nm^3 at 25 ^oC. These numbers define the contrast in SAXS of these polymers in water.

The scattering density profile have been normalized by the number of particles per volume N/V (in nm^{-3}) in order to obtain the scattering of one single particle I_0. The quantity N/V derives from the mass concentration of the dispersion c (in g/cm^3), from the ratio core/shell m_{core}/m_{shell} determined by gravimetry, and from the radius of the core R_c and its density (1.059 g/cm^3) as follows:

$$N/V = \frac{c.(m_{PS}/m_{shell})/(1+m_{PS}/m_{shell})}{(4/3)\pi\varrho_c R_c^3} \tag{2.3}$$

To this purpose the value of R_c was considered equal to 52 nm from the gaussian fit of the size distribution determined from the cryoTEM analysis (see section 2.2). The different parameters for the normalization of the curves are indicated in the table 2.3. Note that the mass ration core/shell of the KS3 has not been determined gravimetrically but derived from the phase diagram present in the section crystallization (see section 2.3).

2.1.3 Theoretical background

Flory-Rehner theory

The macroscopic state of a homogeneous neutral gel is described within the classical Flory-Rehner theory. Here we follow the exposition of this model given in Ref. [49]. Hence, it suffices to delineate the main steps.

The net osmotic pressure within the gel is given by

$$\Pi = \frac{k_b T}{a^3} \left\{ -\phi - \ln(1-\phi) - \chi\phi^2 + \frac{\phi_0}{N_{Gel}} \left[\frac{1}{2} \left(\frac{\phi}{\phi_0} \right) - \left(\frac{\phi}{\phi_0} \right)^{1/3} \right] \right\} \tag{2.4}$$

where k_B is the Boltzmann constant, a is the monomer segment length, χ is the Flory interaction parameter, ϕ is the polymer volume fraction, ϕ_0 refers to the polymer volume fraction at a reference state and N_{gel} is the average degree of polymerization of the polymer chain between two crosslinking points. For systems undergoing isotropic swelling, the swelling of the microgel can be described as the ratio of the average polymer volume fraction ϕ and the average polymer volume fraction ϕ_{ref} in the collapsed state

$$\frac{\phi}{\phi_{ref}} = \left[\frac{{R_{H,ref}}^3 - {R_c}^3}{{R_H}^3 - {R_c}^3} \right] \tag{2.5}$$

with R_H the hydrodynamic radius of the core shell at the temperature T and $R_{H,ref}$ the radius et the reference state after the complete collapse of the shell measured at 45^oC. R_c denotes the radius of the core particles determined from the cryogenized transmission electron microscopy. The Flory interaction parameter χ is given by

$$\chi = \frac{\Delta F}{k_b T} = \frac{\Delta H - T\Delta S}{k_b T} = \frac{1}{2} - A\left(1 - \frac{\Theta}{T}\right) \tag{2.6}$$

where $A = (2\Delta S + k_B)/2k_B$ and $\Theta = 2\Delta H/(2\Delta S + k_B)$. ΔS and ΔH are the changes in entropy and enthalpy of the process, respectively. It has been shown that χ increases nonlinearly with increasing concentration of polymer (see e.g. Ref. [68] and further literature cited therein)

$$\chi(T,\phi) = \chi_1(T) + \chi_2\phi + \chi_3\phi^2 + ... \tag{2.7}$$

with χ_1 corresponding to equation (3). Following Ref. [49] we will only consider the first order of the ϕ-expansion, which leads to the following expression for χ

$$\chi = \frac{\Delta F}{k_b T} = \frac{1}{2} - A\left(1 - \frac{\Theta}{T}\right) + \chi_2\phi \tag{2.8}$$

Thermodynamic equilibrium for the gel is attained when $\Pi = 0$, i.e., if the pressure inside and outside the gel is the same. Combining eq. 2.4 and eq. 2.8, the equilibrium line in the $T - \phi$ phase diagram is given by

$$T_{\Pi=0} = \frac{A\phi^2\Theta}{-\phi - ln(1-\phi) + \left(A - \frac{1}{2}\right)\phi^2 - \chi_2\phi^3 + \frac{\phi_0}{N_{Gel}}\left[\frac{1}{2}\left(\frac{\phi}{\phi_0}\right) - \left(\frac{\phi}{\phi_0}\right)^{1/3}\right]} \tag{2.9}$$

Small-angle X-ray scattering

The scattering intensity $I(q)$ measured for a suspension of particles with spherical symmetry may be rendered as the product of $I_0(q)$, the scattering intensity of an isolated particle, and $S(q)$, the structure factor that takes into account the mutual interaction of the particles:

$$I(q) = (N/V)I_0(q)S(q) \tag{2.10}$$

where N/V denotes the number density of the scattering objects. A previous discussion of S(q) for systems of spherical particles has demonstrated that the influence of the structure factor is restricted to the region of smallest q values when the concentration of the particles is small. Its influence onto the measured scattering intensity can therefore be disregarded in the present analysis. Hence, $S(q) = 1$ will be assumed in the following [67].

The scattering intensity of one single particle can be decomposed in principle in three terms [17, 63, 64, 67]:

$$I_0(q) = I_{part}(q) + I_{fluc,PS}(q) + I_{fluc,shell}(q) \tag{2.11}$$

$I_{part}(q)$ is the part of $I_0(q)$ due to the core-shell structure of the particles (i.e., the scattering intensity caused by composite particles having a homogeneous core and shell) [63, 64]. The core and the shell are characterized by different electron densities. $I_{fluc,PS}(q)$ and $I_{fluc,shell}(q)$ refer to the thermal fluctuation of the PS core and the PNIPAM shell respectively. The shell, however, does not consist of a solid material but of a polymeric network which exhibits static inhomogeneities and thermal fluctuations, for this reason we neglected the contribution of the fluctuation of the PS core and we only take into account $I_{fluc,shell}(q)$. For spherical symmetric particles with radius R, $I_{part}(q)$ is equal to $B^2(q)$ where the scattering amplitude $B(q)$ is given by.

$$B(q) = 4\pi \int_0^R \phi(r)[\varrho_{e,p}(r) - \varrho_{e,w}]r^2 \frac{sin(qr)}{qr} dr \tag{2.12}$$

The scattering contrast is the difference of the scattering length density of the polymer and the surrounding solvent $\Delta\varrho_e(r) = \varrho_{e,p}(r) - \varrho_{e,w}$. By multiplying the polymer fraction $\phi(r)$ profile by the scattering contrast respectively of the polystyrene for the core ($\Delta\varrho_{e,PS} = 7.5\ e.u/nm^3$) and of the cross-linked PNIPAM for the shell ($\Delta\varrho_{e,PNIPAM} = 45.5\ e.u/nm^3$; see section Methods), we obtained the electron density profile necessary for the calculation of the scattering intensity.

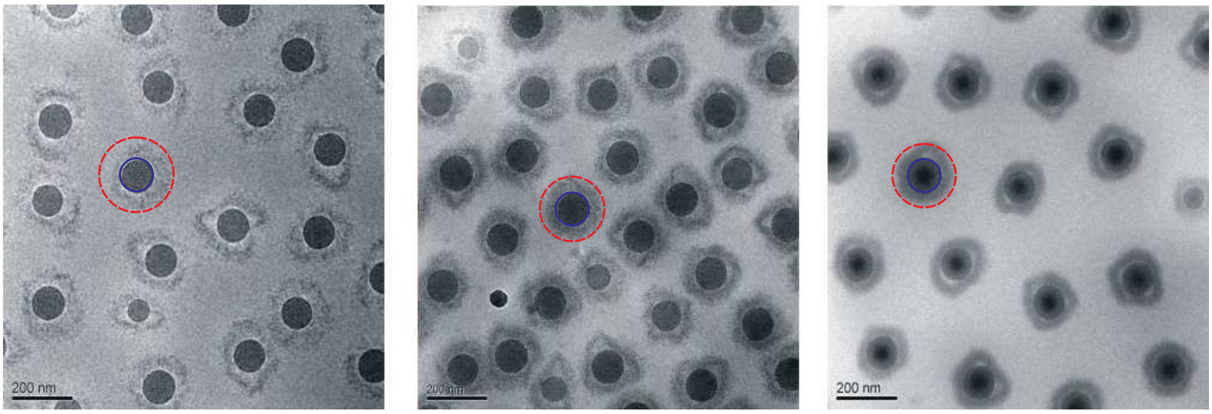

Figure 2.1: *Cryo-TEM micrographs of a 0.2 wt.% aqueous suspension of the PS/PNIPAM core-shell particles for different degrees of crosslinking: (a) KS1 1.25 M%, (b) KS2 2.5 M% and (c) KS3 5 M%. The samples were kept at room temperature before vitrification. The core consists of polystyrene and the corona of PNIPAM cross-linked with BIS. The full and dashed lines show the hydrodynamic radii respectively of the core and core-shell particles as determined by DLS.*

The polydispersity can be described by a normalized Gaussian number distribution [17, 67]:

$$D(R,\sigma) = \frac{1}{\sigma\sqrt{2\pi}} exp\left[-\frac{(R-\langle R\rangle)^2}{2\sigma^2}\right] \tag{2.13}$$

with $\langle R\rangle$ the average radius and σ the standard deviation. Here, it suffices to mention that the polydispersity smears out the deep minima of $I_{part}(q)$ to a certain extent [63, 64]. For the evaluation of the part of the scattering caused by the thermal density fluctuations within the shell $I_{fluc}(q)$ it is appropriate to use the empirical formula [63, 64]:

$$I_{fluc} = \frac{I_{fluct}(0)}{1+\xi^2 q^2} \tag{2.14}$$

where the average correlation length in the network is described by ξ. I_{fluc} contributes significantly only in the high q regime.

2.1.4 Results and discussion

Cryogenic electron microscopy

The synthesis of the core-shell particles proceeds in two steps [17]: First a poly(styrene) core is synthesized by conventional emulsion polymerization. The core particles thus obtained are practically monodisperse and well-defined. A radius of 52.0 nm and a polydispersity of 4% were derived from the cryoTEM micrographs (see section 2.2), whereas the dynamic light scattering gives a value of 55.0 nm between 8 and 45^oC. As expected the radius of the core particles as observed by DLS has no dependence on the temperature.

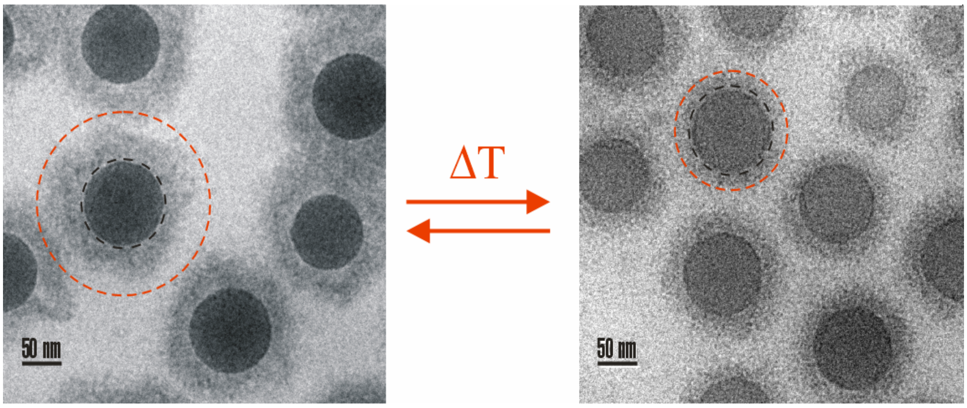

Figure 2.2: *Cryo-TEM micrographs of a 0.2 wt.% aqueous suspension of the PS/PNIPAM core-shell particles. The sample was maintained at 23° C (left-hand side) and 45° C (right-hand side) before vitrification. The cores consists of polystyrene and the corona of cross-linked PNIPAM with BIS. The circle around the core marks the core-radius determined by dynamic light scattering in solution. The circles around the entire particle gives the hydrodynamic radius R_H of the core-shell particles again determined by dynamic light scattering taken from Fig. 2.7*

It needs to be noted that the core particles bear a small number of chemically bound charges on their surface. This is due to the synthesis of the cores which proceeds through a conventional emulsion polymerization. These charges keep the solution stable even at high temperature. In a second step the thermosensitive shell is polymerized at higher temperatures (80^oC) onto these core particles in a seeded emulsion polymerization.

Fig. 2.1 shows the micrographs obtained for different degrees of crosslinking by cryo-TEM. For the analysis a suspension of the particles is shock-frozen in liquid ethane. The water is supercooled by this procedure to form a glass and the particles can directly be studied upon in-situ. Fig. 2.1 shows that the core-shell particles are indeed narrowly distributed. Moreover, the PNIPAM shell is clearly visible in these pictures without using any contrast agent. All the polystyrene cores observed are covered by the PNIPAM shell leading to a partially spherical shape. This is accompanied by parts of the network of higher and lower transmission which can be assigned to the density fluctuations and the spatial inhomogeneities in the network. This corresponds to the additional contribution seen in SAXS measurements of similar core-shell particles. As argued in ref. [49, 63, 64], the scattering intensity contains a term related to spatial inhomogeneities of the network found for macroscopic networks and predicted by theory [3]. Hence, Figure 2.1 provides a direct visual proof of an important conclusion drawn from previous scattering measurements. Moreover, the present micrographs suggest that these fluctuations lead to a slightly irregular shape that may be also embodied in the contribution to the scattering intensity measured at higher scattering angles. The buckling of the shell which is decreasing with increasing crosslinking can be related to the instabilities of swelling gels occurring at the surface of swollen gels affixed to solid substrate. A review of the studies of this effect related to macroscopic systems was given by Boudaoud et al. [69].

Figure 2.1 also demonstrates that the thermosensitive shell is in some cases not fully attached to the core. This sheds new light on the second step in the synthesis of the core-shell particles: The analysis of the core particles by SAXS showed that the addition of 5% NIPAM during the synthesis of the core leads to a thin shell of PNIPAM at the surface of the core particles [17]. The shell will be bound to the core most probably by chain transfer of the growing PNIPAM network to the thin PNIPAM-shell covering the core. The micrographs demonstrate, however, that this binding is incomplete. At high temperatures during the synthesis of the shell the growing network is collapsed onto the core. Thus, the shell is expected to be rather homogeneous at temperatures above the volume transition. This was shown experimentally by SANS [63]. It will also be shown below that the volume fraction ϕ_0 which follows from the Flory-Rehner analysis will be high and demonstrate the small degree of swelling of the network during synthesis. However, chain transfer does not lead to complete attachment of the shell to the cores in this step. Hence, the three-dimensional swelling of the shell below the transition must lead to a partial detachment of the shells. Fig. 2.1 demonstrates that this effect is decreasing with increasing degree of cross-linking as expected.

The phase transition in the shell can be directly imaged by CryoTEM analysis. Fig. 2.2 is an example of the micrographs resulting from the system KS2 quenched from 45^oC. Here we chose a higher magnification to display the details of the particles more clearly. Naturally, this experiment is more difficult because vitrification must be much faster than the relaxation time characterizing the shrinking kinetics of the particles. However, Fig. 2.2b in comparison to 2.2a clearly shows that the particles have shrunken considerably. Moreover, the shell has been compacted by this shrinking process and provides now a tight envelope of the cores. This is expected given the fact that the shell has been attached to the core at even higher temperatures. Moreover, the compactness of the shell had already been deduced from SANS-measurements [63, 64].

Small-angle X-ray scattering

Core particles

First the scattering intensity profile has been evaluated for the core particles. Fig. 2.3 presents the experimental scattering intensity of one isolated particles $I_0(q)$ obtained from the synchrotron and from the modified Kratky camera. Both measurements superpose until $q = 0.6\ nm^{-1}$, even if the resolution of the synchrotron is better for the small q. Above this q value the signal is becoming to noisy to be evaluated in opposition to the Kratky camera, which is more appropriate for the higher q cause of its shorter distance source detector. For this reason the following scattering intensities $I_0(q)$ have been evaluated only up to 0.6 nm^{-1}. A simple fit considering an homogeneous polystyrene particle of 52 nm succeeds to describe the position of the side maxima. At higher q-values the measured scattering is considerably higher than the one calculated for a homogeneous sphere. This fact confirms the presence of a thin PNIPAM layer at the interface.

The best fit was obtained for a core-shell profile with a dense polystyrene core of 48 nm. The SAXS analysis of the core particles demonstrates furthermore that a small fraction of PNIPAM is located in a thin 2 nm shell at the surface of the particles. The electron density of this shell (23.0 $e^{-}nm^{-3}$) exhibits a considerably higher density than the core (7.5 $e^{-}nm^{-3}$) and contributes considerably to the scattering intensity. The sensitivity of

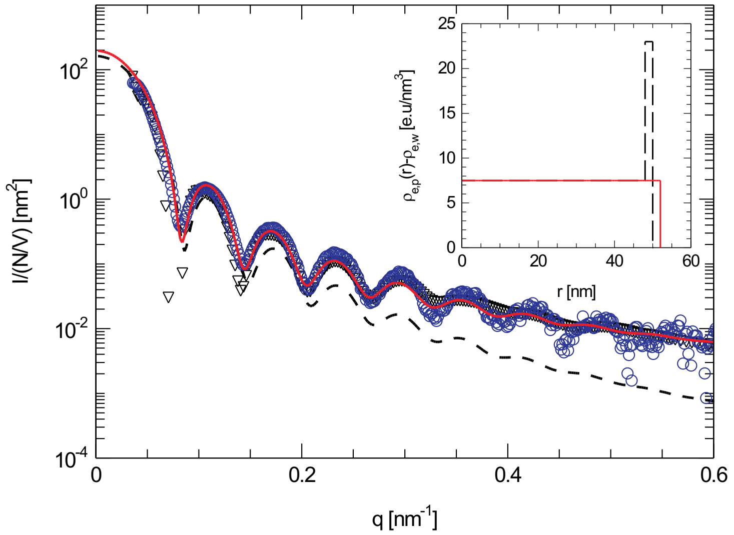

Figure 2.3: *Scattering intensity of an isolated particle, $I_0(q) = I(q)/(N/V)$ obtained for the core particles from the synchrotron (circles) and from the modified Kratky camera (triangles). The dashed line presents the scattering intensity profile of a pure 52 nm polystyrene particles. The solid line is the best fit obtained for a core-shell system with a 48 nm polystyrene core and a 2 nm thin PNIPAM shell with an electronic density of 23 e^-/nm^3 (see inset).*

the SAXS to detect thin polymer layer at solid core interface has been already found in former studies for similar systems [64] and also in the adsorption of surfactant on core latices [70]. The fit procedure also shows that the size distribution of the core particles is rather small with a polydispersity of 5.0%. Considering the electron density of the PNIPAM calculated formerly this value corresponds to a polymer volume fraction of 0.5. The mass percentage of PNIPAM in the core deriving from this analysis is 6.7 %, which remains rather close to the 5 % introduced at the beginning of the copolymerization of the core particles. Moreover the average size of 50 *nm* is in good agreement with the average value obtained by TEM and cryoTEM with a deviation of less than 4 % (see section 2.2). The deviation with the hydrodynamic radius of 55 *nm* determined by DLS is much higher. Nevertheless this value refers to an intensity weighted average whereas the two others methods refer to number weighted average. A number distribution obtained from the CONTIN analysis will thus lay around 50 *nm* in good agreement with the others methods.

Core-shell particles

The same analysis has been performed on different core-shell systems. Fig. 2.4 presents the different $I_0(q)$ obtained for different degrees of crosslinking. $I_0(q)$ describes a single maximum for 1.25 *mol.%* crosslinking, then two maxima for 2.5 *mol.%* and three maxima for 5 *mol.%*. Moreover the intensity in the low q region is increasing. This clearly indicates that increasing the degree of crosslinking leads to more defined and more compact particles. Moreover the first maximum is slightly shifted to the left which is an indication of a decrease in the size of the particles in agreement with the direct observation done by cryoTEM. A parabolic profile has been considered for the shell as proposed by Berndt et al. in their investigation of PNIPAM microgels [60], PNIPAM/PNIPMAM [61, 71] and PNIPMAM/PNIPAM composite microgels [62].

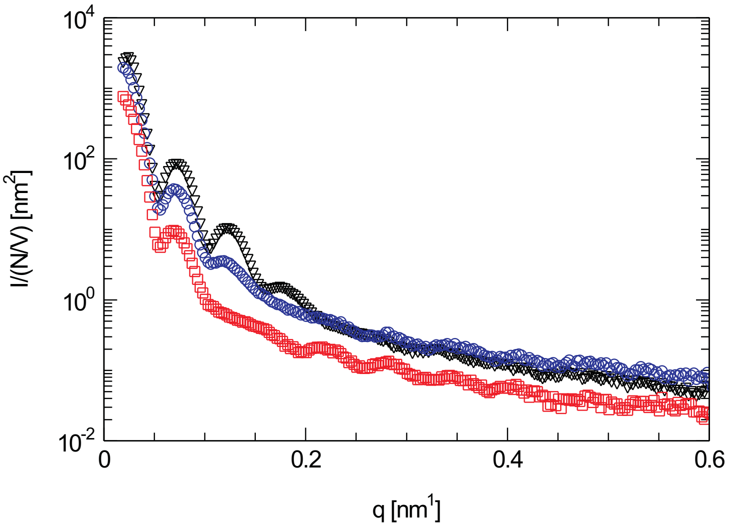

Figure 2.4: *Scattering intensities* $I_0(q) = I(q)/(N/V)$ *obtained for the different degrees of crosslinking: KS1 (1.25 mol.%) (squares); KS2 (2.5 mol.%) (circles) and KS3 (5 mol.%)(triangles).*

Table 2.4: *Fit parameters used for the calculation of the scattering intensity profile* $I_0(q)$ *(see fig. 2.5).* m_{core}/m_{shell}, ξ *and* R *are the mass ratio core/shell, the correlation length and the overall size of the systems derived from this analysis.* R_H *is the hydrodynamic radius derived from the dynamic light scattering at 23°C (see figure 2.7). The corresponding polymer volume fraction profile are given in the fig. 2.6.*

Systems	K	R_{hw} $[nm]$	σ [nm]	PDI [%]	$\frac{m_{core}}{m_{shell}}$	ξ $[nm]$	R $[nm]$	R_H [nm]
KS1	0.160	85	20	8.0	1.38	10	105	124.6
KS2	0.284	77	17	8.0	1.14	7	94	112.4
KS3	0.435	72	12	6.0	1.03	7	84	107.0

The following relation has been used to describe the polymer volume fraction profile for the crosslinked shell [61, 62, 71]:

$$K\phi(r) = \begin{cases} 1 & : \quad r \leq R_c \\ 1 - (R_{hw} - r + \sigma)^2/(2\sigma^2) & : \quad R_c < r \leq R_{hw} \\ (r - R_{hw} + \sigma)^2/(2\sigma^2) & : \quad R_{hw} < r \leq R_{hw} + \sigma \\ 0 & : \quad R_{hw} + \sigma < r \end{cases} \tag{2.15}$$

K is a prefactor, R_c is the radius of the core and R_{hw} is the half-width radius and σ the half-width.

The profile for the core has been kept identical to the one derived from the core analysis in the precedent section. The profile of the core-shell particles has been then introduced in equation 2.12 to calculate $I_{part}(q)$. The polydispersity which is smearing the maximum has been introduced in term of a Gaussian distribution. Fig. 2.5 displays the different scattering intensity profiles normalized by N/V and the best fit obtained for each system. The dashed lines refer to $I_{part}(q)$ and the dotted lines refer to $I_{fluc}(q)$. The best fit derives from the sum of these two contributions and is displayed by the solid line. The fits provide a good description of the experimental set of data on the q range

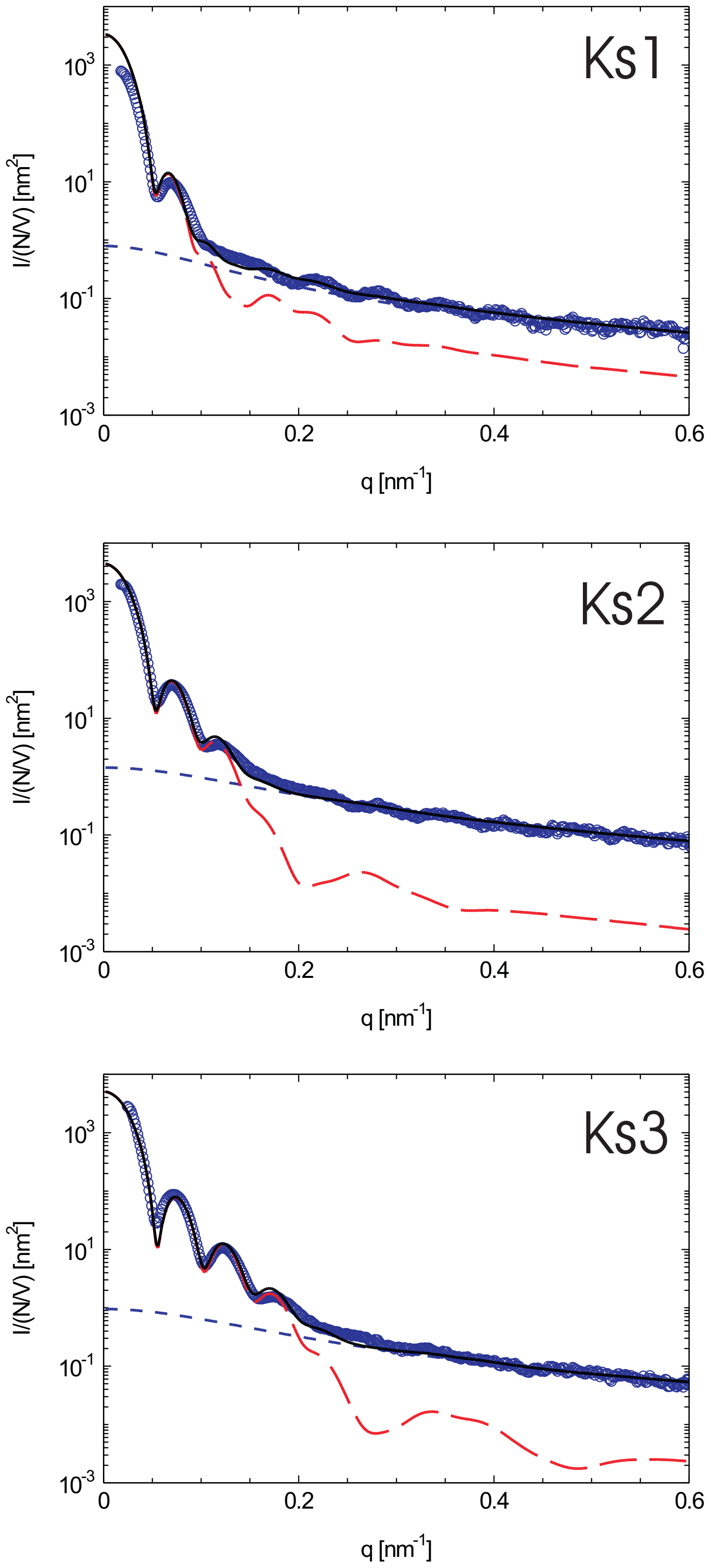

Figure 2.5: *Form factor* $P(q) = I(q)/(N/V)$ *obtained for different degree of crosslinking: KS1 (1.25 mol.%), KS2 (2.5 mol.%), KS3 (5 mol.%). The circles display the experimental measurements. The long dashed lines are the calculated* $I_{part}(q)$*, whereas the dashed lines represent the contribution of the thermal density fluctuations* $I_{fluc}(q)$*. The sum of this two contributions are given by the solid lines, which correspond of the best fit of the experimental data. The fit parameters are given in the table 2.4 and the corresponding polymer volume fraction profile in the fig. 2.6.*

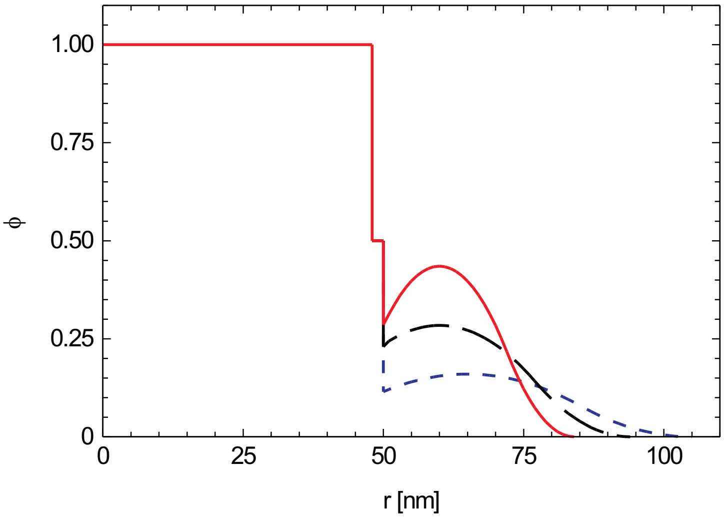

Figure 2.6: *Radial polymer effective volume fraction $\phi(r)$ obtained from the SAXS analysis for the different degrees of crosslinking: KS1 (1.25 mol.%) (dotted line); KS2 (2.5 mol.%) (dashed line), KS3 (5 mol.%)(solid line). The profiles consist on a dense 48 nm polystyrene core with a 2 nm thin PNIPAM shell onto which a the crossslinked shell has been polymerized. The analysis considers a parabolic profile for the shell as given in equation 2.15. The different fit parameters are given in table 2.4.*

investigated. The different fit parameters are summarized in the table 2.4. The polymer volume fraction profile can be extracted from the fit of the scattering experiments and is presented in Fig. 2.6. As already observed by cryoTEM, increasing the degree of crosslinking leads to a more compact structure and to a more pronounced depletion at the core/shell interface . The core/shell mass ratio derived from the different profiles is in good agreement with the value obtained by gravitometry, except for the lower degree of crosslinking. This could be attributed by a lack of contrast for a too diffuse shell. Moreover the size is also decreasing as already observed from the dynamic light scattering experiments (see fig. 2.7). Nevertheless the radius is about 16, 16 and 21 % smaller compared to the hydrodynamic radius of the KS1, KS2 and KS3 determined by dynamic light scattering. This was attributed in a former study to the presence of dangling chains which could not be detected by SAXS or SANS but only by DLS [63]. Nevertheless the direct imaging of the particles by cryoTEM evidenced the strong buckling of the particles.

The discrepancy between the two methods can be explained as follows: Microgels are dynamic structures which exhibit thermal fluctuations. Moreover, the synthesis leads to the buckling up of the shell as discussed already. Hence, the shape of the particles is not perfectly spherical. A rotational average hence will result in a larger size. This point will be discussed in further details in the next chapter dedicating to the quantitative analysis of the cryo-TEM micrograhs (see chapter 2.2).

Thermodynamics of the phase transition

The volume transition within the shell can easily be studied by dynamic light scattering (DLS). Figure 2.7 shows the dependence of the hydrodynamic radius R_H of the composite

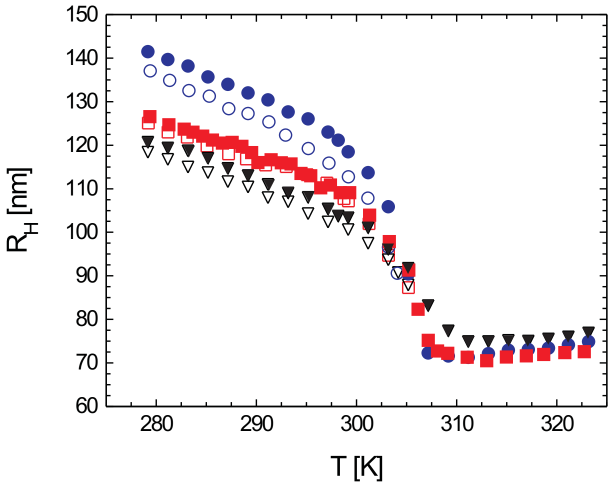

Figure 2.7: *Hydrodynamic radii of the core-shell latexes versus temperature for different degrees of crosslinking, as determined by DLS (circles: 1.25 mol.%, squares: 2.5 mol.%, triangles: 5 mol.%). Full symbols represent the measurements without addition of salt, whereas hollow symbols display the measurements performed by adding* 5.10^{-2} $mol.L^{-1}$ *KCl.*

microgels determined by DLS as function of the temperature. R_H decreases gradually with temperature until a sharp volume transition from swollen to unswollen states takes place, reaching a final collapsed size at a transition temperature between 34 and 38^oC depending on the degree of crosslinking. Increasing the degree of crosslinking the transition becomes more continuous and the collapse state is shifted to higher temperatures. Without addition of salt this process is thermoreversible without any hysteresis.

The comparison between the overall size observed from the micrographs and the hydrodynamic radius as determined by the DLS can be observed in the Fig. 2.7. The hydrodynamic radius R_H as measured by DLS indicated in each case as a shed circle around one particle evidently provides an appropriate measure of the average radius of the particles. Moreover we found that the overall radius of the particles from these micrographs is in good agreement with the hydrodynamic radius measured at 45^oC (dashed circle). This indicates that the process of quenching is sufficiently fast to preserve the high-temperature structure. This finding is quite important inasmuch it shows that the method of preparation does not disturb the structure of the thermosensitive particles. This fact is of great importance when determining the effective volume fraction of the particles in a concentrated suspension. Addition of 5.10^{-2} $mol.L^{-1}$ KCl leads to a slight shrinking of the particles. This phenomenon has been already investigated in a recent study [72]. The addition of salt screens the residual electrostatic interaction of the particles. Hence, at higher temperatures the dispersions become unstable and aggregate [72]. For the systems under consideration aggregation takes place above 32^oC for the KS1 and about 33^oC for the KS2 and KS3. Evidently, experiments aiming at an understanding of the flow behavior of stable suspensions must be done below these temperatures. On the other hand, salt must be added for a sufficient screening of the electrostatic interaction in order to obtain a model dispersions that interacts solely through steric repulsion.

We can now discuss the modeling of the swelling data shown in Fig. 2.7 in terms of the Flory-Rehner theory. Parameter of the different sets of data is the degree of crosslinking.

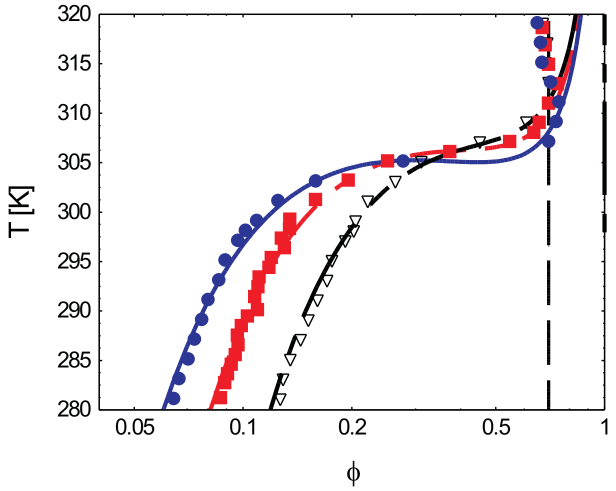

Figure 2.8: *Experimental phase diagram* $T - \phi$ *for different degrees of crosslinkings (full circles: 1.25 mol.%, full squares: 2.5 mol.%, hollow triangles: 5 mol.%). Lines present the fits obtained from eq.(2.9]. The vertical dashed line marks the reference volume fraction* $\phi_0 = 0.7$ *in the collapsed state.*

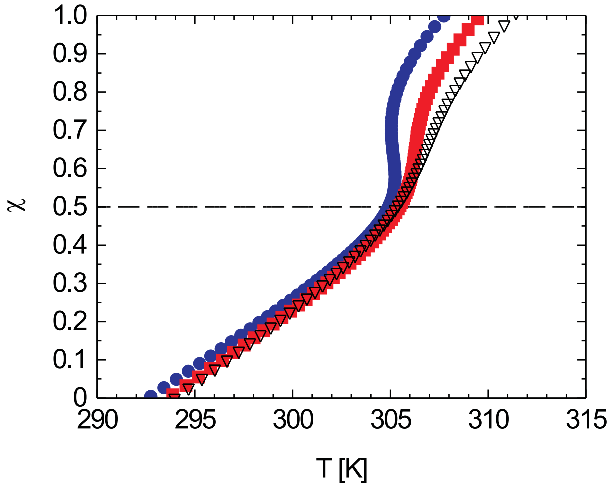

Figure 2.9: *Solvent parameter* χ *as determined from the fits of fig. 2.8 for different degrees of crosslinking (full circles: 1.25 mol.%, full squares: 2.5 mol.%, hollow triangles: 5 mol.%). Decreasing the degree of crosslinking the PNIPAM network shrinks upon heating from a continuous to a discontinuous fashion to reach a collapsed state for* χ *=1.* χ *=0.5 is indicated by the dashed line and lays approximately at 32°C, which corresponds to the LCST of pure PNIPAM in aqueous solution.*

Table 2.5: *Parameters of the Flory-Rehner fit. (eq. 2.9 and Fig. 2.8).*

	KS1	KS2	KS3
n(BIS)/n(NiPAM) [mol.%]	1,25	2,50	5,00
ϕ_0	0,7	0,7	0,7
A	-8,7	-8,7	-8,7
χ_2	0,9	0,9	0,9
Θ [K]	312	314	316
N_{Gel}	80	45	22
LCST [^{o}C]	31.7	32.3	32.2
$T(\chi = 1)$ [^oC]	35.1	36.2	38.2

The fit procedure used to model the phase transition is the same as reported recently [49]. The fits are presented together with the experimental data as shown in the $T-\phi$ diagram (Fig. 2.8). The resultant fitting parameters are summarized in the table 2.5. Considering that only the amount of crosslinker is changing, we keep the same value for ϕ_0, A and χ_2 for all the systems and we only vary θ and N.

For the present system the best agreement for the reference polymer volume fraction in the collapsed state has been found for $\phi_0 = 0.7$. This value has already been expected from the previous analysis of the particles by SAXS and SANS [63]. Indeed as reported by recent nuclear magnetic resonance measurements water molecules are still present in the shell above the LCST but they are strongly confined [58].

The N values (see table 2.4) found are proportional to the degree of crosslinking but are about two times larger than those corresponding to the crosslinking in a homogeneous network. A content of 2.5 $mol.\%$ of the crosslinker BIS would correspond to N_{gel} =20. This discrepancy can be traced back to the inhomogeneities in the PNIPAM microgels. Indeed, Wu et al. [73] investigated the polymerization of NIPAM and BIS during the microgel synthesis. The crosslinker was found to be consumed faster than the NIPAM indicating that the particles are unlikely to have a uniform composition. This finding has been confirmed by SAXS and SANS, revealing that the segment density in the swollen state is not homogeneous, but gradually decays at the surface [60, 63]. Moreover high-sensitive calorimetric study have confirmed this assumption [55]. Given the various uncertainties of the Flory-Rehner analysis, the present fits seem to provide a sufficient description of the data. Moreover, it should be kept in mind that the original theory has been developed for macroscopic, three-dimensional networks while it is applied here to microscopic systems which can swell only along the radial direction.

Fig. 2.9 displays the evolution of the solvent parameter χ derived from the fit from the fig. 2.8 as function of the temperature for the three systems. The LCST then corresponds to the temperature where χ is equal to 0.5. We found that increasing the cross-linking slightly shifts the LCST to higher temperature between 1.25 and 2.5 $mol.\%$ crosslinker, but the LCST found from this analysis is rather close to 32^oC which corresponds to the LCST of linear PNIPAM chains [55]. On the contrary the temperature where the shell is totally collapsed obtained from $\chi = 1$ shifts from 35.1 to 38.2 ^oC with increasing crosslinking, which can be attributed to a higher rubber elasticity of the network. This illustrates the transition from a sharp to a continuous volume transition by increasing the crosslinking of the shell.

The present analysis thus demonstrates that the core-shell microgels can be modelled in the same way as macroscopic systems.

2.1.5 Summary

In this chapter, composite PS/PNIPAM core-shell microgels with different degrees of crosslinking have been synthesized and characterized by cryogenic transmission electron microscopy, small-angle X-rays scattering and dynamic light scattering. The analysis demonstrates that the shell forms a well-defined network around the practically monodisperse core particles. Increasing the degree of crosslinking was also found to lead to smaller and denser particles. Moreover, direct imaging of the particles by Cryo-TEM shows the inhomogeneities within the network. Cryo-TEM shows also the buckling of the shell caused by the one-dimension swelling of the shell. This buckling effect which is well-known from macroscopic systems leads to a slightly irregular shape partially explaining the discrepancies between the SAXS and the DLS. Moreover a parabolic density profile for the shell has been evidenced by SAXS. The volume transition within the shell of these particles can be described very well by the Flory-Rehner theory. All results demonstrate that the two-step synthesis of the particles leads to well-defined particles suitable as model systems for studying the dynamics of concentrated suspensions.

2.2 Quantitative analysis of polymer colloids by normal and cryo-transmission electron microscopy.

2.2.1 Introduction

For many decades, transmission electron microscopy (TEM) is one of the most important techniques for the study of nanostructured materials. In recent years, cryogenic TEM (cryo-TEM) has greatly enlarged the scope of this technique and has thus become an indispensable tool of biological research [74–77]. Aqueous solutions containing e.g. viruses are vitrified by shock-freezing in liquid ethane. Thus, thin films of vitrified solutions can be analyzed by TEM. Evidently, cryo-TEM allows us to study sensitive biological and colloidal [78–85] structures in-situ, that is, in aqueous solution. Thus, there is no need for any further preparatory step. Up to now,there is a large number of morphological studies using cryo-TEM [22, 66, 86–88]. However, there are only few investigations which evaluate the cryo-TEM micrographs in a quantitative manner [75, 76, 78–82].

In a similar fashion, small-angle X-ray scattering (SAXS) [67, 88, 89] and small-angle neutron scattering (SANS) [90] present well-established tools for the analysis of nanostructures. There is a huge number of publications in which one of these methods has been used to analyze particulate structures in solution and the literature in this field is hard to overlook.

Both SAXS and Cryo-TEM are sensitive toward the local electron density in the object and thus lead to similar information about the sample under scrutiny. In principle, the gray scale of TEM-micrographs could be evaluated to yield the electron density of the sample. This in turn will lead directly to the SAXS-intensities and vice versa. To the authors' best knowledge, this obvious relation between SAXS and TEM has hardly been exploited yet. The reasons for this are given by the fact that the quantitative evaluation of TEM-micrographs presents a difficult task because of the multiple scattering of the electrons in thick samples [76, 91–93]. Moreover, any staining procedure or other preparation of the sample will lead to irreversible changes and render a quantitative comparison between TEM and SAXS impossible.

Here we present a quantitative comparison between the analysis of a colloidal system by cryo-TEM and SAXS. Following previous work by Langmore et al. [80, 81], we evaluate the local excess electron density from the gray scale of the cryo-TEM micrographs. In particular, we calculate the SAXS-intensity directly from the cryo-TEM micrograph and compare these results to measured intensities.

As an example for this analysis we first chose aqueous dispersions of the core particles described in the chapter 2.1, which serves as a simple model for particles with well-known structure. Then we investigate the core-shell particles also presented in the previous chapter. The reason for the choice of this system for the present purpose is given by the fact that core-shell microgels PS/PNIPAM have already been the subject of a number of studies employing SAXS and SANS [17, 63, 64] including the SAXS analysis described in the section 2.1.4. In the section 2.1.4, it has been also demonstrated that cryo-TEM is well-suited to investigate the volume transition and the structure of composite PS/PNIPAM core-shell. Hence, this system is well-suited for a quantitative comparison of SAXS and cryo-TEM.

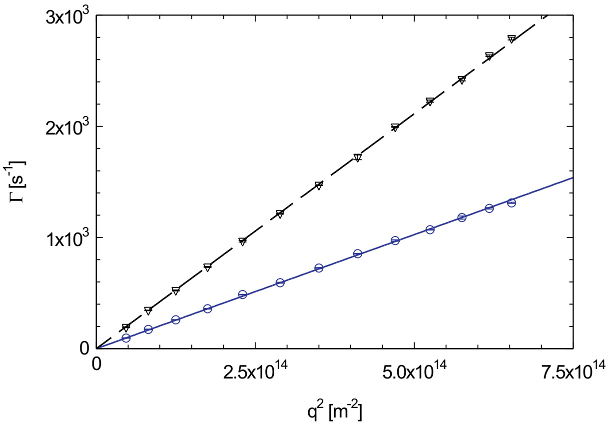

Figure 2.10: *Plot Γ versus q^2 for the core (down triangles) and core-shell (circles) particles measured at 23°C. The diffusion coefficient D_0 of both systems is obtained from the slope of the linear extrapolation given by the dashed and solid lines.*

This chapter is organized as follows: In section 2.2.2 the particles and methods used in this study are presented while section 2.2.3 gives the theoretical background of contrast in electron microscopy. In section 2.2.4 the analysis of the TEM and cryo-TEM micrographs is first validated using homogeneous polystyrene particles carrying a thin layer of PNIPAM. Moreover, the effect of the focusing, dose, sample thickness and energy filtering will be discussed. Finally, the quantitative comparison between the cryo-TEM micrographs of the core-shell system with the respective SAXS-data described in the chapter 2.1 will be given.

The object of the present chapter is three-fold: First, we present a method for the quantitative evaluation of TEM and cryo-TEM pictures which is validated using a simple model system (core V2). Second, we demonstrate that the analysis of such colloidal particles by cryo-TEM and SAXS (see section 2.1.4) can be treated on equal footing and supplement each other in a nearly ideal fashion. Third, the combination of these methods leads to a detailed analysis of a microscopic thermosensitive network and can be compared to earlier investigations by SAXS and SANS carried out on comparable core-shell particles [17, 60–64, 71, 94].

2.2.2 Experimental

Materials

All particles used herein have been synthesized and purified as described in a preceding section (see section 2.1.2). The present analysis was performed on the core particles and on the core-shell particles containing 2.5 $mol.\%$ crosslinker (KS2).

Methods

TEM and cryo-TEM were performed as described in the section 2.1.2 as well as the density measurements. Dynamic light scattering experiments were carried out at 23^oC as described in the section 2.1.2 except that in this case the decay rate Γ was obtained from the second cumulant analysis for scattering angle from 30 to 150^o with an increment of 10^o. As $\Gamma = D_0 q^2$, the diffusion coefficient was determined by linear extrapolation of Γ versus q^2, and the hydrodynamic radii of the core and of the core-shell were determined at 55 nm and 113 nm via Stokes-Einstein equation (see fig. 2.10).

2.2.3 Theory

Contrast transfer function

In principle, the image formation in an electron microscope can be described in terms of the first order theory for amplitude and phase contrast. The relationship between object density, phase and scattering contrast is usually described by the contrast transfer function $CTF(\alpha)$ as function of spatial frequency [78–81, 93]. Considering only the contribution of electron optics, the relationship between object density and the electron intensity can be written as [93, 95]

$$F_i(\alpha, \phi) = CTF(\alpha) \cdot F_0(\alpha, \phi) 2A(\alpha) f(\alpha)/\lambda \tag{2.16}$$

where $F_i(\alpha, \phi)$ is the Fourier transform of the image intensities, $F_0(\alpha, \phi)$ the Fourier transform of the object density, ϕ the azimuthal angle, $A(\alpha)$ the objective aperture function (1 for $\alpha < \alpha_0$, 0 for $\alpha > \alpha_0$) and $f(\alpha)$ the molecular scattering amplitude. The Broglie wavelength λ can be calculated relativistically in the case that the kinetic energy E used for the measurement is close to the rest energy:

$$\lambda = h[2m_0 E(1 + e/2E_0)]^{-1/2} \tag{2.17}$$

with E the electron energy (here 200 keV), and E_0 the rest energy electron ($E_0 = m_0 c^2 = 511\ keV$)(with $m_0 = 9.10912.10^{-31}\ kg$: rest mass, $c = 2.9979.10^8\ ms^{-1}$: speed of light). Given the above approximations, the contrast transfer function $CTF(\alpha)$ can be expressed through

$$CTF(\alpha) = [sin\chi(\alpha) + Q(\alpha) cos\chi(\alpha)] \tag{2.18}$$

with $\chi(\alpha) = 2\pi/\lambda\,(-C_s\alpha^4 + \Delta f \alpha^2/2)$ where C_s is the coefficient of spherical aberration and Δf the defocus. The function $sin\chi(\alpha)$ is the phase contrast transfer function. $Q(\alpha)$ refers to the amplitude contrast transfer function. It represents the maximum contribution from amplitude contrast relative to that deriving from phase contrast. At low resolutions $f(\alpha)$ and $Q(\alpha)$ can be considered constant and the effects of spatial and temporal coherence are ignored, because they are expected to be negligible [96].

The ratios of the Fourier transformations of the core particles at different defoci have been compared to the ratio of the theoretical values (equation 2.18) with Q as adjustable parameter (see fig. 2.11). We determined the value of Q that best describes changes in the images due to defocus as described by Langmore and Smith [80]. An empirical value of $Q = 0.14$ was found. Fig. 2.12 presents the different $CTF(\alpha)$ obtained for different defoci. For a defocus $\Delta f = 0\ nm$, the $CTF(\alpha)$ is almost constant up to approximately

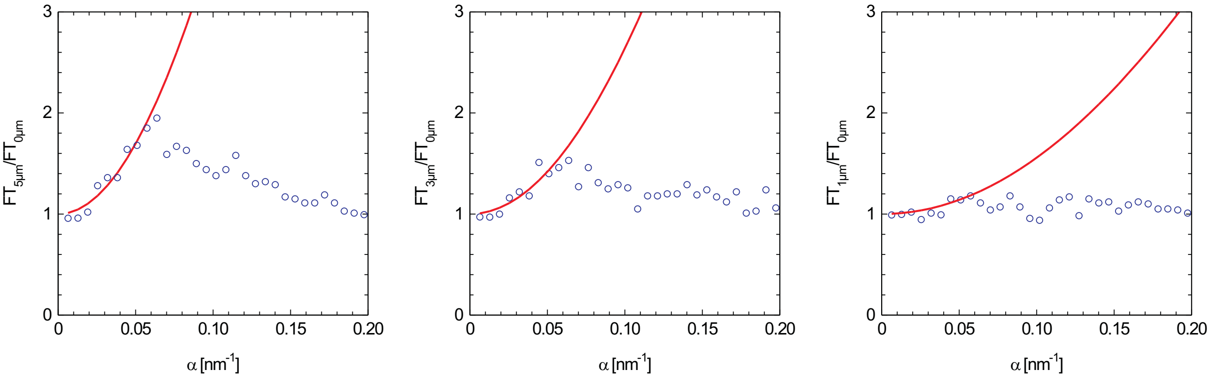

Figure 2.11: *Determination of $Q(\alpha)$ assuming $Q(\alpha) = cste$ (low resolution). The micrographs of a core particle are taken at different defoci and Fourier transformed. The ratio of the Fourier transformations of different defoci (5 µm, 3 µm and 1 µm) are compared to the theoretical values (equation 2.18) with Q as adjustable parameter. The theoretical values are plotted assuming the instrumental parameters of the Zeiss EM922 ($\lambda = 0.0025$ nm, aberration coefficient $C_s = 1.2$ mm). The best description of the experimental data was obtained for $Q = 0.14$.*

0.5 nm^{-1}. Considering the good contrast of our pictures, there was no need to go out of focus. Hence, a compensation of the $CTF(\alpha)$ was not required in the following study.

Thus, phase contrast can be neglected if the image are taken in-focus, that is, $\Delta f = 0\ nm$. Moreover, the following analysis will be restricted to the region of low spatial resolution. From the above discussion of the $CTF(\alpha)$ it is evident, that the range of spatial frequencies must hence be smaller than circa 0.5 nm^{-1}. This leads to circa 2 nm minimal spatial resolution which is smaller than the smallest object which can be seen on the micrographs presented in this study. Hence, it suffices to discuss the evaluation of the images solely in terms of amplitude contrast.

Amplitude contrast

Amplitude contrast is brought about by scattering processes that can be elastic or inelastic. The total electron scattering cross section $\sigma_T(\alpha_0)$ therefore expressed as the sum of the elastic and inelastic cross-sections [80, 81, 93].

$$\sigma_T(\alpha_0) = \sigma_{el}(\alpha_0) + \sigma_{inel}(\alpha_0) \tag{2.19}$$

Elastically scattered electrons are usually scattered through large angles and thus largely contribute to the contrast [93]. The transmission depends on the objective aperture α_0, the electron energy E, the mass-thickness $x = \varrho t$ (ϱ: density, t: thickness) and the material composition (atomic weight A and atomic number Z). The inelastic scattered electrons are mainly transmitted through the objective aperture. In the case of energy filtered electron microscope, the inelastic part will be removed nearly totally. This will enhance the amplitude contrast considerably. Hence, both elastic and inelastic processes must therefore be taken into account when calculating the gray scale of the images [80, 81].

The differential elastic cross sections $d\sigma/d\Omega$ were calculated using the Dirac partial-wave

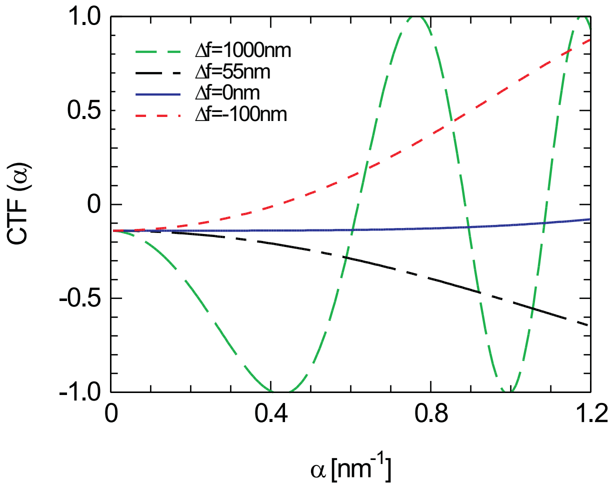

Figure 2.12: *Calculated contrast transfer function for different defoci. The values are plotted assuming the instrumental parameters of the Zeiss EM922 ($\lambda = 0.0025$ nm, aberration coefficient $C_s = 1.2$ mm [93]).*

Table 2.6: *Total elastic cross sections (σ_{el}) and partial elastic cross-sections $\sigma_{el}(\alpha_0)$ calculated from the Dirac partial-wave analysis using the NIST electron elastic-scattering cross-section database [103]. The inelastic cross-sections σ_{in} have been calculated from eq. 2.24 with the expression given by Wall [104]. All cross-sections have been derived in pm^2 for an acceleration voltage of 200 kV for an aperture $\alpha_0 = 10$ mrad.*

Z	σ_{el}	$\sigma_{el}(\alpha_0)$	σ_{in}
1	2.26	1.18	32.41^1 11.22^2
6	50.48	27.85	79.38
7	54.12	34.23	85.74
8	56.89	39.57	91.66

^{1} equation 9 ^{2} empirical

analysis described by Walker [97]. The scattering potential was obtained from the self-consistent Dirac Hartree Fock (DHF) charge density for free atoms [98, 99] with the local exchange potential of Furness and McCarthy [100]. The numerical calculations were performed with the algorithm described by Salvat and Mayol [101]. Further details have been given by Jablonski et al. [102]. The calculation was done using the NIST electron elastic-scattering cross-section database (SRD 64) (version 3.1) for an energy of 200 keV (see fig. 2.13 and table 2.6) [103]. Given the differential cross sections $d\sigma/d\Omega$, the number of electrons elastically passing through an aperture α_0 can be expressed through the partial elastic cross-section $\sigma_{el}(\alpha_0)$:

$$\sigma_{el}(\alpha_0) = \int_{\alpha_0}^{\pi} \frac{d\sigma}{d\Omega} 2\pi sin\alpha d\alpha \tag{2.20}$$

Table 2.5 gathers all partial elastic cross-section $\sigma_{el,PW}$.

An estimate of the total elastic cross section given by the integral over the entire solid angle was proposed by Langmore [80]. It can be expressed by

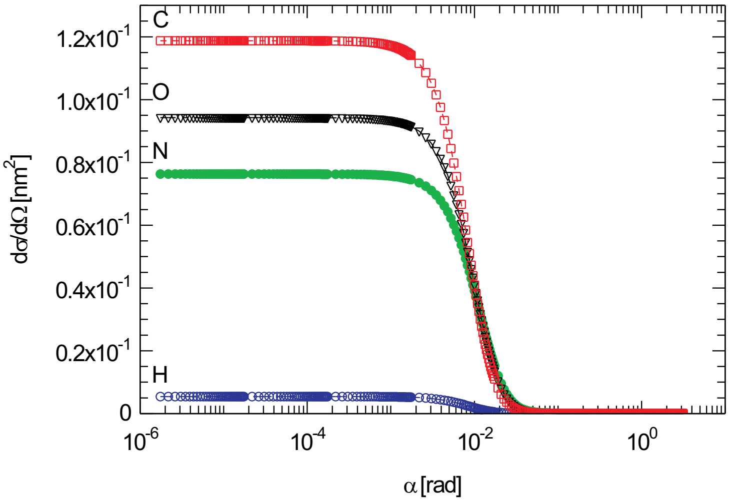

Figure 2.13: *Differential elastic scattering cross section based on the single-atom complex partial wave solutions to elastic scattering from a Hartree-Fock potential as obtained from ref [101, 102, 105]. for different atoms: hydrogen (hollow circles), carbon (hollow squares), nitrogen (hollow down triangles) and oxygen (full circles).*

$$\sigma_{el} = \frac{1.4.10^{-6} Z^{3/2}}{\beta^2}[1 - 0.26Z/(137\beta)] \tag{2.21}$$

where β is the ratio of the speed of the electrons to that of the light ($\beta^2 = 1 - [E_0/(E + E_0)^2]$). Furthermore, σ_{el} can be calculated for small angles to a good approximation:

$$\sigma_{el}(\alpha_0) = \sigma_{el}\eta_{el}(\alpha_0) = \sigma_{el}[1 - s_0/10] \tag{2.22}$$

where η_{el} defines the number of electrons scattered outside the aperture and is called the elastic efficiency expressed as function of s_0 the maximum spatial frequency

$$s_0 = 2sin(\alpha_0/2)/\lambda \tag{2.23}$$

with the objective aperture half-angle $\alpha_0 = 10\ mrad$, the maximum spatial frequency $s_0 = 4\ nm^{-1}$ and the electron wavelength $\lambda = 2.5.10^{-3}\ nm$.

For the calculation of the inelastic scattering cross sections we used the expression derived by Wall et al. [104]:

$$\sigma_{in} = \frac{1.5.10^{-6} Z^{1/2}}{\beta^2} ln(2/\vartheta_e) \tag{2.24}$$

where $\vartheta_e = \overline{E}/[\beta^2/(V_0 + mc^2)]$ and $\overline{E}$ is the average energy loss, assumed to be 20 eV from the calculation of Wall et al. for organic materials [104].

Eq. 2.24 is not valid for hydrogen [104]. Here we use an estimate of the cross-section given by 11.2 pm^2 at 200 kV. This value was obtained from the apparent inelastic mean free path of ice, the calculated inelastic scattering from oxygen and density for hyperquenched glassy water (0.92 g/cm^3) [106, 107]. We took the inelastic mean free path length of

Table 2.7: *Densities (in g/cm^3) and TEM contrast ($\frac{\varrho_p}{x_{k,p}}$) (in nm^{-1}) for the hyperquenched glassy water (HGW) [106, 107], the polystyrene core, and the crosslinked PNIPAM shell. The quantity ($\frac{\varrho_p}{x_{k,p}} - \frac{\varrho_w}{x_{k,w}}$) is the contrast in cryo-TEM calculated in nm^{-1}. Both contrasts are calculated for an acceleration voltage $U = 200$ kV and an aperture $\alpha_0 = 10$ $mrad$ with or without filtering of the inelastic contribution.*

		filter		no filter	
molecules	ϱ	$(\frac{\varrho_p}{x_{k,p}})$	$(\frac{\varrho_p}{x_{k,p}} - \frac{\varrho_w}{x_{k,w}})$	$(\frac{\varrho_p}{x_{k,p}})$	$(\frac{\varrho_p}{x_{k,p}} - \frac{\varrho_w}{x_{k,w}})$
HGW	0.92	$4.803 \cdot 10^{-3}$	0	$1.546 \cdot 10^{-3}$	0
Polystyrene	1.0525	$5.828 \cdot 10^{-3}$	$1.025 \cdot 10^{-3}$	$1.702 \cdot 10^{-3}$	$1.57 \cdot 10^{-4}$
PNIPAM+BIS	1.1492	$6.305 \cdot 10^{-3}$	$1.503 \cdot 10^{-3}$	$1.869 \cdot 10^{-3}$	$3.22 \cdot 10^{-4}$

ice from the work of Langmore measured to 180 nm at 80 kV. The inelastic mean free path length of ice then results to 284.6 nm at 200 kV if we consider its dependence on the acceleration voltage given by $U^{1/2}$ [108]. Table 2.6 gathers the inelastic scattering cross-sections thus obtained for the elements of interest.

Calculation of the gray scales from cross sections

In the present approximation, the gray value obtained at a given point in an image is solely related to the amplitude contrast, that is, to the weakening of the intensity I of the electron beam by scattering processes. In principle, there are two different ways to evaluate the gray scales from the images: One may treat this weakening in terms of the difference ΔI between the rays passing through the sample and through the aqueous phase [80]. Here we use a slightly different approach shown schematically in fig. 2.14: The weakening of the intensity I of the electron beam passing through the sample may be treated within the frame of the Lambert-Beer law. Therefore the ratio I/I_0 of the rays passing through the particle and through the aqueous phase (marked in fig. 2.14), respectively, is only related to the contrast within the particle. Other factors as e.g. multiple scattering will weaken both rays outside the particle in the same way. Their ratio is thus not affected by these effects. On the other hand, the colloidal objects under consideration here have dimensions of the order of a few 100 nanometers only. Hence, the prerequisites of theory, most notable the assumption that multiple scattering within the particle can be neglected are fully justified.

When the inelastic scattered electrons are filtered both the elastic and the inelastic cross sections obtained for atoms can be used to calculate the respective quantities of molecules of known composition and molecular weight M. Without energy filtering only the elastic cross-sections are taken into account. In absence of chemical shifts we can assume that the scattering cross-section of a molecule composed of n_k elements is the sum of the cross-sections of the atoms ($\sigma_{T,i}$) weighted by their proportion in mass in the molecule [80]. Thus, the decrease of the transmission with increasing mass-thickness $x = \varrho t$ can be expressed by

$$\frac{dI}{I} \simeq -\sum_{i=1}^{n_k} \frac{\nu_i}{N_A M} \sigma_{T,i}(\alpha_0) dx \tag{2.25}$$

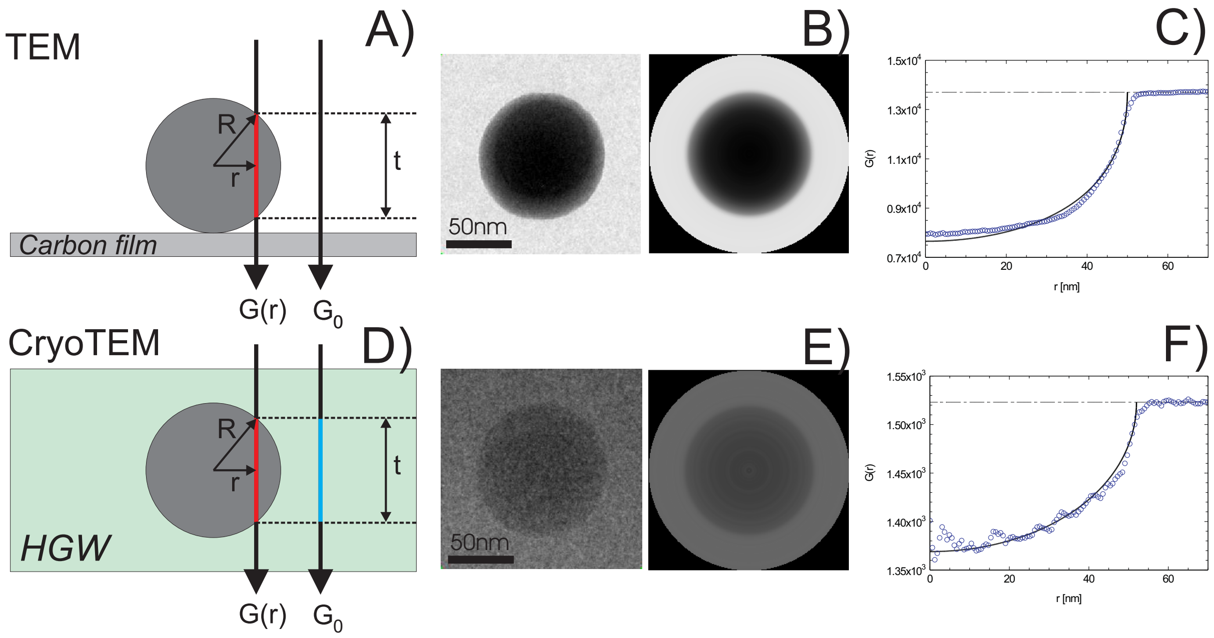

Figure 2.14: *(A) TEM evaluation of the gray scale of a homogeneous spherical particle dried on a thin carbon film. Application of the Lambert-Beer law leads to eq. 2.28 (B) Polystyrene core particle and its corresponding radial average: Considering the gray value from the border to the center of the particle, enables the determination of its radial density profile with a resolution of 0.61 nm given by* Δr *(pixel resolution). (C) Radial average of the intensity* $G(r)$*. The dashed line represents the value of the average intensity* G_0 *outside the particles. The solid line displays the fit from eq. 2.28 (*$G_0 = 1.37.10^4$, $R = 50$ *nm,* $\phi = 1$, $\frac{\varrho_p}{x_{k,p}} = 5.828 \cdot 10^{-3}$ nm^{-1} *(polystyrene) (see Table 2.7)). (D) CryoTEM evaluation of the gray scale of a homogeneous spherical particle embedded in a thin film of hyperquenched glassy water (HGW). Application of the Lambert-Beer law leads to eq. 2.29. (E) Core particle and its corresponding radial average. (F) Radial average of the intensity* $G(r)$*. The solid line displays the fit from eq. 15 (*$G_0 = 1523$, $R = 52$ *nm,* $\phi = 1$, $(\frac{\varrho_p}{x_{k,p}} - \frac{\varrho_w}{x_{k,w}}) = 1.025 \cdot 10^{-3}$ nm^{-1} *(polystyrene) (see Table 2.7)).*

where ν_i is the stoichiometric coefficient of the i^{th} element in the compound. We can then define the contrast thickness x_k of the material as follows:

$$\frac{1}{x_k(\alpha_0)} \simeq \sum_{i=1}^{n_k} \frac{\nu_i}{N_A M} \sigma_{T,i}(\alpha_0) \tag{2.26}$$

The image intensity I can be obtained by integration

$$I = I_0 exp\left(-\frac{x}{x_k(\alpha_0)}\right) = I_0 exp\left(-\frac{\varrho t}{x_k(\alpha_0)}\right) \tag{2.27}$$

where I_0 is the intensity of incident electron beam. The quantity $(\varrho/x_k(\alpha_0))^{-1}$ is the total mean free path length of the respective material through which the electron beam is passing (see Table 2.7).

In the case of the normal TEM, where a sphere with a radius R is absorbed and dried on a thin carbon film for example (see fig. 2.14 A). The gray values in the image are proportional to the respective intensities. The transmitted electron beam crossing the particles is characterized by the gray value $G(r)$ dependent on the distance to the center of the particle r. Out of the particles and thus for $r > R$ the gray value is constant. This defines the contribution of the film G_0. We can derive the following relation:

$$\frac{G(r)}{G_0} = exp\left(-2\phi\sqrt{R^2 - r^2}\left(\frac{\varrho_p}{x_{k,p}}\right)\right) \tag{2.28}$$

where ϕ is the volume fraction of the material in the particle. For dense sphere, ϕ is equal to 1. It is then important to remark that in a normal preparation the contrast is defined by the reciprocal mean free path length in the material ($\varrho_p/x_{k,p}$). The radial gray value profile is obtained by an azimuthal average of the gray values of one isolated particle. An example is given in fig. 2.14 B) in form of one core particle with the corresponding azimuthal average of the gray scale. The resulting radial gray scale values are displayed by the symbols in fig. 2.14 C). The dashed line represents the average value G_0 out of the particle. The full line presents a direct application of the equation 2.28 considering the contrast of pure polystyrene.

For the cryoTEM analysis we have to consider a thin layer of vitrified water in which spherical particles are embedded (see Fig. 2.14 D). For $r > R$ the ray passes only through vitrified water. Hence, it corresponds to the contribution of the vitrified water only and is characterized by the gray value $G_0 \propto I_0 exp(-\varrho_w t/x_{k,w})$. Thus, for spheres embedded in glassy water we obtain from eq. 2.28:

$$\frac{G(r)}{G_0} = exp\left(-2\phi\sqrt{R^2 - r^2}\left(\frac{\varrho_p}{x_{k,p}} - \frac{\varrho_w}{x_{k,w}})\right)\right) \tag{2.29}$$

For systems impenetrable by the solvent water, $\phi = 1$. In this experiment the contrast is not defined by the contrast of the system itself but by the difference of the reciprocal mean free path length in the material and in glassy water, respectively ($\varrho_p/x_{k,p} - \varrho_w/x_{k,w}$). Fig. 2.14 E) presents an example in the form of one core particle embedded in vitrified water and the corresponding azimuthal average of the gray values. The dashed line represent the average value G_0 out of the particle. The symbols in the figure 2.14 F) present the resulting radial gray scale values. The full line corresponds to a fit with the equation 2.29 considering the contrast of pure polystyrene.

Table 2.7 provides values of the TEM and cryo-TEM contrasts k obtained from the partial wave calculation of the elastic cross-section and from the equation 2.24 as described above for hyperquenched glassy water, polystyrene and the PNIPAM crosslinked shell with or without energy filtering. The table clearly shows the difference of contrast between the different experiments. If we take as a reference the polystyrene with energy filter, TEM experiments have a contrast approximately 5.7 times higher than in the Cryo-TEM. The same comparison without filter gives a factor around 10.8. Comparing now the contrasts with and without filter gives a factor of 3.4 for the TEM and 6.5 for the CryoTEM. This clearly indicates the great advantage of the energy filtered microscopy respect to conventional instruments.

If the polymer is porous or has taken up water, the volume fraction of the polymer within

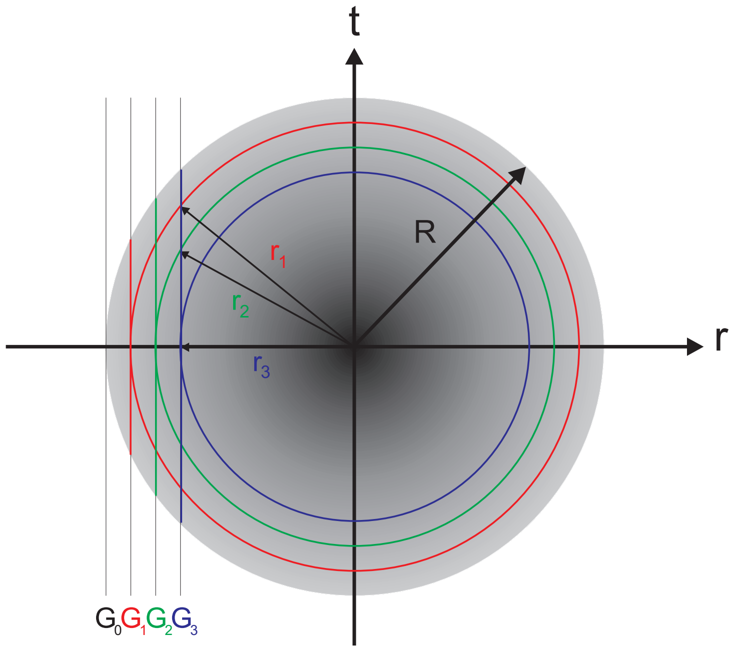

Figure 2.15: *Schematic representation of the spherical multilayer model for the determination of complex material volume fraction* $\phi(r)$ *and contrast profile* $k(r)$. *The analysis is performed from* R *to the center of the particles. The relative gray values* (G_n/G_0) *in each layer is successively calculated by recurrence (equation 2.30) from the value of the contrast* k_n *and the material volume fraction* ϕ_n *following the distance to the center of the particle* r_n.

the particle is no longer unity but ϕ. For complex radial volume fraction profile, like microgels in solution for instance, ϕ is no longer constant but is varying as a function of r. Moreover in the case of composite core-shell particles the contrast is also depending on the different materials composing the particles and also depends on r.

The profile $k(r)\phi(r)$ has then to be determined. To this purpose we have to applied a multilayers approach. The size of each layer is restricted by the size of the pixel. We have to consider $G(r_n)/G_0$ for r varying from R to 0. Fig. 2.15 shows a schematic representation of the multilayer model applied to a spherical geometry. We can calculate numerically the normalized gray value $G(r_n)/G_0$ by recurrence with the contrast k_n and the material volume fraction ϕ_n following the distance to the center r_n considering $r_0 = R$, $\phi_0 = 0$ and $k_0 = 0$. We can then used the recurrence:

$$\frac{G(r_n)}{G_0} = \sum_{j=1}^{j=n} exp(-2k_n\phi_n(r_{j-1}^2 - r_n^2)^{1/2}) \tag{2.30}$$

In this approach the function $k(r)\phi(r)$ can be introduced in equation 2.30 to fit the normalized gray values.

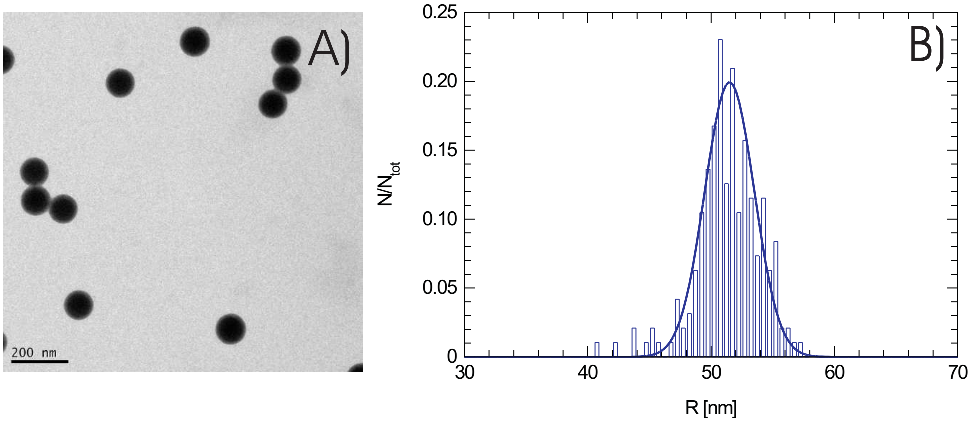

Figure 2.16: *(A) TEM micrographs of the core particles. (B) Distribution in size obtained from the TEM analysis, the population can be described by a Gaussian distribution* ($\langle R \rangle = 51.5$ *nm*, $\sigma = 2$ *nm) (solid line).*

2.2.4 Results and Discussion

Core particles

TEM analysis

A monodisperse core solution used for the synthesis of the core-shell system described in the section 2.1.2 has been first put under scrutiny. The particles were obtained by emulsion copolymerization of styrene and NIPAM (about 5 *wt.*%). The particles thus consist on a polystyrene core of constant density with a thin layer of PNIPAM [17]. The dispersion has been first investigated by transmission electron microscopy. Fig. 2.16 presents the TEM micrographs obtained from this analysis and the normalized distribution of the radius obtained on a population of more than 200 particles. All the micrographs were taken as close as possible to the focus with the same dose conditions. The particles appear spherical and monodisperse. The average radius was found equal to 51.3 ± 2.6 *nm*. The distribution can be described by a Gaussian considering an average radius of 51.5 *nm* and a standard deviation of 2 *nm*. This results are in good agreement with the polydispersity of 5 % determined from the SAXS analysis. The normalized gray values has been calculated for more than 100 particles as described in the preceding section in order to check the theory. The average gray values are depicted on the fig. 2.17. The variation between the measurement represented by the size of the error bars is rather small, which attests on the reproducibility of the measurement from one picture to another. The experimental result has been directly compared to the theory considering the sphericity of the particles, an average radius of 51.5 *nm* determined from the Gaussian distribution and first the contrast of pure polystyrene particles. The theory described relatively well the experimental results, nevertheless the experimental $G(r)/G_0$ values are lower between 30 and 45 *nm* and higher below 30 *nm*. This was attributed to the adsorption and drying of the particles on the grid. The gray value can then simply be converted in height t as considering the equation:

$$t = -ln\left(\frac{G}{G_0}\right)/\frac{\varrho_p}{x_{k,p}} \tag{2.31}$$

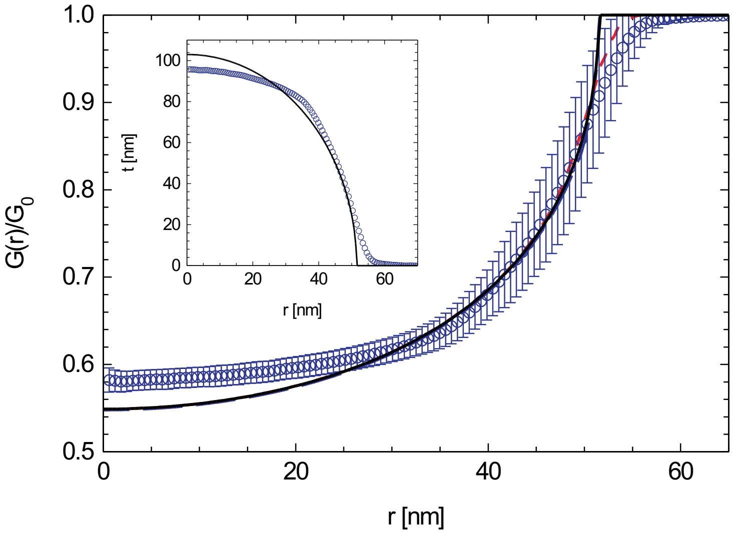

Figure 2.17: *Radial relative gray values $G(r)/G_0$ of the core particles analyzed by TEM (circles). The full line refers to the theoretical calculation considering a contrast* $5.8.10^{-3}$ nm^{-1} *(see table 2.7) and an average radius of 51.5 nm determined from the statistic (see fig. 2.16). The dotted line is the calculation for a core-shell system with 49.5 nm polystyrene core and a dense 2 nm thin PNIPAM shell. The dashed refers to polydisperse polystyrene particles considering the distribution of the fig. 2.16. The inset presents a comparison of the profile of the particles determined from this analysis with a spherical profile. The small deviation can be attributed to a small deformation of the particles following the adsorption and the drying on the carbon grid.*

The inset of fig. 2.17 displays the average thickness of the particles deriving from equation 2.31 considering a pure polystyrene core. This profile was then directly compared to the profile obtained for a sphere.

The average profile of the dryed particles thus present a maximum deviation of 7 nm in the center of the particles respect to a perfect sphere of 103 nm diameter. As mentioned before in the section dedicated to the SAXS analysis, a thin layer of PNIPAM of about 2 nm is adsorbed on the the particles. The relative gray values $G(r)/G_0$ of the core particles has been compared to the theory calculated for a core-shell system with a polystyrene core with a radius of 49.5 nm and a PNIPAM layer of 2 nm. As can be seen in the fig. 2.17 no significant deviation can be observed from the TEM. The polydispersity has been introduced considering the gaussian distribution determined previously and pure polystyrene particles. This partially explained the deviation observed for $r > 51.5$ nm, on the other hand the results for $r < 51.5$ are not significantly affected by the polydispersity. The remaining discrepancy can be mainly explained by the uncertainty on the determination of the center of the particles during the rotational average and on the deviation from the sphericity. Nevertheless this approach described the TEM experiments within the experimental error.

As an application, this kind of analysis can by directly applied on the TEM images to obtain a three dimensional representations of the particles absorbed on the grid. This simply requires a constant background with an average gray value G_0 and the knowledge

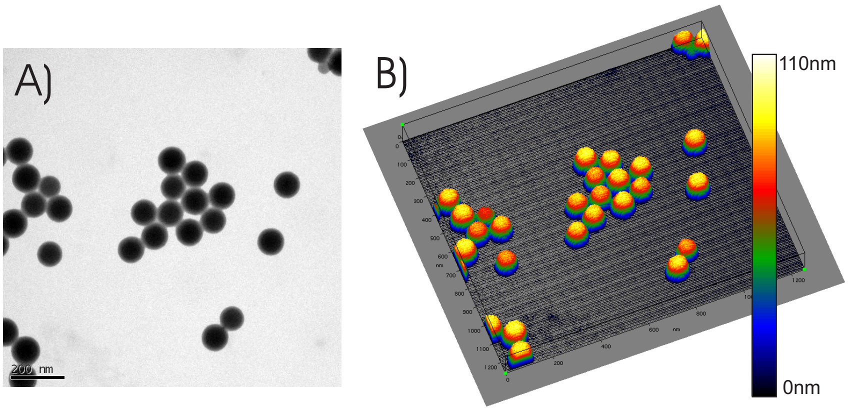

Figure 2.18: *(A) TEM micrographs of the core particles. (B) Transformation considering the equation 2.31 to access to the height of the particles adsorbed on the grid (see text for further details). (C) Tomographic representation of the grid. The color bar is a linear scale of the height between 0 and 110 nm.*

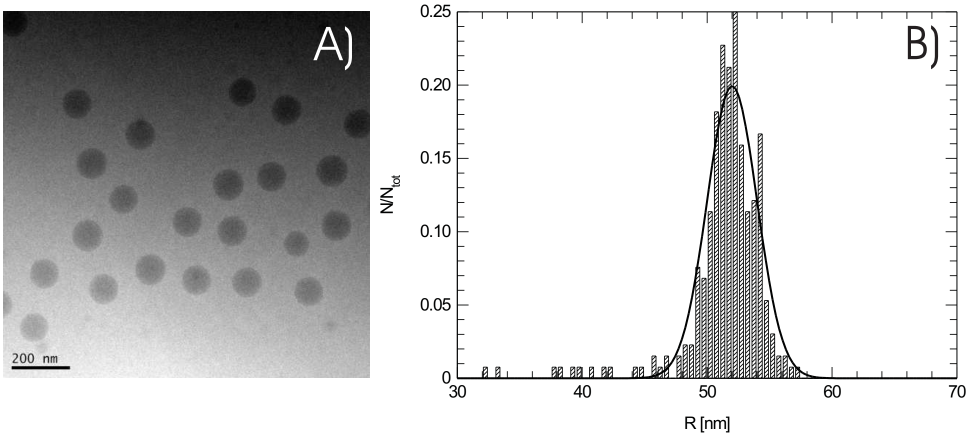

Figure 2.19: *(A) CryoTEM micrographs of the core particles. (B) Distribution in size obtained from the CryoTEM analysis, the population can be described by a Gaussian distribution ($\langle R\rangle = 52$ nm, $\sigma = 2$ nm) (solid line).*

of the contrast of the particles absorbed on the grid $\frac{\varrho_p}{x_{k,p}}$.

An example is given in the fig. 2.18, which presents the treatment performed on a TEM micrographs of our core particles (assimilated to polystyrene particles) to access to the tomography of the sample. First the initial picture (fig. 2.18 A) is transformed following the equation 2.31 (fig. 2.18 B)). In this sense the gray value correspond to the height of the particles absorbed on the film. Fig. 2.18 C) presents a 3 dimensional representation of the tomography of the grid thus obtained. Due to its simplicity this kind of analysis presents an elegant way to access to the third dimension without requiring complex tomographic methods and can complement other analysis such as scanning force microscopy performed on the dried state.

CryoTEM

Cryogenic electron microscopy was then performed on the same system. Fig. 2.19 displays the micrographs obtained and the resulting normalized distribution of the radius of the

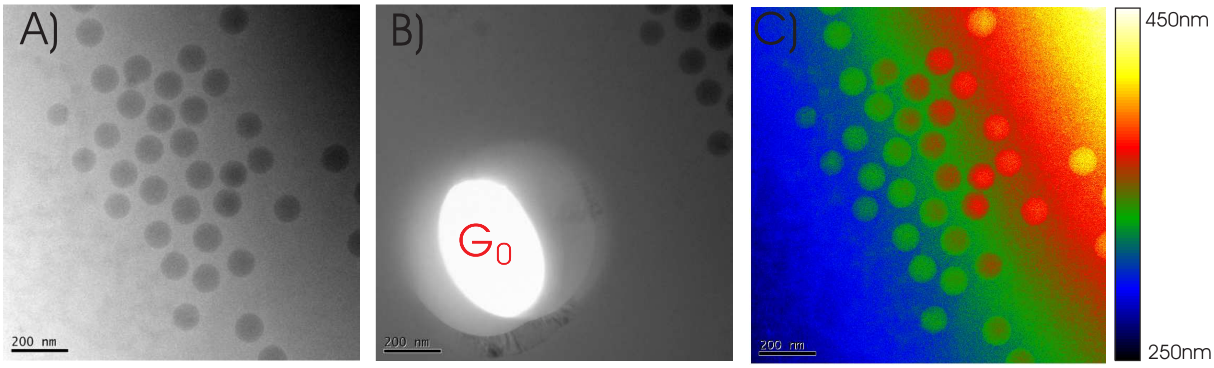

Figure 2.20: *(A) CryoTEM micrographs of the core particles. (B) Micrographs of a hole performed in the film by electronic irradiation in the vicinity of the caption A. The picture is taken under the same conditions as in the caption A, and the average gray values in the hole are defined by G_0. C) 3D representation of the thickness of the HGW film (only the points outside of the particles can be considered) deriving from G_0 and equation 2.32 The color bar is a linear scale of the height between 250 and 450 nm.*

particles. The same feature as in the TEM analysis can be observed. The particles appears as spheres with a narrow size distribution. The average radius from this analysis also determined over more than 200 particles is equal to $51.4 \pm 3.2\ nm$. The distribution can be described by a Gaussian centered on 52 nm with a standard deviation of 2 nm, which is in good agreement with the TEM, with the SAXS analysis of the core (50 nm) and the dynamic light scattering (55.0 nm). The contrast between the particles and the background is less pronounced than in the TEM as expected from the theoretical calculation. Indeed the contrast is this time determined by the difference between the contrast of the polystyrene and water ($\varrho_p/x_{k,p} - \varrho_w/x_{k,w}$), which is approximately under our experimental conditions six times smaller than the one of the pure polystyrene $\varrho_p/x_{k,p}$ (see Table 2.7). Moreover the background is not constant on the whole micrographs, which is directly related to the variation of the thickness of the film. This parameter is crucial for the rest of the analysis. Indeed the film has to be sufficiently thick to embedded the whole particles.

A simple method has been applied to estimate the thickness of the vitrified water film (see fig. 2.20). An identical approach is described in the ref. [80]. First the micrographs were captured as close as possible to the focus (fig. 2.20 A)). Then in an area close to the particles a hole was done in the film following an excessive irradiation. A picture of the hole was taken in the same conditions as the particles before, the gray value inside the hole then define our G_0 (see fig. 2.20 B)). Considering the contrast of the HGW film $\frac{\varrho_w}{x_{k,w}}$ it is possible to determined its thickness in all the points outside of the particles in the first picture following the same approach as described for the TEM analysis. This time we can use the relation:

$$t = -ln\left(\frac{G}{G_0}\right) / \frac{\varrho_w}{x_{k,w}} \tag{2.32}$$

Fig. 2.20 C) is a colour representation of the film thickness following the equation 2.32. Only the values out of the particles have to be taken into account. A strong variation

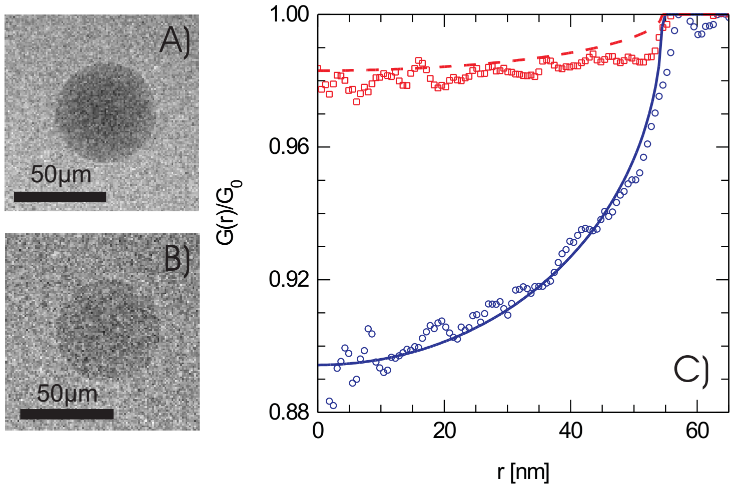

Figure 2.21: *Cryo-TEM micrographs of one core particle with (A) and without (B) filter of the inelastic scattered electrons. $G(r)/G_0$ has been calculated in the two cases (with filter (hollow circles), without filter (hollow squares)) and fitted following the equation 2.29 and the contrast values of the table 2.7 (full and dotted lines) assuming a pure polystyrene core of 55 nm.*

of the thickness from approximately 250 to 450 nm within 1.7 μm was observed in this example. Considering the average size of the particles this thickness should be sufficient in order to perform a correct analysis. Particles observed in very thin film present a strong contrast in their center. This effect can be attributed to a film thickness which is smaller than the diameter of the particles, or to the deformation of the film by the particles. In this case the prerequisites of eq. 2.29 are no longer given. If the film is sufficiently thick and not deformed by the particles, the thickness gradient does not play a role because it will be compensate by the rotational average of the gray values. In the rest of the analysis only particles embedded in a film with a thickness superior as the diameter of the particles have been processed.

The effect of the focusing has been investigated by taking different pictures for different defocusing. If taken in focus, the micrographs exhibit a sharp interface with the surrounding solvent. With increasing defocus, diffraction phenomena occur at the edge of the particles under the form of Fresnels fringes as expected. Considering the picture taken in the focus as reference, the defocusing can be relatively estimated for the other pictures. Evidently, these micrographs would need a correction through the $CTF(\alpha)$ before doing a qualitative evaluation. Fig. 2.19 demonstrates, however, that the contrast between the particles and the vitrified water is sufficient. As mentioned above, no defocusing is needed to enhance the contrast and the evaluation of the gray scale proceeds from micrographs taken in focus. The effect of the energy filtering has also been investigated. Fig. 2.21 presents the cryo-TEM micrographs of one single particles taken with (fig. 2.21 A)) and without (fig. 2.21 B)) energy filter. The normalized gray values have been derived for the two micrographs and fitted following the equation 2.29 considering the contrasts presented in the table 2.7 considering a 55 nm polystyrene particle (fig. 2.21 C)). Equation 2.29 gives a good description of the radial normalized gray values in the two cases. Nevertheless the experiments without energy filtering clearly lack of contrast, which is more than six times lower than with filter (see table 2.7). Thus any small variations of

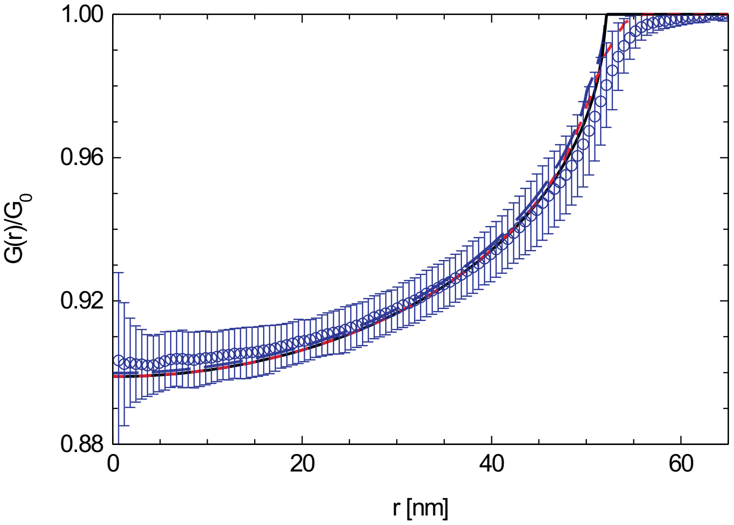

Figure 2.22: *$G(r)/G_0$ of the core particles analyzed by cryoTEM (circles). The full line refers to the theoretical calculation considering the contrast of pure polystyrene particles (see table 2.7) and a radius of 52 nm determined from the statistic (see fig. 2.19). The dotted line is the calculation for a core-shell system with 50 nm polystyrene core and a swollen 2 nm thin PNIPAM shell ($\phi = 0.5$). The dashed refers to polydisperse pure polystyrene particles considering the distribution of the fig. 2.19.*

the transmitted electron intensity will induce a dramatic error in the evaluation of the relative gray values. For this reason we only consider zero loss images in the rest of the analysis.

The normalized gray values shown in fig. 2.22 have been obtained by averaging over 100 particles. The symbols displays the mean values while the error bars gives the standard deviation in each point. The results has been then directly compared to the theoretical values. The average size was directly taken equal to 52 nm from the statistic performed on the cryo-TEM micrographs and we first have considered the contrast $(\frac{\varrho_p}{x_{k,p}} - \frac{\varrho_w}{x_{k,w}})$ of pure polystyrene in HGW. The obtained values presented by the full line described the experimental result very well confirming the sphericity of the particles in solution and the interest of the cryo-TEM respect to normal TEM. The small deviation between the two results can be attributed to possible errors in the determination of the absolute density of the HGW and of the inelastic cross section of hydrogen. We also investigated the influence of the thin PNIPAM shell on the absorbance. This time a swollen PNIPAM shell has been considered as obtained during the SAXS analysis (see section 2.1.4). The normalized gray values were calculated for a 50 nm dense polystyrene core, and a 2 nm thin PNIPAM shell in the swollen state ($\phi = 0.5$))(dotted lines). The deviation between the two results is rather small as already observed by TEM. The method presents herein to evaluate the micrograph is thus not sensitive enough to reveal this thin layer of PNIPAM in term of contrast. For this reason we only consider pure polystyrene particles. The polydispersity obtained from the statistic was also introduced, and partially explained the deviation for $r > 52$ nm as observed for the TEM analysis.

As a conclusion a new method for extracting the excess electron density of colloidal particles from TEM and cryo-TEM micrographs has been developed. This method has been applied to the core particles which can be assimilated to pure polystyrene particles.

The calculated contrast as well as the size is in good agreement with the experimental values both for TEM and cryoTEM analysis. On another hand, the normalized gray values can be directly used to access to the tomography of the particles investigated by TEM as long as the contrast of the particles is known. The results obtained for the cryoTEM are even closer to the theory as the particles are investigated in solution and not absorbed and dried on a surface. Good agreement is found between the microscopy and the SAXS, even if the SAXS was more sensitive to the presence of a thin layer of PNIPAM at the surface of the particles and presents about 2 nm smaller particles.

Core-shell particles

Figure 2.23 displays the micrographs of the core-shell microgels obtained by cryo-TEM in pure water. The samples have been kept at 23 ^{o}C prior cryogenization (see section 2.1.4). The thermosensitive shell is clearly visible in these pictures because of sufficient contrast between the shell and the core. Moreover, the micrographs show directly the thermal fluctuations and inhomogeneous cross-linking which lead to a further contribution to the scattering intensity [3, 63, 64]. This is directly obvious from fig. 2.23 A), which presents a zoom-in on a particle to evidence the inhomogeneities of the shell.

As discussed in the section 2.1.4 a feature directly visible in the cryo-TEM images is the buckling of the shell (see fig. 2.23 and fig. 2.1). This finding can be related to the instabilities of swelling or deswelling gels occurring at the surface of swollen gels affixed to solid substrates [69, 109–114]. This results corroborates recent small-angles neutron scattering analysis performed on core-shell PNIPAM/PNIPMAM also synthesized in a seed emulsion polymerization, which pointed out the presence of a depletion zone at the interface core-shell [62].

As a consequence, the core-shell particles deviate from an ideal spherical symmetry. In order to demonstrate this, we have evaluated the relative gray scale $G(r)/G_0$ along the lines indicated in fig. 2.23 A). Fig. 2.23 B) shows that the size along these lines may differ appreciably. As already discussed above, this difference is mainly due to the buckling of the shell. Fig. 2.23 C) displays the polymer volume fractions that have been evaluated using eq. 2.30 together with the contrasts of polystyrene (core) and PNIPAM (shell). For specimens embedded in HGW, the calculated ratio of the contrast between polystyrene and PNIPAM is 0.682 (see Table 2.7). Note that the ratio calculated with the approximation given by Langmore for the elastic cross-section (eq. 2.21 and eq. 2.22 [80] would give a ratio of 0.650. Fig. 2.23 C) demonstrates that the strong fluctuations of the shell lead to strong local variations. This fact must be kept in mind when considering the comparison with SAXS-data discussed further below.

In order to arrive at an average profile that can be compared to a profile deriving from SAXS-measurements, the analysis of the particles has been performed on 45 particles taken from different micrographs similar to fig. 2.23 A). Only isolated particles were be analyzed in this way. Prior to taking the gray values, a rotational average has been performed as shown in Fig. 2.14 B) and E). The average relative gray values resulting from this analysis are displayed in the figure 2.24. $G(r)/G_0$ can be decomposed in two parts: the contribution of the core and the contribution of the shell. The average result has been fitted considering a dense polystyrene core and a parabolic density profile for

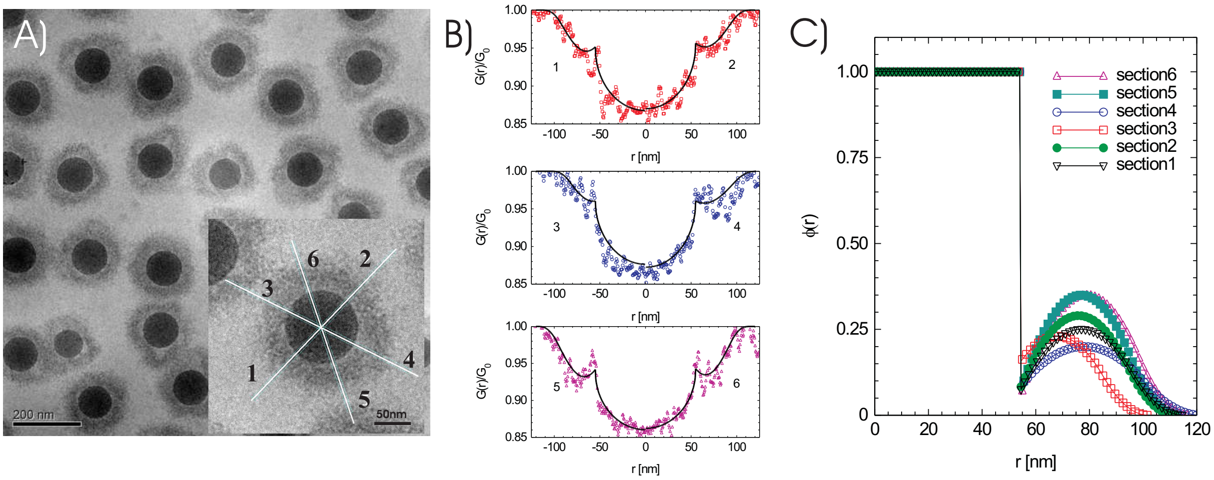

Figure 2.23: *Comparison of cryo-TEM and SAXS. A) Average profile $\phi(r)$ evaluated from $G(r)/G_0$ according to eq. 2.29 and the contrasts of polystyrene and PNIPMAM given in Table 2.7. The inset gives the average relative gray scale that has been used for this calculation. B) Measured SAXS-intensity and the profile $\phi(r)$ deriving therefrom. C) Comparison of the overall size as determined by DLS and cryo-TEM (solid line) and by SAXS (dashed line). See text for further explanation.*

the shell. This parabolic profile follows the same description as for the SAXS analysis and is given by the equation 2.15 (see discussion in section 2.1.4).

The same procedure was repeated this time after fitting each particle individually. The average $k(r)\phi(r)$ over the 45 particles is presented by the open symbols in the inset of the fig. 2.24. The full line in fig. 2.24 presents the corresponding calculation of $G(r)/G_0$. Both approaches lead to the same results which can be attributed to the low polysdispersity of the system.

Fig. 2.25 A) presents the average density profile obtained from the fit of the average $G(r)/G_0$ shown in the inset. As expected, this profile exhibits a plateau within the core up to R_c =54 nm which is in good agreement with the 52 nm of the core found in the previous section. The average profile can be fitted by the eq. 2.15 with $K = 0.23$, $R_{hw} = 94$ nm and $\sigma = 19$ nm. Between 55 and 75 nm the contrast increases to reach a maximum at 75 nm showing that the shell is not totally attached to the core. After this, the contrast decreases parabolically until $r = 113$ nm is reached. This value closely matches the hydrodynamic radius of the particles at 23^{o}C equals to 113 nm. The average volume fraction ϕ of PNIPAM in the shell is 0.116 in good agreement with data derived from a combination of SANS and SAXS [63].

As a comparison the density profile used for the SAXS analysis (see section 2.1.4) is also displayed in Fig. 2.25 A). The weight percent of the core in the particle derived from this analysis was found equal to 53.3 % which is in good agreement with the 53.4 % from the gravitometry and with the 50 % from the cryo-TEM.

The overall size obtained from the SAXS has been compared from the results obtained from the Cryo-TEM micrographs. Fig. 2.25 B) displays the micrograph of a single particle together with the overall size determined by cryo-TEM (solid line) as well as by SAXS (dashed line). The difference between both methods amounts to ca. 13 %. However, this

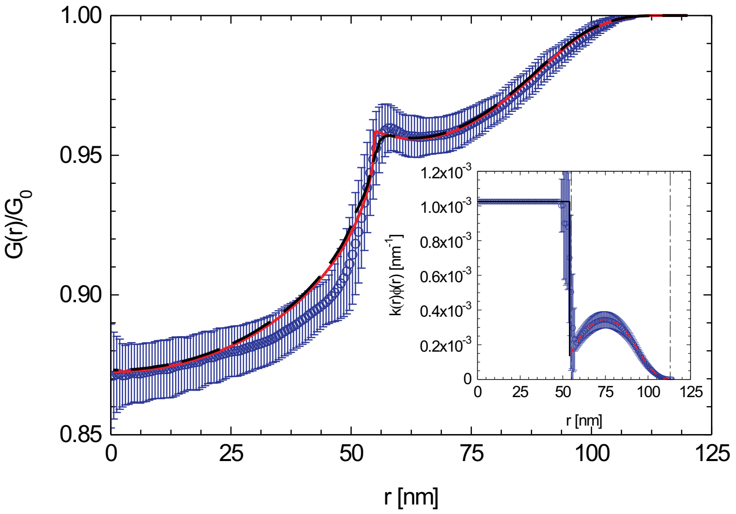

Figure 2.24: *Average relative gray values $G(r)/G_0$ of the composite microgels (circles). The full line refers to the fit obtained considering the function $k(r)\phi(r)$ of a core-shell with a solid polystyrene 54 nm core (full line in the inset) and a parabolic PNIPAM shell (dashed line in the inset) described by equation 2.15. The relative gray values have been fitted for each particles using equation 2.30 and the average $k(r)\phi(r)$ is represented by the symbols in the inset. The corresponding $G(r)/G_0$ values are indicated by the dashed line. The thin dashed lines of the inset display the hydrodynamic radius from the DLS at 55 nm and 113 nm obtained for the core and the core-shell particles at 23°C.*

marked discrepancy has already observed before when comparing the overall size from DLS and SAXS/SANS and explained by single polymer chains protruding from the shell [63]. Now the origin of the discrepancy becomes obvious from close inspection of fig. 2.25 B): SAXS is only sensitive to the average structure of the particles while cryo-TEM takes fully account the deviations from this average caused by the buckling of the shell. In this way the present analysis corroborates the previous conjecture of ref. [63] to a certain extend.

The buckling of the PNIPAM-shell must be a dynamic phenomenon. This is supported by recent investigations performed on similar system by dynamic light scattering (DLS) and depolarized dynamic light scattering (DDLS). The latter method requires a non-centrosymmetric particle. From a strong DDLS signal the deviations from spherical symmetry could be inferred directly which was most pronounced in the swollen state [115]. In this investigation a strong coupling of the rotational diffusion and the translational diffusion was found which could only be explained by the dynamic fluctuations of the shell.

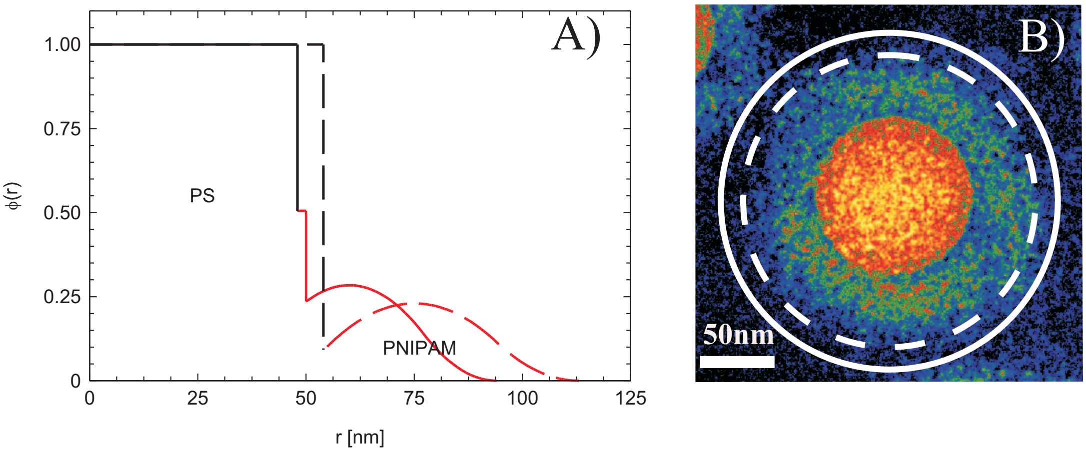

Figure 2.25: *Comparison of cryo-TEM and SAXS. A) Average profile $\phi(r)$ evaluated from $G(r)/G_0$ (see fig. 2.24) according to eq. 2.29 and the contrasts of polystyrene and PNIPMAM given in table 2.7 (dashed lines). The full line presents the profile $\phi(r)$ deriving from the SAXS analysis in the section 2.1.4. B) Color representation of a single core-shell particle and comparison of the overall size as determined by DLS and cryo-TEM (solid line) and by SAXS (dashed line). See text for further explanation.*

2.2.5 Summary

A new method for extracting the excess electron density of colloidal particles from TEM and cryo-TEM micrographs has been developed. The method rests on the application of the Lambert-Beer law to the TEM and the cryo-TEM images, respectively. The contrast leading to different gray values inside and outside the particles could be calculated from the elastic and the inelastic scattering cross sections of the material. This new way of evaluation of the images has been validated using spherical polystyrene particles. A analysis of these particles by DLS leads to the same overall size of the particles. However, SAXS is sensitive to the presence of a thin layer of PNIPAM at the surface of the particles which cannot be seen in the cryo-TEM images.

The method has also been applied to core-shell particles consisting of a polystyrene core and a shell of crosslinked poly(N-isopropylacrylamide) (PNIPAM). The shell is partially swollen by the solvent water. Using the calculated contrast of PNIPAM in hyperquenched glassy water (HGW) in which these particles are embedded, the volume fraction and the average radial profile of the polymer in the shell could be determined quantitatively. The resulting radial profile demonstrates that the swollen PNIPAM-shell can buckle off the surface of the core particles. The particles are also analyzed by SAXS. We find that SAXS "sees" mainly the bulk part of the shell while Cryo-TEM together with dynamic light scattering is also sensitive to small parts and protrusions of the shell.

2.3 Crystallization

2.3.1 Introduction

Crystallization of colloidal systems provides not only the knowledge of complex fluids but also insights into the phase transitions in atomic systems [116–136]. On the other hand , colloidal crystals have been extensively used in recent years for the fabrication of nanostructured materials such as photonic crystals and membranes for device applications [137–140]. Monodisperse colloidal particles that interact through a steep repulsive potential follow the so-called hard spheres diagram, which is the simplest system to show a freezing/melting transition (see Fig. 2.26). At a low volume fraction, the particles show a disordered liquid-like structure. When ϕ_{eff} is increased to the freezing volume fraction ϕ_F, an ordered crystalline phase can coexist with the liquid phase. Above the melting volume fraction ϕ_M, the complete system assumes crystalline order [116–118]. Finally, above the volume fraction for glass formation ϕ_G the motion of particles becomes so much hindered that the formation of the crystalline phase takes an "infinite" time and a mainly disordered glassy structure remain [117]. For charge stabilized colloids we can, in addition to the volume fraction, also vary the ionic strength of the solvent. Decreasing the ionic strength effectively increases the range over which the particles interact, causing the phase transitions to occur at a lower volume fraction.

Most works on the kinetics of colloidal crystallization have been focused on weakly charged or hard-sphere-like colloids using light scattering methods [116, 118, 122–124, 133–135] or UV light spectroscopy [134]. Only recently direct imaging of the nucleation and growth by bright field light microscopy [124, 135] or by confocal microscopy [120] has been used to investigated the crystallization of colloidal systems. Meanwhile, the phase behavior of the aqueous dispersions of poly-N-isopropylacrylamide (PNIPAM) spheres has been intensively investigated [7, 10, 18, 27, 34, 134, 141–149]. In particular, it was found that the volume transition of microgel particles affects the solvent-mediated interparticle forces and leads to a novel phase behavior [28, 29]. Furthermore, due to the temperature-responsive shrinkage of PNIPAM particles [2, 28, 29] the attractive interparticle potential increases with temperature, resulting in phase behavior that deviates from the hard sphere systems at high temperatures [28, 29]. The kinetics of crystallization at different volume fractions can be conveniently measured by varying the temperature.

The equilibrium crystal structure for colloidal hard spheres systems should be face centered cubic (fcc) [150] but if the volume fraction is low enough or in the first step of the crystallization a body centered cubic structure (bcc) should dominate. But it is rarely the case even in the most ideal conditions [132]. Instead, a random hexagonal close-packing structure, energetically close to fcc is usually observed [118]. Nevertheless it has been shown by neutron scattering experiments that the crystal of PNIPAM dispersions exhibits a face-centered cubic (fcc) structure [141–143].

The crystallization influences, among other things, the rheological properties of the dispersion and is itself, in return, affected by the shearing of the solution [151, 152]. The relation between rheology and crystallization is a complex process which will be discussed here and in the section dynamics. This section is dedicated to the crystallization of the thermosensitive core-shell particles. The phase diagram has been investigated for different

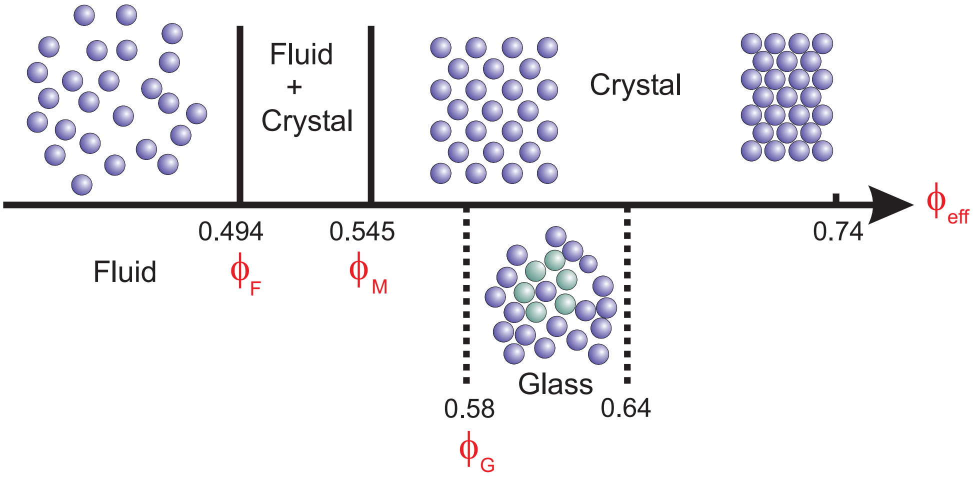

Figure 2.26: *Phase diagram of a hard spheres dispersion [116–118].*

degrees of crosslinking. The nucleation and growth of the crystallites has been visualized by polarized light microscopy and the influence on the rheological properties is discussed.

2.3.2 Experimental

The different core-shell latices presented in the chapter 2.1 were used in this section. Following the systems the crosslinking defined by the amount of BIS in the shell was adjusted to 1.25 $mol.\%$ (KS1), 2.5 $mol.\%$ BIS (KS2) and 5 $mol.\%$ (KS3) (see section 2.1.2).

The flow curves and the dynamic measurements performed on the KS2 suspensions have been investigated using a strain-controlled rotational rheometer RFS II from Rheometrics Scientific, equipped with a Couette system (cup diameter: 34 mm, bob diameter: 32 mm, bob length: 33 mm). Measurements have been performed on 12 mL solution and the temperature was set with an accuracy of 0.05^{o}C. A stress controlled rheometer MCR 301 (Physica) has been used for the experiment performed on the KS3.

Polarized microscopy has been performed with a Leica DMRXE. Sample were filled into a 0.1 mm thick capillary thermostated with an accuracy of 0.05^{o}C. In order to follow the crystallization process a thermostated cell was designed for 0.1 and 0.5 mm thick capillary (see fig. 2.27). The cell is thermostated and the temperature within the cell is controlled by a thermocouple with a precision of 0.1 ^oC. The large surface of contact between the cell and the capillary allows a fast quenching of the sample and makes it ideal for the direct observation of the crystallization process. Images of the samples were taken in a dark room without filter.

2.3.3 Effective volume fraction and crystallization

The established liquid-crystal coexistence domain for hard spheres lays between the freezing volume fraction ϕ_F at $\phi_{eff} = 0.494$ and the melting volume fraction ϕ_M at $\phi_{eff} = 0.545$ as obtained from computer simulation [153]. An experimental phase diagram could be achieved by determining the crystal fraction of the samples from the position of the

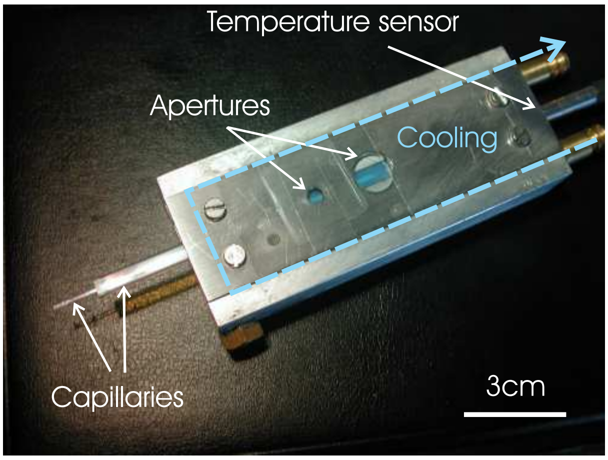

Figure 2.27: *Thermostated cell.*

coexistence liquid-crystal boundaries after sedimentation. This can be linearly extrapolate to determine the beginning and the end of the coexistence domain [117, 154]. To this purpose solutions with weight concentrations ranging between 6 and 14 $wt.\%$ have been prepared. The samples KS1 and KS3 were shaken after preparation to destroy residual crystallites and stored for more than one month at room temperature $20.5^oC \pm 0.5^oC$. In the case of the KS2 the suspensions have been heated to 30^{o}C in order to destroy possible crystals that may have formed at room temperature . These suspensions are subsequently cooled down quickly to 21 ^oC and kept at this temperature for a time of typically two months.

After screening of the electrostatic interactions by adding 5.10^{-2} $mol.L^{-1}$, all the samples crystallize at defined concentrations. This hints to the low polydispersity of the particles. The hydrodynamic radius of the microgel R_H can be used to calculate the effective volume fraction ϕ_{eff} for temperatures below 25^oC by

$$\phi_{eff} = \phi_c \left(\frac{R_H}{R_c}\right)^3 \tag{2.33}$$

where R_c is the core radius calculated from the cryo-TEM and ϕ_c is the volume fraction of the cores in the system. The latter quantity can be approximated from the weight concentration of the particles in the system and the mass ratio between the core and the shell of the particles. To avoid possible errors due to the small experimental uncertainty of R_H, averaged values have been taken from this graph by approximating R_H by a straight line in this region of temperatures.

The density of the particles and their size is not high enough to ensure rapid sedimentation of the crystalline phase. Only after two months, crystals which can be seen by eye by means of the Bragg-reflections, have sedimented. Fig. 2.28 exhibits the liquid-crystalline region of the different samples and the corresponding phase diagram. The experimental phase diagram was taken from the change in the position of the coexistence boundary indicated by the dashed lines. As expected the experimental points describe a linear dependence in the biphasic region. The data have been rescaled to $\phi_F = 0.494$ in order to compare the different experimental phase diagrams. For the KS1, the coexistence domain

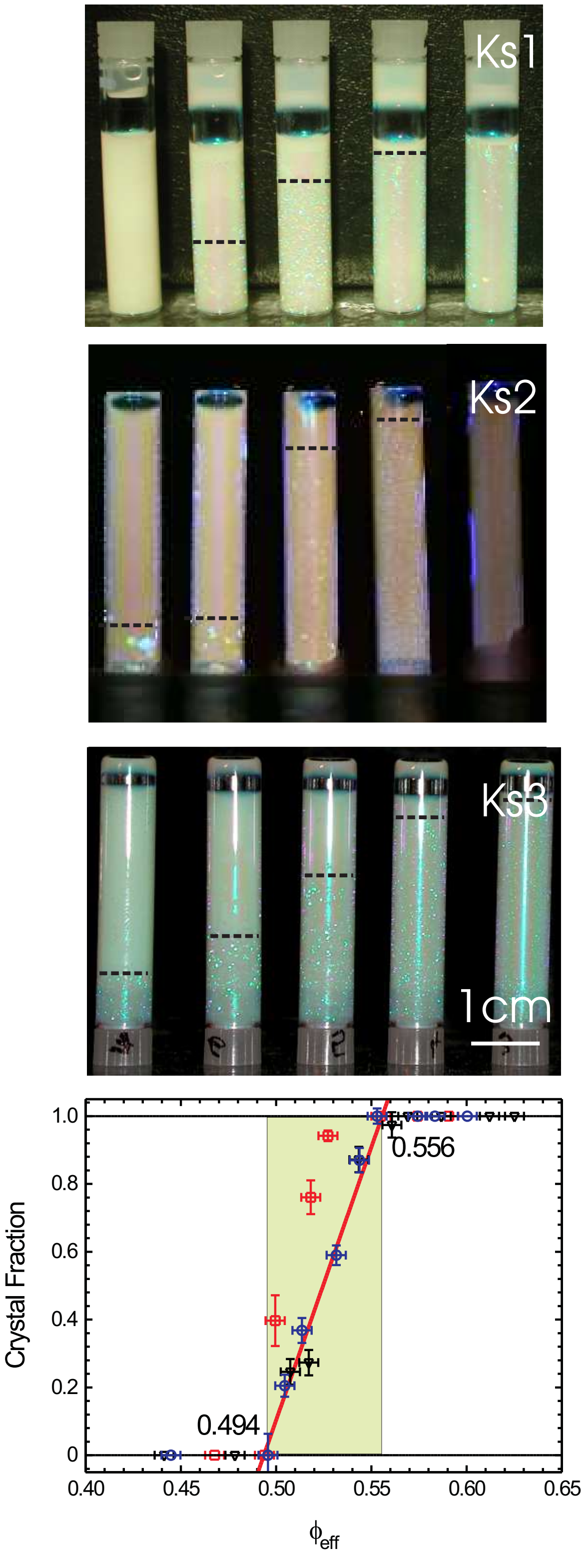

Figure 2.28: *Different core-shell suspensions in the biphasic region with 1.25 mol.% (KS1), 2.5 mol.% (KS2) and 5 mol.% (KS3) crosslinking after two months and their corresponding experimental phase diagram. The crystal fractions determined from the height of the coexistence boundaries indicated by the dashed lines on the photographs were fitted by a linear regression (solid line) for the KS2 (hollow triangles) and the KS3 (hollow circles). The results obtained for the KS1 are indicated by hollow squares. The data have been rescaled to* $\phi_F = 0.494$*. The coexistence domain for the KS2 and KS3 is indicated by the green area.*

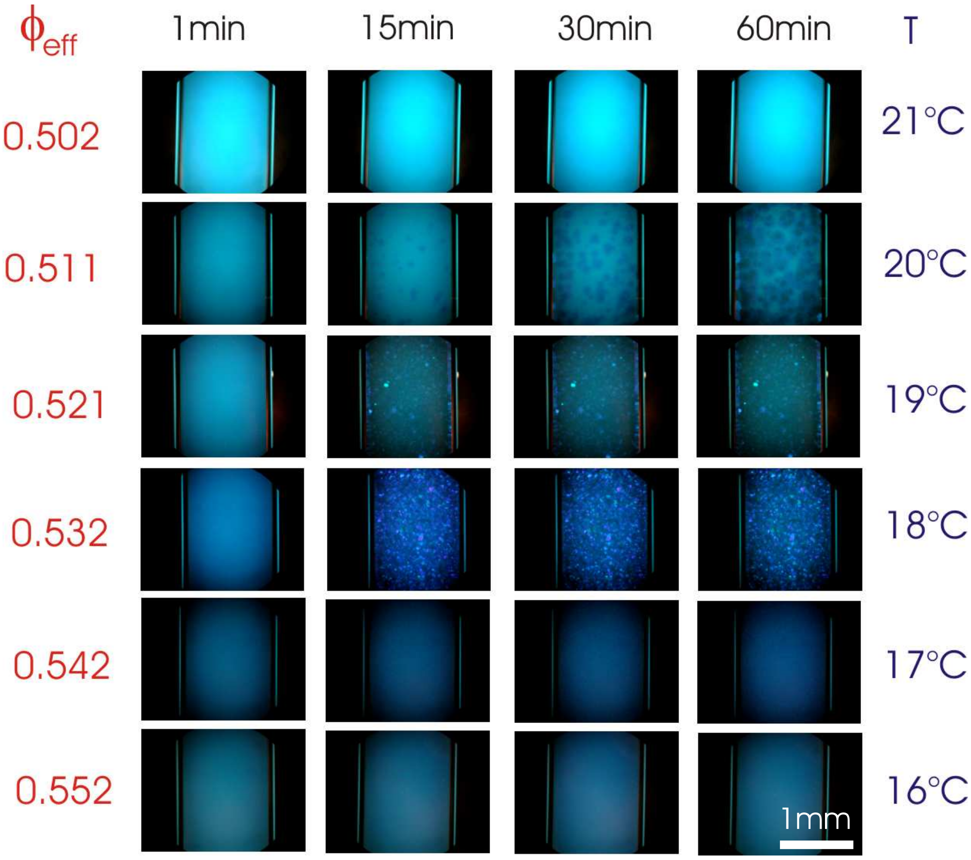

Figure 2.29: *Crystallization of a 9.48 wt.% solution at different temperatures corresponding to different effective volume fractions*

manifested by the presence of distinct crystals has been observed for effective volume between 0.494 and 0.535, which is smaller as what is expected for hard spheres. This can be related to the softness of the system as already observed for PNIPAM microgel [7]. At higher degrees of crosslinking (KS2 and KS3) the rescaled coexistence domain has been found between 0.494 and 0.556. This is in accord with the theoretical values $\phi_M = 0.545$ [153].

Fig. 2.28 shows also that the crystallization study of the thermosensitive particles is partially hampered by the strong turbidity of the system. This motivates the use of thin capillary for a direct observation of the crystallites. In this case polarized microscopy can be used to investigate the crystallization kinetics [135]. These experiments have been performed on the KS2, for a concentration of 9.48 $wt.\%$ (see fig. 2.29) and 8.22 $wt.\%$ (see fig. 2.30) at different temperatures. The same experiment was repeated for the KS3 at a concentration of 13.01 $wt\%$ at 20^oC and will be discussed in the next section. The samples were first maintained at about 30^{o}C in the 0.1 mm thick capillary and then quickly cooled-down to the temperature of investigation in the thermostated cell (see fig. 2.27).

Below the melting temperature the crystallization process of colloidal particles can be interpreted in the framework of nucleation and growth. The first crystals have been observed around $\Phi_{eff} = 0.50$. Considering the time of observation of one hour, this value is in good agreement with the phase diagram. The onset of the crystallization

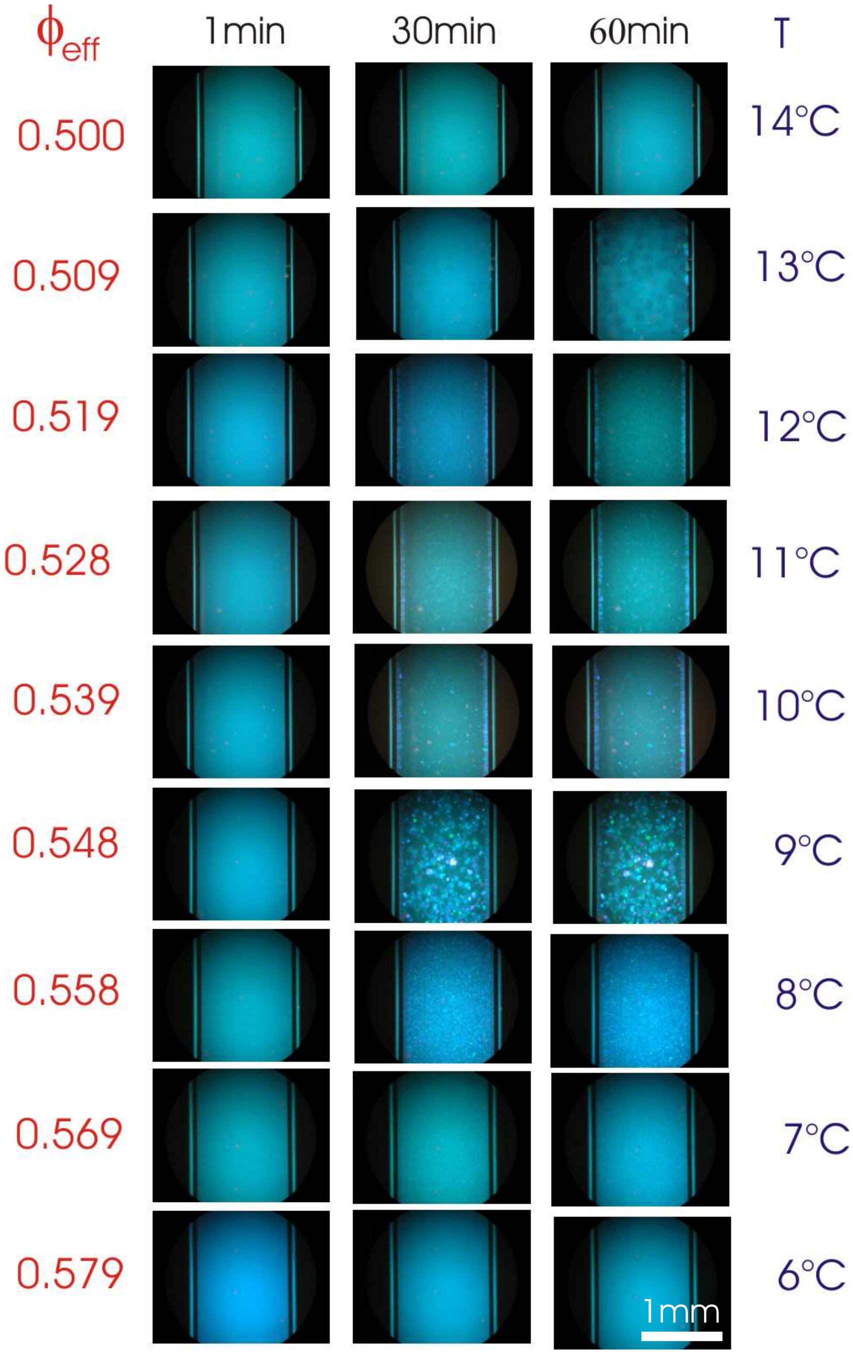

Figure 2.30: *Crystallization of a 8.22 wt.% solution at different temperatures corresponding to different effective volume fractions*

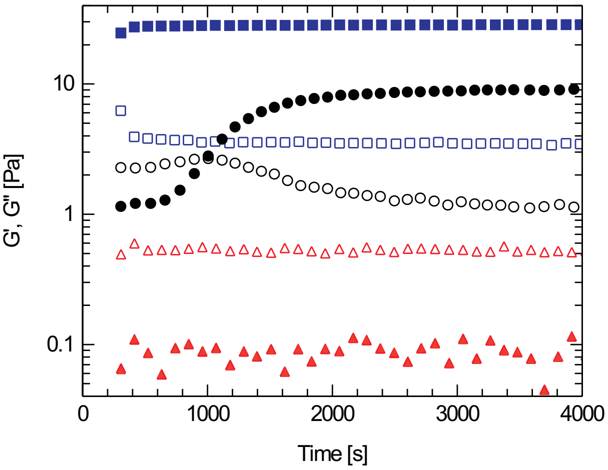

Figure 2.31: *Viscoelastic behavior of crystallizing suspensions vs. glassy systems: The storage modulus* G' *(filled symbols) and the loss modulus* G'' *(open symbols) are measured as function of time in the linear viscoelastic regime at 1Hz and 1% after 5 min of shearing at 100* s^{-1} *for a crystallizing system (circles) and a glassy system (squares). The triangles refer to the liquid state* ($\phi_{eff} = 0.49$)*, The circles to a volume fraction of 0.52 (two-phase regime) whereas the squares give the results for the glassy state* ($\phi_{eff} = 0.65$).

is manifested by the apparition of large crystals growing on the walls of the capillary. At lower temperatures corresponding to higher Φ_{eff} most crystals are formed in bulk, the nucleation increases, whereas the size decreases. Above $\Phi_{eff} = 0.542$ no crystal was observed in the 9.48 *wt.%* solution. This is in good agreement with observations performed on colloidal hard spheres assimilated suspension by light scattering [123]. It was demonstrated that when the melting concentration is exceeded, nucleation events become correlated and high nucleation rate densities suppress crystal growth. At higher effective volume fractions the crystals are indeed strongly compressed impeding their growth. On the contrary some crystals can still be observed until $\Phi_{eff} = 0.57$ for the 8.22 *wt.%* solution, which can be attributed to a slight variation of the softness of the particles for the lower temperatures.

2.3.4 Linear viscoelastic behavior

The previous section has clearly revealed that the thermosensitive suspensions crystallize if the effective volume fraction ϕ_{eff} is above 0.49. Moreover, the evolution of the samples as function of the time suggests that the induction time until crystallization occurs depends on ϕ_{eff} as expected for hard spheres system. Crystallization strongly affects the mechanical properties of the solution. For this reason rheological measurements were carried on concentrated suspensions to explore the crystallization kinetics in further details.

The linear viscoelastic behavior is studied first for different KS2 solutions. For this purpose the storage modulus G' and the loss modulus G'' is measured from a suspension with 9.48 *wt.%* at different temperatures, corresponding to different volume fractions

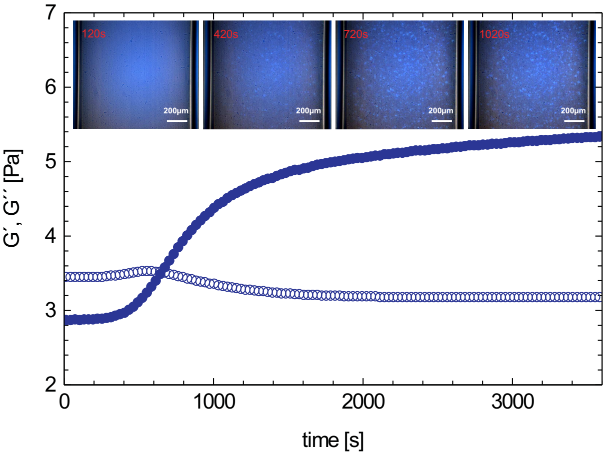

Figure 2.32: *Comparison between the linear viscoelasticity measurement and the polarized microscopy during the crystallization process of a 13.01 wt. % KS3 solution at 20°C* ($\phi_{eff} = 0.54$)*. The storage modulus* G' *(filled symbols) and the loss modulus* G'' *(open symbols) are measured as function of time in the linear viscoelastic regime at 1Hz and 1% after 5 min of shearing at 100* s^{-1}*. The results are compared to the polarized microscopy observations at 20°C for different times after a fast quenching from 30°C to 20°C.*

ϕ_{eff}. A deformation of 1 % and a frequency of 1 Hz has been chosen. Additional measurements have shown that the linear viscoelastic regime is attained for these parameters. To remove the samples history, all suspensions were sheared for 5 minutes with a shear rate of 100 s^{-1} prior analysis. In all cases reported here the time of observation was more than one hour.

The solution was measured at 22^oC which corresponds to an effective volume fraction $\phi_{eff} = 0.49$. G' is higher than G'' for the entire time of observation indicating a stable fluid phase. Lowering the temperature to 19 ^oC leads to a regime where $G' \ll G''$ where no crystallization is expected. However after an induction time of 700 s a marked increase in G' is observed as shown in fig. 2.31. G'' goes through a slight maximum and finally decreases markedly so that $G' \gg G''$ in the final stage attained after ca. 1 hour. The highest effective volume fraction 0.65 was reached by lowering the temperature to 8 ^oC. Note that this very high volume fraction can easily be reached by adjusting the temperature. In this case fig. 2.31 demonstrates that $G' >> G''$ as expected for the glassy state. At this high volume fraction local rearrangements are slowing down which is marked by a slow increase of G' with the time.

The same experiment has been performed for the KS3. Fig. 2.32 presents the timesweep obtained for a 13.01 $wt.\%$ solution at 20^oC ($\phi_{eff} = 0.54$) and is compared to the observation by polarizing microscopy. The increase of G' follows the apparition of the first crystallites after 420 s. After 720 s corresponding to the crossover of G' and G'' no further change can be observed from the polarized microscopy even if the G' is still increasing. The same observation was done on the others solutions investigated in the coexistence domain. This underlines the good agreement and the complementarity of this two technics. We determined the induction time of the crystallization. This time was estimated from timesweep experiments as the time where crystallization induces a 10% increase of

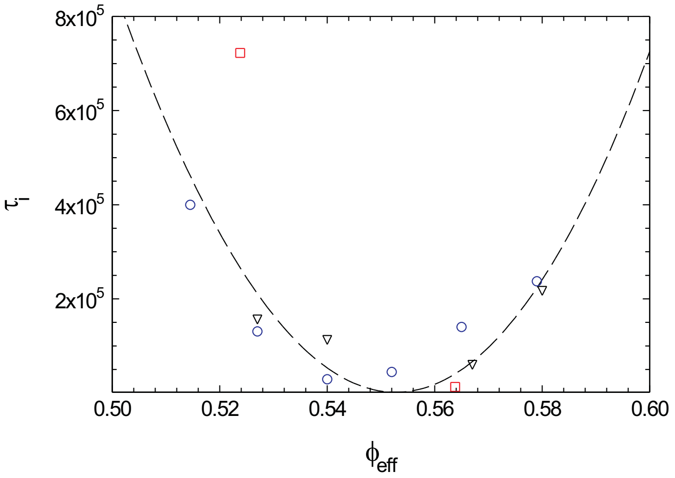

Figure 2.33: *Beginning of the crystallization described by the dependence of the characteristic time τ_i on the effective volume fraction ϕ_{eff} for different concentrations (12.1 wt.%: circles, 13.01 wt.%: down triangles, 13.58 wt.%: squares) at different temperatures. The dashed line is here to guide the eyes.*

the complex modulus G^*. This time was then normalized by the diffusion time defined as R_H^2/D_0, where R_H is the hydrodynamic radius and D_0 the free-particle diffusion constant. This gives the characteristic time τ_i. Fig. 2.33 presents the dependence of τ_i on ϕ_{eff} obtained for different concentrations at different temperatures.

τ_i first decreases with increasing volume fractions and reaches a minimum around $\phi_{eff} = 0.55$. An increase is observed again for higher effective volume fractions. The minimum is in good agreement with the literature [123]. This corroborates the framework of crystallization and growth. Close to $\phi_{eff,f}$ the growth process predominates as the nucleation is slow. This results in a slow crystallization and in the formation of large crystals. The growth process decreases with increasing volume fraction in the benefit of a faster nucleation. The crystallization kinetics reaches then a maximum around $\phi_{eff} = 0.55$, which corresponds to the maximum of the nucleation rate for hard spheres colloidal suspension as found experimentally in ref. [123] and theoretically [119]. To higher ϕ_{eff} the crystallization is slowed down as the self diffusion of the particles is decreasing. Moreover the proximity of the nuclei hinders the growth of the crystals. For $\phi_{eff} > \phi_g$ the suspensions still crystallize, at least partially, by the slow growth of large and irregularly shaped crystals on secondary nuclei, such as the container walls and regions of shear-aligned structures remaining from the tumbling action [121].

Hence, we conclude that the rheological experiments shown in fig. 2.31 and fig. 2.32 corroborates all findings of the previous section: Crystallization takes place at sufficiently high volume fractions. However, the kinetics of crystallization depends markedly on ϕ_{eff} as expected from previous investigations [122, 123, 155, 156]. The study of the viscoelastic behavior therefore gives direct information on the time scale in which the systems remains in the nonergodic state.

This indicates that the thermosensitive core-shell particles behave as hard spheres when considering their crystallization. Moreover, the fact that these systems crystallize again points to the narrow size distribution.

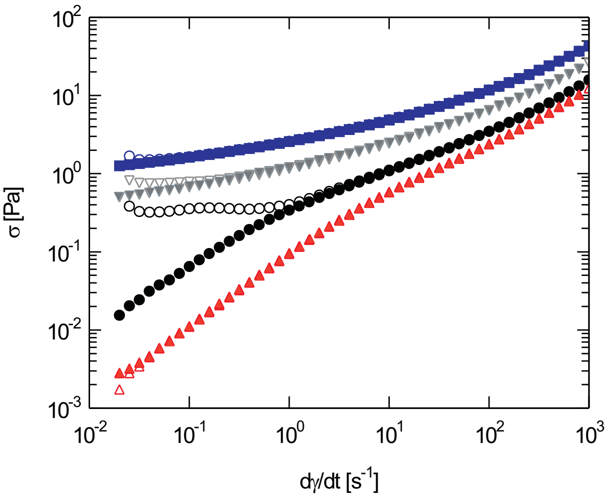

Figure 2.34: *Shear melting of crystallized suspensions. Shear stress as function of shear rate for a thermosensitive suspension containing 9.48 wt.% of the particles. The open symbols mark the measurements with increasing shear rate whereas the filled symbols show the results with decreasing shear rate. Parameter of the different curves is the temperature adjusting the effective volume fraction* ϕ_{eff}. *The effective volume fractions* ϕ_{eff} *are: triangles up: 0.49; circles: 0.52; triangles down: 0.57; squares: 0.64.*

2.3.5 Flow curves and shear melting

The study of the linear elastic behavior demonstrates that crystallization may intervene at time scales which are typical for rheological experiments necessary for measuring flow curves. Evidently, crystallization leads to a marked change of the flow behavior and must be excluded in a meaningful study of the flow curves. However, crystallites formed at sufficiently high concentrations may be shear-melted: Fig. 2.34 displays the shear stress σ as the function of the shear rate $\dot{\gamma}$, that is, the flow curves of the suspensions. Parameter of the curves is the effective volume fraction. For all volume fractions the solutions were aged for more than one hours. Hence, we used the systems discussed in conjunction with fig. 2.31. This means that the shear flow was started after crystallization has taken place for the intermediate volume fractions. The hollow symbols in fig. 2.34 indicate flow curves measured by raising $\dot{\gamma}$ slowly (5 s per point) from 0.02 to 1000 s^{-1} whereas filled symbols indicate the results obtained by slowly lowering the shear rate. In case of the fluid phase ($\phi_{eff} = 0.49$) both sets of data agree and practically superimpose. The same holds true for the highest volume fraction studied here ($\phi_{eff} = 0.64$). Fig. 2.34 hence demonstrates that flow curves present meaningful data for the present system even at exceedingly high volume fractions. However, there is a strong hysteresis for the partially crystalline sample having an effective volume fraction $\phi_{eff} = 0.52$. A critical shear stress is obviously needed to shear-melt the crystals and to attain a fluid state. Lowering the shear rate again then leads to a flow curve exhibiting a first Newtonian regime at sufficiently low $\dot{\gamma}$. The same observations were made when adjusting the same effective volume fraction by a different concentration and temperature. This demonstrates that the flow curves represent fully reproducible data once the crystallites are molten by shear (see also Ref. [151] and the discussion in the section 3.2).

2.3.6 Summary

Concluding this section and the preceding one we can state that suspensions of the thermosensitive core-shell particles behave expected for hard spheres for crosslinking higher than 1.25 *mol.%*. Thus, the effective volume fraction of the particles as derived from their hydrodynamic radius R_H provides the base for all further analysis. The effective volume fraction can be adjusted by quenching the system at different temperatures, and the crystallization kinetics can be investigated by polarizing microscopy and by rheological measurements in the linear viscoelastic regime. Thus this composite system present a good candidate for the crystallization study of pseudo hard spheres colloidal systems.

Quenching samples to effective volume fractions above the freezing effective volume fraction may still lead to the formation of crystallites that must be shear-molten prior to measurements of the flow curves. This problem of shear-melting will be addressed in another section (see section 3.2).

3 Dynamics

3.1 Characterization of the viscoelastic behavior of complex fluids using the piezoelectric axial vibrator

3.1.1 Introduction

Rheological properties of complex fluids as, e.g., polymer solutions or suspensions of colloid particles give important information about the microstructure and the dynamics of these systems [157]. They thus provide the base for the applications of these systems. Complex fluids exhibit structural features that range over many orders of magnitude [158]. Their relaxation times span over an equally broad range as well. Measurements of the rheological properties as the storage modulus G' and the loss modulus G'' must therefore cover an enormous scale in the time or in the frequency domain in order to capture all relaxation processes in these materials. Considering G' and G'' as functions of the frequency f it is obvious that low values of f are necessary to attain the first Newtonian region. On the other hand, the modulus G' measured at high frequencies provides insight into the interparticular forces [159]. Hence, the highfrequency limiting values $G'(\omega)$ and $\eta'(\omega)$ of colloidal suspensions can be used to probe the magnitude of hydrodynamic interactions between the particles and their repulsive potential. Moreover, G' and G' of suspensions of hard spheres measured over a sufficiently wide range of frequencies may be evaluated to yield information about the structural arrest of the spheres at high volume fractions that can be related to the theory of the glass transition in these systems [39, 40, 160–165].

This brief introduction demonstrates that techniques capable of measuring viscoelasticity of complex fluids over a wide range of frequencies are needed [159, 166]. Conventional mechanical rheometers, however, can only access the range of low frequencies ($<50\ Hz$) because of the inertial effects. Mellema and co-workers have introduced the use of torsional resonators for the study of colloidal suspensions [167]. More recent developments in this field have been summarized by Romoscanu et al. [168]. In particular, Willenbacher and co-workers demonstrated that torsional resonators can be used for measurements at high frequencies in the kilohertz range [159]. The obvious disadvantage of torsional resonators is the fact that these devices can be used only at given frequencies. Intermediate frequencies have often been accessed by use of the time-temperature superposition principle [157]. An example for this approach in the field of suspension rheology is the work of Shikata and Pearson on hard sphere colloids [169]. But in general, the time-temperature superposition principle is not applicable for complex fluids. Therefore measurement techniques that span the entire frequency range without resorting to the time-temperature superposition principle are of central interest in the field of complex fluids. Microrheological techniques recently introduced by Mason and Weitz [160, 170, 171] give access to a wide range of frequencies. Moreover, the mechanical spectra are derived for a continuous range of frequencies. Microrheology, however, relies on the so-called "generalized Stokes–Einstein relation" which may hold only for certain systems. It has been shown to be inadequate for charged colloids [172], and its applicability to complex fluids must be checked in each case. Finally, for the intermediate frequency only a few instruments were able to give a continuous and reliable measurement as, e.g., the piezorheometer described in the work of Cagnon and Durand [173–175] or the piezoelectric rotary vibrator [176] both working in shear strain. Recently, Pechhold and co-workers introduced a new device named "piezoelectric axial vibrator" (PAV). It consists of a dynamic press with a thin gap in which the liquid is confined. A squeeze flow is generated by a piezoelectric drive and the answer of the system measured by piezosensors can be evaluated to lead to G' and G'' between 10 and 3000 Hz. In this way the PAV closes the gap in the frequency range of conventional rheometers and the torsional resonators. In principle, the concept of the PAV is very appealing and the frequency range accessible by this instrument is exactly in the range that must be probed for the study of typical complex fluids. Based on earlier work by Kirschenmann [177] we present a comprehensive test of the PAV as applied to typical complex fluids as polymer solutions and colloidal suspensions. The results obtained with this instrument are compared to data from conventional rotational rheometry at low frequencies and from a set of torsional resonators at high frequencies. Moreover, the data obtained from rotational rheometry at various temperatures are shifted according to the time temperature superposition principle in order to cover the same frequency range as the PAV. The purpose of this study is twofold: (i) At first to examine the reliability of the PAV and its possible limitations and (ii) to demonstrate that the combination of the three rheometers, namely the mechanical spectrometer, the PAV, and the torsional resonators provides a convenient and reliable access to the viscoelastic properties of complex fluids over 5–7 orders of magnitude in frequency. This will be further demonstrated by analyzing the viscoelasticity of a suspension of thermosensitive particles.

3.1.2 Theory

The general theory of squeeze flow is well exposed in standard textbooks of rheology [178] and the theory of the PAV has been already presented in the work of Kirschenmann [177]. Here it suffices to delineate the main features. Figure 3.1 gives a scheme of the PAV. The lower plate oscillates with constant force amplitude $\hat{F}$. When the PAV is unloaded, the dynamic displacement $\hat{x}$ of the lower plate is measured at a given frequency leading to the compliance $\hat{x}/\hat{F}$. The same measurement is repeated at the same frequencies with the material under consideration filling the gap (see fig. 3.1). This gives the modulated compliance $\hat{x}/\hat{F}$. From the complex ratio $\hat{x}_0/\hat{x}$, the complex squeeze stiffness K^* of the material can be calculated by use of an appropriate mechanical equivalent circuit (see fig. 3.1) and solving its equations of motion [177]:

$$\left\{ \begin{array}{ccc} -\omega^2 m_1 x_1 & = & -K^*(x_1 - x_0) - K_1 x_1 \\ -\omega^2 m_0 x_0 & = & -K^*(x_0 - x_1) - K_{01}(x_0 - x_2) + F \\ 0 & = & -K_{01}(x_2 - x_0) - K_{02} x_2 - F \end{array} \right. \tag{3.1}$$

For linear viscoelasticity this calculation leads to the formula

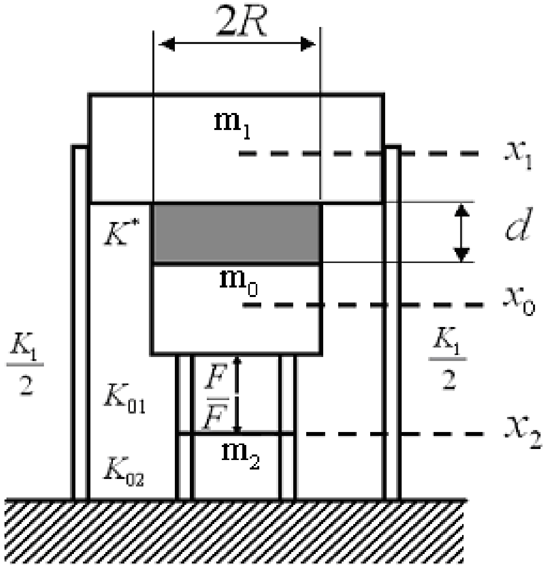

Figure 3.1: *Mechanical equivalent model of the PAV. The material with the complex stiffness K^* is enclosed in the gap (shaded area) of radius R and thickness d. The lower plate oscillates with a given frequency with constant force amplitude $\hat{F}$. The dynamic displacement of the lower plate leads to K^* and in turn to the complex modulus G^*. See text for further explanation.*

$$K^* = \frac{3\pi}{2} R \frac{R^3}{d} G^* / (1 + \frac{\varrho \omega^2 d^2}{10 G^*}) + ... \tag{3.2}$$

where R is the radius of the plate, $(d \ll R)$ is the gap width, ϱ is the density of the squeezed material, and G^* is its complex shear modulus. The expression of the numerator agrees with that derived in the literature [178, 179]. The denominator contains the first term (slit approximation) of a series expansion that takes into account the inertia of the material in the gap. This effect may become important at very high frequencies. Equation 3.2 tacitly assumes an incompressible material and hence only considers the complex shear modulus G* or the complex compliance $J^* = 1/G^*$.

For precise measurement, however, the dynamic compressibility κ^* must be introduced as well. For squeeze flow (in the limit of small amplitudes) one obtains [177]:

$$\frac{1}{K^*} = \frac{2}{3\pi} \frac{d^3}{R^4} \left(\frac{1}{G^*} + \frac{3}{2} \frac{R^2}{d^2} \kappa^* \right) \tag{3.3}$$

Equation 3.3 demonstrates that the correction due to a finite compressibility depends strongly on the ratio R/d. Its magnitude can be obtained through performing measurements at different gap thickness d.

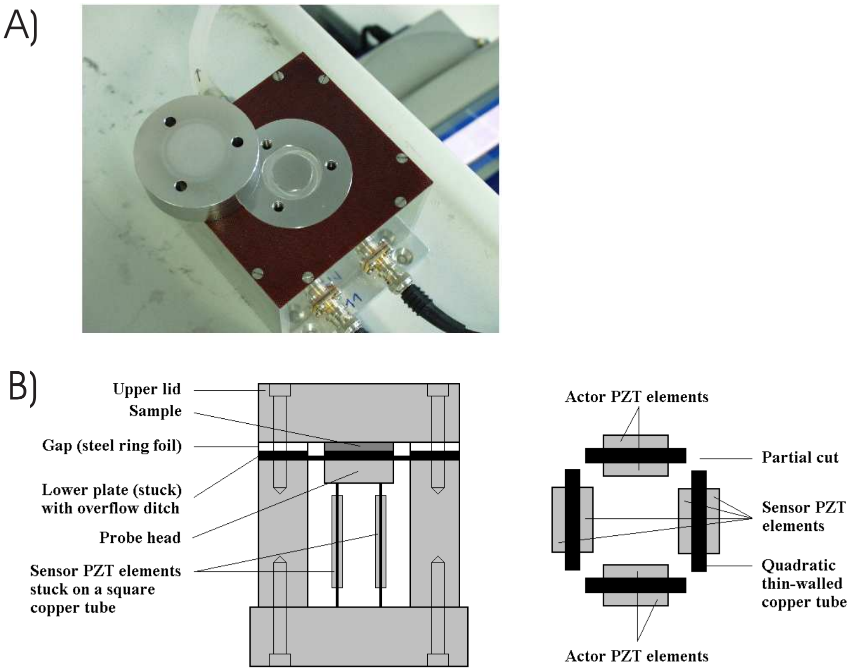

Figure 3.2: *A) Piezoelectric axial vibrator used in this study. The upper lid is removed to show the plate moved by the piezodrives. B) Longitudinal cut of the PAV (left-hand side) and transversal cut (right-hand side) of the quadratic tube containing the actor and the sensor piezoelements. Four actor piezoelements elements are stuck on both side of two opposite tube walls. Another four sensor piezoelements elements are stuck on both of the remaining walls. Four partial cuts avoid direct coupling between actor and sensor elements.*

3.1.3 Instruments

The PAV is a dynamic press working at frequencies between 10 and 3000 Hz. The actor/sensor is a thin-walled quadratic copper tube carrying on top a thick stainless steel plate, which serves as the lower boundary of the sample gap (see fig. 3.2).

As shown in fig. 3.2(b), four piezoelements are attached to two opposite walls of the tube in order to exert the vibrations while four additional piezos are fixed to the remaining sides in order to pickup the response signal. Direct coupling of excitation and detection is avoided by four lengthwise cuts of the tube (see fig. 3.2(b)). This lower part of the device is surrounded by a double walled cylinder allowing the circulation of a thermostating fluid. The whole setup is covered by a thick metal lid, which is the upper boundary of the gap and provides a complete sealing of the fluid. The rigidity K_0 of the cylinder must at least attain 1.108 Nm^{-1} to assure a high resonance frequency for the head of the probe and the sensor cylinder. Therefore the sample rigidity, K^*, should be lower than 109 Nm^{-1}. The PAV is operated by a lock-in-amplifier. The exciting voltage of the driving piezos is proportional to the axial force. The measured voltage of the piezos that monitor the deformation is the signal used for determining K^*. The width d of the gap of the squeeze-flow rheometer is defined by the lid mounted onto the rheometer (see fig. 3.2). In order to vary the gap, several rings of 10, 35, 50, 100 μm thickness can be used. The variation of the gap turned out to be necessary in order to perform the measurements in the correct

Table 3.1: *Viscosities of different glycerol/water mixtures at 20 °C [180] used for the calibration of the PAV.*

Weight fraction of glycerol	η at 20^oC ($mPas$).
0	2.26
35	3.040
50	6.050
65	15.54
75	36.46
85	112.9
95	545
100	1499

range. Systems with low viscosities must be measured using a small d whereas higher viscosities needed a wider gap (see later). Hence, variation of the gap width between 20 and 200 μm covers measurements of the viscosity in the range between 1 and 2000 $mPas$. The required sample volume is on the order of 100 mL depending on the width of the gap. In all case the amount of liquid was accurately adjusted by a microsyringe. The temperature was controlled with an accuracy of ± 0.02^oC.

3.1.4 Calibration of the instrument and accuracy

The instrument was calibrated using Newtonian liquids of different viscosity to determine the optimal gap for each range of viscosities. For this purpose a set of different glycerol/water mixtures was used. The viscosities of these mixtures are summarized in Table I. In order to compare the viscosities obtained by the PAV to data from other systems, two rheometers have been employed: A rheometrics fluid spectrometer for the range of low frequencies (0.01–15 Hz), and the torsional resonators introduced recently by Willenbacher and co-workers for the region of high frequencies [159]. In the following we give a brief description of the measurements using these devices. The Fluids Spectrometer RFS II from Rheometrics Scientific is a strain-controlled rotational rheometer equipped with a Couette system (cup diameter: 34 mm, bob diameter: 32 mm, bob length: 33 mm).

Strains are applied in the range starting from 500 % for the low viscosity liquids to provide an accurate response up to 0.5% for the more viscoelastic solutions. For each measurement the deformation was set to remain in the linear viscoelastic regime. Measurement were performed on 10 mL of the fluid and the temperature was set with an accuracy of ± 0.05^oC. Two torsional resonators supplied by the Institut für dynamische Materialprüfung, Ulm, Germany, have been used to obtain data at high frequencies [159]. Two geometries are available (cylinder or double-dumbbell) allowing for measurements at 13, 25, and 77 kHz. The penetration depth of the shear wave is typically on the order of 50 nm for the samples investigated here. This ensures that the method probes the viscoelastic properties of the bulk phase. The measuring cell, however, is much larger than this penetration depth and no disturbance may result from the walls of the container. The small amplitudes of the torsion of the cylinder (< 50 nm) ensure that the maximum strain is small. The measurements are hence taken in the linear viscoelastic

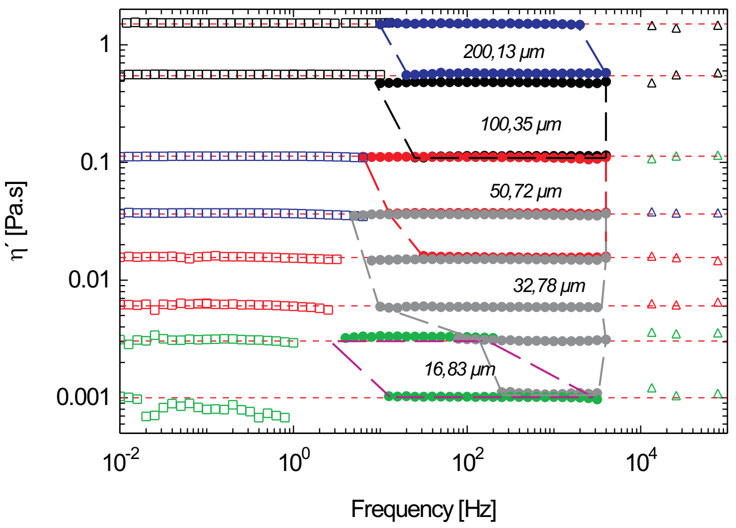

Figure 3.3: *Viscosities of water-glycerin mixtures measured with fluid spectrometer RFS II (open squares), PAV (filled symbols), and torsional resonators (open triangles). The weight percent of glycerol is varied between 0% and 100% as indicated in the graph in order to adjust a wide range of viscosities. The values of Table I are indicated by the dashed lines. Different gap thickness were used for the PAV: 20, 35, 50, 100, and 200 nm to obtain the optimal measurement. An experimental value of the true gap thickness was also calculated for each gap and given directly in the graph.*

regime. The experimental procedure and the evaluation of data have been described recently [159]. The real part of the complex viscosity of water-glycerine mixtures is plotted against the frequency in fig. 3.3. Here data obtained by all the three devices are presented. The gaps of the PAV was varied (d =20, 35, 50, 100, and 200 μm) in order to adjust for the viscosity of the sample ranging from 1 to 1500 $mPas$ (dashed lines in fig. 3.3). The viscosity was calculated using eq. 3.2 and the width d of the gap was slightly adjusted so that the experimental value was matched. This calibration of the width of the gap is used in subsequent measurements. Moreover, results obtained for one sample but different gap widths demonstrated that the contribution due to the dynamic compressibility (cf. eq. 3.3) is negligible for these Newtonian liquids as expected. Figure 3.3 also delineates the optimal domains of the measurement of the PAV by dashed lines. In these domains the measured viscosity is independent of the frequency.

In the following only data from these optimal domains will be shown. The good correspondence between the three apparatus illustrates the quality of the measurements provided by the PAV for the Newtonian solutions.

3.1.5 Viscoelastic fluids

Polystyrene solution

A commercial polystyrene grade (PS 148 H from BASF) dissolved in ethylbenzene is used as a benchmark system to check the accuracy of the measurements of G' and G'' by the PAV. Concentrated polymer solutions present well-studied examples of viscoelastic fluids

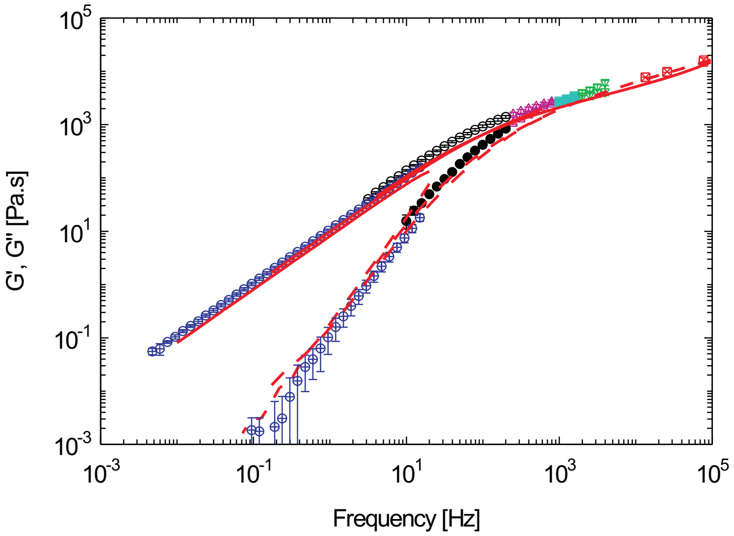

Figure 3.4: *Validation of G' (full symbols) and G'' (hollow symbols) measured with fluids spectrometer RFS II (quadrangles), PAV (circlesd), and torsional resonators (triangles) obtained for a 30% polystyrene solution in ethylbenzene. The data are compared to results derived from the time temperature superposition principle. Values of G' are indicated by dashed lines whereas G'' is given by solid lines. The data obtained by the PAV have been measured at the optimal gap thickness.*

that exhibit moduli varying over many orders of magnitude with increasing frequency [181]. The ethylbenzene used was of commercial grade without special purification. The solution contains 30% polystyrene with $M_w = 148000\ g.mol^{-1}$. Solutions of polystyrene were carefully studied and precise data based on the time-temperature superposition principle are available [181, 182]. G' and G'' of this solution as the function of frequency was obtained as follows: Rheological measurements with a mechanical rheometer were done at -80, -50, and 24^oC. In order to obtain a wide range of frequencies, the frequency-temperature superposition principle has been used as already discussed by Baumgärtel and Willenbacher [182]. The temperature dependence can be described by a universal, concentration invariant Williams–Landel–Ferry-shift parameter a_T [183]:

$$log_{10}a_T = \frac{-c_1(T - T_{ref})}{c_2 + T - T_{ref}}. \tag{3.4}$$

We have chosen $T_{ref} = 20^oC$ and obtain $c_1 = 1.47$ and $c_2 = 143\ K$. Figure 3.4 displays G' and G'' as the function of the frequency. Data at low frequency have been obtained by the mechanical spectrometer RFS II whereas the three points referring to the highest frequencies have been measured using the torsional resonators.

The data at intermediate frequencies have been obtained with the PAV using the optimal width of the gap (see the discussion of Fig. 3.3). The data obtained by the three widely different instruments fit together within the limits of error of the respective devices. The lines give the respective values of G' (dashed) and G'' (full) derived from eq. 3.4. Good agreement is seen over six orders of magnitude. There are only small deviations between the measured data and the spectra calculated from the time-temperature superposition

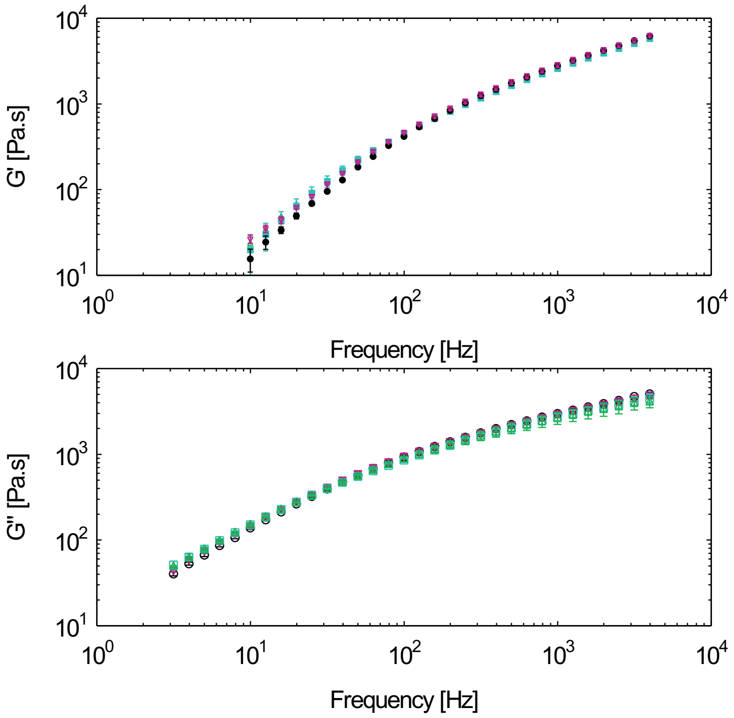

Figure 3.5: *Enlarged portion of Fig. 4 showing G' and G'' measured by the PAV with different width d of the gap: 100 (down triangles), 150 (squares), 185 (up triangles), and 200 μm (circles).*

principle. We assign these small discrepancies to the limitation of eq. 3.4 and to the experimental uncertainties in obtaining the moduli in such a wide temperature range. Figure 5 demonstrates that the width d of the gap has a minor influence on the resulting values of G' and G''. Here G' and G'' obtained from the polystyrene solution by the PAV for different width of the gap are plotted against the frequency f. Evidently, G' and G'' do not depend on d within the given limits of error. The maximum of error amounts to 20% if the width of the gap is not optimal. This further confirms the reliability of the instrument and justifies the neglect of the dynamic compressibility (cf. eq. 3.3). Thus, the earlier discussion has established two criteria for the accuracy of the measurement: First, the optimal width of the gap is obtained by measurement of Newtonian liquids.

The small corrections for the width of the gap, which followed from this calibration demonstrates that eq. 3.3 provides a accurate description of the flow in the instrument. Second, the measured spectra of G' and G'' must be independent of the width d. This is seen indeed in Fig. 3.5 and the residual discrepancies at low frequency can be traced back to a width of the gap which is not optimal. From these data and the foregoing comparison using a polystyrene solution as a benchmark system we conclude that the PAV gives reliable data for polymer systems that exhibit a marked viscoelastic behavior. The range of concentrations that can be studied is only limited by the smallest gap available (see the discussion of fig. 3.3). Hence, highly dilute polymer solutions in which the viscosity exceeds hardly the one of the solvent cannot be measured with the PAV with sufficient accuracy (see the discussion of this problem in Stokich et al. [184]).

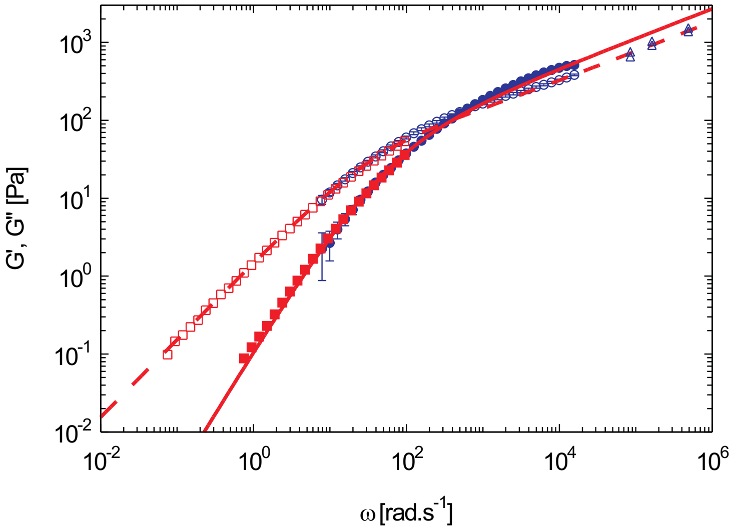

Figure 3.6: *Elastic (full symbols) and loss (hollow symbols) modulus of a 1.5 wt.% methylcellulose solution at 20°C measured with fluids spectrometer RFS II (squares), PAV (circles); measured at optimal thickness of the gap 100 µm, and torsional resonators (triangles). The fit was done using the generalized Maxwell's model including the high frequency contribution [Eq. (5)]. The fitted parameters are:* η_0 *=1.4 Pas,* η_∞ *=2.5 mPas,* τ_0 *=0.002 s, h =0.32.*

Methylcellulose in solution

Aqueous solutions of methylcellulose (MC) gel upon heating [185]. The gelation is thermoreversible and ascribed to the presence of hydrophobic interactions. The rheology of this system was already investigated in a study of Desbrières [186] and the rheological experiments were carried out on the piezorheometer built by Palierne [173–175]. Hence, these solutions provide another benchmark system. Methylcellulose has been purchased from Sigma-Aldrich. The weight average molecular weight of MC is 86000 $g.mol^{-1}$. The degree of substitution is ranging from 1.6 to 1.9 as indicated by the manufacturer. It was purified by dialysis in order to remove salts and other low molecular weight impurities. Solutions of 0.2 $wt.\%$ of methylcellulose were prepared in de-ionized water and stirred for 2 days to ensure a homogeneous solution. This solution was then packed in Spectra/Por® dialysis tube membranes which were bought from Spectrumlabs (MWCO-2000). Dialysis was carried out until the conductivity of water became equal to pure de-ionized water. Later the solution was dried in a vacuum oven at 80^oC. The pure methylcellulose was then stored for further use. The measurements were performed on a solution of 1.5 $wt.\%$ at 20^oC. Again the range of frequencies was covered by measurement using the three instruments. The rheogram shown in Fig. 6 is typical of an entangled polymer solutions. As can be seen from Fig. 3.6, a good correspondence between the three instruments is seen. The residual differences between the instruments are within their respective limits of error. This demonstrates again that concentrated polymer solutions can be measured by the combination of the three instruments. Following earlier work [186] a general Maxwell's model was used to describe the data. The expression that includes the high-frequency contribution reads

$$\eta^* = \frac{\eta_0}{1 + (i\omega\tau_0)^{1-\eta} + \eta_\infty}, \tag{3.5}$$

where η_0 is the zero-shear viscosity and η_∞ denotes the high-shear viscosity. Finally, t_0 is the average time of relaxation and the parameter h describes the width of the relaxation time distribution. Figure 3.6 demonstrates that eq. 3.5 provides a good description of the results over the entire range of frequencies under consideration here. This is in agreement with the earlier studies [186].

Thermosensitive latex particles.

As an example for a complex fluids we analyze here a thermosensitive latex that has been under scrutiny recently [34, 35]. The particles consist of a solid polystyrene core and a shell composed of crosslinked poly-N-isopropylacrylamide (PNIPAM) chains. Suspended in water these particles swell when lowering the temperature below room temperature through the uptake of water in the shell. Going to temperatures above 25–30^oC leads to a marked decrease of the particles radius because the water is expelled from the thermosensitive PNIPAM-layer again. This swelling transition within the layer is fully reversible [17, 63] and can be used to adjust the effective volume fraction ϕ_{eff} of the particles by increasing or lowering the temperature [34]. Evidently, the time-temperature superposition principle cannot be applied for determining G' and G''. The core-shell latex used in this study was prepared as described in the section 2.1.2 and corresponds to the KS4. The core particles has a radius of 52.0 nm and the shell a thickness of 53.3 nm at 10^oC as determined by light scattering. The degree of crosslinking was 2.5 $mol.\%$ with regard to monomer N-isopropylacrylamide. The latex was purified by ultrafiltration. The weight concentration of the latex was 10.85 $wt.\%$ and the corresponding effective volume fraction ϕ_{eff} was calculated as described in the section 2.3. For the suspension under consideration here ϕ_{eff} =0.585 at a temperature of 10^oC. The rheological measurements were realized with the set of the three instruments. A period of 1 h was allowed for thermal equilibrium before starting each measurement. Figure 3.7 displays $G'(\omega)$ and $G''(\omega)$ obtained in this way over the entire range of frequencies. As already discussed by Mason et al. [160, 161], a suspension of hard spheres in the vicinity of the glass transition should exhibit the features seen in Fig. 3.7: The storage modulus G$'$ is expected to exhibit a marked plateau for a rather wide range of frequencies while G$''$ is expected to go through a pronounced minimum.

The model proposed by Mason and Weitz [160, 161] has been first used for the qualitative description of the data thus obtained. It is based on the combination of three major effects. The low frequency behavior is described within mode coupling theory [162–165]. It assumes that the stress autocorrelation function has the same functional form as the density autocorrelation function. The high-frequency the data analysis is complicated due to an anomalous contribution to both G' and G'' proportional to $\omega^{0.5}$ which arises from a diffusional boundary layer between the spheres [187]. The high frequency suspension viscosity η'_∞ 8 leads to a contribution to G'' that is proportional to ω. It can be taken from the experimental data obtained at highest frequencies by use of the torsional resonators. The resulting expressions for G' and G'' are [160, 161]:

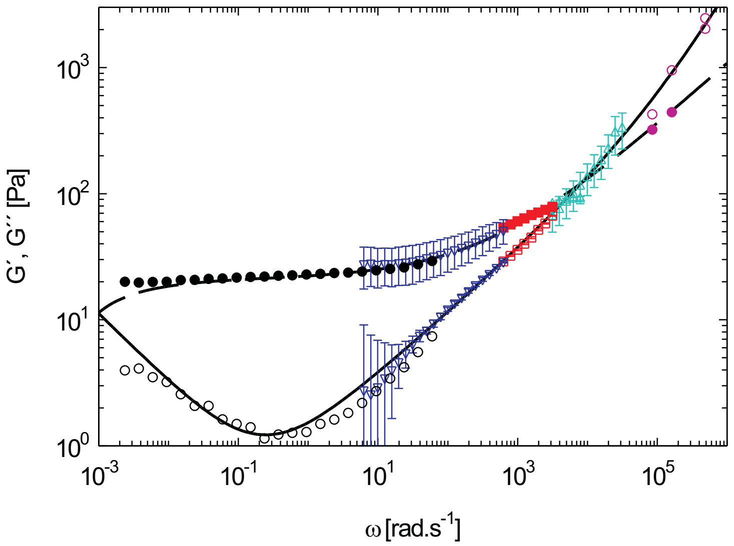

Figure 3.7: *Elastic (full symbols) and loss (hollow symbols) moduli of a concentrated thermosensitive latex 10.85 wt.% at 10ºC (ϕ_{eff} =0.585) measured with fluid spectrometer RFS II (squares), PAV (circles), and torsional resonators (triangles). The data obtained by the PAV have been measured at the optimal thickness of the gap. The experimental data are fitted by the model proposed by Mason and Weitz (eq. 3.6–3.7) with G_P =21 Pa, G_σ =0.4 Pa, t_σ =1 srad^{-1}, ϕ_{eff} =0.585, D_S =4.10^{-13} m^{2}s^{-1}, and η'_∞ =3 mPas.*

$$G'(\omega) = G_P + G_\sigma \left[\Gamma(1-a')cos\left(\frac{\pi a'}{2}\right)(\omega t_\sigma)^{a'} - B\Gamma(1+b')cos\left(\frac{\pi b'}{2}\right)(\omega t_\sigma)^{b'}\right] + G'_D(\omega) \tag{3.6}$$

and

$$G''(\omega) = G_\sigma \left[\Gamma(1-a')sin\left(\frac{\pi a'}{2}\right)(\omega t_\sigma)^{a'} - B\Gamma(1+b')sin\left(\frac{\pi b'}{2}\right)(\omega t_\sigma)^{b'}\right] + G''_D(\omega) + \eta'_\infty(\omega) \tag{3.7}$$

where $\Gamma(x)$ is the gamma function, a' =0.301, B =0.963, as and b' =0.545 are parameters predicted for suspensions of hard spheres [162]. G_σ is a fit parameter. The storage modulus has an inflection point at the plateau value G_P, and the frequency at the minimum of the loss modulus is set by the value of the plateau, $1/t_\sigma$. Following the approach of Mason et al. [160, 161] the frequency dependence of G'_D and G''_D for hard sphere suspensions is used here as given by Lionberger et al. [187] and by De Schepper et al. [188]:

$$G'_D(\omega) = G''_D(\omega) = \frac{6}{5\pi}\frac{k_BT}{a^3}\phi^2 g(2a,\phi)[\omega\tau_D]^{1/2} \tag{3.8}$$

where $\tau_D = a^2/D_s$, is the diffusional time determined by the ϕ-dependent short-time diffusion coefficient with a being to the radius of the particles. The radial pair distribution function at contact is approximated by $g(2a,\phi) = 0.78/(0.64-\phi)$ again mapping this suspension onto an effective hard sphere system (see the discussion of this point by Mason [171]). Moreover, we equate $\phi = \phi_{eff}$. Hence, G_σ and D_s are the only free fit parameters remaining here. Figure 3.7 demonstrates that there is good agreement between the data obtained by the three instruments. Moreover, good agreement is seen over eight orders of magnitude. The lines give the respective values of G' (solid line) and G'' (dashed line) derived from eqs. 3.6 and 3.7. This agreement is more remarkable when considering that only two fit parameters had to be used in this comparison. Hence, the model of Mason et al. [160, 161] based on the mode-coupling theory explains the measured viscoelasticity of suspensions very well. Nevertheless it fails to describe the relaxation of the system for the very long times below the glass transition. Biased on this pioneer work a new model proposed by Fuchs has been developed to come to a quantitative description of the linear viscoelasticity of hard spheres suspensions in the vicinity of the glass transition and will be presented in the next section of this chapter.

3.1.6 Summary

A new rheometer, the PAV, has been introduced and tested by using Newtonian liquids and viscoelastic polymer solutions. The data presented here demonstrate that the PAV works reliably between 10 and 3000 Hz. It thus closes the gap between conventional mechanical spectrometers and the torsional resonators. The combination of all three devices gives access to G' and G'' as the function of frequency over 7–8 orders of magnitude. This provides a sound basis for a comprehensive study of the viscoelasticity of complex fluids as was shown for the case of polymer solutions and suspensions of colloidal particles.

3.2 Shear stresses of colloidal dispersions at the glass transition in equilibrium and in flow

3.2.1 Introduction

Complex fluids and soft materials in general are characterized by a strong variability in their rheological and elastic properties under flow and deformations [158, 189]. Within the linear response framework, storage- and loss- (shear) moduli describe elastic contributions in solids and dissipative processes in fluids. Both moduli are connected via Kramers-Kronig relations and result from Fourier-transformations of a single time-dependent function, the shear modulus $g^{\mathrm{lr}}(t)$. Importantly, the linear response modulus $g^{\mathrm{lr}}(t)$ itself is defined in the quiescent system and (only) describes the small shear-stress fluctuations always present in thermal equilibrium [33, 158].

Viscoelastic materials exhibit both, elastic and dissipative, phenomena depending on external control parameters like temperature and/ or density. The origins of the change between fluid and solid like behavior can be manifold, including phase transitions of various kinds. One mechanism existent quite universally in dense systems is the glass transition, that structural rearrangements of particles become progressively slower [164]. It is accompanied by a structural relaxation time which grows dramatically. Maxwell was the first to describe this fluid-solid transition phenomenologically. Dispersions consisting of colloidal, slightly polydisperse (near) hard spheres arguably constitute one of the most simple viscoelastic systems, where a glass transition has been identified. It has been studied in detail by dynamic light scattering measurements [155, 156, 190–195], confocal microscopy [126], linear [161, 196], and non-linear rheology [7, 34, 197–201]. Computer simulations are available also [202–204]. Mode coupling theory (MCT) has provided a semi-quantitative explanation of the observed glass transition phenomena, albeit neglecting ageing effects [205] and decay processes at ultra-long times that may cause (any) colloidal glass to flow ultimately [162–165]. Importantly, MCT predicts a purely kinetic glass transition and describes it using only equilibrium structural input, namely the equilibrium structure factor S_q [33, 206] measuring thermal density fluctuations.

The stationary, nonlinear rheological behavior under steady shearing provides additional insight into the physics of dense colloidal dispersions [33, 158]. A priori it is not clear, whether the mechanisms relevant during glass formation also dominate the nonlinear rheology. Solvent mediated interactions (hydrodynamic interactions), which do not affect the equilibrium phase diagram, may become crucially important. Also, shear may cause ordering or layering of the particles [207]. Simple phenomenological relations between the frequency dependence of the linear response and the shear rate dependence of the nonlinear response, like the Cox-Merz rule, have been formulated, but often lack firm theoretical support or are limited to special shear history [158, 208].

On the other hand, within a number of theoretical approaches a connection between steady state rheology and the glass transition has been suggested. Brady worked out a scaling description of the rheology based on the concept that the structural relaxation arrests at random close packing [209]. In the soft glassy rheology model, the trap model of glassy relaxation by Bouchaud was generalized to describe mechanical deformations and ageing [210–212]. The mean field approach to spin glasses was generalized to systems with broken detailed balance in order to model flow curves of glasses under shear [213, 214]. The application of these novel approaches to colloidal dispersions has lead to numerous insights, but has been hindered by the use of unknown parameters in the approaches. MCT, also, was generalized to include effects of shear [215–217], and, within the *integrations through transients* (ITT) approach, to quantitatively describe all aspects of stationary states under steady shearing [41, 44, 45], Some aspects of the ITT approach to flow curves have already been tested [218], but the connection, central in the approach, between fluctuations around equilibrium and the nonlinear response, has not been investigated experimentally up to now.

In the present chapter the connection between structural relaxation close to glassy arrest and the rheological properties far from equilibrium is explored. We used the theory developed by the Prof. Matthias Fuchs and his coworkers. Within the scope of this collaboration we crucially test the ITT approach, which aims to unify the understanding of these phenomena. It requires, as sole input, information on the equilibrium structure (namely S_q), and, first gives a formally exact generalization of the shear modulus to finite shear rates, $g(t, \dot{\gamma})$, which is then approximated in a consistent way. We investigate a model dense colloidal dispersion at the glass transition, and determine its linear and nonlinear rheology. Thermosensitive core-shell particles consisting of a polystyrene core and a crosslinked poly(N-isopropylacrylamide)(PNIPAM) shell were synthesized and their dispersions characterized in detail. Data over an extended range in shear rates and frequencies are compared to theoretical results from MCT and ITT.

This chapter is organized as follows: first the experimental and methods are presented as well as an introduction of the linear and non linear rheology. The next part summarizes the equations of the microscopic ITT approach in order to provide a self-contained presentation of the theoretical framework. Afterwards some of the universal predictions of ITT are discussed in order to describe the phenomenological properties of the non-equilibrium transition studied in this work. Building on the universal properties, a simplified model which reproduces the phenomenology is introduced. The comparison of combined measurements of the linear and non-linear rheology of the model dispersion is then compared with calculations in microscopic and simplified theoretical models.

3.2.2 Experimental system and methods

The core-shell particles with 5 *mol.*% crosslinking (KS3) are used in this study. The synthesis and characterization of this system are described in chapter 2.1. Different solutions were prepared between 10.75 and 13.58 *wt.*%. The concentration in salt (KCl) was adjusted to 5.10^{-2} molL^{-1} KCl to screen the remaining electrostatic interactions. The dependence of ϕ_{eff} on the temperature is given by the hydrodynamic radius R_H determined from the dynamic light scattering in the dilute regime. R_H was linearly extrapolated between 14 and 25^{o}C ($R_H = -0.85925T + 123.78$ with T the temperature in ^{o}C and ϕ_{eff} was calculated following eq. 2.33 following the procedure described in chapter 2.3.

Three instruments were employed in the present study to investigate the rheological properties of the suspensions. The flow behavior and the linear viscoelastic properties for the range of the low frequencies were measured with a stress-controlled rotational rheometer MCR 301 (Anton Paar), equipped with a Searle system (cup diameter: 28.929

mm, bob diameter: 26.673 mm, bob length: 39.997 mm). Measurements have been performed on 12 mL solution and the temperature was set with an accuracy of $\pm$ 0.05^oC. The shear stress σ versus the shear rate $\dot{\gamma}$ (flow curve) was measured after a pre-shearing of $\dot{\gamma} = 100\ s^{-1}$ for two minutes and a timesweep of 1 hour at 1 Hz and 1 % deformation in the linear regime. The flowcurve experiments were performed setting $\dot{\gamma}$, first with increasing $\dot{\gamma}$ from $\dot{\gamma} = 10^{-4} - 10^{3}\ s^{-1}$ with a logarithmic time ramp from 600 to 20 s, and then with decreasing $\dot{\gamma}$. The frequency dependence of the loss G'' and elastic G' moduli has been measured for 1 % strain from 15 to 10^{-3} Hz with a logarithmic time ramp from 20 to 600 s. The measurements were first performed without pre-shearing after the timesweep, before the flowcurves experiments, and then after the flowcurves experiments 10 s two minutes after pre-shearing at $\dot{\gamma} = 100\ s^{-1}$ to melt eventual crystallites. We only considered experiments performed after pre-shearing in the following discussion of G' and G'' for the lowest frequencies.

Additional rheological experiments were carried out on Piezoelectric vibrator (PAV) and cylindrical torsional resonator described in the previous chapter (see chapter 3.1). The PAV was operated from 10 to 3000 Hz. The gap was adjusted with a 100 μm ring. Only the measurements in the glassy state have been performed with the PAV as the instrument does not allow any pre-shearing. The cylindrical torsional resonator used was operated at a single frequency (25 kHz). The experimental procedure and the evaluation of data have been described recently [35, 159].

The effect of the shear rate $\dot{\gamma}$ on the particle dynamics is measured by the Peclet number [33], $Pe_0 = \dot{\gamma} R_H^2/D_0$, which compares the rate of shear flow with the time an isolated particle requires to diffuse a distance identical to its radius. Similarly, frequency will be reported in the following rescaled by this diffusion time, $\omega' = \omega R_H^2/D_0$. The self diffusion coefficient D_0 at infinite dilution was calculated from the hydrodynamic radius R_H and the viscosity of the solvent η_s with the Stokes-Einstein relation so that $D_0 = k_BT/6\pi\eta_S R_H$. In dense dispersions, however, the structural rearrangements proceed far slower than diffusion at infinite dilution, and therefore, very small Peclet numbers and rescaled frequencies ω' are of interest in the following. Stresses will be measured in units of k_BT/R_H^3 in the following.

3.2.3 Linear and non linear rheology

This section presents the basics of the rheology of colloidal suspensions. In the rest of the chapter the mode coupling theory is introduced to give a quantitative description of the viscoelasticity of the system in the linear regime and of the flow behaviour in the stationary regime. By linear viscoelasticity we consider a system experiencing an oscillatory strain. The dependence of the stress to the amplitude γ and frequency of the solicitation is used to estimate the elastic and loss contribution usually represent by the moduli G' and G''. If we fix the frequency, the linearity is considered per definition for strains γ where these two moduli are constant. At this point the structure of the system is not disturbed and the system is in equilibrium. If the strain exceeds a certain value γ_o this condition is not respected anymore and the structure is disturbed leading

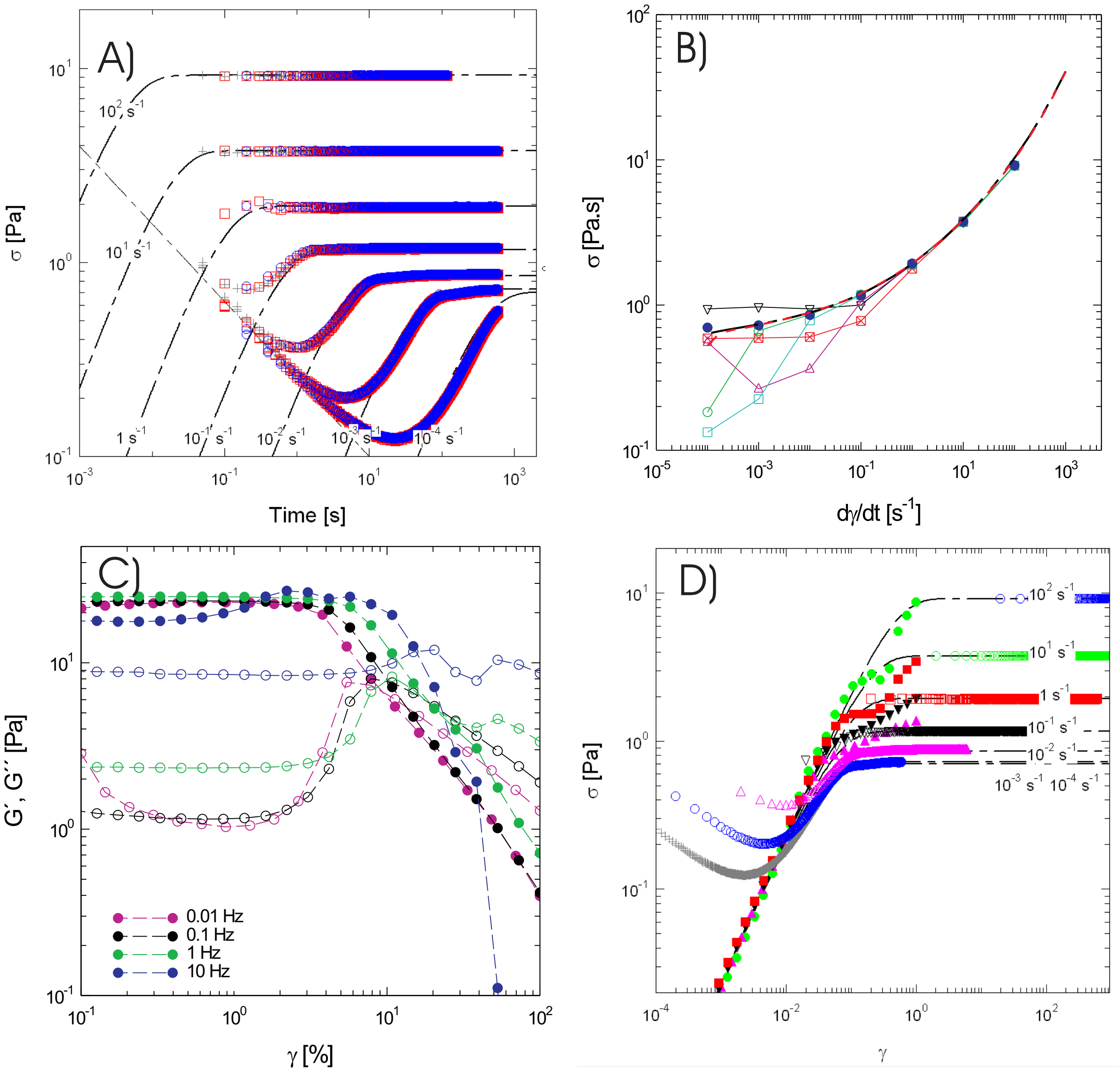

Figure 3.8: *A) step flow experiment performed at different shear rate with different time increments: 50 ms (crosses), 100 ms (squares), 200 ms (circles). The lines present the fits obtained from equation 3.10. B) Comparison of the flowcurves measured experimentally with increasing and decreasing shear rates (full and dashed lines) with the stresses measured for different waiting times from the step flow experiments: 50 ms (down triangles), 100 ms (checked boxes), 1 s (up triangles), 10 s (hollow squares), 100 s (hollow circles) and stationary regime (full circles). C) Strain sweep at different frequencies. D) Shear stress measured as function of the strain from the step flow experiments at different shear rates (hollow symbols) and frequencies (full symbols). The same symbols are used for the same values of the frequency and shear rates. The dashed lines present the fits from equation 3.10.*

to the relaxation and flow of the system. The simplest representation of such a system is the model of Maxwell. In the rest of the experiments the theory was applied to the frequency dependent measurement of G' and G'' in the linear regime. For this reason the moduli have been measured as function of the strain for different frequencies in order to ensure that the deformations used in the frequency dependent experiment belong for all the frequencies to the linear regime. An example is given by the figure 3.8 C). A dense solution with an effective volume $\phi_{eff} = 0.622$ is subject deformationsweep experiment is presented for a dense 13.01 $wt\%$ solution at 14^oC for different frequency. The moduli are constant until a strain around 4 %. This solution represents the highest effective volume fraction investigated in this work, for this reason a strain of 1 % fulfil the condition of linearity in all the frequency sweep experiments presented in this chapter.

The flow curves have been measured in the stationary regime. This means practically that the solution is sheared at a constant shear rate $\dot{\gamma}$ long enough, to ensure a laminar flow resulting in a constant stress that we will define as $\sigma(\dot{\gamma})$, which is the prerequisite of the theory. The stationarity has been checked by step flow experiments also for the highest effective volume fraction (13.01 $wt\%$ solution at 14^oC, $\phi_{eff} = 0.622$). Figure 3.8 A) presents the experiments performed for different shear rates, with different time increments (50, 100, 200 ms). No significant variations could be observed between the different times. For the lowest shear rates ($\dot{\gamma} = 10^{-4} - 10^{-1}\ s^{-1}$). The stress $\sigma(\dot{\gamma}, t)$ first decreases in the very small time, and then increases again to reach the constant value $\sigma(\dot{\gamma})$. The experimental values of $\sigma(\dot{\gamma})$ (solid circles) have been reported in the figure 3.8 B) and compared to the flow curves measured with increasing and decreasing shear rates (full and dashed curves) in the experimental conditions described above and with the measurement for different time. No significant difference can be observed which proves that the flow curves are measured in the stationary regime. On the contrary a marked discrepancy can be observed if the time of measurement is not long enough. This result can be directly compared to the work of Heymann et al. [219, 220] where the authors investigated the influence of the measurement time on the flow curves of concentrated suspensions of spherical particles.

Step flow and strain sweep experiments are very close in the sense that they describe the evolution of the system as function of the time and strain and have been the object of recent studies [208, 221, 222]. If we consider the step flow experiments of the figure 3.8 A) the origin of the first decay in the short time is not fully understood and must be related to short time relaxation process. Nevertheless the experimental points in the short times for the low shear rates superpose into a master curve, which can be described as a power law with an exponent -0.4. Then the stress increases again quasi linearly for the slowest shear rate to finally relax and reach a constant value. The two experiments can be compared, if we consider the evolution of the stress as a function of the strain. For this the moduli of the strain sweep are first transformed into complex modulus $G^* = ((G')^2 + (G'')^2)^{0.5}$ and then converted in stress $\sigma^* = G^*/\gamma$. Concerning the step flow experiments the strain is obtained by multiplying the time t with the shear rate $\dot{\gamma}$. To this high volume fraction the system is in the glassy state and the complex modulus is almost constant between 10^{-2} and 10 Hz and the value at the plateau G_p^* is approximately equal to 23 Pa. The comparison is presented in the figure 3.8 D). σ^* is increasing linearly with the strain for the small strain and relax for the higher strain. This kind of rescaling underlines the correspondence of the two experiments in the linear regime. For the non linear regime a direct comparison is obtained if the stress is measured for both experiments are done at the same strain and shear rate. For this purpose we have to define the strain-rate defined as $\dot{\gamma}_0 = \gamma\omega$. The comparison is done on the figure 3.9, where both experiments superpose each other to describe the second relaxation of the stress.

A simple approach close to the one proposed by Wyss et al. [208] was used to account of the linear viscoelasticity defined by the complex modulus $G^*(\dot{\gamma}_0 = \dot{\gamma})$ (in the linear regime) at the lower strains and of the stationarity and flow at higher strains defined by the constant stress $\sigma(\dot{\gamma})$.

The model consists on a simple Maxwell element, defined with its general equation of movement:

$$\frac{d\gamma}{dt} = \frac{1}{G}\frac{d\sigma}{dt} + \frac{\sigma}{\eta} \tag{3.9}$$

We consider now a steady shear ($d\gamma/dt = \dot{\gamma}$), $G = G^*(\dot{\gamma}_0 = \dot{\gamma})$ the linear viscoelastic contribution, $\eta = \sigma(\dot{\gamma})/\dot{\gamma}$ with $\sigma(\dot{\gamma})$ the stress in the stationary regime. Considering that at $t = 0$, $\sigma(t) = 0$, the resolution of this equation gives the following expression for the stress:

$$\sigma(\dot{\gamma}, t) = \sigma(\dot{\gamma})\left(1 - exp(-G^*(\dot{\gamma}_0 = \dot{\gamma})\dot{\gamma}t/\sigma(\dot{\gamma}))\right) \tag{3.10}$$

This expression have been used for the step flow and strain sweep experiments considering $G^*(\dot{\gamma}_0 = \dot{\gamma}) = G_p^* = 23\ Pa$ (see fig. 3.8 A) and D) and fig. 3.9). This simple approach describes very well the second relaxation observed experimentally in the glassy regime for both experiments. Of course this kind of experiment is much more complicated and the correlation between the time, frequency, strain and shear rate has to be addressed more in depth. Nevertheless it shows clearly the connection between linear and non linear rheology which will be presented in the rest of the chapter.

3.2.4 Theory

Microscopic approach

The next sections provide a full description of the theory developed as mentioned in the introduction by the professor Matthias Fuchs and his coworkers. We consider N spherical particles with radius R_H dispersed in a volume V of solvent (viscosity η_s) with imposed homogeneous, and constant linear shear-flow. The flow velocity points along the x-axis and its gradient along the y-axis. The motion of the particles (with positions $\mathbf{r}_i(t)$ for $i = 1, \ldots, N$) is described by N coupled Langevin equations [206]

$$\zeta\left(\frac{d\mathbf{r}_i}{dt} - \mathbf{v}^{\mathrm{solv}}(\mathbf{r}_i)\right) = \mathbf{F}_i + \mathbf{f}_i\ . \tag{3.11}$$

Solvent friction is measured by the Stokes friction coefficient $\zeta = 6\pi\eta_s R_H$. The N vectors $\mathbf{F}_i = -\partial/\partial\mathbf{r}_i\, U(\{\mathbf{r}_j\})$ denote the interparticle force on particle i deriving from potential

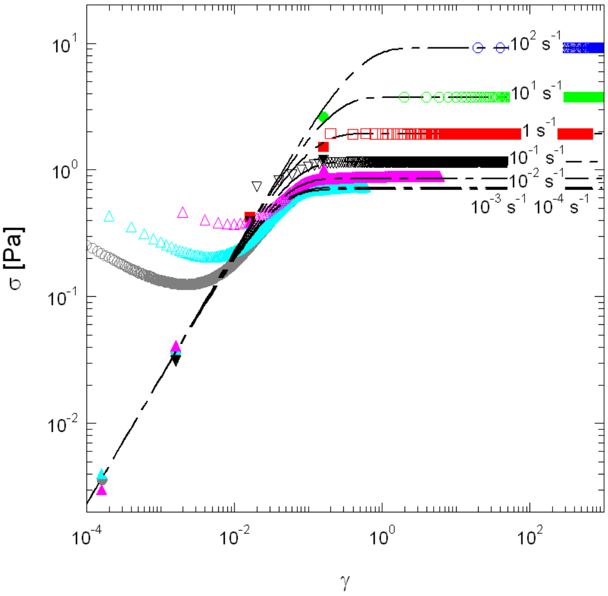

Figure 3.9: *Shear stress measured as function of the strain from the strain sweep (full symbols) and step flow experiments (hollow symbols). The same symbols are used for the same values of shear rates* $\dot\gamma$ *and strain rates* $\dot\gamma_0 = \omega\gamma$.

interactions with all other particles; U is the potential energy which depends on all particles' positions. The solvent shear-flow is given by $\mathbf{v}^{\text{solv}}(\mathbf{r}) = \dot\gamma\, y\, \hat{\mathbf{x}}$, and the Gaussian white noise force satisfies (with α, β denoting directions)

$$\langle f_i^\alpha(t)\; f_j^\beta(t')\rangle = 2\zeta\, k_BT\, \delta_{\alpha\beta}\, \delta_{ij}\, \delta(t-t')\ ,$$

where k_BT is the thermal energy. Each particle experiences interparticle forces, solvent friction, and random kicks. Interaction and friction forces on each particle balance on average, so that the particles are at rest in the solvent on average. The Stokesian friction is proportional to the particle's motion *relative to* the solvent flow at its position; the latter varies linearly with y. The random force on the level of each particle satisfies the fluctuation dissipation relation.

An important approximation in Eq. (3.11) is the neglect of hydrodynamic interactions, which would arise from the proper treatment of the solvent flow around moving particles [33, 206]. In the following we will argue that such effects can be neglected at high densities where interparticle forces hinder and/or prevent structural rearrangements, and where the system is close to arrest into an amorphous, metastable solid. Another important approximation in Eq. (3.11) is the assumption of a given, constant shear rate $\dot\gamma$, which does not vary throughout the (infinite) system. We start with this assumption in the philosophy that, first, homogeneous states should be considered, before heterogeneities and confinement effects are taken into account. All difficulties in Eq. (3.11) thus are connected to the many-body interactions given by the forces $\mathbf{F}_i$, which couple the N Langevin equations. In the absence of interactions, $\mathbf{F}_i \equiv 0$, Eq. (3.11) leads to superdiffusive particle motion termed 'Taylor dispersion' [206].

While formulation of the considered microscopic model handily uses Langevin equations, theoretical analysis proceeds more easily from the reformulation of Eq. (3.11) as

Smoluchowski equation. It describes the temporal evolution of the distribution function $\Psi(\{\mathbf{r}_i\}, t)$ of the particle positions

$$\partial_t \Psi(\{\mathbf{r}_i\}, t) = \Omega \; \Psi(\{\mathbf{r}_i\}, t) \;, \tag{3.12}$$

employing the Smoluchowski operator [33, 206],

$$\Omega = \sum_{j=1}^{N} \left[D_0 \, \frac{\partial}{\partial \mathbf{r}_j} \cdot \left(\frac{\partial}{\partial \mathbf{r}_j} - \frac{1}{k_B T} \mathbf{F}_j \right) - \dot{\gamma} \, \frac{\partial}{\partial x_j} \, y_j \right] \;, \tag{3.13}$$

built with the (bare) diffusion coefficient $D_0 = k_B T/\zeta$ of a single particle. We assume that the system relaxes into a unique stationary state at long times, so that $\Psi(t \to \infty) = \Psi_s$ holds. Homogeneous, amorphous systems are studied so that the stationary distribution function Ψ_s is translationally invariant but anisotropic. Neglecting ageing, the formal solution of the Smoluchowski equation within the ITT approach can be brought into the form [41, 44]

$$\Psi_s = \Psi_e + \frac{\dot{\gamma}}{k_B T} \int_0^\infty dt \; \Psi_e \; \sigma_{xy} \; e^{\Omega^\dagger t} \;, \tag{3.14}$$

where the adjoint Smoluchowski $\Omega^\dagger$ operator arises from partial integrations. It acts on the quantities to be averaged with Ψ_s. Ψ_e denotes the equilibrum canonical distribution function, $\Psi_e \propto e^{-U/(k_B T)}$, which is the time-independent solution of Eq. (3.12) for $\dot{\gamma} = 0$; in Eq. (3.14), it gives the initial distribution at the start of shearing (at $t = 0$). The potential part of the stress tensor $\sigma_{xy} = -\sum_{i=1}^{N} F_i^x \, y_i$ entered via $\Omega \Psi_e = \dot{\gamma} \, \sigma_{xy} \, \Psi_e$. The simple, exact result Eq. (3.14) is central to the ITT approach as it connects steady state properties to time integrals formed with the shear-dependent dynamics. The latter contains slow intrinsic particle motion.

In ITT, the evolution towards the stationary distribution at infinite times is approximated by following the slow structural rearrangements, encoded in the transient density correlator $\Phi_{\mathbf{q}}(t)$. It is defined by [41, 44]

$$\Phi_{\mathbf{q}}(t) = \frac{1}{N S_q} \, \langle \, \delta\varrho_{\mathbf{q}}^* \, e^{\Omega^\dagger t} \, \delta\varrho_{\mathbf{q}(t)} \, \rangle^{(\dot{\gamma}=0)} \;. \tag{3.15}$$

It describes the fate of an equilibrium density fluctuation with wavevector $\mathbf{q}$, where $\varrho_{\mathbf{q}} = \sum_{j=1}^{N} e^{i\mathbf{q}\cdot\mathbf{r}_j}$, under the combined effect of internal forces, Brownian motion and shearing. Note that because of the appearance of Ψ_e in Eq. (3.14), the average in Eq. (3.15) can be evaluated with the equilibrium canonical distribution function, while the dynamical evolution contains Brownian motion and shear advection. The normalization is given by S_q the equilibrium structure factor [33, 206] for wavevector modulus $q = |\mathbf{q}|$. The *advected* wavevector enters in Eq. (3.15)

$$\mathbf{q}(t) = \mathbf{q} - \dot{\gamma} t \; q_x \; \hat{\mathbf{y}} \;, \tag{3.16}$$

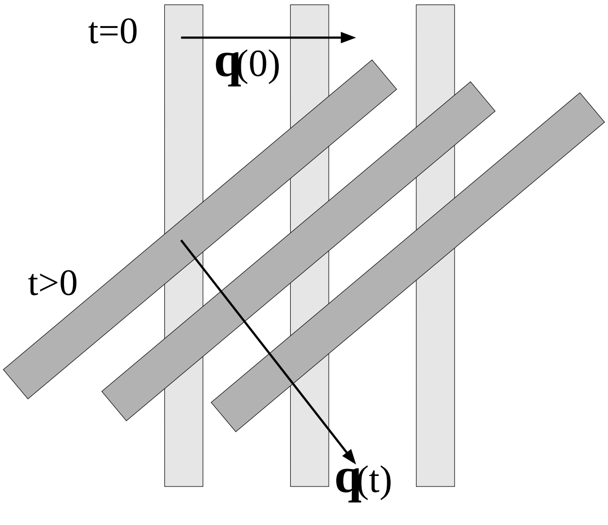

Figure 3.10: *Shear advection of a fluctuation with initial wavevector in x-direction, $\mathbf{q}(t{=}0) = q\,(1,0,0)^T$, and advected wavevector at later time $\mathbf{q}(t{>}0) = q\,(1,-\dot\gamma t,0)^T$. At all times, $\mathbf{q}(t)$ is perpendicular to the planes of constant fluctuation amplitude. Note that the magnitude $q(t) = q\sqrt{1+(\dot\gamma t)^2}$ increases with time. Brownian motion, neglected in this sketch, would smear out the fluctuation.*

where unit-vector $\hat{\mathbf{y}}$ points in y-direction) The time-dependence in $\mathbf{q}(t)$ results from the affine particle motion with the shear flow of the solvent. Translational invariance under shear dictates that at a time t later, the equilibrium density fluctuation $\delta\varrho^*_{\mathbf{q}}$ has a nonvanishing overlap only with the advected fluctuation $\delta\varrho_{\mathbf{q}(t)}$ (see fig. 3.10), where a non-decorrelating fluctuation is sketched under shear. In the case of vanishing Brownian motion, viz. $D_0 = 0$ in Eq. (3.13), we find $\Phi_{\mathbf{q}}(t) \equiv 1$, because the advected wavevector takes account of simple affine particle motion [223]. The relaxation of $\Phi_{\mathbf{q}}(t)$ thus heralds decay of structural correlations. Within ITT, the time integral over such structural decorrelations provides an approximation to the stationary state:

$$\Psi_s \;\approx\; \Psi_e + \frac{\dot\gamma}{2k_BT}\int_0^\infty dt \sum_{\mathbf{k}} \frac{k_xk_y\,S'_k}{k\,NS^2_{\mathbf{k}(t)}}\,\Phi^2_{\mathbf{k}}(t)\,\left(\Psi_e\,\varrho^*_{\mathbf{k}(t)}\,\varrho_{\mathbf{k}(t)}\right)\,, \tag{3.17}$$

with $S'_k = \partial S_k/\partial k$ [224]. The last term in brackets in Eq. (3.17) expresses, that the expectation value of a general fluctuation A in ITT-approximation contains the (equilibrium) overlap with the local structure, $\langle \varrho^*_{\mathbf{k}}\,\varrho_{\mathbf{k}}\,A\rangle^{(\dot\gamma=0)}$. The difference between the equilibrium and stationary distribution functions then follows from integrating over time the spatially resolved (viz. wavevector dependent) density variations.

The general results for Ψ_s, the exact one of Eq. (3.14) and the approximation Eq. (3.17), can be applied to compute stationary expectation values like for example the thermodynamic transverse stress, $\sigma(\dot\gamma) = \langle\sigma_{xy}\rangle/V$. Equation (3.14) leads to an exact non-linear Green-Kubo relation:

$$\sigma(\dot\gamma) = \dot\gamma\int_0^\infty dt\; g(t,\dot\gamma)\;, \tag{3.18}$$

where the generalized shear modulus $g(t,\dot\gamma)$ depends on shear rate via the Smoluchowski operator from Eq. (3.13)

$$g(t,\dot\gamma) = \frac{1}{k_BTV}\,\langle\,\sigma_{xy}\,e^{\Omega^\dagger t}\,\sigma_{xy}\,\rangle^{(\dot\gamma=0)}\;. \tag{3.19}$$

In ITT, the slow stress fluctuations in $g(t,\dot\gamma)$ are approximated by following the slow structural rearrangements, encoded in the transient density correlators. The generalized modulus becomes, using the approximation Eq. (3.17), or, equivalently, performing a mode coupling approximation [44, 45, 216]:

$$g(t,\dot\gamma) = \frac{k_BT}{2}\int\frac{d^3k}{(2\pi)^3}\,\frac{k_x^2k_yk_y(t)}{k\,k(t)}\,\frac{S'_kS'_{k(t)}}{S^2_{k(t)}}\,\Phi^2_{\mathbf{k}}(t)\;, \tag{3.20}$$

Summation over wavevectors has been turned into integration in Eq. (3.20) considering an infinite system.

The familiar shear modulus of linear response theory describes thermodynamic stress fluctuations in equilibrium, and is obtained from Eqs. (3.19,3.20) by setting $\dot\gamma = 0$ [33, 158, 225]. While Eq. (3.19) then gives the exact Green-Kubo relation, the approximation Eq. (3.20) turns into the well-studied MCT formula. For finite shear rates, Eq. (3.20) describes how affine particle motion causes stress fluctuations to explore shorter and shorter length scales. There the effective forces, as measured by the gradient of the direct correlation function, $S'_k/S^2_k = nc'_k = n\partial c_k/\partial k$, become smaller, and vanish asymptotically, $c'_{k\to\infty}\to 0$; the direct correlation function c_k is connected to the structure factor via the Ornstein-Zernicke equation $S_k = 1/(1-n\,c_k)$, where $n = N/V$ is the particle density. Note, that the equilibrium structure suffices to quantify the effective interactions, while shear just pushes the fluctuations around on the 'equilibrium energy landscape'.

Structural rearrangements of the dispersion affected by Brownian motion is encoded in the transient density correlator. Shear induced affine motion, viz. the case $D_0 = 0$, is not sufficient to cause $\Phi_{\mathbf{k}}(t)$ to decay. Brownian motion of the quiescent correlator $\Phi^{(\dot\gamma=0)}_k(t)$ leads at high densities to a slow structural process which arrests at long times in (metastable) glass states. Thus the combination of structural relaxation and shear is interesting. The interplay between intrinsic structural motion and shearing in $\Phi_{\mathbf{k}}(t)$ is captured by (*i*) first a formally exact Zwanzig-Mori type equation of motion, and (*ii*) second a mode coupling factorisation in the memory function built with longitudinal stress fluctuations [41, 44]. The equation of motion for the transient density correlators is

$$\partial_t\Phi_{\mathbf{q}}(t) + \Gamma_{\mathbf{q}}(t)\,\left\{\Phi_{\mathbf{q}}(t) + \int\limits_0^t dt'\;m_{\mathbf{q}}(t,t')\;\partial_{t'}\,\Phi_{\mathbf{q}}(t')\right\} = 0\;, \tag{3.21}$$

where the initial decay rate $\Gamma_{\mathbf{q}}(t) = D_0\,q^2(t)/S_{q(t)}$ generalizes the familiar result from linear response theory to advected wavevectors; it contains Taylor dispersion. The memory equation contains fluctuating stresses and similarly like $g(t,\dot\gamma)$ in Eq. (3.17), is calculated in mode coupling approximation

$$m_{\mathbf{q}}(t,t') = \frac{1}{2N}\sum_{\mathbf{k}} V_{\mathbf{qkp}}(t,t')\;\Phi_{\mathbf{k}(t')}(t-t')\;\Phi_{\mathbf{p}(t')}(t-t')\;, \tag{3.22}$$

where we abbreviated $\mathbf{p} = \mathbf{q} - \mathbf{k}$. The vertex generalizes the expression in the quiescent case [44]:

$$
\begin{aligned}
V_{\mathbf{qkp}}(t,t') &= \frac{S_{\mathbf{q}(t)}\, S_{\mathbf{k}(t')}\, S_{\mathbf{p}(t')}}{q^2(t)\, q^2(t')}\, \mathcal{V}_{\mathbf{qkp}}(t)\, \mathcal{V}_{\mathbf{qkp}}(t')\,, \\
\mathcal{V}_{\mathbf{qkp}}(t) &= \mathbf{q}(t) \cdot \big(\mathbf{k}(t)\, nc_{k(t)} + \mathbf{p}(t)\, nc_{p(t)} \big)\ . \qquad (3.23)
\end{aligned}
$$

With shear, wavevectors in Eq. (3.23) are advected according to Eq. (3.16).

Equations (3.17,3.21,3.22), with the specific example of the generalized shear modulus Eq. (3.20), form a closed set of equations determining rheological properties of a sheared dispersion from equilibrium structural input [41, 44]. Only the static structure factor S_q is required to predict (i) the time dependent shear modulus within linear response, $g^{\mathrm{lr}}(t) = g(t, \dot\gamma = 0)$, and (ii) the stationary stress $\sigma(\dot\gamma)$ from Eq. (3.18). The loss and storage moduli of small amplitude oscillatory shear measurements [33, 158] follow from Eq. (3.19) in the linear response case (i)

$$
G'(\omega) + i\, G''(\omega) = i\omega \int_0^\infty dt\, e^{-i\omega t}\, g(t, \dot\gamma = 0)\ . \qquad (3.24)
$$

While, in the linear response regime, modulus and density correlator are measurable quantities, outside the linear regime, both quantities serve as tools in the ITT approach only. The transient correlator and shear modulus provide a route to the stationary averages, because they describe the decay of equilibrium fluctuations under external shear, and their time integral provides an approximation for the stationary distribution function, see Eq. (3.17). Determination of the frequency dependent moduli under large amplitude oscillatory shear has become possible recently only [226], and requires an extension of the present approach to time dependent shear rates in Eq. (3.13) [221].

Universal aspects

The summarized microscopic ITT equations contain a bifurcation in the long-time behavior of $\Phi_{\mathbf{q}}(t)$, which corresponds to a non-equilibrium transition between a fluid and a shear-molten glassy state. Close to the transition, (rather) universal predictions can be made about the non-linear dispersion rheology and the steady state properties. The central predictions are introduced in this section and summarized in the overview given by fig. 3.11. It is obtained from the schematic model which is also used to analyse the data, and which is introduced in section 3.2.4.

A dimensionless separation parameter ε measures the distance to the transition which is situated at $\varepsilon = 0$. A fluid state ($\varepsilon < 0$) possesses a (Newtonian) viscosity, $\eta_0(\varepsilon < 0) = \lim_{\dot\gamma \to 0} \sigma(\dot\gamma)/\dot\gamma$, and shows shear-thinning upon increasing $\dot\gamma$. Via the relation $\eta_0 = \lim_{\omega \to 0} G''(\omega)/\omega$, the Newtonian viscosity can also be taken from the loss modulus at low frequencies, where $G''(\omega)$ dominates over the storage modulus. The latter varies like $G'(\omega \to 0) \sim \omega^2$. A glass ($\varepsilon \geq 0$), in the absence of flow, possesses an elastic constant G_∞, which can be measured in the elastic shear modulus $G'(\omega)$ in the limit of low frequencies,

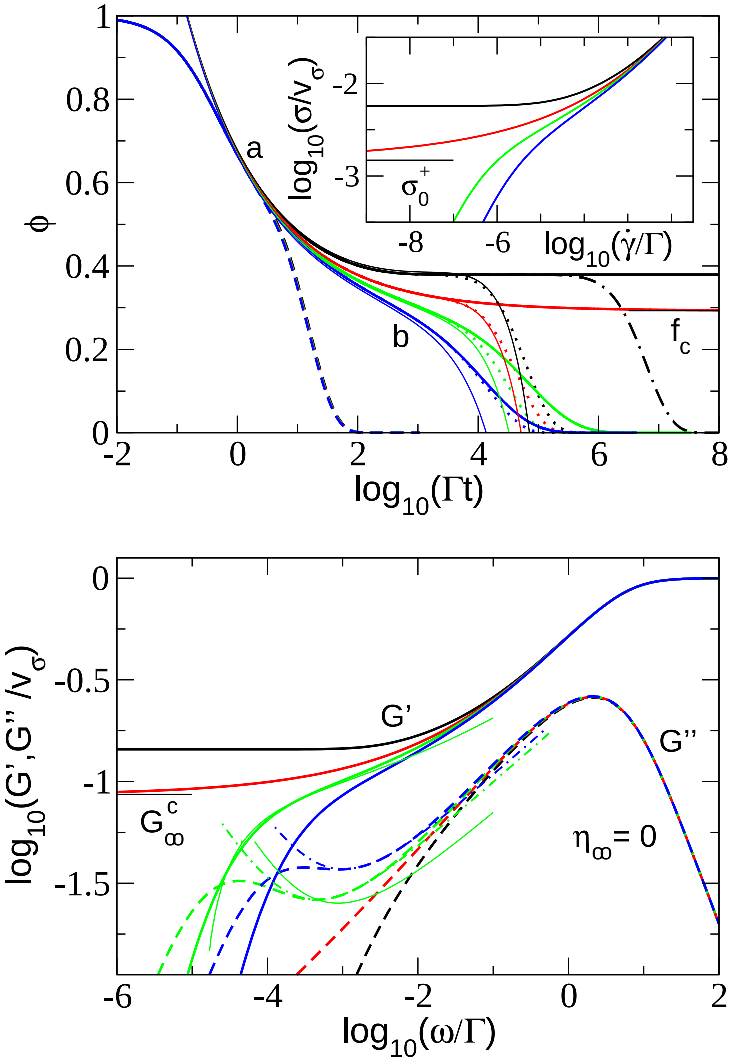

Figure 3.11: *Overview of the properties of the* $F_{12}^{(\dot\gamma)}$*-model characteristic for the transition between fluid and yielding glass. The upper panel shows numerically obtained transient correlators* $\Phi(t)$ *for* $\varepsilon = 0.01$ *(black curves),* $\varepsilon = 0$ *(red),* $\varepsilon = -0.005$ *(green), and* $\varepsilon = -0.01$ *(blue). The shear rates are* $|\dot\gamma/\Gamma| = 0$ *(thick solid lines),* $|\dot\gamma/\Gamma| = 10^{-6}$ *(dotted lines), and* $|\dot\gamma/\Gamma| = 10^{-2}$ *(dashed lines). For the glass state at* $\varepsilon = 0.01$ *(black),* $|\dot\gamma/\Gamma| = 10^{-8}$ *(dashed-dotted-line) is also included. All curves were calculated with* $\gamma_c = 0.1$ *and* $\eta_\infty = 0$*. The thin solid lines give the factorization result Eq. (3.25) with scaling functions* $\mathcal{G}$ *for* $|\dot\gamma/\Gamma| = 10^{-6}$*; label a marks the critical law (3.27), and label b marks the von Schweidler-law (3.28). The critical glass form factor* f_c *is indicated. The inset shows the flow curves for the same values for* ε*. The thin black bar shows the yield stress* σ_c^+ *for* $\varepsilon = 0$*. The lower panel shows the viscoelastic storage (solid line) and loss (broken line) moduli for the same values of* ε*. The thin green lines are the Fourier-transformed factorization result Eq. (3.25) with scaling function* $\mathcal{G}$ *taken from the upper panel for* $\varepsilon = -0.005$*. The dashed-dotted lines show the fit formula Eq. (3.39) for the spectrum in the minimum-region with* $G_{\min}/v_\sigma = 0.0262$*,* $\omega_{\min}/\Gamma = 0.000457$ *at* $\varepsilon = -0.005$ *(green) and* $G_{\min}/v_\sigma = 0.0370$*,* $\omega_{\min}/\Gamma = 0.00105$ *at* $\varepsilon = -0.01$ *(blue). The elastic constant at the transition* G_∞^c *is marked also.*

$G'(\omega \to 0, \varepsilon \geq 0) \to G_\infty(\varepsilon)$. Here the storage modulus dominates over the loss one, which drops like $G''(\omega \to 0) \sim \omega$. Enforcing steady shear flow melts the glass. The stationary stress of the shear-molten glass always exceeds a (dynamic) yield stress. For decreasing shear rate, the viscosity increases like $1/\dot\gamma$, and the stress levels off onto the yield-stress plateau, $\sigma(\dot\gamma \to 0, \varepsilon \geq 0) \to \sigma^+(\varepsilon)$.

Close to the transition, the zero-shear viscosity η_0, the elastic constant G_∞, and the yield stress σ^+ show universal anomalies as functions of the distance to the transition: the viscosity diverges in a power-law $\eta_0(\varepsilon \to 0-) \sim (-\varepsilon)^{-\gamma}$ with material dependent exponent γ around $2-3$, the elastic constant increases like a square-root $G_\infty(\varepsilon \to 0+) - G^c_\infty \sim \sqrt{\varepsilon}$, and the dynamic yield stress $\sigma^+(\varepsilon \to 0+)$ also increases with infinite slope above its value σ^+_c at the bifurcation. The quantities G^c_∞ and σ^+_c denote the respective values at the transition point $\varepsilon = 0$, and measure the jump in the elastic constant and in the yield stress at the glass transition; in the fluid state, $G_\infty(\varepsilon < 0) = 0$ and $\sigma^+(\varepsilon < 0) = 0$ hold.

The described results follow from the stability analysis of Eqs. (3.21,3.22) around an arrested, glassy structure f_q of the transient correlator [44, 45]. Considering the time window where $\Phi_{\mathbf{q}}(t)$ is metastable and close to arrest at f_q, and taking all control parameters like density, temperature, etc. to be close to the values at the transition, the stability analysis yields the 'factorization' between spatial and temporal dependencies

$$\Phi_{\mathbf{q}}(t) = f^c_q + h_q\, \mathcal{G}(\, t/t_0, \varepsilon, \dot\gamma t_0\,) + \dots\ , \tag{3.25}$$

where the (isotropic) glass form factor f^c_q and critical amplitude h_q describe the spatial properties of the metastable glassy state. The critical glass form factor f^c_q gives the long-lived component of density fluctuations, and h_q captures local particle rearrangements. Both can be taken as constants independent on shear rate and density, as they are evaluated from the vertices in Eq. (3.23) at the transition point. All time-dependence and (sensitive) dependence on the external control parameters is contained in the function $\mathcal{G}$, which often is called 'β-correlator' and obeys the non-linear stability equation

$$\varepsilon - c^{(\dot\gamma)}\, (\dot\gamma t)^2 + \lambda\, \mathcal{G}^2(t) = \frac{d}{dt} \int_0^t dt'\, \mathcal{G}(t-t')\, \mathcal{G}(t')\ , \tag{3.26}$$

with initial condition

$$\mathcal{G}(t \to 0) \to (t/t_0)^{-a}\ . \tag{3.27}$$

The two parameters λ and $c^{(\dot\gamma)}$ in Eq. (3.26) are determined by the static structure factor at the transition point, and take values around $\lambda \approx 0.73$ and $c^{(\dot\gamma)} \approx 3$ for S_q taken from Percus-Yevick approximation [33] for hard sphere interactions [44, 45, 227]. The transition point then lies at packing fraction $\phi_c \approx 0.52$ (index c for critical), and the separation parameter measures the relative distance, $\varepsilon = C\,(\phi - \phi_c)/\phi_c$ with $C \approx 1.3$. The 'critical' exponent a is given by the exponent parameter λ via $\lambda = \Gamma(1-a)^2/\Gamma(1-2a)$ [162, 164].

The time scale t_0 in Eq. (3.27) provides the means to match the function $\mathcal{G}(t)$ to the microscopic, short-time dynamics. The Eqs. (3.21,3.22) contain a simplified description of the short time dynamics in colloidal dispersions via the initial decay rate $\Gamma_{\mathbf{q}}(t)$. From this model for the short-time dynamics, the time scale $t_0 \approx 1.6\, 10^{-2} R_H^2/D_0$ is obtained. Solvent mediated effects on the short time dynamics are well known and are neglected in $\Gamma_{\mathbf{q}}(t)$ in Eq. (3.21). If hydrodynamic interactions were included in Eq. (3.21), all of the mentioned universal predictions of the ITT approach would remain true. Only the value of t_0 will be shifted and depend on the short time hydrodynamic interactions. This statement remains valid, as long as the hydrodynamic interactions do not affect the mode coupling vertex in Eq. (3.23). In this sense, hydrodynamic interactions can be incorporated into the theory of the glass transition, and amount to a rescaling of the matching time t_0, only.

Obviously, the matching time t_0 also provides an upper cut-off for the time window of the structural relaxation. At times shorter than t_0 the specific short-time dynamics matters. The condition $\dot{\gamma} t_0 \ll 1$ follows and translates into a restriction for the accessible range of shear rates, $\dot{\gamma} \ll \dot{\gamma}_*$, where the upper-cut off shear rate $\dot{\gamma}_*$ is connected to the matching time.

The parameters ε, λ and $c^{(\dot{\gamma})}$ in Eq. (3.26) can be determined from the equilibrium structure factor S_q at or close to the transition, and, together with t_0 and the shear rate $\dot{\gamma}$ they capture the essence of the rheological anomalies in dense dispersions. A divergent viscosity follows from the prediction of a strongly increasing final relaxation time in $\mathcal{G}$ in the quiescent fluid phase

$$\mathcal{G}(t \to \infty, \varepsilon < 0, \dot{\gamma} = 0) \to -(t/\tau)^b \quad , \text{ with } \frac{t_0}{\tau} \propto (-\varepsilon)^{\gamma} \, . \tag{3.28}$$

The entailed temporal power law, termed von Schweidler law, initiates the final decay of the correlators, which has a density and temperature independent shape $\tilde{\Phi}_q(\tilde{t})$. The final decay, often termed α-relaxation, depends on ε only via the time scale $\tau(\varepsilon)$ which rescales the time, $\tilde{t} = t/\tau$. Equation (3.26) establishes the crucial time scale separation between t_0 and τ, the divergence of τ, and the stretching (non-exponentiality) of the final decay; it also gives the values of the exponents via $\lambda = \Gamma(1+b)^2/\Gamma(1+2b)$, and $\gamma = (1/a + 1/b)/2$. Using Eq. (3.20), the divergence of the Newtonian viscosity follows [162, 164]. During the final decay the shear modulus becomes a function of rescaled time, $\tilde{g}(\tilde{t} = t/\tau, \dot{\gamma} = 0)$, leading to $\eta_0 \propto \tau(\varepsilon)$; its initial value is given by the elastic constant at the transition, $\tilde{g}(\tilde{t} \ll 1, \varepsilon \to 0-, \dot{\gamma} = 0) = G_\infty^c$.

On the glassy side of the transition, $\varepsilon \geq 0$, the transient density fluctuations stays close to a plateau value for intermediate times which increases when going deeper into the glass,

$$\mathcal{G}(t_0 \ll t \ll 1/|\dot{\gamma}|, \varepsilon \geq 0) \to \sqrt{\frac{\varepsilon}{1-\lambda}} + \mathcal{O}(\varepsilon) \, . \tag{3.29}$$

Entered into Eq. (3.20), the square-root dependence of the plateau value translates into the square-root anomaly of the elastic constant G_∞, and causes the increase of the yield stress close to the glass transition.

Only, for vanishing shear rate, $\dot{\gamma} = 0$, an ideal glass state exists in the ITT approach for steady shearing. All density correlators arrest at a long time limit, which from Eq. (3.29) close to the transition is given by $\Phi_{\mathbf{q}}(t \to \infty, \varepsilon \geq 0, \dot{\gamma} = 0) = f_q = f_q^c + h_q \sqrt{\varepsilon/(1-\lambda)} + \mathcal{O}(\varepsilon)$. Consequently the modulus remains elastic at long times, $g(t \to \infty, \varepsilon \geq 0, \dot{\gamma} = 0) = G_\infty > 0$. Any (infinitesimal) shear rate, however, melts the glass and causes a final decay of the transient correlators. The function $\mathcal{G}$ initiates the decay around the critical plateau of the transient correlators and sets the common time scale for the final decay under shear

$$\mathcal{G}(t \to \infty, \varepsilon \geq 0) \to -\sqrt{\frac{c^{(\dot\gamma)}}{\lambda - \frac{1}{2}}}\, |\dot\gamma t| \ . \tag{3.30}$$

Under shear all correlators decay from the plateau as function of $|\dot\gamma t|$. Steady shearing thus prevents non-ergodic arrest and restores ergodicity. This aspect of Eq. (3.26) has two important ramifications for the steady state of shear molten glasses [44, 45]. First, ITT finds that shear melts a glass and produces a unique steady state at long times. This conclusion is restricted by the assumption of homogeneous states and excludes the possible existence of ordering or layering under shear. Also, ageing was neglected, which could remain because of non-ergodicity in the initial quiescent state. Ergodicity of the sheared state however suggests ageing to be unimportant under shear [212, 213]. Second, all stationary averages, which in ITT are obtained from integrating up the transient fluctuations, do not exhibit a linear response regime in the glass. Rather they take finite values for vanishing shear rate, which jump discontinuously at the glass transition. This holds because the shear-driven decay of Eq. (3.30) initiates a scaling law where the transient correlators decay as function of $|\dot\gamma t|$ down from the plateau f_q to zero, denoted as $\Phi^+_{\mathbf{q}}(t|\dot\gamma|)$. When entered into Eq. (3.17), time appears only in the combination together with shear rate and thus after time integration the shear rate dependence drops out, yielding a finite result even in the limit of infinitesimal shear rate. Prominent example of a stationary average that has no linear response regime with respect to $\dot\gamma$ in the glass phase is the shear stress $\sigma(\dot\gamma, \varepsilon \geq 0)$. It takes finite values for vanishing shear rate, $\sigma^+(\varepsilon) = \sigma(\dot\gamma \to 0, \varepsilon \geq 0)$, and jumps at the glass transition from zero to a finite value. Because of Eq. (3.29) it increases rapidly when moving deeper into the glass.

Schematic model

The universal aspects described in the previous section are contained in any ITT model that contains the central bifurcation scenario and recovers Eqs. (3.25,3.26). Equation (3.25) states that spatial and temporal dependences decouple in the intermediate time window. Thus it is possible to investigate ITT models without proper spatial resolution. Because of the technical difficulty to evaluate the anisotropic functionals in Eqs. (3.20,3.22), it is useful to restrict the description to few or to a single transient correlator. In the schematic $F_{12}^{(\dot\gamma)}$-model [45], a single 'typical' density correlator $\Phi(t)$, conveniently normalized according to $\Phi(t \to 0) = 1 - \Gamma t$, obeys a Zwanzig-Mori memory equation which is modeled according to Eq. (3.21)

$$\partial_t \Phi(t) + \Gamma \left\{ \Phi(t) + \int_0^t dt'\, m(t-t')\, \partial_{t'} \Phi(t') \right\} = 0 \ . \tag{3.31}$$

The parameter Γ mimics the microscopic dynamics of the 'typical' density correlator chosen in Eq. (3.31), and will depend on structural and hydrodynamic correlations. The memory function describes stress fluctuations which become more sluggish together with density fluctuations, because slow structural rearrangements dominate all quantities. A self consistent approximation closing the equations of motion is made mimicking Eq.

(3.22). In the $F_{12}^{(\dot\gamma)}$-model one includes a linear term (absent in Eq. (3.22)) in order to (*i*) sweep out the full range of λ values in Eq. (3.26), and (*ii*) retain algebraic simplicity:

$$m(t) = \frac{v_1\,\Phi(t) + v_2\,\Phi^2(t)}{1 + (\dot\gamma t/\gamma_c)^2} \tag{3.32}$$

This model, for the quiescent case $\dot\gamma = 0$, had been suggested by Götze in 1984 [162, 228], and describes the development of slow structural relaxation upon increasing the coupling vertices $v_i \geq 0$; they mimic the dependence of the vertices in Eq. (3.22) at $\dot\gamma = 0$ on the equilibrium structure given by S_q. Under shear an explicit time dependence of the couplings in $m(t)$ captures the accelerated loss of memory by shear advection (see eq. Eq. (3.22)). Shearing causes the dynamics to decay for long times, fluctuations are advected to smaller wavelengths where small scale Brownian motion relaxes them. Equations (3.31,3.32) lead, with $\Phi(t) = f^c + (1-f^c)^2\,\mathcal{G}(t,\varepsilon,\dot\gamma)$, and the choice of the vertices $v_2 = v_2^c = 2$, and $v_1 = v_1^c + \varepsilon\,(1-f^c)/f^c$, where $v_1^c = 0.828$, to the critical glass form factor $f^c = 0.293$ and to the stability equation (3.26), with parameters

$$\lambda = 0.707\,,\ c^{(\dot\gamma)} = 0.586/\gamma_c^2\,,\ \text{and}\ \ t_0 = 0.426/\Gamma\,.$$

The choice of transition point (v_1^c, v_2^c) is motivated by its repeated use in the literature. Actually, there is a line of glass transitions where the long time limit $f = \Phi(t \to \infty)$ jumps discontinuously. It is parameterized by $(v_1^c, v_2^c) = ((2\lambda-1), 1)/\lambda^2$ with $0.5 \leq \lambda < 1$, and the present choice is just a typical one, which corresponds to the given typical λ-value. The separation parameter ε is the crucial control parameter as it takes the system through the transition. The parameter γ_c is a scale for the magnitude of strain that is required in order for the accumulated strain $\dot\gamma t$ to matter [229]. In Eq. (3.26), it is connected to the parameter $c^{(\dot\gamma)}$.

For simplicity, the quadratic dependence of the generalized shear modulus on density fluctuations is retained from the microscopic Eq. (3.20). It simplifies because only one density mode is considered, and as, for simplicity, a possible dependence of the vertex (prefactor) v_σ on shear is neglected

$$g(t) = v_\sigma\,\Phi^2(t) + \eta_\infty\,\delta(t)\,. \tag{3.33}$$

The parameter η_∞ characterizes a short-time, high frequency viscosity and models viscous processes which require no structural relaxation. Together with Γ (respectively t_0), it is the only model parameter affected by solvent mediated interactions. Steady state shear stress under constant shearing, and viscosity then follow via integrating up the generalized modulus:

$$\sigma = \eta\,\dot\gamma = \dot\gamma\int_0^\infty dt\; g(t) = \dot\gamma\int_0^\infty dt\; v_\sigma \Phi^2(t) + \dot\gamma\,\eta_\infty\,. \tag{3.34}$$

Also, when setting shear rate $\dot\gamma = 0$ in Eqs. (3.31,3.32), so that the schematic correlator belongs to the quiescent, equilibrium system, the frequency dependent moduli are obtained from Fourier transforming:

$$G'(\omega) + i\,G''(\omega) = i\,\omega\int_0^\infty dt\; e^{-i\,\omega\,t}\; v_\sigma\;\Phi^2(t)\big|_{\dot\gamma=0} + i\omega\,\eta_\infty\,. \tag{3.35}$$

Because of the vanishing of the Fourier-integral in Eq. (3.35) for high frequencies, the parameter η_∞ can be identified as high frequency viscosity:

$$\lim_{\omega\to\infty} G''(\omega)/\omega = \eta_\infty^\omega \quad , \text{ with } \eta_\infty^\omega = \eta_\infty \, . \tag{3.36}$$

At high shear, on the other hand, Eq. (3.32) leads to a vanishing of $m(t)$, and Eq. (3.31) gives an exponential decay of the transient correlator, $\Phi(t) \to e^{-\Gamma t}$ for $\dot\gamma \to 0$. The high shear viscosity thus becomes

$$\eta_\infty^{\dot\gamma} = \lim_{\dot\gamma\to\infty} \sigma(\dot\gamma)/\dot\gamma = \eta_\infty + \frac{v_\sigma}{2\,\Gamma} = \eta_\infty^\omega + \frac{v_\sigma}{2\,\Gamma} \, . \tag{3.37}$$

Representative solutions of the $\mathrm{F}_{12}^{(\dot\gamma)}$-model are summarized in fig. 3.11, which bring out the discussed universal aspects included in all ITT models.

Extended model including hopping

The ITT equations contain the feed back mechanism that the friction increases because of slow structural rearrangements. In the schematic $\mathrm{F}_{12}^{(\dot\gamma)}$-model this is captured by the approximation for the generalized friction kernel $m(t)$ in Eq. (3.32). For $\dot\gamma = 0$ it leads to non-ergodic glass states at large enough vertices $v_{1,2}$. A dissipative process explaining the fluidity of glassy states should renormalize the diffusion kernel $\Delta(t)$. Moreover, this mechanism should become more important the longer the relaxation time in $m(t)$. If, however, the additional dissipative process is too strong, all effects of the bare ITT approach are smeared out and the described phenomenology of the glass transition can not be observed.

Götze and Sjögren found when considering (possibly unrelated) dissipative processes in simple liquids that this can by achieved by splitting the diffusion kernel into two decay channels, one connected to the original $m(t)$, and the other one connected to the new dissipation mechanism. In order for the second decay channel to take over in glassy states, it suffices to model it by one additional parameter δ in a linear ansatz $\Delta^{\mathrm{dissip}}(t) = \delta\, m(t)$. This leads to the following replacement of Eq. (3.31) in the $\mathrm{F}_{12}^{(\dot\gamma)}$-model

$$\partial_t \Phi(t) + \Gamma \left\{ \Phi(t) + \int_0^t dt'\, m(t-t')\; [\partial_{t'}\Phi(t') + \delta\, \Phi(t')] \right\} = 0 \tag{3.38}$$

The memory function $m(t)$ is still given by Eq. (3.32) because shearing decorrelates arbitrary fluctuations via shear-advection. All parameters of the model are kept and solutions of this extended model with parameter δ given in the caption are included in fig. 3.14. Importantly, the fluid like behavior in the rheology at exceedingly small $\dot\gamma$ and ω can now be captured without destroying the agreement with the original ITT at higher parameters. As it will be shown later in this study, a single parameter δ is not sufficient to model the non-exponential shape of the final relaxation process in the glass. Yet, further extensions of the model in order to describe this non-exponentiality go beyond our present aim.

3.2.5 Comparison of theory and experiment

Shear stresses measured in non-linear response of the dispersion under strong steady shearing, and frequency dependent shear moduli arising from thermal shear stress fluctuations in the quiescent dispersion were measured and fitted with results from the schematic $\mathrm{F}_{12}^{(\dot{\gamma})}$-model. Some results from the microscopic MCT for the equilibrium moduli are included also; see section 3.2.5 for more details [230]. In the following discussion, we first start with more general observations on typical fluid and glass like data, and then proceed to a more detailed analysis. Figures 3.12 and 3.13 show measurements in fluid states, at $\phi_{\mathrm{eff}} = 0.540$ and $\phi_{\mathrm{eff}} = 0.567$, respectively, while fig. 3.14 was obtained in the glass at $\phi_{\mathrm{eff}} = 0.627$. From the fits to all ϕ_{eff}, the glass transition value $\phi_{\mathrm{eff}}^c = 0.58$ was obtained, which agrees well with the measurements on classical hard sphere colloids [121, 191, 194].

Crystallization effects

We start the comparison of experimental and theoretical results by recalling the interpretation of time in the ITT approach. Outside the linear response regime, both $\Phi(t)$ and $g(t)$ describe the decorrelation of equilibrium, fluid-like fluctuations under shear and internal motion. Integrating through the transients provides the steady state averages, like the stress. While theory finds that transient fluctuations always relax under shear, real systems may either remain in metastable states if $\dot{\gamma}$ is too small to shear melt them, or undergo transitions to heterogeneous states for some parameters. In these circumstances, the theory can not be applied, and the rheological response of the system, presumably, is dominated by the heterogeneities. Thus, care needs to be taken in experiments, in order to prevent phase transitions, and to shear melt arrested structures, before data can be recorded.

The small size polydispersity of the present particles enables the system to grow crystallites according to its equilibrium phase diagram. Fortunately, when recording flow curves, viz. stress as function of shear rate, data can be taken when decreasing the shear rate. We find that the resulting 'down' flow curves correspond to amorphous states and reach the expected low-$\dot{\gamma}$ asymptotes ($\sigma = \eta_0 \, \dot{\gamma}$, see fig. 3.12), except for very low $\dot{\gamma}$, when an increase in stress indicates the formation of crystallites. 'Up' flow curves, however, obtained when moving upwards in shear rate during the measurement of the stress are affected by crystallites formed after the initial shearing at 100 s^{-1} during the timesweep and the first frequency sweep experiments. See the hysteresis between 'up' and 'down' flow curves in figs. 3.12 and 3.13, where measurements for two fluid densities are reported. Above a critical shear stress $\dot{\gamma}_c \sim 4^{-1}$ no hysteresis has been observed, which proved that all the crystallites have been molten. In the present work we focus on the 'down' flow curves, and consider only data taken either for $\dot{\gamma} > \dot{\gamma}_c$, or (for $\dot{\gamma} < \dot{\gamma}_c$) before the time crystallization sets in. This time was estimated from timesweep experiments as the time where crystallization caused a 10% deviation of the complex modulus G^*. Thus, only the portions of the flow curves unaffected by crystallization are taken into account. In fig. 3.12,fig. 3.13,fig. 3.15 and fig. 3.19 vertical bars denote the limits. We find that the effect of crystallization on the flow curves is maximal around $\phi = 0.55$ and becomes progressively smaller and shifts to lower shear rates for higher densities as discussed in the chapter crystallization (see chap. 2.3 and fig. 2.33). This agrees with the notion that

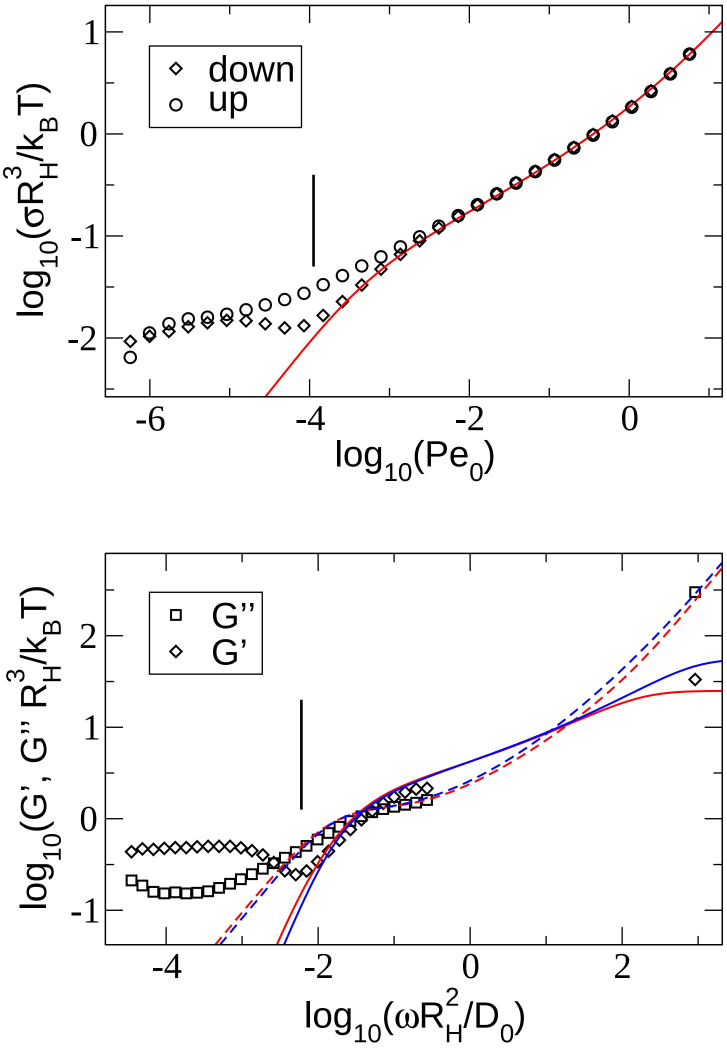

Figure 3.12: *The reduced flow curves and the corresponding moduli for a fluid state at 13.01wt%,* $T = 20^oC$*, and* $\phi_{\rm eff} = 0.540$*. Flow curves measured proceeding from higher to lower shear rates (called 'down' flow curves) and dynamic experiments were fitted where effects from crystallization can be neglected; the lower limits of the unaffected-data regions are marked by vertical bars. The red lines show the fits with the schematic* $F_{12}^{(\dot\gamma)}$*-model while the blue lines show the results from microscopic MCT (solid* G'*, broken* G''*), with parameters:* $\varepsilon = -0.05$*,* $\frac{D_S}{D_0} = 0.14$*, and* $\eta_\infty = 0.3\,k_BT/(D_0R_H)$*; the moduli were scaled up by a factor* $c_y = 1.4$*.*

the glass transition slows down the kinetics of crystallization and causes the average size of crystallites to shrink [191]. For the highest densities, which are in the glass without shear, the hysteresis in the lowest $\dot{\gamma}$ has been attributed to a non stationarity of the up curve (see fig. 3.14). This effect has been confirmed by step flow experiments, but does not affect the back curves (see section 3.2.3).

The linear response moduli similarly are affected by the presence of small crystallites at low frequencies. $G'(\omega)$ and $G''(\omega)$ increase above the behavior expected for a solution ($G'(\omega \to 0) \to \eta_0 \, \omega$ and $G''(\omega \to 0) \to c \, \omega^2$) even at low density, and exhibit elastic contributions at low frequencies (apparent from $G'(\omega) > G''(\omega)$) (see figs. 3.12 and 3.13). This effect follows the crystallization of the system during the measurement after the shearing at $\dot{\gamma} = 100 \ s^{-1}$. The data have only been considered before the crystallization time. For higher effective volume fraction other effects such as ageing and an ultra-slow process had to be taken into account and will be discussed more in detail in the next section.

Shapes of flow curves and moduli and their relations

The flow curves and moduli exhibit a qualitative change when increasing the effective packing fraction from around 50% to above 60%. For lower densities (see Fig. 3.12), the flow curves exhibit a Newtonian viscosity η_0 for small shear rates, followed by a sublinear increase of the stress with $\dot{\gamma}$; viz. a region of shear thinning behavior. For the same densities, the frequency dependent spectra exhibit a broad peak or shoulder, which corresponds to the final or α-relaxation discussed in section 3.2.4. Its peak position (or alternatively the crossing of the moduli, $G' = G''$) is roughly given by $\omega\tau = 1$ (see fig. 3.13). These properties characterize a viscoelastic fluid. For higher density, see fig. 3.14, the stress in the flow curve remains above a finite yield value even for the smallest shear rates investigated. The corresponding storage modulus exhibits an elastic plateau at low frequencies. The loss modulus drops far below the elastic one. These observations characterize a soft solid. The loss modulus rises again at very low frequencies, which may indicate that the colloidal solid at this density is metastable and may have a finite lifetime (an ultra-slow process is discussed in section 3.2.5).

Simple relations, like the 'Cox-Merz rule', have sometimes been used in the past to compare the shapes of the flow curves $\sigma(\dot{\gamma})$ with the shapes of the dissipative modulus $G''(\omega)$. Both quantities can be interpreted in terms of a (generalized) viscosity, on the one hand as function of shear rate $\eta(\dot{\gamma}) = \sigma(\dot{\gamma})/\dot{\gamma}$, and on the other hand as function of frequency $\eta(\omega) = G''(\omega)/\omega$. The Cox-Merz rule states that the functional forms of both viscosities coincide.

Figures 3.12 to 3.14 provide a sensitive test of relations in the shapes of $\sigma(\dot{\gamma})$ and $G''(\omega)$. Figure 3.13 shows most conclusively, that no simple relation between the far-from equilibrium stress as function of external rate of shearing exists with the equilibrium stress fluctuations at the corresponding frequency. While $\sigma(\dot{\gamma})$ increases monotonically, the dissipative modulus $G''(\omega)$ exhibits a minimum for fluid states close to the glass transition. It separates the low-lying final relaxation process in the fluid from the higher-frequency relaxation.

As shown in Fig. 3.11, the frequency dependence of G'' in the minimum region is given by

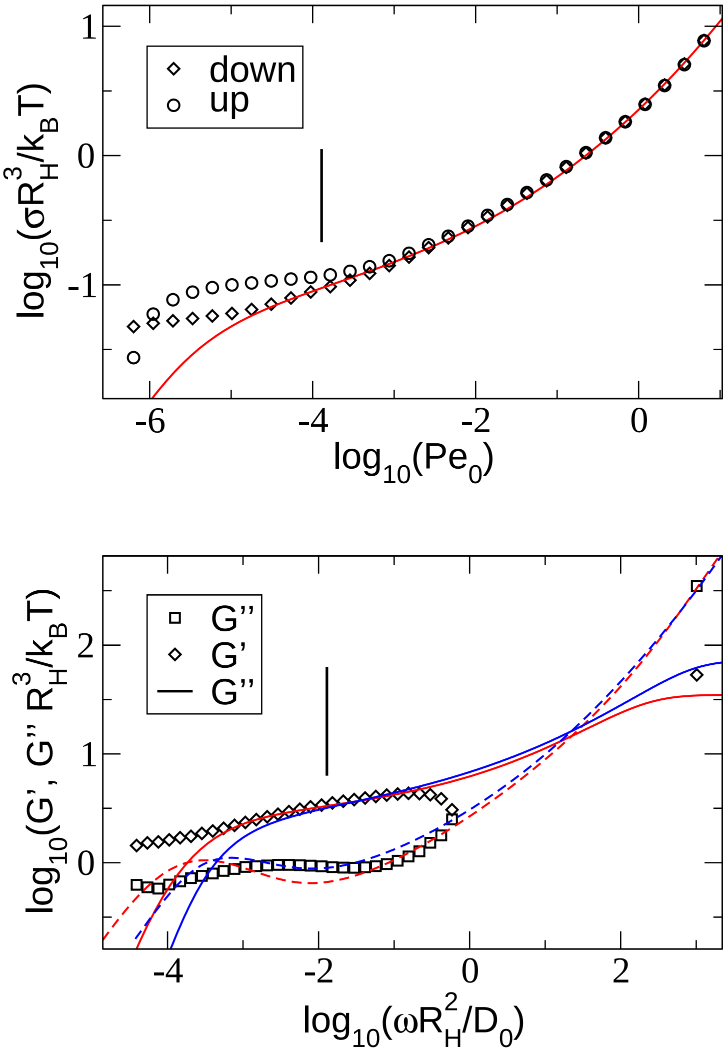

Figure 3.13: *The reduced flow curves and the corresponding moduli for a fluid state at 13.01wt%, T=* 18^oC*, and* $\phi_{\text{eff}} = 0.567$*. The vertical bars mark the minimal Peclet number or rescaled frequency for which the influence of crystallization can be neglected. Microscopic parameters:* $\varepsilon = -0.01$*,* $\frac{D_S}{D_0} = 0.14$*, and* $\eta_\infty = 0.3\, k_B T/(D_0 R_H)$*; moduli scale factor* $c_y = 1.4$*.*

the scaling function $\mathcal{G}$ of section 3.2.4, which describes the minimum as crossover between two power laws. The approximation for the modulus around the minimum

$$G''(\omega) \approx \frac{G_{\text{min}}}{a+b} \left[b \left(\frac{\omega}{\omega_{\text{min}}} \right)^a + a \left(\frac{\omega_{\text{min}}}{\omega} \right)^b \right] \tag{3.39}$$

has been found in the quiescent fluid ($\varepsilon < 0$, $\dot{\gamma} = 0$), and works quantitatively if the relaxation time τ is large, viz. time scale separation holds for small $|\varepsilon|$ [162]. The parameters in this approximation follow from Eqs. (3.27,3.28) which give $G_{\text{min}} \propto \sqrt{-\varepsilon}$ and $\omega_{\text{min}} \propto (-\varepsilon)^{1/2a}$. For packing fractions too far below the glass transition, the final relaxation process is not clearly separated from the high frequency relaxation. This holds in fig. 3.12, where the final structural decay process only forms a shoulder. Closer to the transition, in fig. 3.13, it is separated, but crystallization effects prevent us from fitting Eq. (3.39) to the data.

Asymptotic power-law expansions of $\sigma(\dot{\gamma})$ exist close to the glass transition, which were deduced from the stability analysis in section 3.2.4 [45, 231, 232]; yet we refrain from entering their detailed discussion and describe the qualitative behavior in the following. For the same parameters in the fluid, where the minimum in $G''(\omega)$ appears, the flow curves follow a S-shape in a double logarithmic plot, crossing over from a linear behavior $\sigma = \eta_0\,\dot{\gamma}$ at low shear rates to a downward curved piece, followed by a point of inflection, and an upward curved piece, which finally goes over into a second linear behavior at very large shear rates, where $\sigma = \eta_\infty^{\dot{\gamma}}\,\dot{\gamma}$. This S-shape can be recognized in figs. 3.12 and 3.13. Because of the finite slope of $\log_{10}\sigma$ versus $\log_{10}\dot{\gamma}$ at the point of inflection, one may speculate about an effective power-law $\log_{10}\sigma \approx c + c' \log_{10}\dot{\gamma}$. In Fig. 3.12 this happens at $\text{Pe}_0 \approx 10^{-2}$. Yet, the power-law is only apparent because the point of inflection moves, the slope changes with distance to the glass transition, and the linear bit in the flow curve never extends over an appreciable window in $\dot{\gamma}$ [232].

A qualitative difference of the glass flow curves to the fluid S-shaped ones, is that the shape of $\sigma(\dot{\gamma})$ constantly has an upward curvature in double-logarithmic representation. The yield stress can be read off by extrapolating the flow curve to vanishing shear rate. In Fig. 3.14 this leads to a value $\sigma^+ \approx 0.24\,k_BT/R_H^3$ at $\phi_{\text{eff}} = 0.622$, which is in agreement with previous measurements in this system over a much reduced window of shear rates [39]. While this agreement supports the prediction of an dynamic yield stress in the ITT approach, and demonstrates the usefulness of this concept, small deviations in the flow curve at low $\dot{\gamma}$ are present in fig. 3.14. We postpone to section 3.2.5 the discussion of these deviations, which indicate the existence of an additional slow dissipative process in the glass. Its signature is seen most prominently in the loss modulus $G''(\omega)$ in fig. 3.14. On the contrary the storage modulus of the glass shows striking elastic behavior. $G'(\omega)$ exhibits a near plateau over more than three decades in frequency, which allows to read off the elastic constant G_∞ easily.

Microscopic MCT results

Included in figures 3.12 to 3.14 are calculations using the microscopic MCT given by Eqs. (3.20) to (3.24) evaluated for hard spheres [230]. This is presently possible without shear only ($\dot{\gamma} = 0$), because of the complications arising from anisotropy and time dependence in Eq. (3.22). The only a priori unknown, adjustable parameter is the matching time scale

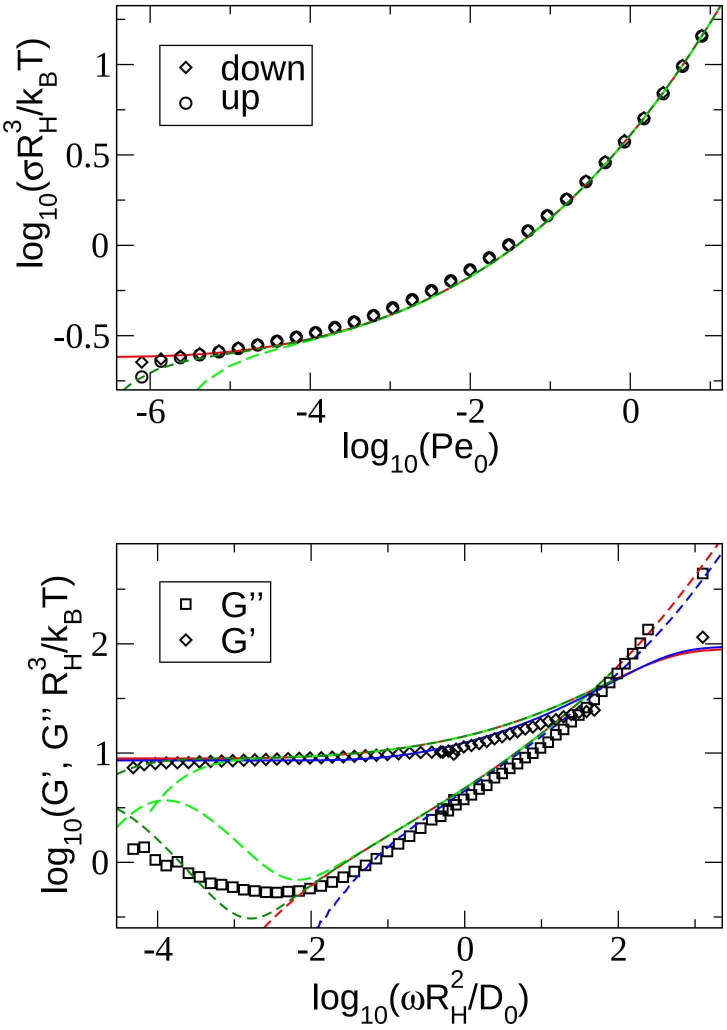

Figure 3.14: *The reduced flow curves and the corresponding moduli for a glass state at 13.01wt%, T= 14°C, and* $\phi_{\text{eff}} = 0.622$*. See figure 3.12 for further explanations. Microscopic parameters:* $\varepsilon = 0.03$*,* $\frac{D_S}{D_0} = 0.08$*, and* $\eta_\infty = 0.3\, k_BT/(D_0R_H)$*; moduli scale factor* $c_y = 1.4$ *(blue). Curves from the schematic* $F_{12}^{(\dot\gamma)}$*-model with an additional dissipative process included (Eq. 3.38) are shown as dashed lines;* $\delta = 10^{-7}\,\Gamma$ *(long dashes, light green) and* $\delta = 10^{-8}\,\Gamma$ *(short dashes, dark green). Here* $\Gamma = 88\, D_0/R_H^2$*. The red curves give the schematic model calculations for identical parameters but without additional dissipative process (viz.* $\delta = 0$*).*

t_0, which we adjusted by varying the short time diffusion coefficient appearing in the initial decay rate in Eq. (3.21). The computations were performed with $\Gamma_{\mathbf{q}}(t) \equiv \Gamma_q = D_s\, q^2/S_q$, and values for D_s/D_0 are reported in the captions of Figs. 3.12 to 3.14, and in table 3.2.

Gratifyingly, the stress values computed from the microscopic approach are close to the measured ones; they are too small by 40% only, which may arise from the approximate structure factors entering the MCT calculation; the Percus-Yevick approximation was used here [33]. In order to compare the shapes of the moduli the MCT calculations were scaled up by a factor $c_y = 1.4$ in figs. 3.12 to 3.14. Microscopic MCT also does not hit the correct value for the glass transition point [162, 164]. It finds $\phi_c^{\mathrm{MCT}} = 0.516$, while our experiments give $\phi_c^{\mathrm{exp}} \approx 0.58$. Thus, when comparing, the relative separation from the respective transition point needs to be adjusted as, obviously, the spectra depend sensitively on the distance to the glass transition; the fitted values of the separation parameter ε are included in fig. 3.16.

Considering the low frequency spectra in $G'(\omega)$ and $G''(\omega)$, microscopic MCT and schematic model provide completely equivalent descriptions of the measured data. Differences in the fits in Figs. 3.12 to 3.14 for $\omega R_H^2/D_0 \leq 1$ only remain because of slightly different choices of the fit parameters which were not tuned to be close. These differences serve to provide some estimate of uncertainties in the fitting procedures. Main conclusion of the comparisons is the agreement of the moduli from microscopic MCT, schematic ITT model, and from the measurements. This observation strongly supports the universality of the glass transition scenario which is a central line of reasoning in the ITT approach to the non-linear rheology.

At large $\dot\gamma$ and large ω hydrodynamic interactions become important. In the flow curves, $\eta_\infty^{\dot\gamma}$, and, in the loss modulus, η_∞^{ω} become relevant parameters, and the structural relaxation captured in ITT and MCT is not sufficient alone to describe the rheology. Qualitative differences appear in the moduli, especially in $G'(\omega)$, between the schematic model and the microscopic MCT. While the storage modulus of the $\mathrm{F}_{12}^{(\dot\gamma)}$-model crosses over to a high-ω plateau already at rather low ω, the microscopic modulus continues to increase for increasing frequency, especially at lower densities; see the region $\omega \gtrsim 10^2 D_0/R_H^2$ in Figs. 3.12 to 3.13. The latter aspect is connected to the high-frequency divergence of the shear modulus of particles with hard sphere potential [161], as captured within the MCT approximation [225, 230], As carefully discussed by Lionberger and Russel, lubrication forces may suppress this divergence and its observation thus depends on the surface properties of the colloidal particles [187]. Clearly, the region of (rather) universal properties arising from the non-equilibrium transition between shear-thinning fluid and yielding glass is left here, and particle specific effects become important.

Parameters

In the microscopic ITT approach from section 3.2.4 the rheology is determined from the equilibrium structure factor S_q alone. This holds at low enough frequencies and shear rates, and excludes the time scale parameter t_0 of Eq. (3.27), which needs to be found by matching to the short time dynamics. This prediction has as consequence that the flow curves and moduli should be a function only of the thermodynamic parameters characterizing the present system, viz. its structure factor.

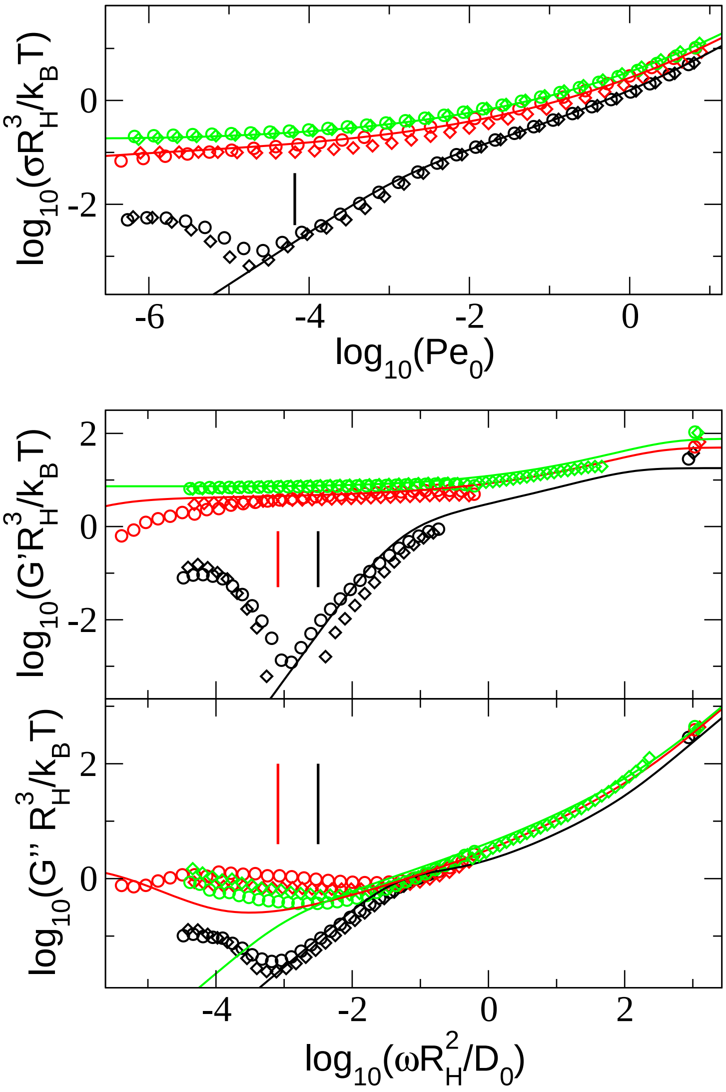

Figure 3.15: *The plots demonstrate that the reduced flow curves and the reduced moduli are unique functions only depending on* ϕ_{eff}. *All flow curves are down curves. The fits using the schematic* $F_{12}^{(\dot\gamma)}$*-model were performed with the data points at 13.01wt% taken before the onset of crystallization (data to the right of the vertical bars). Black diamonds: 12.10wt% and* $\phi_{\text{eff}} = 0.527$. *Black circles: 13.01wt% and* $\phi_{\text{eff}} = 0.527$. *Red diamonds: 12.10wt% and* $\phi_{\text{eff}} = 0.578$. *Red circles: 13.01wt% and* $\phi_{\text{eff}} = 0.580$. *Green diamonds: 13.01wt% and* $\phi_{\text{eff}} = 0.608$. *Green circles: 13.58wt% and* $\phi_{\text{eff}} =$ 0.606.

Figure 3.15 supports this claim by proving that the rheological properties of the dispersion only depend on the effective packing fraction, if particle size is taken account of properly. Figure 3.15 collects flow curves and moduli measured for different concentrations of particles according to weight, and for different radii R_H adjusted by temperature. Whenever the effective packing fraction, $\phi_{\rm eff} = (4\pi/3)nR_H^3$, is close, the rheological data overlap in the window of structural dynamics. Obviously, appropriate scales for frequency, shear rate and stress magnitudes need to be chosen to observe this. The dependence of the vertices on S_q (Eqs. (3.20,3.23)) suggests that k_BT sets the energy scale as long as repulsive interactions dominate the local packing. The length scale is set by the average particle separation, which can be taken to scale with R_H in the present system. The time scale of the glassy rheology within ITT is given by t_0 from Eq. (3.27), which we take to scale with the measured dilute diffusion coefficient D_0. Thus the rescaling of the rheological data can be done with measured parameters alone. Figure 3.15 shows quite satisfactory scaling. Whether the particles are truely hard spheres is not of central importance to the data collapse in Fig. 3.15 as long as the static structure factor agrees for the $\phi_{\rm eff}$ used. Fits with the $\mathrm{F}_{12}^{(\dot\gamma)}$-model to all data are possible, and are of comparable quality to the fits shown in Figs. 3.12 to 3.14.

The fitted parameters used in the schematic $\mathrm{F}_{12}^{(\dot\gamma)}$-model are summarized in Fig. 3.16. Parameters corresponding to identical concentrations by weight are marked by identical colours. Within the scatter of the data one may conclude that all fit parameters depend on the effective packing fraction only. This again supports the mentioned dependence of the glassy rheology on the equilibrium structure factor. The initial rate Γ, which sets t_0, appears a unique function of $\phi_{\rm eff}$, also; an observation which is not covered by the present ITT approach. It suggests that hydrodynamic interactions appear determined by $\phi_{\rm eff}$ in the present system also.

Importantly, all fit parameters exhibit smooth and monotonous drifts as function of the external thermodynamic control parameter, viz. $\phi_{\rm eff}$ here. Nevertheless, the moduli at low frequencies (e.g. $G'(\omega)$ at $\omega R_H^2/D_0 = 0.01$), or the stresses at low shear rates (e.g. $\sigma(\dot\gamma)$ at $\dot\gamma R_H^2/D_0 = 10^{-4}$) change by more than an order in magnitude in Figs. 3.12 to 3.14. Even larger changes may be obtained from taking experimental data not shown, whose fit parameters are included in Fig. 3.16. It is this sensitive dependence of the rheology on small changes of the external control parameters that ITT addresses.

When comparing the parameters from the schematic model to the ones obtained from the microscopic MCT calculation of the moduli, one observes qualitative and semi-quantitative agreement (see the captions to Figs. 3.12 to 3.14, table 3.2, and the upper inset of Fig. 3.16). For example, the increase of the prefactor v_σ of stress fluctuations is captured in the microscopic vertex where S_q enters (this follows because the rescaling factor c_y is density independent). Also the hydrodynamic viscosity $\eta_\infty = \eta_\infty^\omega$ roughly agrees and may be taken $\phi_{\rm eff}$-independent in the fits with the microscopic moduli. On closer inspection, one may notice that the separation parameter of the microscopic hard sphere calculation obtains larger positive values than ε fitted with the schematic model. Moreover, it follows an almost linear dependence on the effective packing fraction as asymptotically predicted by MCT, $\varepsilon \approx 0.65\,(\phi_{\rm eff} - \phi_{\rm eff}^c)/\phi_{\rm eff}^c$ with glass transition density $\phi_c = 0.587$ slightly higher than from the schematic model fits. The differing behavior of the separation parameter from the fits with the $\mathrm{F}_{12}^{(\dot\gamma)}$-model in the glass is not understood presently. The microscopic calculation signals glassy arrest more clearly than the

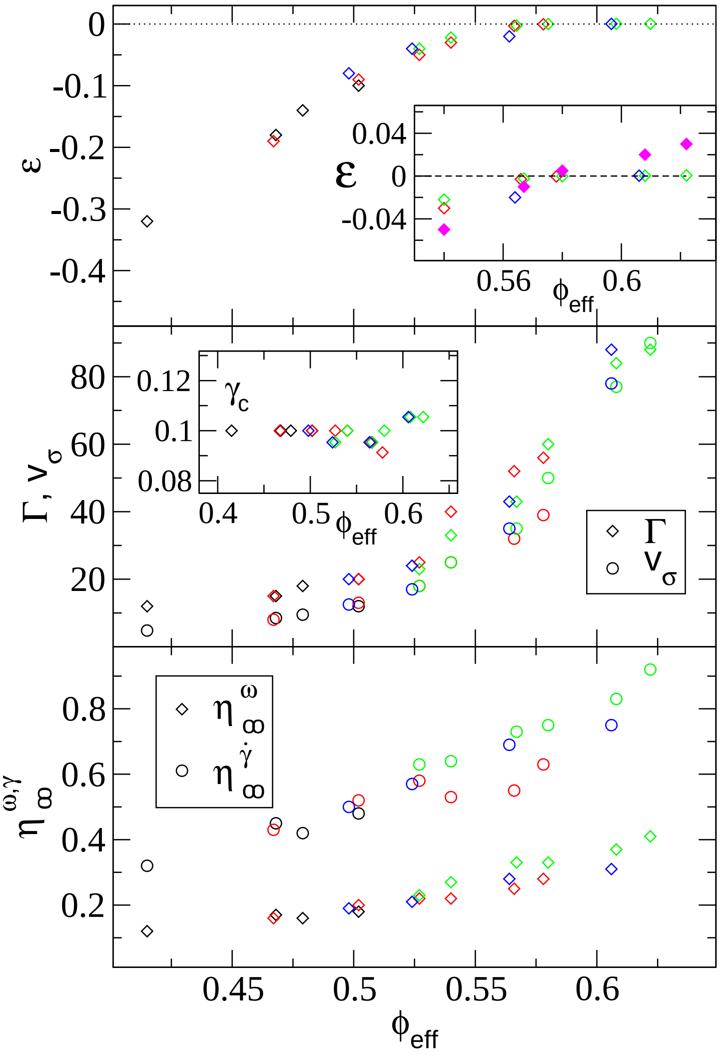

Figure 3.16: *The fitted parameters of the* $F_{12}^{(\dot\gamma)}$*-model (open symbols). Black symbols: 10.75wt%, red symbols: 12.10wt%, green symbols: 13.01wt%, blue symbols: 13.58 wt%.* ε *and* γ_c *are dimensionless. Filled magenta symbols, included in the upper inset, give the* ε *values fitted in the microscopic MCT calculations for 13.01wt%. The unit of* v_σ *is* k_BT/R_H^3 *while* Γ *is given in units of* D_0/R_H^2*. The high frequency and high shear viscosities* $\eta_\infty^{\omega;\dot\gamma}$ *are given in units of* $k_BT/(D_0R_H)$*.*

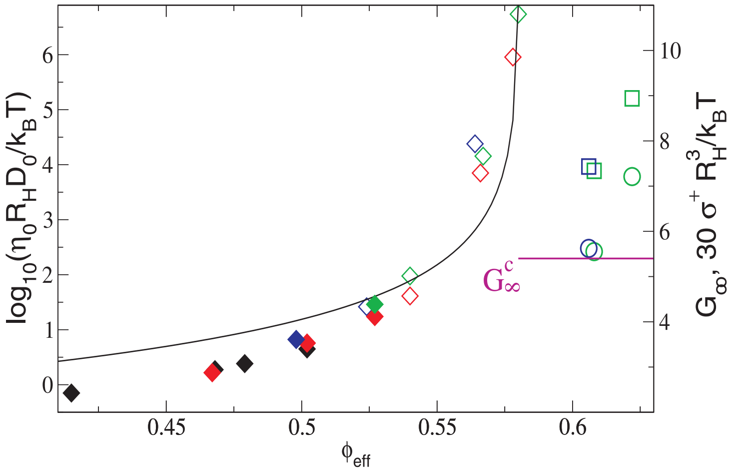

Figure 3.17: *Newtonian viscosity* η_0 *(diamonds, left axis), elastic constant* G_∞ *(squares), and yield stress* σ^+ *(circles; data rescaled by a factor 30; both* G_∞ *and* σ^+ *right axis), as functions of the effective packing fraction* ϕ_{eff} *as obtained from the fits performed with the* $F_{12}^{(\dot\gamma)}$*-model. Filled symbols indicate where direct measurements of* η_0 *were possible. Black symbols: 10.75wt%, red symbols: 12.10wt%, green symbols: 13.01wt%, blue symbols: 13.58 wt%. The line gives a power-law fit to the viscosity-date over the full range using the known* $\gamma = 2.34$ *exponent from MCT,* $\log_{10}\eta_0 = A - \gamma \cdot \log_{10}(\phi_{\text{eff}}^c - \phi_{\text{eff}})$*; the critical packing fraction is found as* $\phi_{\text{eff}}^c = 0.580$*. The horizontal bar denotes the critical elastic constant* G_∞^c*.*

schematic model fit. The short time diffusion coefficient D_s/D_0 in the microscopic calculation decreases as expected from considerations of hydrodynamic interactions. The initial rate Γ, however, of the schematic model increases with packing fraction. The ad hoc interpretatation of Γ as microscopic initial decay rate evaluated for some typical wavevector q_*, viz. the ansatz $\Gamma = D_s q_*^2/S_{q_*}$, thus apparently does not hold.

While the model parameters adjusted in the fitting procedure only drift smoothly with density, the rheological properties of the dispersion change dramatically. Figure 3.17 shows the Newtonian viscosity as obtained from extrapolations of the fits in the $F_{12}^{(\dot\gamma)}$-model. It changes by 6 orders in magnitude. From the combination of $G''(\omega)$- and flow curve data we can follow this divergence over more than one decade in direct measurement. From the divergence of η_0 the estimate of the critical packing fraction can be obtained using the power-law Eq. (3.28), because the exponent γ is known. We find $\phi_{\text{eff}}^c = 0.580$ in nice agreement with the value expected for colloidal hard spheres. On the glass side, the elastic constant and yield stress jump discontinuously into existence. Reasonable values are obtained from the $F_{12}^{(\dot\gamma)}$-model fits compared to data from comparable systems. The strong increase of the elastic quantities upon small increases of the density is apparent.

Additional dissipative process in glass

One of the major predictions of the ITT approach concerns the existence of glass states, which exhibit an elastic response for low frequencies under quiescent conditions, and which flow only because of shear and exhibit a dynamic yield stress under stationary shear. Figure 3.14 shows such glassy behavior, as is revealed by the analysis using the

Table 3.2: *Parameters of the fits with the microscopic MCT to the linear-response moduli* $G'(\omega)$ *and* $G''(\omega)$*. The first two columns of separation parameter* ε *and short-time diffusion coefficient ratio* D_s/D_0 *correspond to the fits shown in Figs. 3.12 to 3.14 and Fig. 3.19 (solid lines), while the second columns of* ε' *and* D'_s/D_0 *correspond to the dashed-lines in Fig. 3.19; when no value is given, the values from the first two columns apply. In all cases* $c_y = 1.4$ *and* $\eta_\infty = 0.3\,k_BT/(D_0R_H)$ *are used.*

ϕ_{eff}	ε	D_s/D_0	ε'	D'_s/D_0
0.527	- 0.08	0.15		
0.540	- 0.05	0.15		
0.567	- 0.01	0.15		
0.580	0.005	0.13	- 0.01	0.15
0.608	0.02	0.11	- 0.003	0.15
0.622	0.03	0.08	- 0.003	0.15

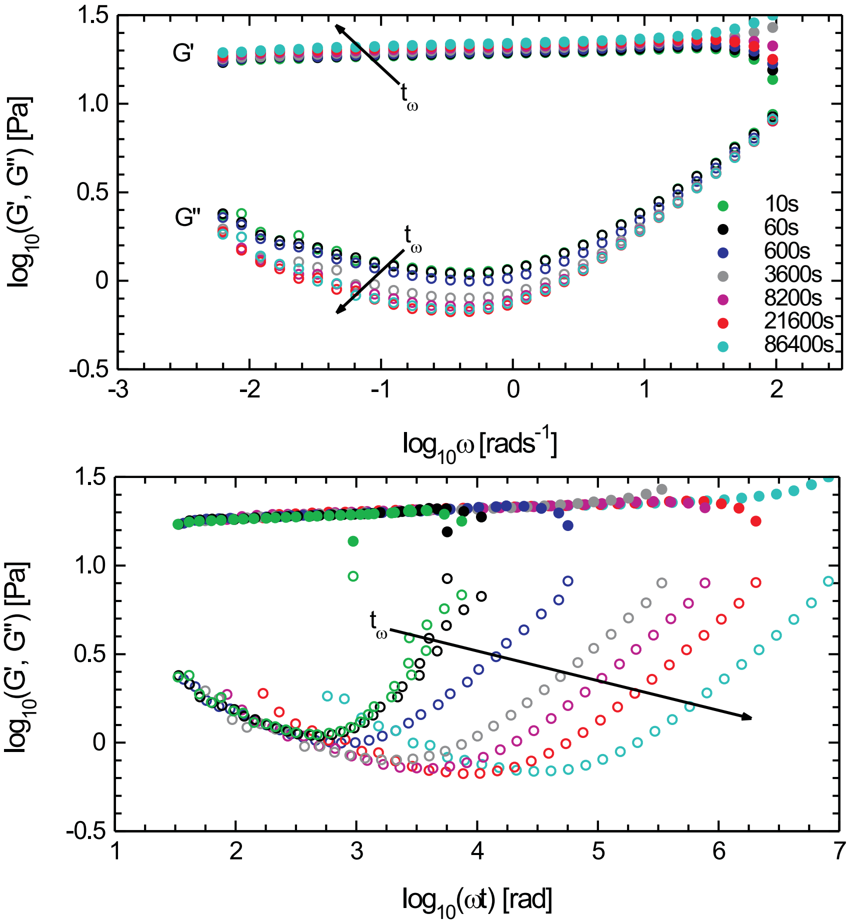

Figure 3.18: *Ageing experiment on a dense core shell suspension in the glassy state* ($\phi_{\text{eff}} = 0.622$, $T = 14$ *°C). The storage* $G'(\omega)$ *and loss* $G''(\omega)$ *moduli for different waiting times* t_w*. The data have been also plotted as function of* ωt *as suggested recently [205, 233]. See text for further explanation.*

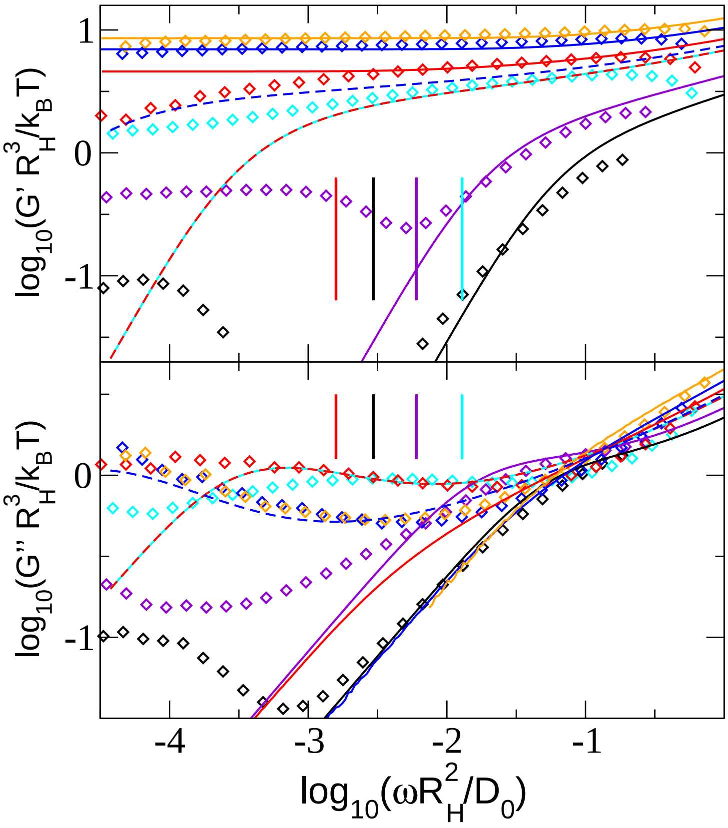

Figure 3.19: *Fits with microscopic MCT to the linear-response moduli* $G'(\omega)$ *(upper panel) and* $G''(\omega)$ *(lower panel) for the packing fractions* $\phi_{\mathrm{eff}} = 0.527$ *(black diamonds and lines),* $\phi_{\mathrm{eff}} = 0.540$ *(violet),* $\phi_{\mathrm{eff}} = 0.567$ *(light blue),* $\phi_{\mathrm{eff}} = 0.580$ *(red),* $\phi_{\mathrm{eff}} = 0.608$ *(dark blue), and* $\phi_{\mathrm{eff}} = 0.622$ *(orange). Continuous lines give the fits optimized for describing the storage modulus* $G'(\omega)$*; these fits are also shown in Figs. 3.12 to 3.14, and the corresponding parameters are included in Fig. 3.16, and summarized in the left two columns in table 3.2. Broken lines for* $\phi_{\mathrm{eff}} = 0.580$ *(red, overlapping with the solid light blue curve), and* $\phi_{\mathrm{eff}} = 0.608$ *(dark blue; the same curve would fit* $\phi_{\mathrm{eff}} = 0.622$*) show microscopic MCT calculations attempting to fit the minima in* $G''(\omega)$ *enforcing negative separation parameters* ε *(parameters included in table 3.2). These fluid like spectra can rationalize* $G''(\omega)$*, but fail qualitatively to describe* $G'(\omega)$*. Vertical bars in corresponding colors denote the frequencies below which crystallization affects the data at the different* ϕ_{eff}*.*

schematic and the microscopic model. Nevertheless, the loss modulus $G''(\omega)$ rises at low frequencies, clearly indicating the presence of a dissipative process. It is not accounted for by the present theory. Also, the storage modulus $G'(\omega)$ shows some downward bend at the lowest frequencies.

These deviations can not be rationalized by ageing effects or non-linearities in the response; see Fig. 3.18. We checked the dependence on time since quench to this glass state and also the linear dependence of the stress on the shear amplitude. While we find ageing effects shortly after cessation of pre-shear [205, 210, 211], these saturate after one day, when the drifts of the spectra come to a stop. Ageing effects do not change the spectra qualitatively, as the dissipative process appears to possess a finite equilibrium relaxation time. As suggested recently for dense PNIPAM microgel dispersions [205, 233] the same data have been plotted as function of ωt. Here, t is the total waiting time and is defined as function of the waiting time t_w before starting the measurement and the time $\delta(t(\omega_n))$ expired between t_w and the acquisition of the data as $t = t(\omega_n) = t_w + \delta(t(\omega_n))$. The curves collapsed in the master curve in the low frequency range up to $\omega t \approx 3000$ as expected from ageing theory for waiting time $t_w < 8200$ s. This prediction is no more respected for longer waiting times, where an additional relaxation process is identified. This supports the introduction of hopping phenomenon in our model, with a characteristic relaxation time of the order of 10^4 s ($\approx R_H^2/\delta D_0 = 10^8 R_H^2/\Gamma D_0 = 8.8\,10^3$ s see Fig.3.14).

Let us stress, moreover, that the state shown in Fig. 3.14 is not a fluid state within the present approach. The presence of an elastic window in $G'(\omega)$, its increase as function of packing fraction, and the upward curvature of the flow curves rule out a negative separation parameter $\varepsilon < 0$ of this state at $\phi_{\text{eff}} = 0.622$. Calculations within the microscopic MCT document this convincingly. Figure 3.19 compares the MCT calculations for hard spheres with moduli ranging from fluid to glassy states. By adjusting the effective packing fraction, MCT semi-quantitatively describes the dominating modulus, either loss or storage one, for all states (corresponding curves already shown in Figs 3.12 to 3.14). At high concentrations, it describes the storage modulus $G'(\omega)$ on an error level of $1 k_B T/R_H^3$, and misses the loss modulus $G''(\omega)$ by a similar absolute error. Yet, because the latter is itself of the order of $G''(\omega) \approx 1 k_B T/R_H^3$ in the measurements, MCT fails to describe $G''(\omega)$ adequately. If, however, the effective packing fraction in the MCT calculations is adjusted to match the loss modulus $G''(\omega)$, then this fit fails completely to capture $G'(\omega)$ at high densities; see the dashed lines in Fig. 3.19. Because the storage modulus, however, dominates the linear mechanical response of the glass, the second fit needs to be rejected. In conclusion, MCT correctly identifies the transition to a glass at high densities with dominating elastic response and yielding behavior under flow. It misses an additional dissipative process, which contributes on the 10% level to the shear moduli and stresses in the frequency and shear rate window explored in our experiments.

The existence of an additional dissipative process contradicts the notion of 'ideal' glass states as described by the present ITT or MCT approach. Clearly, the system at $\phi_{\text{eff}} = 0.622$ becomes a fluid at even longer times, or lower shear rates and frequencies than observed in Fig. 3.14. This does not, however, contradict the observation that the structural relaxation as captured in the ITT equations has arrested. In an extension of the ITT approach, it is possible to account for the additional decay channel in a an extended schematic model (see section 3.2.4). Results from this extended $\mathrm{F}_{12}^{(\dot\gamma)}$-model are included in Fig. 3.14 and demonstrate that none of the qualitative features discussed within ITT change at finite frequencies or shear rates. The additional process leads to fluid behavior at even lower ω or $\dot{\gamma}$, and needs to be taken into account only, if exceedingly small frequencies or shear rates are tested; its relaxation time at $\phi_{\mathrm{eff}} = 0.622$ exceeds $10^8 R_H^2/D_0 = 8.8.10^3$ s. It does not shift the location of the 'glass transition' as defined within the idealized ITT (MCT) approach, because this is already determined by the shapes of the flow curves and spectra in the observed windows.

3.2.6 Summary

In the present chapter, we explored the connection between the physics of the glass transition and the rheology of dense colloidal dispersions, including in strong shear flow. Using model colloidal particles made of thermosensitive core-shell particles, we could investigate in detail the vicinity of the transition between a (shear-thinning) fluid and a (shear-molten) glass. The high sensitivity of the particle radius to temperature enabled us to closely vary the effective packing fraction around the critical value. We combined measurements of the equilibrium stress fluctuations, viz. linear storage and loss moduli, with measurements of flow curves, viz. nonlinear steady state shear stress versus shear rate, for identical external control parameters. In this way we could verify the consequences from the recent suggestion, that the glassy structural relaxation can be driven by shearing and in turn itself dominates the low shear or low frequency rheology.

In the employed theoretical approach developed in the group of Prof. M. Fuchs, the equilibrium structure as captured in the equilibrium structure factor S_q sufficed to describe all phenomena qualitatively. As only exception, we observed an ultra-slow decay of all glassy states that is yet not accounted for by theory. Microscopic calculations were possible for the linear response quantities using mode coupling theory applied to hard spheres. Schematic model calculations were possible within the integration through transients approach, and simultaneously captured the linear and nonlinear rheology using identical parameter sets. Semi-quantitative agreement between microscopic and schematic model calculations and with the measured data for varying effective packing fraction could be achieved adjusting a small number of fit parameters in smooth variations.

4 Association

4.1 Reversible self-assembly of composite microgels.

4.1.1 Introduction

Poly(N-isopropylacrylamide) microgels present a versatile phase behavior: on one hand they can behave like hard sphere with a liquid-crystal transition below the critical temperature as discussed in the chapter 2.3. On the other hand in the absence of electrostatic stabilization or in saturated salt concentrations the particles become attractive after the low critical solution temperature [28, 29].

This leads to a partially or totally reversible aggregation of the system in the dilute regime and to the gelation of the system for higher concentrations [25, 27, 30, 234]. The dependence of the critical flocculation temperature (CTF) of PNIPAM microgels on the concentration of $CaCl_2$ was reported by Pelton and Chibante [235]. The influence of the temperature and of the NaCl concentration was studied by Rasmusson et al. [236]. The authors demonstrated that the flocculation of the PNIPAM particles is consistent with a weak reversible flocculation model. Zhu and Napper investigated the aggregation kinetics of composite PS/PNIPAM core-shell particles in the presence of different electrolyte and reported some unexpected ion effects [237, 238]. Duracher et al. described the stability of cationic core-shell systems PS/PNIPAM [239]. The influence of the initiator concentration on the CFT was discussed as well. They also measured the electrophoretic mobility of the particles below the LCST, which was supported by a more recent study on anionic and cationic core-shell particles given by López-León et al. [72]. These two studies reported the decrease of the LCST with increasing salt concentrations.

The phase transition in the PNIPAM shell of composite Polystyrene/Poly(N-isopropylacrylamide) core-shell particles has been investigated by diverse methods as discussed in the chapter 2.1. Moreover it was considered as suitable model system for the understanding on the nature of liquids, solids and glasses as shown in the chapter 3.2. Ishikawa et al. [240, 241] and Hofkens et al. [242] investigated the laser-induced phase transition of linear PNIPAM in aqueous solutions. Submicrometer aggregates have been obtained as a result from the phase separation occurring by locally heating the system with an IR laser beam. Besides the photothermal effect, the influence of the radiation pressure upon the phase transition has been discussed carefully [242]. This approach has been used recently for microgels mixed with gold nanoparticles. The local annealing was used to obtain transition from glass to crystal and crystal to liquid after radiation with a green laser [11, 243].

In this chapter we present a comprehensive investigation on the temperature controlled self-assembly of the core-shell particles presented in the chapter 2.1. The accent is first put on the reversibility of the coagulation process. In presence of salt the particles reversibly coagulate after 32^oC as shown by dynamic light scattering. To our best knowledge we investigate for the first time for this kind of system the coagulation kinetics in the early stage by dynamic light scattering following the method proposed by Holthoff et al. [244].

The second part is dedicated to the thermogelation of the concentrated solutions followed by rheological measurements. The influence of the attractive interactions on the structure of the samples after drying has been imaged by atomic force microscopy and optical microscopy. The transition from liquid to attractive glass is accompanied by a strong increase of the turbidity. In the last section of this chapter we investigate the self-assembly of the particles at the microscale induced by focusing a laser on the solutions.

4.1.2 Coagulation kinetics

As shown by Holthoff et al. [244] the kinetics of Brownian coagulation of particles in the earliest stage with the transition from single particles to doublets can be described by

$$\frac{dN_z}{dt} = \frac{1}{2}\sum_{i+j=2} k_{12}N_iN_j - N_z\sum_{i=1}^{\infty} k_{iz}N_i \tag{4.1}$$

where k_{ij} is a second-order coagulation rate constant, t is the time, and N_z is the total particle concentration of z-fold aggregates.

The particle concentration of singlets N_1 and doublets N_2 as a function of time can be obtained by solving eq. 4.1 analytically. Assuming $k_{ij} = k_{11}$ and the initial particle concentration N_0 we obtain

$$N_1 = \frac{2N_0}{2 + k_{11}N_0t} \tag{4.2}$$

using eq. 4.1 and integrating leads to

$$N_2 = \frac{4N_0^2k_{11}t}{(2 + k_{11}N_0t)^3} \tag{4.3}$$

Developing N_1 and N_2 for the short times leads to

$$\frac{N_1}{N_0} = 1 - k_{11}N_0t + ... \tag{4.4}$$

$$\frac{N_2}{N_0} = \frac{k_{11}N_0t}{2} + ... \tag{4.5}$$

If we consider that the coagulation of spherical particles is just controlled by Brownian diffusion, according to the theory of Smoluchsovski [245, 246], the coagulation rate constant becomes:

$$k_{11} = 2k_s = \frac{8k_BT}{3\eta} \tag{4.6}$$

where k_B is the Boltzmann constant, T the temperature, and η the viscosity of the fluid. Considering the hydrodynamic interactions and the interparticles potential leads to a more complicated expression [247].

In the early stage of the aggregation, where the doublets are formed, the scattering intensity can be expressed as the sum of the scattering intensity $I(q,t)$ of the single particles $I_1(q)$ and doublets $I_2(q)$.

$$I(q,t) = N_1(t)I_1(q) + N_2(t)I_2(q) \tag{4.7}$$

Using the expression of the singlets and the doublets of the equations 4.4 and 4.5, the scattered light intensity results in

$$\frac{1}{I_(q,t=0)}\left(\frac{dI(q,t)}{dt}\right)_{t\to 0} = \left(\frac{I_2(q)}{2I_1(q)} - 1\right) k_{11}N_0 \tag{4.8}$$

the value for the form factor of an aggregate of z identical spheres can be calculated within the Rayleigh-Gans-Debye approximation [247, 248], considering that independent primary particles within an aggregate with identical scatterers. The coagulation rate can be determined from the static intensity with

$$\frac{1}{I(q,t=0)}\left(\frac{dI(q,t)}{dt}\right)_{t\to 0} = \left(\frac{sin(2aq)}{2aq}\right) k_{11}N_0 \tag{4.9}$$

with a the radius of the primary particles.

In the dynamic light scattering the intensity-weighted average of the diffusion coefficient $D(q,t)$ between single particles and doublets can be calculated from the first moment or mean decay rate $\Gamma(q,t)$.

$$|D(q,t)| = \frac{|\Gamma(q,t)|}{q^2} = \frac{N_1(t)I_1(q)D_1 + N_2(t)I_2(q)D_2}{N_1(t)I_1(q) + N_2(t)I_2(q)} \tag{4.10}$$

According to the Stokes-Einstein equation, the diffusion coefficient is related to the hydrodynamic radius of the particle

$$D(q,t) = \frac{k_bT}{6\pi\eta r_h(q,t)} \tag{4.11}$$

If we consider coagulation at the early stage, where only doublets are formed, and if we assume that $a = r_h(q,t=0) = r_{h,1}$ we obtain

$$\frac{1}{r_h(q,t)} = \frac{N_1(t)I_1(q)/r_{h,1} + N_2(t)I_2(q)/r_{h,2}}{N_1(t)I_1(q) + N_2(t)I_2(q)} \tag{4.12}$$

where $r_{h,1}$ and $r_{h,2}$ are the hydrodynamic radii of the singlet and doublet, respectively. Eliminating the number of particles with eq. 4.4 and 4.5 and after differentiation, eq. 4.13 can be written as

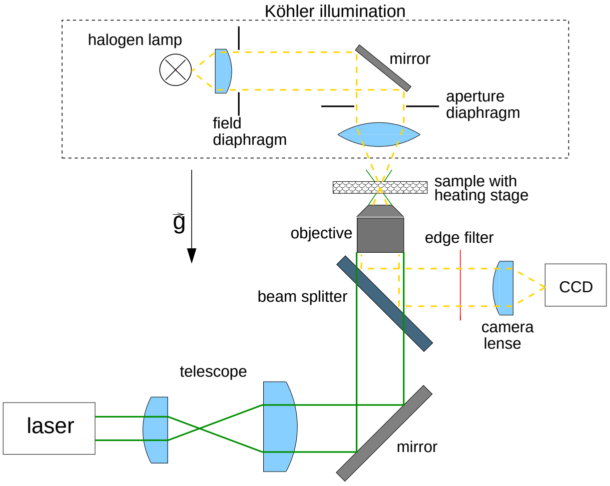

Figure 4.1: *Experimental setup for the laser controlled coagulation experiment.*

$$\frac{1}{r_h(q,t=0)}\frac{dr_h(q,t)}{dt} = 1 + \left(\frac{sin(2r_{h,1}q)}{2r_{h,1}q}+1\right)\left(1-\frac{r_{h,1}}{r_{h,2}}\right)k_{11}N_0t \tag{4.13}$$

where the doublet hydrodynamic radius is given by $r_{h,2} \approx 1.38r_{h,1}$ [249].

A combination of both static and dynamic light scattering from the equation 4.9 and 4.13 allows the determination of k_{11} independently on the form factor.

$$k_{11}N_0 = \frac{r_{h,2}}{r_{h,2}-r_{h,1}}\left(\frac{dr_h(q,t)/dt}{r_h(q,t=0)}\right) - \left(\frac{dI(q,t)/dt}{I(q,t=0)}\right) \tag{4.14}$$

4.1.3 Experimental

The core-shell particles with 5 $mol.\%$ crosslinker described in the chapter 2.1 were used in this chapter. The kinetics of the coagulation was investigated by dynamic light scattering (DLS) using a Peters ALV 5000 light scattering goniometer where the temperature was controlled with an accuracy of ± 0.1^oC as. The reversibility of coagulation was measured by DLS with a Zetaziser (Malvern model nanoZS) in back scattering at 173^o with a strict control of the temperature set by Peltier elements at ± 0.1^oC. Cryogenic electron microscopy was performed as described in section 2.1.2.

Scanning force microscopy (SFM) experiments were carried on at room temperature a Dimension 3100 microscope (Veeco Instruments Inc.). The SFM was operated in tapping mode using silicon tips with a spring constant of circa 40 Nm^{-1} and a resonance frequency ranging from 200 to 300 Hz. The scan rate was varied between 0.5 and 1.0 Hz to optimize the image quality. The samples have been prepared as followed: a drop 30 μL 0.1 $wt\%$ latex solution has been deposited on silicium wafer and dried at 60^oC. The same samples were then examined in a Zeiss Axiotech vario polarized optical microscope in reflection.

The experimental setup for the laser controlled self-assembly consists on an inverted microscope with a laser port (Olympus IX-71) (see fig. 4.1). Two mirrors mounted on magnet closed loop galvano scanners are situated in a conjugate confocal plane with a

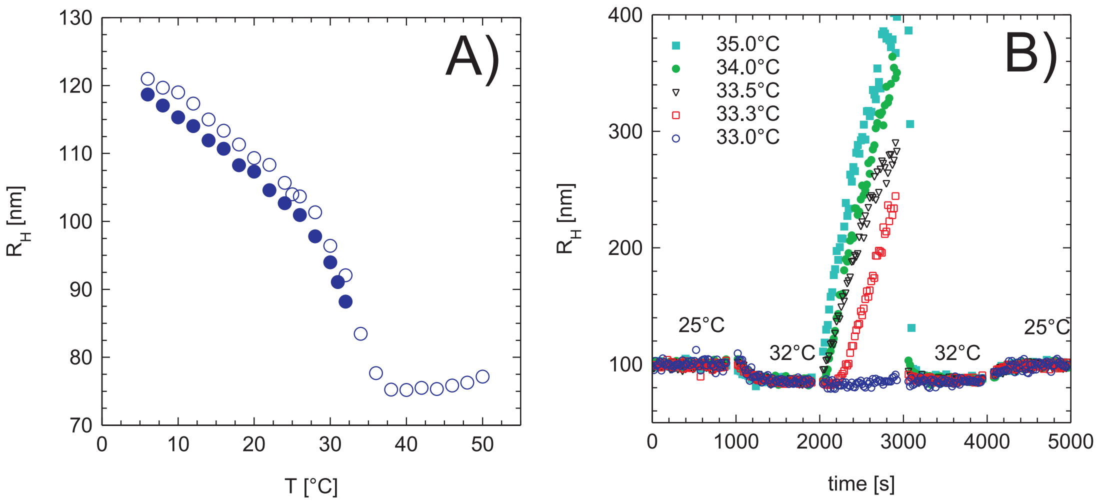

Figure 4.2: *A) Hydrodynamic radius of the core-shell latex versus temperature, as determined by dynamic light scattering. Without salt (hollow symbols) the PNIPAM network shrinks upon heating and remains stable even at high temperature. With addition of salt* (5.10^{-2} *M KCl) the particles coagulate above the Low Critical Solution Temperature (LCST) around* 33^oC. *B) Reversible coagulation of a* $2.5.10^{-3}$ *wt. % dispersion measured by dynamic light scattering with the Zetasizer as function of the time changing the temperature above and beyond the LCST.*

scanning point in the sample. The conjugate planes are formed with the help of two lenses telecentric system and an objective. The latter serves both for focusing of the laser beam and for observation of the sample. The laser (Coherent Verdi V-5, $\lambda = 532\ nm$) can be focused down to below 1 μm by the objective (Olympus LCACHN 40xPH) and typical power values are between 0.1 and 100 mW. The cell is mounted horizontally in a temperature-controlled xyz-stage. It has a gap thickness of 50 μm (Hellma 106-QS) . The sample is illuminated by a white light source (halogen lamp) with Köhler illumination [250]. The interference filter in front of the camera avoids damage to the CCD chip by focussed laser or fluorescent light [251]. The pictures are taken with a CCD camera (PCO pixelfly).

4.1.4 Results and Discussion

Reversible coagulation and stability

The structure and the swelling of the particles used in this section have been carefully investigated in chapter 2. The volume transition within the shell can easily be studied by dynamic light scattering (DLS) as described in the section 2.1.4. Figure 4.2 A) shows the dependence of the hydrodynamic radius R_H determined by DLS on the temperature. R_H decreases gradually with temperature until a sharp volume transition from swollen to unswollen states takes place, reaching a final collapsed size at a transition temperature around 38 ^oC. Without addition of salt this process is thermoreversible without any hysteresis.

Addition of 5.10^{-2} $mol.L^{-1}$ KCl leads to a slight shrinking of the particles. This phenomenon has been already investigated in recent studies [72]. The addition of salt screens the residual electrostatic interaction of the particles as shown by electrophoretic mobility measurements [72]. Hence, at higher temperatures the dispersions become unstable and aggregate [72]. Aggregation takes place between 32 and 33 ^oC, which is close to the LCST value determined from the dynamic light scattering analysis at 32.2^oC (see section 2.1.4). This asserts that the system interacts solely through steric interaction below the LCST, which makes it suitable as a model dispersion as demonstrate in the section crystallization (see chapter 2.3) and in the investigation of the dynamics in equilibrium and in flow (see chapter 3.2). In the dilute regime the reversibility of the aggregation process has been investigated by dynamic light scattering (see fig. 4.2b)). For this purpose the Zetasizer was used, where the temperature controlled by Peltier elements can be rapidly adjusted. In this experiment the system is first maintained 10 min at 25^oC, then heated first at 32^oC, and after at different temperatures from 33^oC to 35^oC. The cooling process was then recorded first at 32^oC and then at 25^oC. Whereas the system is stable at 25 and 32^oC it aggregates at 33^oC. The aggregation speed was found to increase with increasing temperature and the hydrodynamic radius varies between 150 and 400 nm within 10 min. Cooled down at 32^oC the hydrodynamic radius sharply decreased to reached the same value as before the aggregation occurred, which was also checked at 25^oC. In opposition to core-shell system with linear PNIPAM, which usually aggregates in a non reversible way [237], the aggregation was found to be totally reversible in this experiment. Above 32^oC the particles shrink which is accompanied by a diminution of steric interactions. This last ones are not able to compensate the van der Waals attractive interactions which results in the aggregation of the system. The dense cross-linked shell around the polystyrene particles prevents the interpenetration of the networks. Cooling down induces the reswelling of the particle and the onset of the strong osmotic pressure bringing the system to separate again. The response of the system is fast due to the size of the microgel. Moreover when the aggregation process is mostly limited to the diffusion of the particles in the fast mode regime [244] the dissolution of the aggregates was found to be much faster for the investigated concentrations.

The kinetics of the aggregation process has been investigated by DLS as function of the temperature for different concentrations in presence of 5.10^{-2} $molL^{-1}$ KCl. The treatment was performed following the method proposed by Holthof et al. [244]. Fig. 4.3 presents the evolution of the normalized hydrodynamic radius for the different temperatures measured at 90^o for a $1.25.10^{-3}$ $wt\%$ solution. The same experiment has been repeated for different concentrations ranging between $2.5.10^{-3}$ and $2.5.10^{-5}$ $wt\%$. The experiment was performed as follow: 2.3 mL of the latex solution was equilibrated at the wished temperature in the DLS for 20 min. Then 0.2 mL of a 0.625 $molL^{-1}$ KCl maintained at the same temperature were quickly added to set the salt concentration at 5.10^{-2} $molL^{-1}$. After homogenization the measurement was started. The countrate and the hydrodynamic radius resulting from the second cumulant analysis were then monitored as function of the time at a scattering angle of 90^o. The hydrodynamic radius was first found to decrease after the addition of the salt and then to increase following the aggregation process. The intensity was first constant and then increased. After few minutes the intensity decreased. This can be attributed to the form factor of the aggregates following the aggregation process [244, 247, 248]. Only the dynamic light scattering experiments have been treated in the following study considering the difficulty to analyze the static light scattering experiments. The initial hydrodynamic radius $R_{H,0}$ was considered at the

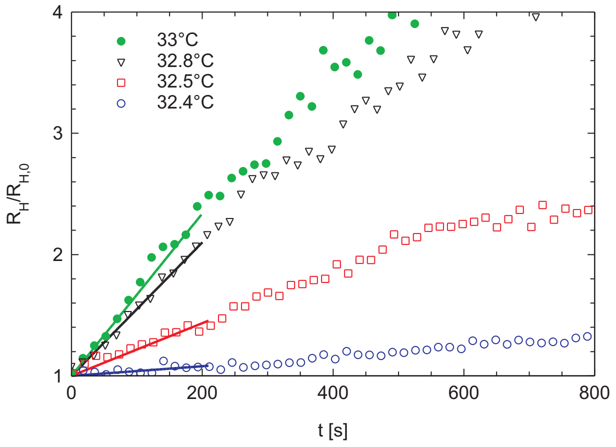

Figure 4.3: *Normalized hydrodynamic radius as a function of time measured by dynamic light scattering at 90º for a $1.3.10^{-3}$ wt% solution at different temperatures. The time has been rescaled to the beginning of the coagulation process. The full lines indicate the initial slope considered in the calculation of the coagulation rate constant (see eq. 4.13).*

beginning of the aggregation. The initial slope of the normalized hydrodynamic radius or intensity was used to calculate the coagulation rate constant k_{11} from the dynamic light scattering experiment using the equation 4.13. This method considers the form factor and the hydrodynamic radius of a doublet of hard spheres [244, 247, 248]. The assumption does not necessary fully hold in the case of the composite microgel which are rather compressible at least below 40^oC.

The different results are presented in the Fig. 4.4 in form of a stability ratio W which corresponds to the ratio between diffusion limited coagulation rate constant $2k_s$ according to the Smoluchsovski theory (see equation 4.6) and the experimental coagulation rate constant k_{11}. W becomes nearly constant after 34^oC with an average value of $3.8.10^{-18} \pm 0.4$ m^2s^{-1}. Holthof et al. investigated the influence of different salts on the coagulation rate measurement of sulfonate stabilized polystyrene particles [244]. They report a value of $4.3.10^{-18} \pm 0.4$ m^2s^{-1} for the fast coagulation rate constant using KCl as electrolyte [244]. Our experiment is in reasonable agreement with the ones reported particularly considering the complexity of our system and the experimental error mostly related to the sensitivity of k_{11} to the presence of trace amounts of impurities [244]. As a conclusion the coagulation of the composite particles can be controlled by the temperature and by the salt concentration. Steric interactions contribute mostly to the stability of the system. The fast coagulation rate constant is reached in the vicinity of the end of the volume transition in the polymeric shell after 34^oC.

In fig. 4.5 the hydrodynamic floc size is plotted as function of the time in a log-log representation for the longer times. Four sets of data are presented for a $1.3.10^{-3}$ $wt\%$ solution at 32.8^oC, 33^oC, 36^oC and 40^oC. For aggregates showing fractal structures, with fractal dimension d_f, the radius R of the flocs increases with the time t according to a power law [252], $R \propto t^z$ where $z = 1/d_f$. The fractal dimension can be calculated from the slope. For temperature higher than 32.8^oC the slope becomes constant and a mean value of $d_f = 2.05 \pm 0.03$ is obtained. This value is significantly greater than the value of 1.7-1.8, which is normally expected for particles undergoing diffusion-controlled

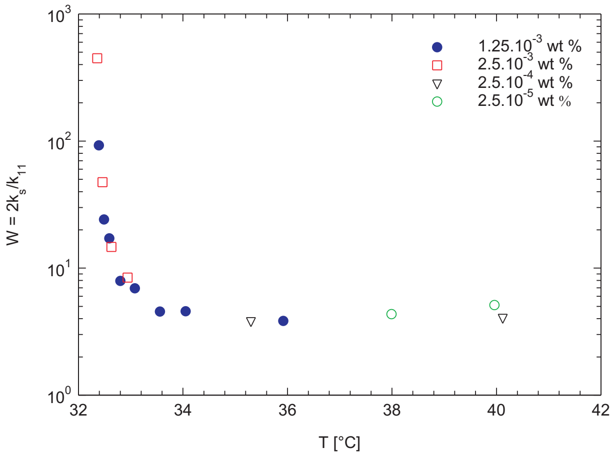

Figure 4.4: *Stability ratio ($W = 2k_s/k_{11}$) measured at different temperatures and concentrations. The experimental aggregation rate constant k_{11} has been determined by dynamic light scattering from the equation 4.13 whereas $2k_s$ is obtained from the expression derived by Smoluchsovski (see eq. 4.6) .*

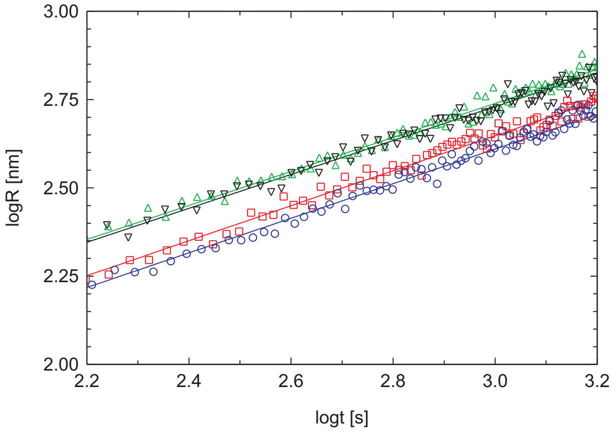

Figure 4.5: *Log-log plots of average floc radius (symbols) as function of time for the longer times for a 1.3.10^{-3} wt% solution at 32.8°C (circles), 33°C (squares), 36°C (down triangles) and 40°C (up triangles).*

irreversible aggregation. The same observation was done by Rasmusson et al. [236] on the temperature controlled flocculation of microgels particles with sodium chloride. The authors reported a fractal dimension of about 2.0 from the same kind of analysis below the LCST. They interpreted this value as an indication of a weak reversible flocculation model, which was supported by their estimation of the depth of the minimum in the interparticle pair potential. Nevertheless for similar PNIPAM based microgels Routh and Vincent reported that the d_f decreases from 2 around the CTF to 1.75 at temperature greatly higher than the CFT and than the LCST [253]. It is not the case for the core-shell particles were the fractal dimension remains equal to approximately 2.0 even at higher temperatures. This hints to the higher stability of the core-shell system under these experimental conditions. The reversibility of the coagulation presented in fig. 4.2 B) confirms this assumption.

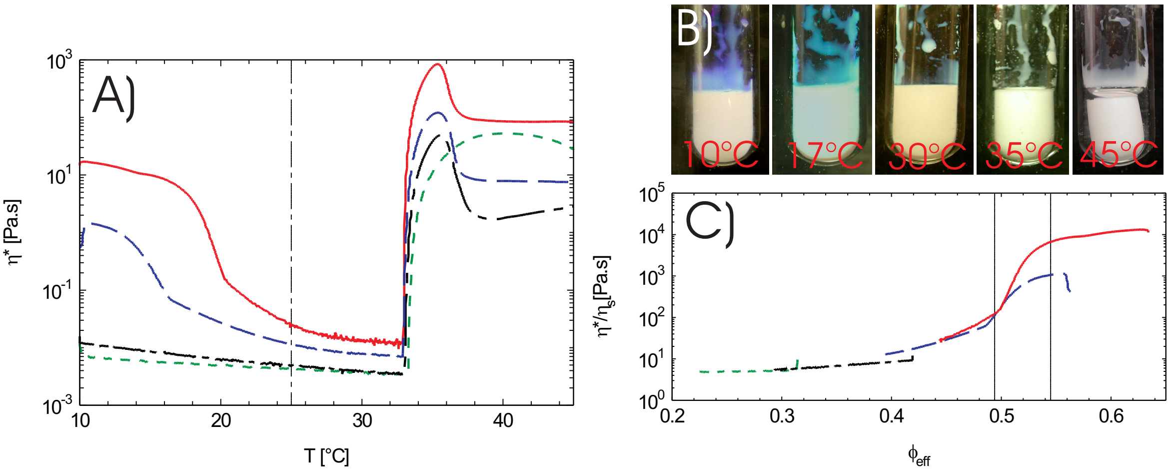

Figure 4.6: *A) Complex viscosity* η^* *as function of the temperature (10 min/*^oC*) for 1 Hz and 1 % for different concentrations with* $5.10^{-2}M$ *KCL: 12.1 wt % (full line), 10.75 wt % (dashed line), 8 wt % (dotted-dashed line) and 6 wt % (dotted line). B) Direct observation of the 12.1 wt % solution at different temperatures. C) Reduced viscosity* η^*/η_s *of the different concentrations as function of the effective volume fraction* ϕ_{eff} *for temperatures below* 25^oC*.*

From repulsive to attractive glasses

The influence of the attractive interactions has been then investigated for more concentrated solutions varying between 6 and 12 $wt\%$. The phase diagram of the PNIPAM microgels has been already intensively studied experimentally [7, 25–27, 30, 234], and is rather well understood theoretically [27]. The composite microgels were found to follow the same features. Indeed the crystallization and the glass transition of this system has been presented in the chapter 2.3 and 3.2. It was found that below 25^oC the system behaves like hard spheres. For effective volume fractions below 0.49 the solution are in the liquid state which is characterized by a smaller turbidity. Raising the temperature above 32^oC the system becomes white and opaque. After a longer time a phase separation occurs. For less concentrated systems this results immediately in the coagulation of the system. As an example fig. 4.6 B) displays the a 12.1 $wt\%$ solution maintained at different temperatures for half an hour. At 10^oC the solution is in the glassy state and the solution appears bluish. The corresponding volume fraction calculated for this temperature is equal to 0.63. At 17^oC which corresponds to an effective volume fraction of 0.54, particles rearrange into crystals. This is accompanied by the change of the solution color to green due to the Bragg's reflections. At 30^oC the solution is in the liquid state. The samples at 35 and 40^oC present the solution after the offset of the attractive interactions. The solution becomes white and opaque and remains relatively stable after 30 min, whereas the solution at 45^oC clearly shows a phase separation.

An appropriate method to follow the phase transition of the system is to measure the complex viscosity η^* of the system as function of the temperature (see fig. 4.6 A)) [25, 30]. A deformation of 1% and a frequency of 1 Hz have been used which remains in the linear viscoelastic domain at least for temperatures below 32^oC. Thus the transitions within the system can be measured without disturbing the system. The measurements were performed on four concentrations (6, 8, 10.75 and 12.1 $wt\%$) by increasing the

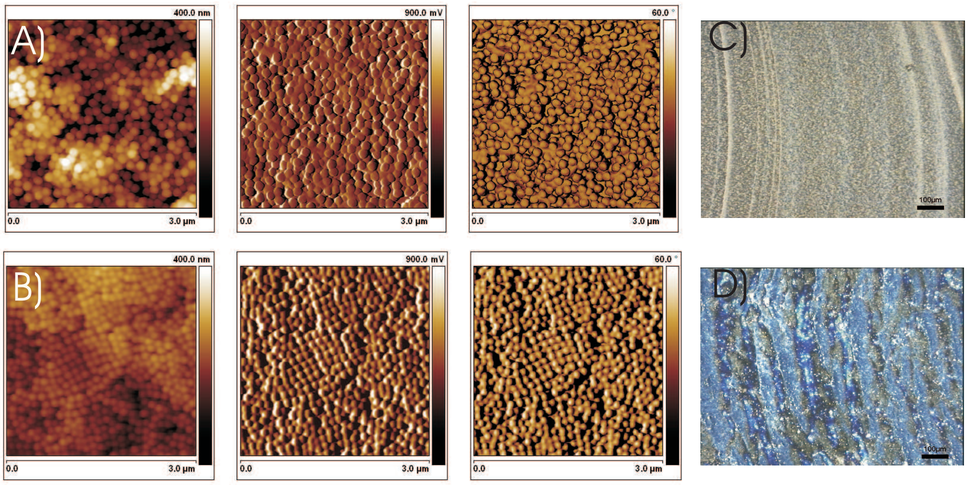

Figure 4.7: *A)C) SFM micrographs and optical microscopy of a 0.1 wt% composite microgels solution containing 5.10^{-2} $molL^{-1}$ KCl after dropcasting and drying at 60^oC on silicium wafer. C)D) SFM micrographs and polarized optical microscopy of a 0.1 wt% composite microgels solution without addition of salt after dropcasting and drying at 60^oC on silicium wafer.*

temperature at a rate of $0.175^oC/min$ after shearing 5 min at 100 s^{-1} to remove all the history of the sample. As shown in fig. 4.2 the hydrodynamic radius decreases with increasing temperatures. This leads to a decrease of the effective volume fraction ϕ_{eff} accompanied by a decrease of η^*. For a better understanding of this experiment when the system is purely repulsive, which corresponds to temperatures below 25^oC, the reduced viscosity η^*/η_s has been plotted as function of ϕ_{eff}. The calculation of ϕ_{eff} for this system described in the section 2.3.3 considers the evolution of the hydrodynamic radius as function of the temperature. η^*/η_s decreases slowly between 0.63 and 0.545, which corresponds to the crystalline and glassy state (solid state). In the liquid/crystalline coexistence domain between 0.494 and 0.545 the reduced complex viscosity decreases much faster. For effective volume below 0.494, corresponding to the melting of the crystallites, the solution is in the liquid state and the reduced viscosity decreases slower. After 33^oC a gelation process can be observed, where the complex viscosity increases for more than four decades within approximately 2^oC. A maximum was observed at 35.3^oC for 12.1, 10.7 and 8.0 $wt\%$ solutions, whereas the 6 $wt\%$ solution continuously increases. This can be related to a earlier phase separation for less concentrated systems. After this maximum the viscosity decreases again and reaches a plateau. This can be attributed to the phase separation of the system as shown on the photograph in fig. 4.6 B) at 45^oC. At this point the measurement can just be considered qualitatively as the assumption of an isotropic material is not respected anymore.

Scanning Force Microscopy and optical microscopy were performed in order to image the influence of the attractive interactions on the structure of a dense suspensions after drying on a silicium wafer at temperature above the LCST (see fig. 4.7). To this purpose 0.1 $wt\%$ solutions have been prepared, one without salt and one with 5.10^{-2} $molL^{-1}$ KCl. After drop casting on silicium wafer, the solution have been quickly dried at 60^oC in the oven. The salty solution shows a metastable structure and a rather rough surface arising from the attractive interactions. This was confirmed by the optical microscope equipped

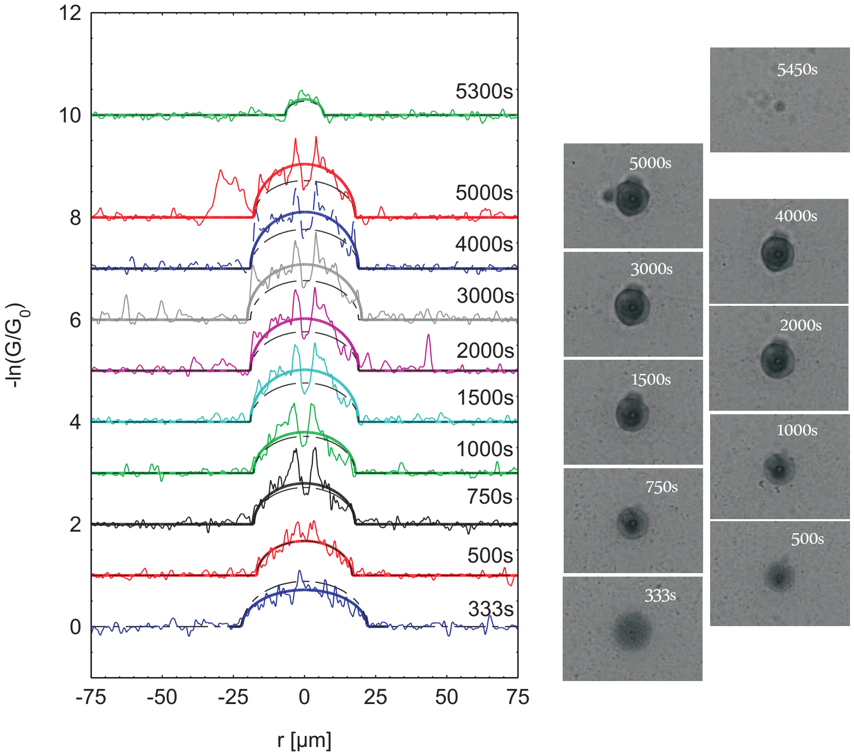

Figure 4.8: *Microaggregation of the composite microgels maintained at 34°C after different time of irradiation of a 10.75 wt.% latex solution with a laser power of 1W. The absorbance $A(r)$ is plotted as function of the radial distance. The dashed line presents the calculation from the absorbance calculated after the LCST at 35.4°C from eq. 4.15. The full lines present the best fit considering the adsorption of the aggregate as adjustable parameter.*

with a polarizer where no iridescence could be observed. Indeed at high temperatures the particles start to stick together, which prevents any ordering with increasing concentration. On the contrary without salt the solution is still stable at high temperatures. The electrostatic interactions prevent the particles to come into contact, and allow them to order during the drying process. Ordered domains and a more compact structure can then be observed by SFM, as already shown for similar systems by Hellweg and al. [59]. The ordering can be visualized by polarized optical microscopy in the form of photonic crystals.

Laser controlled micro-patterning

As shown by Lyon and coworkers, phase transition can be obtained on the microscale by focusing a green laser on a microgel solution doped with gold nanoparticles [11, 243]. A transition from the glassy to the crystalline state, and from crystal to liquid could thus be obtained by locally heating the sample.

We have performed similar experiments, however, with a temperature closely below the LCST in order to induce a transition from liquid to attractive glass. Due to a slight absorption of the sample at the laser wavelength of 532 *nm* we did not have to use to

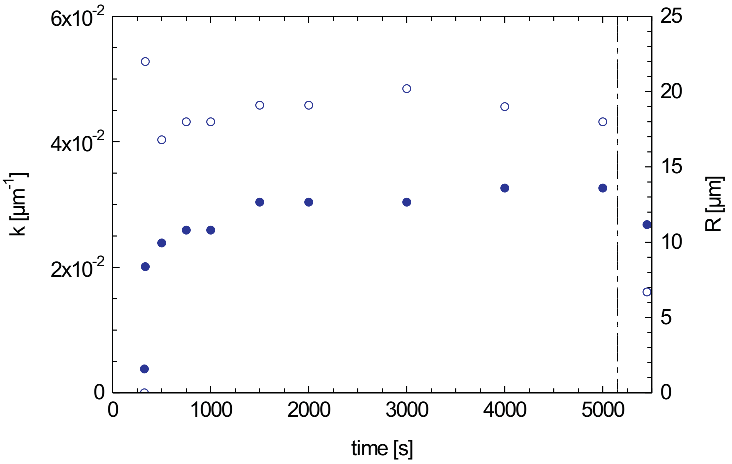

Figure 4.9: *Evolution of the radius in μm (hollow symbols) and of the absorption A (in μm^{-1}) (full symbols) of the aggregate obtained during the irradiation of a 10.75 wt% solution. Dashed line indicates the cessation of the irradiation.*

additional dye or gold doping. The reason for the optical absorption is still unclear and the absorption spectrum is difficult to measure by conventional UV-VIS-spectroscopy due to the strong scattering background. Nevertheless, as will be demonstrated below, we have been able to determine the absorption coefficient, at least at the laser wavelength, from the observed sample heating.

The whole experiment was performed with an inverted optical microscope equipped with a CCD camera and a laser port through which the beam of a diode-pumped frequency doubled solid state laser could be coupled in and focused onto the sample. A cell of $d = 50$ μm thickness was employed and the sample was equilibrated at a measured temperature of 32.2^oC for 30 min before starting the experiment. Since the temperature is measured at the sample holder, it does not represent the exact temperature within the liquid and needs to be corrected. The temperature offset was determined by slowly heating the sample with a rate of $0.013^oC/min$, thereby keeping the laser off and observing the overall optical transmittance. The collapse of the PNIPAM shell and the formation of aggregates are accompanied by a strong increase of the turbidity at a temperature of 33.0^oC (fig. 4.6). This temperature has been used as an internal reference in order to correct the temperature measured outside of the sample cell.

The laser power was adjusted to 100 mW and focused into the center of the cell. Immediately, a strong convective flow is observed. Because of the strong convection, the temperature of the illuminated volume increases only moderately. After approximately 300 s suddenly a stable cluster forms within the laser focus. The accompanying strong viscosity increase (see fig. 4.6 A)) leads to an immediate jamming and convection ceases. Without convection, heat is no longer efficiently transported away from the laser focus and a conductive state with a stationary temperature distribution develops within a few seconds. Due to the increased scattering, the aggregated region appears as a dark spot in the transmission micrograph.

Fig. 4.8 shows the time evolution of the aggregated spot over a longer time. Already from a visual inspection of the micrographs it is apparent that the spot quickly reaches its final diameter and that there is only a slight increase of contrast over time. At $t = 5100$

s the laser was switched off and the aggregates dissolved within a few seconds. Only a small 'bubble' at the position of the laser focus persisted even after five minutes. For a shorter exposure time of 500 s no irreversible change was observed and the whole spot dissolved instantaneously without leaving any residue. Possibly, the bubble is caused by a macroscopic phase separation as observed in fig. 4.6 at 45 ^oC, but also thermodiffusion [254–256] may play an important role.

Since above 33.0^oC the collapse of the PNIPAM-shell and the aggregate formation occur very rapidly, the dark region marks the volume where the stationary temperature profile exceeds this critical value, just reaching it at the perimeter.

Since the aggregation process is not expected to change the refractive index, we use the picture of a spherical object where the light passes through without refraction. Then, the attenuation of a beam traversing the sphere at a distance r from the center is given by

$$A(r) = -\ln\frac{G(r)}{G_0} = 2(\alpha^{agg} - \alpha^{liq})(R^2 - r^2)^{-1/2} \tag{4.15}$$

$G(r)$ and G_0 are the gray values measured at the position r and far away from the aggregate. α^{agg} and α^{liq} are the attenuation coefficients of the aggregate and the liquid state, respectively. Numerical values of the attenuation coefficients will be given later in the text.

In fig. 4.8 we have fitted semicircles to cross sections through the center of the spot in order to obtain some quantitative parameterization. The determined diameter and gray scale amplitude are plotted in fig. 4.9. As described above, the constant radius of $R \approx 20$ μm and the slight amplitude increase can clearly be seen.

The diameter $2R \approx 40$ μm is comparable to the cell thickness of $d = 50$ μm and renders the object, in a crude approximation, spherical. In a different context, we have performed detailed numerical calculations of the temperature profile created by a laser in a thin liquid layer sandwiched between two optical windows [255]. There, the isothermal surfaces resemble the shape of a football rather than a sphere. Such a detailed treatment is, however, beyond the scope of the present study.

Knowing the temperature $T_0 = 32.2^oC$ far away from the center and the temperature $T(R)$ on the surface of the 'sphere', we can use this information to determine the power $\dot{Q}$ absorbed from the laser beam and, hence, the optical absorption coefficient. Integration of the total heat flux through a sphere centered around the laser focus from infinity to R yields

$$\dot{Q} = 4\pi\kappa R\,(T(R) - T_0)\,. \tag{4.16}$$

We take $\kappa = 1.0$ $W(mK)^{-1}$ as average heat conductivity for the window material (Suprasil, $\kappa = 1.36$ $W(mK)^{-1}$) and water ($\kappa = 0.6$ $W(mK)^{-1}$). Inserting the numbers yields $\dot{Q} = 200$ μW.

In the weak absorption limit ($\alpha_a d \ll 1$) the absorbed power is related to the optical absorption coefficient α_a by

$$\dot{Q} = P_0\alpha_a d \tag{4.17}$$

$P_0 = 100\,mW$ is the laser power at the position of the sample. With above assumptions we obtain $\alpha_a = 4\times10^{-5}\ \mu m^{-1}$. In order to compare this to the scattering losses in the sample we measured the intensity transmitted through a homogeneously heated sample below and above the transition temperature. After normalization to the transmittance of an empty cuvette, we could derive white-light averaged attenuation coefficients of $\alpha^{liq} = 3.8 \times 10^{-3}$ μm^{-1} and $\alpha^{agg} = 2.4 \times 10^{-2}\ \mu m^{-1}$, respectively. Thus, even in the transparent non-aggregated state, the scattering losses are much larger than the absorption losses, and the attenuation coefficients $\alpha^{liq/agg} = \alpha_s^{liq/agg} + \alpha_a$ are almost identical to the scattering coefficients $\alpha_s^{liq/agg}$.

In order to obtain an estimation of the temperature inside the aggregate, we consider a sphere of radius $r < R$ that is centered around the laser focus. The total power $\dot{Q}_s$ absorbed within the sphere is proportional to the optical path length inside this sphere: $\dot{Q}_s = \dot{Q}\,2r/d \approx \dot{Q}\,r/R$. Assuming isotropic heat transport for simplicity, this power is conducted through the surface of the sphere according to

$$\frac{\dot{Q}r}{R} = -4\pi\kappa r^2 \delta_r T(r) \tag{4.18}$$

Integration of Eq. 4.18 yields a weak logarithmic temperature increase towards the center of the sphere:

$$T(r < R) = \frac{\dot{Q}}{4\pi\kappa R} \ln\frac{R}{r} + T(R) \tag{4.19}$$

Remember that $T(R)$ is the transition temperature that defines the surface of the aggregated sphere of radius R. If we insert $r = 1\ \mu m$ for the laser focus, we can estimate a temperature of 36.2^oC in the center.

An interesting question arises with respect to the observed convection prior to aggregate formation. Within above model the radiation force due to the scattering and absorption processes, $F_r = P_0\alpha^{liq}d/c$, with c being the speed of light, exceeds the buoyancy force acting on the heated volume by several orders of magnitude. Hence, the observed convection is not of thermal origin but rather caused by the radiation pressure of the laser beam.

4.1.5 Summary

Composite particles PS/PNIPAM reversibly swell and deswell as function of the temperature cause of their remaining electrostatic interaction. Adding $5.10^{-2}\ molL^{-1}$ KCl, the system is only sterically stabilized, which results in a reversible coagulation process after 32^oC. The reversibility of the process was attributed to the dense crosslinked shell avoiding the interpenetration of the network. The kinetics have been investigated by dynamic light scattering. The fast regime was reached after 34^oC which corresponds approximately to the end to the phase transition of the PNIPAM shell. Increasing the concentration over $8\ wt\%$, the onset of the attractive interaction was accompanied by an increase over 4 decades of the complex viscosity between 33 and 35^oC accompanied by a strong increase of the turbidity. This can be considered as a transition from liquid to attractive glass, for higher temperatures or a longer time the system presents a phase separation. Even after the phase separation the system can be easily redispersed after cooling down and agitation. This phenomenon can be controlled on the microscale by focusing a laser in the solution maintained close to the transition temperature. Stable aggregates of about 20 μm were obtained after 5 min irradiation. The aggregates quickly get dissolved after switching off the laser for exposure time lower than 15 min, for longer exposure times a small aggregate of the size of the focal volume remained. The origin of the convection was clarified. The temperature gradient after the formation of the aggregate could be successfully approximated in agreement with the experimental observations.

This chapter presents this system as the ideal candidate for the study of attractive glasses or for the local phase transition. Moreover its responsivity, its reversibility and the strong thickening above the transition temperature makes him suitable for number of future applications.

4.2 Electrostatic Dipole Formation by Association between Composite Microgels and Gold Nanoparticles

4.2.1 Introduction

Biological colloidal systems like virus and proteins often present a complex and defined structure with different functionalities which is the prerequisite of their specific and targeted applications. They can be considered in many cases as complex polyelectrolytes with a patchy structure, a mosaic of negative, positive or neutral areas.

Obtaining such structures synthetically is much more challenging. Complex geometries and defined clusters could be obtained via pickering emulsion and evaporation of the solvent as initiated by Pine et al. on micrometric particles [257] and on bidisperse colloids [258, 259]. This approach was recently extended by Wagner et al. to colloidal system [260]. Another strategy consists on the use of a template as shown recently by Xia et al. [261]. Nevertheless most of the time these clusters are not specifically functionalized and lack of long ranged interactions.

At the same time many efforts have been put into the synthesis and characterization of Janus systems [262–268], which present a versatile behavior and interesting properties as stabilizers for instance [265, 267]. Most of these new systems rely on their ambivalent nature, nevertheless it remains difficult to synthesized stable colloidal electrostatic dipoles.

Indeed mixing oppositely charged colloids most of the time leads to the destabilization of the system [269]. In this section we considered the association of cationic gold nanoparticles with thermosensitive anionic core-shell microgels polystyrene/poly(N-isopropylacrylamide) in the dilute regime.

For this purpose cationic gold nanoparticles were prepared as described formerly by Niidome, where the authors illustrated their application in the functional gene delivery and cancerous cells detection [270]. The use of inorganic nanoparticles for gene therapy such as amino-modified silica nanoparticles and cationic gold nanoparticles was recently reported [270–272]. The special character of these nanoparticles differs from that of organic gene carrier molecules, and they are expected to be a novel base material for the next generation of functional gene carriers. Gold nanoparticles have the advantages of easy preparation and the possibility of chemical modification of the surface. Moreover they have been found suitable in many applications spanning from catalysis and nano-electronic to treatment and detection of cancerogenic cells [273–275].

On the other hand composite microgels have been intensively studied and used in many applications from the protein adsorption [19, 20] to the use as template for the reduction of metal nano-particles [21–23]. Increasing the temperature these microgels swell and deswell in a continuous or discontinuous fashion following their degree of cross-linking as shown in the section 2.1.4. Not only the size of the particles can be controlled with the temperature, but also their potential. As presented in the former section, systems synthesized by seeded emulsion polymerization with an anionic initiator were found to present some electrostatic originated from remaining initiator fragments mostly based on the surface of the core particles. This ensures the stability of the system even after the volume phase transition. Thus the interaction potential can be adjusted controlling the size and salt concentration of the dispersion. In an excess of salt, the system is not stable anymore above the volume phase transition and was found to reversibly coagulate (see chapter 4.1).

The electrostatic stabilization related to the presence of negative charges combined with the steric stabilization ensured by the shell has already been used to absorb cationic gold nanorods [31, 32] and silver nanoparticles [276]. Whereas most of the studies focussed on the adsorption of small particles, we investigate the adsorption of larger particles (size ratio in the range 1 to 4). We present a simple way to successfully adsorbed the gold on our composite microgels to obtain anorganic/organic doublet or triplet keeping the dipolar character of the association. The influence on the size ratio and on the preparation is first discussed. Afterwards we investigate the correlation between both particles by turbidimetric titration, UV light spectroscopy, zeta potential measurement, dynamic light scattering and microscopic methods. The structure and stability of the association is considered at the end of this section.

4.2.2 Experimental

Materials

The system used in this study consists on a polystyrene core with a crosslinked PNIPAM shell containing 2.5 $mol\%$ BIS (KS2) (see section 2.1.2 for further details). The gold nanoparticles were synthesized following the recipe described by Niidome et al. [270]. The gold nanoparticles were prepared by $NaBH_4$ reduction of $HAuCl_4$ in the presence of 2-aminoethanethiol at a Au/$NaBH_4$/ 2-aminoethanethiol ratio of 56 : 0.1 : 85 (mol/mol/mol). Immediately after the $NaBH_4$ reduction, the solution was opaque and become a red wine color. The particles were then used for the association without further purification.

The sample were prepared by slow addition of the 0.28 gL^{-1} gold solution on dilute microgel solutions. The microgel concentration was either set at 0.2 gL^{-1} for the zeta potential and for the UV light spectrometry measurement, and between 4.10^{-2} and $2.6.10^{-2}$ gL^{-1} for the sample prepared by titration. The gold nanoparticles were stable for approximately two weeks, afterwards they started to get adsorbed at the surface of the glass container. Thus the characterization of the gold nanoparticles and the preparation of the different solutions were done with a fresh gold solution within one week.

Methods

Scanning force microscopy (SFM) experiments were carried on a commercial SFM (Model Dimension 3100, from Veeco Instruments Inc.) (see section 4.1.3 for further details). Field-emission scanning electron microscopy (FESEM) was performed using a LEO Gemini microscope equipped with a field emission cathode. The samples have been prepared by spin coating at 2000 rpm on silicium waver for the FESEM experiments, whereas the SFM samples have been prepared by dipcoating on mica. Transmission electron microscopy (TEM) and cryogenized Transmission Electron Microscopy (Cryo-TEM) have

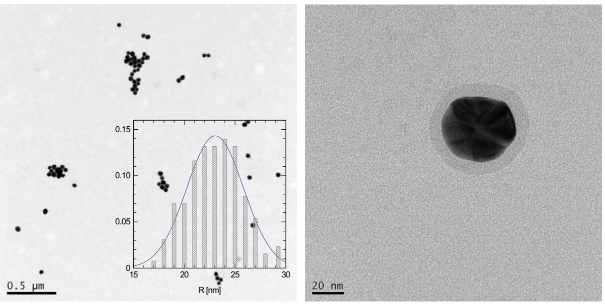

Figure 4.10: *Transmission electron micrograph of a 0.2 wt.aqueous suspension of cationic gold particles obtained by $NaBH_4$ reduction of $HAuCL_4$ in the presence of aminoethanethiol. The average radius of the gold particles was determined at 22.7 ± 3.7 nm (see histogram). The stabilization of the particles by the aminoethanethiol has been evidence by the presence of a 5-8 nm thin shell around the particles.*

been performed on a Zeiss EM922 EFTEM (Zeiss NTS GmbH, Oberkochen, Germany). A few microliters of the solution were placed on a bare copper TEM grid (Plano, 600 mesh) and the excess of liquid was removed with filter paper.

The turbidity measurement of the adsorption of the gold nanoparticles on the composite microgel was performed on a titrator (Titrando 809, Metrohm, Herisau, Switzerland) equipped with a turbidity sensor ($\lambda_0 = 523\ nm$, Spectrosense, Metrohm). The 0.28 gL^{-1} gold solution was added at a rate of 0.25 mL/min on a 16 mL 0.04 gL^{-1} microgel solution at 25^oC.

Dynamic light scattering was done using a Peters ALV 5000 light scattering goniometer. The samples were highly diluted ($c = 2.5.10^{-3}\ wt\%$) to prevent multiple scattering. The decay rate Γ was obtained from the second cumulant analysis for scattering angle from 30^o to 150^o with an increment of 10^o. The zeta potential was determined with the Zetasizer with a strict control of the temperature set by Peltier elements at ± 0.1^oC. For the direct observation of the stability of the different solutions, the sample were equilibrated 30 min in a thermostated chamber.

4.2.3 Results and Discussion

Cationic gold nanoparticles

Transmission electron microscopy has been performed on the cationic gold particles stabilized by the aminoethanethiol (see fig. 4.10). The radius of the particles calculated from the TEM has been determined at 22.7 ± 3.7 nm. The stabilization at the surface of the particle can be directly image, by a thin layer of between 5 and 8 nm around the particles. The thiol groups have a strong affinity with the gold, under neutral conditions the amine groups are hydrolyzed into $NH_3^{\oplus}$ providing the cationic character of the particles. Moreover the size of the corona respect to the size of the molecule supposes the organization in a multilayer. In order not to damage this layer the picture have been taken under low dose conditions. Nonetheless the surfactant is still very sensitive to the radiation and get easily damage after too long exposure. Thus it is not easy to determine its thickness precisely. The average hydrodynamic radius has been also measured by dynamic light

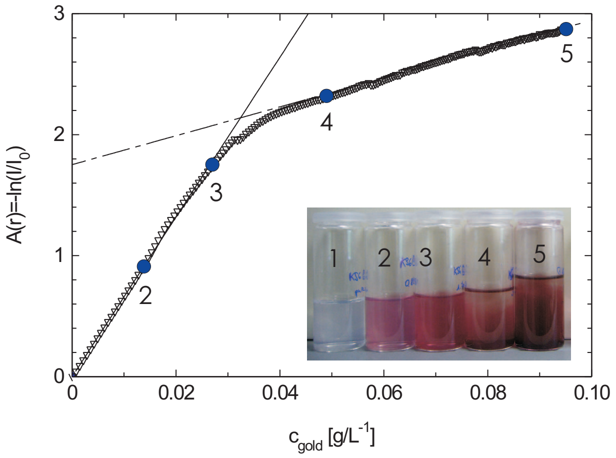

Figure 4.11: *Adsorption of the cationic gold nanoparticles on the composite microgels. The 0.28* gL^{-1} *gold solution was added to 16* mL 4.10^{-2} gL^{-1} *latex solution. The turbidity of the solution was measured during the addition process. The turbidity was expressed in term of the absorbance* $A = -ln(I/I_0)$ *where* I_0 *corresponds to the initial intensity of the latex solution (see text for further details). The different number corresponds to the different solutions prepared following the same procedure for different gold concentrations.*

scattering between 25 and 45^{o}C in back scattering at 173^o with the Zetasizer. No significant dependence on the temperature was observed. The average hydrodynamic radius obtained from the second cumulant analysis was found equal to 27 nm with a relative high polydispersity index (0.28). On the contrary of the evaluation of the size by TEM, the DLS is more sensitive to the presence of aggregates in the solution. Nonetheless this value presents a nice agreement with the TEM if we consider the contribution of the surfactant layer. The electrophoretic mobility has been expressed by the way of a Zeta potential calculated from the Smoluchowski approximation between 25 and 45^{o}C. This value was also not sensitive to the temperature and the average zeta potential was found equal to 27 mV. This confirms the cationic character of the particles, nevertheless this value is lower than the one reported in the literature for the same sample preparation (36.2 mV).

Turbidimetric titration

Whereas a slow addition of latex on an excess of gold particles directly leaded to the destabilization of the solution, it was possible to add gold on an excess of latex particles. For this reason the solutions have been prepared by slow addition of the gold on the core-shell particles. We performed turbidimetric titration in order to follow the association of the cationic gold nanoparticles onto the composite migrogels. To this purpose we prepared a 16 mL latex solution with an initial concentration of 4.10^{-2} gL^{-1} and added at a rate of 0.25 mL/min a 0.28 gL^{-1} gold solution. The turbidity of the solution was measured during the whole addition process. The gold solution as a strong absorption at 525 nm closed to the wavelength of the probe (523 nm). For this reason we used the transmitted intensity I_0 of the latex solution as reference to normalize the transmitted intensity I of the solution and we followed the evolution of the absorbance defined by $A = -ln(I/I_0)$ as function of the gold concentration (see fig. 4.11). As expected, the absorbance increases first

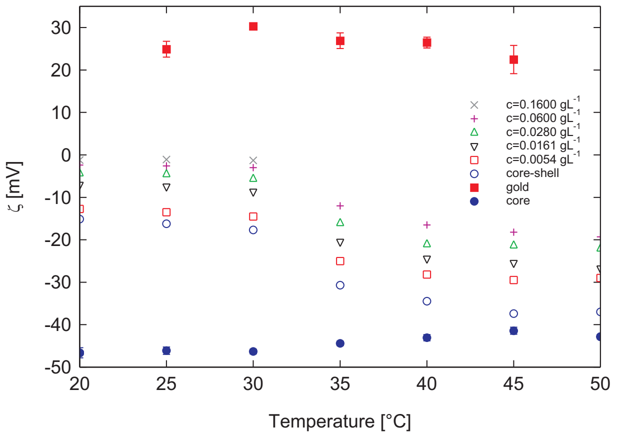

Figure 4.12: *Zeta potential of the gold nanoparticles (hollow squares), of core (full circles) and Core-Shell (full squares) particles calculated with the Smoluchowski approximation as function of the temperature with and without addition of gold for a 0.2* gL^{-1} *latex solution. Remaining electrostatic interactions explain the stability of the latex at high temperature. Addition of the gold solution is screening the Zeta potential (see the different concentrations in the legend). An aggregation can be observed for a concentration of 0.160* gL^{-1} *at* 35^oC.

linearly until a gold concentration of 0.03 gL^{-1}. After this concentration the absorbance still increased linearly but with a lower slope. This deviation was attributed to a fast aggregation process followed by the destabilization of the solution, to the shift of the plasmon maximum towards higher wavelengthes confirmed by a change of the solution from red to blue and to the presence of free gold particles. Four different samples were prepared following the same procedure (see fig. 4.11). For a concentration higher than 0.03 gL^{-1}, the solution were not stable and sedimented within an hour. We approximated the corresponding number ratio between the gold and latex particles considering the density of gold (19.3 gcm^{-3}), the size of the gold particles determined from the transmission electron microscopy and the number of composite microgel particle present in solution (as described in section 2.1.2). We found out a ratio of 1.05, which basically means that in average no more than one gold particles could be adsorbed onto the microgels under this conditions. This finding was confirmed after keeping the solutions for more than six months. Below this critical concentration the solution could be very easily redispersed and no gold was absorbed on the surface of the glass container which is a strong indication of the correlation of the gold with the microgel. On the contrary for higher concentrations the solutions could not be redispersed anymore after two months and a part of the gold was absorbed on the surface of the glass container, which confirmed the assumption of free gold particles in the solution.

Zeta potential measurement

We measured the Zeta potential of solution consisting on 0.2 gL^{-1} latex solution with different concentrations of gold varying between $5.4.10^{-3}$ and $1.6.10^{-1}$ gL^{-1}. The polystyrene core particles used for the synthesis of the composite microgels has been measured as well as the pure gold nanoparticles solution and the pure core-shell particles as function of the temperature (see fig. 4.12). The core particles presented a relatively constant zeta poten-

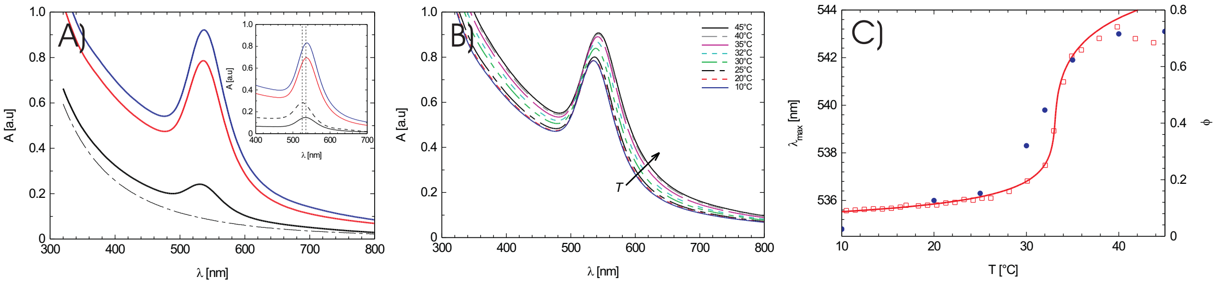

Figure 4.13: *A) UV visible extinction spectrum of a pure 0.2 gL^{-1} core-shell dispersion (dashed line) and of 0.2 gL^{-1} core-shell dispersion with 0.0280, 0.120 and 0.160 gL^{-1} cationic gold measured at 20°C. The inset display the adsorption of the pure gold (dashed line) and of the three solutions after substraction of the latex contribution. The position of the maximum adsorption λ_{max} of the gold shifts from 525 to 535 nm after adsorption on the composite microgels as shown by the thin dotted lines). B) Adsorption of a 0.02 gL^{-1} core-shell dispersion with 0.120 gL^{-1} cationic gold solution measured with increasing temperature. C) Maximum of the corresponding plasmon band of the gold nanopaticles as a function of temperature (full circles) compared with the evolution of polymer volume fraction of the PNIPAM shell (hollow squares). The full line presents the fit following the Flory-Rehner theory (see section 2.1.4).*

tial at -43 mV over all the temperature range. Concerning the pure core-shell dispersion below 32^{o}C, the electrophoretic mobility was found to around -15 mV, reflecting both the low surface charge density and the high friction coefficient of the swollen particles. However, a dramatic change in the electrophoretic mobility versus temperature was observed above the volume transition temperature. As expected, the absolute values of the zeta potential increased with increasing temperature due to the thermal sensitivity and shrinking of the PNIPAM shell to reach approximately the value of the core zeta potential at high temperatures as described by López-León et al. [72]. The temperature dependence of the zeta potential could be interpreted by the increase in the surface charge density due to the reduction in the particle size, the enhancement of the local charge concentration on the particle's surface and the frictional coefficient reduction of the collapsed particles. This effect could be directly visualized considering the strong buckling up of the shell at low temperature and the collapsed form of the shell at higher temperature as shown in figure 2.2.

Adding gold induced the decrease of the absolute value of the zeta potential to be almost equal to zero for a concentration for a concentration of 1.6.10^{-1} gL^{-1} below the volume phase transition. At higher temperatures the thermosensitivity was maintained with a transition around 32^oC. All the measurements presented a mononodale distribution of the zeta values confirming the association of the gold with the microgel. For the higher concentration corresponding to a number ratio of one gold for one microgel a coaggulation process has been observed for temperatures higher than 40^oC. The diminution of the zeta potential could be interpreted as an indication of the association of the oppositely charged particles leading first to the distortion of the charge distribution, to the increase in the size of the particles and to the increase of the surfactant concentration in the solution.

Thermoresponsive optical properties

The association of the gold nanoparticles with the microgels was investigated by UV-vis spectroscopy. The dependence of the plasmon adsorption on the size and temperature of colloidal gold particles in aqueous solution has been already discussed by Link et al. [277]. They found out that monodisperse 21.7 nm gold particles have a maximum adsorption at 521 nm. The maximum in the adsorption was observed at 525 nm for our solution which is in good results with the literature if we consider the influence of the polydispersity and of the surfactant adsorbed at the surface of the gold particles.

In order to confirm the association between the gold and the microgel we investigate the different solutions by UV-vis spectroscopy. The pure gold solution was first measured. A maximum in the adsorption was obtained at 525 nm which is common for particles in this size range [277]. On the contrary the latex solution did not present any specific adsorption. After adsorption of the gold (fig. 4.13 A)), the plasmon maximum measured after substraction of the latex contribution shifted from 525 to 535 nm (see inset fig. 4.13 A)).

The adsorption was measured for a 0.2 gL^-1 core-shell dispersion with 0.120 gL^{-1} cationic gold varying the temperature between 10 and 45^oC (see fig. 4.13 B)) as described recently [31, 32]. The adsorption was found to increase with the temperature followed by a red shift from 535 to 543 nm between 10 and 45^oC which have been attributed to the increase of the local refractive index upon microgel collapse for low surface coverage [31]. The position of the maximum λ_{max} has been monitored for the different temperature and compared to the variation of polymer volume fraction ϕ of the shell of uncoated composite microgel taken from the section 2.1.4 (see fig. 4.13 C)). The line displays the theoretical fit using the Flory-Rehner theory. The transition observed in the variation of λ_{max} follows the same feature as the transition in the PNIPAM network except that the transition occurs about 2^oC before the LCST of the pure microgel. This again corroborates the association of the gold with the microgels.

Colloidal stability and coagulation

The stability of the particles has been checked by adding different concentrations of gold on a 2 gL^{-1} microgels solution (see fig. 4.14). At 32^oC the system was perfectly stable. Increasing the temperature at 35^oC leads to the coagulation of the system for concentrations higher than 0.107 gL^{-1}. Dark red aggregates were observed, which quickly sediment letting a clear solution in comparison to the pure gold and core-shell solutions. This confirms the association of the gold with the microgel. The system recovered its original form 25^oC after a small redispersion. The understanding of the aggregation process is quite challenging. First we check if it was correlated to the ratio between gold and microgels. For the same particle ratio but after a dilution by ten the system did not aggregate. We considered the influence of the gold concentration for different latex concentration. For a concentration of 0.160 gL^{-1} the system was found to aggregate for 2 and 0.2 gL^{-1} latex concentrations. Thus, the concentration of gold and not the number ratio gold/microgels seems to be the determinant factor for the reversible coagulation at high temperatures. The composite microgels are sterically stabilized by the PNIPAM shell and electrostatically due to the use of an anionic initiator and to the remaining SDS providing from the

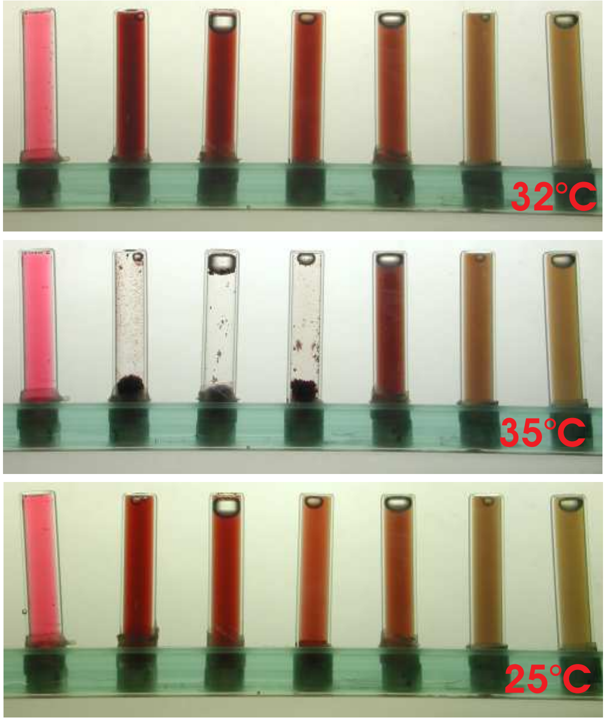

Figure 4.14: *Stability and coagulation of the solutions as function of the gold concentration and of the temperature. The different solutions are from the right to the left: a pure 2 gL^{-1} core-shell solution, a 2 gL^{-1} core-shell solution + 0.054, 0.107, 0.160, 0.220, 0.280 gL^{-1} gold respectively and a pure 0.2 gL^{-1} gold solution. All solutions were observed first at 32°C, then at 35 °C and 25°C. The samples at 25°C were redispersed to point out the reversibility of the coagulation process.*

synthesis. As discussed in the section 4.1, addition of salt reduces the Debye length and the stability of the system at high temperature. Fig. 4.12 clearly shows this effect in term of a diminution of the zeta potential with increasing gold concentration. It is still not fully understood how the gold nanoparticles and the remaining surfactant contribute to the screening of the electrostatics.

Electric dipoles formation and dynamic clusters

The former experiments clearly show the association of the gold with the microgels. Nevertheless the structure of the complex has not been investigated until now. For this purpose dynamic light scattering was performed on the solution 1, 2 and 3 of the fig. 4.11 at 23, 33 and 45^oC (see fig. 4.15). Solution 2 and 3 corresponds to a number ratio between gold and microgel of 0.47 and 0.93, whereas the solution 1 refers to the pure composite microgels. After addition at 23^oC of the gold the solution develops large cluster as can be directly see on the correlation function at 90^o (fig. 4.15 A)). In order to evaluate the size of the cluster the angular dependence of the decay rate Γ has been evaluated from the second cumulant analysis. Plotting Γ versus q^2 presents a linear dependence and thus allows the determination of the diffusion coefficient from the slope (fig. 4.15 B)). Fig. 4.15 C) displays the hydrodynamic radius derived from the Stoke-Einstein relation as for the different solutions at different temperature. Adding gold results in an increase of the

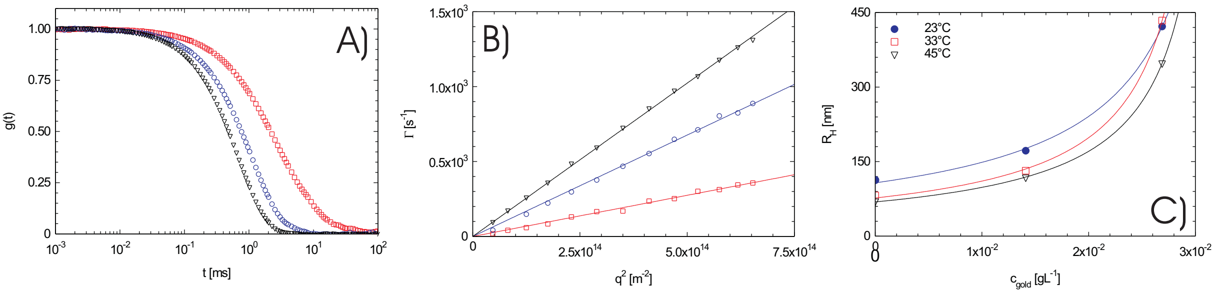

Figure 4.15: *A) normalized field autocorrelation function for the solution 1 (down triangles), 2 (circles) and 3 (squares) measured at 23°C. B) Dependence on* Γ *on the squared scattering vector* q^2 *for the three corresponding solutions. C) Hydrodynamic radius obtained from the linear extrapolation as function of the gold concentration at 23°C (full circles), 33°C (squares) and 45°C (down triangles). Lines are here to guide the eyes.*

hydrodynamic radius from 113 to 170 and 440 nm for number ratio of 0.47 (solution 2) and 0.93 (solution 3). Moreover the hydrodynamic radius was found to decrease with increasing temperature following the same feature as for the pure microgels as already observed from the former analysis (see fig. 4.15 C)). The addition of gold thus results in the formation of stable clusters. The different solutions have been investigated by transmission electron microscopy (TEM), scanning electron microscopy (SEM) and scanning force microscopy (SFM) (see fig. 4.16). The TEM micrograph presents the solution 4 freshly prepared absorbed on a carbon grid after blotting the liquid excess. SEM was performed on the solution 2. The two months old solution was spin coated on silicium wafer. SFM was performed on the solution 2 and 3 after dipcoating on mica. Both gold and microgels could be clearly distinguished from their difference in size and contrast. The different preparations have been considered to determine the influence of the substrate (neutral in the case of the carbone grid, negative for silicium and mica) during the drying process. The different microscopies and preparations lead to the same result, most of the gold is adsorbed on the composite microgels. The adsorption is not uniform and many free composite microgels are free whereas, some of them bear up to three gold nanoparticles. No cluster in term of a dense aggregates between many gold nanoparticles and composite microgels could be observed on the different micrographs. Fig. 4.16 D) focusses on one of this dipole. The SFM clearly images the PNIPAM shell adsorbed on the surface. The gold is strongly correlated to the shell as can be seen from the deformation of the shell. The dashed lines indicates the radius of the polystyrene core determined by TEM, and the radius of the core-shell and gold particles measured by DLS. These different methods gives a good estimation of the size of the different particles.

Following the different investigations we consider that the association of the two oppositely charged particles results in the formation of cluster composed of one microgels bearing one to three gold nanoparticles. In solution the strong asymmetry of the clusters results in the formation of electric dipoles which rearrange in solution in larger dynamic cluster as shown by the dynamic light scattering experiments.

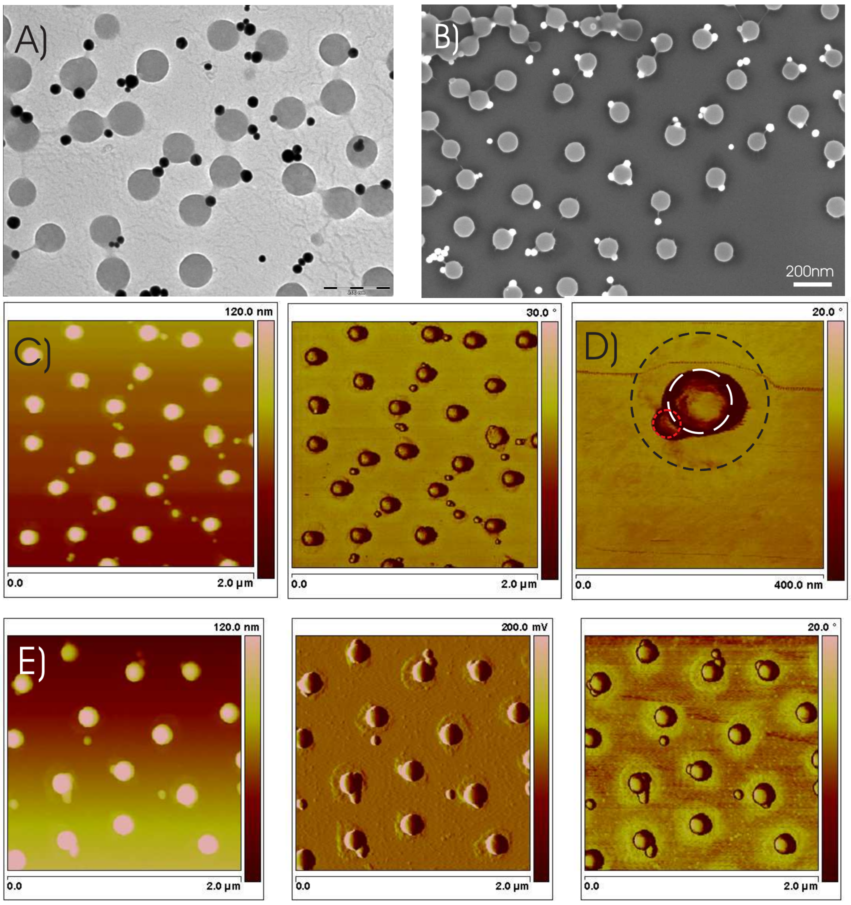

Figure 4.16: *A) TEM micrographs of the solution 4. B) SEM micrographs of the solution 3. C) SFM micrographs of the solution 2 (links: height, right: phase). D) Phase contrast of a single dipole. The long dashed line refers to the average radius of the core particles equal to 52 nm as determined by cryogenic electron microscopy (see section 2.2). The short dashed line gives presents the hydrodynamic radius of the pure core-shell particles determined by DLS at 23°C (=113 nm) and the dotted line the average radius of the gold nanoparticles determined by TEM (=22.7 nm). E) SFM micrographs of the solution 3 (links: height, middle:amplitude, right: phase)*

4.2.4 Summary

Cationic gold nanoparticles have been adsorbed on anionic core-shell particles consisting on a polystyrene core and a crosslinked PNIPAM shell. The difference of size between the small gold nanoparticles and the larger composite microgels allows the adsorption of in average up to one gold for one microgel. The correlation between the two particles was clearly demonstrated by zeta potential measurement, UV vis spectroscopy and dynamic light scattering. Moreover above the volume phase transition temperature of the microgels for a gold concentration higher than 0.160 gL^{-1} the system reversibly coagulate as shown by direct observation.

Whereas different microscopies corroborate the association of the gold with one microgel, and the formation of separated clusters, the dynamic light scattering demonstrates the formation of larger complex in solution. We attributed this effect to the formation of electric dipoles which dynamically reorganize into larger structures.

The association between cationic anorganic particles and anionic organic systems opens a new fascinating research field. First it is a new and simple way to obtain Janus particles based on electrostatic interactions, keeping the functionality of both components known for their applications in drug delivery and gene therapy. The thermosensitivity of the system can also be used to achieve a reversible coagulation process. Combined to the adsorption this approach could be applied in control released or in purification processes.

Moreover the formation of electric dipoles results into a dynamic reorganization of the system without application of external field which presents a nice system for the fundamental physics.

5 Synopsis

This thesis reports the synthesis, characterization, dynamics and association of thermosensitive core-shell particles. The particles consist of a solid core of poly(styrene) with a thin layer of poly(N-isopropylacrylamide) (PNIPAM) onto which a network of PNIPAM is affixed. The core-shell particles were synthesized in a two-step reaction. The core particles were obtained by emulsion polymerization and used as seed for the radical polymerization of the cross-linked shell. The degree of crosslinking of the PNIPAM shell effected by the crosslinker N, N'-methylenebisacrylamide (BIS) was varied leading between 1.25 and 5 $mol\%$. Immersed in water the shell of these particles is swollen at low temperatures. Raising the temperature above 32°C leads to a volume transition within the shell. Cryogenic transmission electron microscopy (Cryo-TEM), small angle X-ray scattering and dynamic light scattering have been used to investigate the structure and swelling of the particles. Cryo-TEM micrograph show directly inhomogeneities of the network. Moreover, a buckling of the shell from the core particle was observed. The buckling increases with decreasing degree of crosslinking. A comparison of the overall size of the particles determined by DLS and Cryo-TEM demonstrates that the hydrodynamic radius provides a valid measure for the size of the particles. The phase transition in the PNIPAM network has been for the first time directly imaged by cryo-TEM. The swelling behavior of the particles measured by DLS could be described successfully by the Flory-Rehner theory. It was shown that this model captures the main features of the volume transition within the core-shell particles including the dependence of the phase transition on the degree of crosslinking.

A quantitative method was developed to access to the structure of colloidal latex particles in dilute suspension at room temperature by cryo-TEM. The density profile derived from the cryo-TEM micrographs by image processing for the core and core-shell particles was compared to the results obtained by SAXS. Full agreement was found for the core particles. The discrepancy between the two methods in case of the core-shell particles was attributed to the buckling of the network affixed to the surface. The buckling, clearly visible in the cryo-TEM pictures is a dynamic phenomenon and the overall dimensions derived from cryo-TEM agree well with the hydrodynamic radius of the particles. The present analysis shows that SAXS is only sensitive to the average radial structure. This work demonstrates that cryo-TEM micrographs can be evaluated to yield quantitative information about the average and local structure of colloidal particles in solution.

The phase diagram and the colloidal crystallization of the different systems was investigated by a combination of direct observation, polarized optical microscopy and rheology. The effective volume fraction of the particles as derived from their hydrodynamic radius R_H provides the base for all further analysis. After addition of 5.10^{-2} M KCl all dispersions crystallize at volume fractions above 0.5. The resulting phase diagram is identical to the phase behavior of hard spheres for crosslinkings higher than 1.25 $mol.\%$. This demonstrates that the core-shell microgels can be treated as hard spheres up to volume fractions of at least 0.55. These suspensions can thus be used as model systems for rheological experiments.

We considered the dynamics of these model dense colloidal suspensions at the glass transition. For this purpose a new instrument and its calibration was first presented. The piezoelectric axial vibrator (PAV) is a squeeze-flow rheometer working at frequencies between 1 and 3000 Hz. It can be used to measure the storage modulus G' and the loss modulus G'' of complex fluids in this frequency range. Using polymer solutions with known G' and G'' it is shown that the PAV gives reliable mechanical spectra for frequencies between 10 and 3000 Hz. The measurements done with the PAV were combined with a conventional mechanical rheometer (10^{-3}-15 Hz) and a set of torsional resonators (13, 25, and 77 kHz) to obtain G' and G'' between 10^{-3} Hz and 77 kHz, which represents more than seven decades. It was demonstrated that the combination of the three devices gives the entire mechanical spectra without resort to the time-temperature superposition principle.

The connection between equilibrium stress fluctuations as measured in the frequency dependent linear shear moduli, $G'(\omega)$ and $G''(\omega)$, and the shear stresses under strong flow conditions far from equilibrium $\sigma(\dot{\gamma})$, viz. flow curves was investigated. Data over an extended range in shear rates and frequencies were compared to theoretical results from integrations through transients and mode coupling approaches developed by the Prof. Matthias Fuchs and his coworkers. The microscopic mechanisms and approximations inherent in the theoretical approaches were discussed. The connection between non-linear rheology and glass transition was clarified. For the first time in the rheology of suspensions we achieved a semi-quantitative description of both regimes with the same model. While the theoretical models describes the data taken in fluid states and the predominant elastic response of glass, a yet unaccounted dissipative mechanism was identified in glassy states. This proves that the dynamics of colloidal dispersions can be considered on a pure statistical matter. Nevertheless additional processes like ageing or hopping are still not fully described by the theory which implies further developments of the model in the future.

In presence of salt the composite core-shell particles reversibly aggregate above the Low Critical Solution Temperature (LCST) at 33°C. The kinetics of reversibility of the phenomenon was investigated by dynamic light scattering. As shown by the rheological measurements in the semi-dilute and concentrated regime the onset of the attractive interactions above the LCST leads to a strong thickening of the solution followed by a phase separation. This effect was applied locally for solutions, maintained close to LCST, after irradiation with a focused laser. Reversible micro-aggregates of a few μm diameter were obtained in the irradiated area under this local heating. The tunability and reversibility of the system presents a great advantage to extend the present investigations to the understanding of complex colloidal solutions in the attractive regime.

Cationic gold nano-particles were synthesized and adsorbed onto the anionic core-shell particles. The association between the two particles was investigated via turbidimetric titration, electrophoretic mobility measurements, UV-visible spectroscopy, dynamic light scattering, microscopy and the stability of the solution above the volume phase transition temperature was discussed. All analysis corroborate the correlation between the two particles. Whereas the microscopy demonstrates the formation of defined and separated electrostatic dipoles, the dynamic light scattering points out the reorganization in solution into larger structures.

The novelty of this dissertation relies on a detailed characterization of thermosensitive colloidal core-shell particles and a new way to quantitatively characterize colloids by cryo-TEM. As a main feature, the rheology of these colloidal suspensions and the understanding of the glass transition are discussed. The experimental results supported by the application and comprehension of the theory provide an extended contribution to the dynamics of colloidal dispersions. To conclude the investigation of the aggregation in various colloidal systems enlarges the scope of the thesis to new interesting applications.

6 Zusammenfassung

Im Rahmen dieser Arbeit wurden die Struktur, die Dynamik und die Assoziierung von thermoempfindlichen kolloidalen Partikeln untersucht. Die Teilchen bestehen aus einem Polystyrol-Kern mit einer dünnen Poly-N-Isopropylacrylamid-Schale (PNIPAM), die von einem PNIPAM-Netzwerk eingehüllt ist. Die Kern-Schale-Teilchen wurden in zwei Stufen hergestellt. Die Polystyrol-Kerne wurden durch Emulsionspolymerisierung synthetisiert und in einem zweiten Schritt als Saat für die radikalische Polymerisierung der vernetzten PNIPAM-Schale verwendet. Der Vernetzungsgrad der PNIPAM-Schale konnte durch verschiedene Konzentrationen von N, N'-Methylenbisacrylamid (BIS) zwischen 1.25 and 5 $mol\%$ eingestellt werden. Die Schale ist bei niedrigen Temperaturen in Wasser gequollen. Durch Erwärmen auf über 32^oC findet ein Volumenübergang der Schale statt. Die Struktur und das Quellungsverhalten wurden anhand von Kryo-Elektronenmikroskopie (Kryo-TEM), Röntgen-Kleinwinkelstreuung (SAXS) und dynamischer Lichtstreuung (DLS) untersucht. Durch Kryo-Elektronmikroskopie konnte die Unhomogenität des Netzwerkes *insitu* abgebildet werden. Weiter zeigte sich mit dieser Methode, dass die Schale nicht vollständig mit dem Kern verbunden war und Verformungen (Buckling) aufwies. Dieses Buckling wurde mit niedrigerem Vernetzungsgrad größer. Der Vergleich der Radien, die mit DLS und Kryo-TEM bestimmt wurden, zeigte, dass der hydrodynamische Radius eine zuverlässige Abschätzung der Größe der Teilchen lieferte. Der Volumenübergang in der PNIPAM-Schale wurde zum ersten Mal direkt mit Kryo-TEM beobachtet. Schließlich wurde die Flory-Rehner-Theorie erfolgreich auf die Untersuchungen des Quellungsverhaltens mit DLS angewendet. Es gelang mit diesem Model, den Volumenübergang der Kern-Schale-Teilchen und dessen Abhängigkeit vom Vernetzungsgrad zu beschreiben.

Zur strukturellen Charakterisierung der kolloidalen Teilchen wurde eine quantitative Analyse der Kryo-TEM-Aufnahmen entwickelt. Das Dichteprofil der homogenen und Kern-Schale-Teilchen wurde mit Kryo-TEM bestimmt und mit der SAXS-Analyse verglichen. Sehr gute Übereinstimmung wurde für die homogenen Teilchen gefunden. Der Unterschied zwischen beiden Methoden bei der Analyse der Kern-Schale-Teilchen wurde auf das Buckling des Netzwerks zurückgeführt, das in Kryo-TEM deutlich sichtbar war. Die mittleren Gesamtdimensionen, die mit Kryo-TEM bestimmt wurden, waren in sehr guter Übereinstimmung mit der Analyse aus der DLS. Mit SAXS konnte ebenfalls eine gemittelte radiale Struktur erhalten werden. In der Arbeit ist es gelungen, ein Verfahren zur erweiterten Analyse der Aufnahmen aus der Kryo-TEM zu entwickeln, mit dem direkt quantitative Informationen über die lokale und mittlere Struktur kolloidaler Partikel erhalten werden kann.

Das Phasendiagram und die Kristallisation der Kolloide wurden in direkter Beobachtung und mit optischer Polarisationsmikroskopie und Rheologie untersucht. Die Basis für die weiteren Analysen war der effektive Volumenbruch der Teilchen, der aus dem hydrodynamischen Radius R_H erhalten wurde. Alle Dispersionen mit einem effektiven Volumenbruch über 0.5 kristallisierten nach Zugabe von 5.10^{-2} M KCl. Das Phasendiagram, das für Vernetzungsgrade der Schale höher als 1.25 $mol.\%$ erhalten wurde, war vergleichbar mit dem Phasendiagram für harte Kugeln. Es zeigte sich, dass Kern-Schale-Mikrogele bei effektiven Volumenbrüchen unter 0.55 als harte Kugeln betrachtet werden können und als Modelsysteme für rheologische Experimente geeignet sind.

Die Dynamik solcher konzentrierter kolloidaler Suspensionen wurde in der Nähe des Glasübergangs untersucht. Dazu wurde ein neues Instrument, der piezoelektrische Axial-Vibrator (PAV), zum ersten Mal beschrieben und seine Kalibrierung durchgeführt. Der PAV ist ein "squeeze-flow"-Rheometer, das in einem Frequenzbereich zwischen 10 und 3000 Hz betrieben wird. Die Messung der Speicher- G' und Verlustmodule G'' für Polymerlösungen mit bekannten Werten für G' und G'' zeigte, dass der PAV eine zuverlässige Messung des mechanischen Spektrums erlaubt. Die Messungen mit dem PAV wurden durch Messungen mit einem konventionellen mechanischen Rheometer (10^{-3}-15 Hz) und Torsionsresonatoren (13, 25, and 77 kHz) ergänzt, um das vollständige Spektrum von G' and G'' zwischen 10^{-3} Hz and 77 kHz zu erhalten. Auf diese Weise konnte das vollständige mechanische Spektrum aus einer Kombination der drei Geräte erhalten werden, ohne von der Zeit-Temperatur-Überlagerung Gebrauch zu machen.

Der Zusammenhang zwischen den Gleichgewichtsfluktuationen der Scherspannung und den Scherspannungen unter starken Fließbedingungen fern vom Gleichgewicht wurde für die kolloidalen Lösungen durch rheologische Messungen untersucht. Dazu wurden die frequenzabhängigen linearen Schermodule und die Fließkurven für endliche Schergeschwindigkeiten über einen großen Bereich von Scherraten gemessen. Die experimentellen Daten wurden mit theoretischen Ergebnissen der Integration Through Transient (ITT)- und Mode Coupling Theory (MCT)-Ansätze verglichen. Der mikroskopische Mechanismus und die Näherungen der beiden Ansätze wurden diskutiert und ein Zusammenhang zwischen nicht-linearer Rheologie und Glasübergang hergestellt. Die Messungen der flüssigen Systeme und das überwiegend elastische Verhalten des Glases konnte mit den Modellen sehr gut semi-quantitativ beschrieben werden. Dabei wurde ein bislang nicht berücksichtigter dissipativer Mechanismus erkannt. Die detaillierte Diskussion der Ergebnisse ergab weiter, dass die Dynamik kolloidaler Dispersionen auf rein statistischer Weise ausreichend genau beschrieben werden kann. Prozesse wie Alterung und Hopping werden jedoch noch nicht vollständig theoretisch erfasst und erfordern eine Weiterentwicklung der Modelle.

Nach Salzzugabe findet über der kritischen Lösungstemperatur (LCST) eine reversible Aggregation statt. Die Kinetik und Reversibilität des Phänomens in verdünnter Lösung wurde mit DLS untersucht. Rheologische Messungen in halbverdünnten und konzentrierten Lösungen zeigten, dass die Aggregation der Kolloide über der kritischen Temperatur ein starkes Eindicken der Lösung verursachte, auf die eine Phasentrennung folgte. Dieser Effekt konnte in Systemen, die sich nahe der kritischen Temperatur befanden, auch lokal durch einen fokussierten Laserstrahl hervorgerufen werden. In der bestrahlten Fläche von wenigen Mikrometern Durchmesser formten sich durch den zusätzlichen Energieeintrag reversibel Mikroaggregate. Das System stellt eine interessante Möglichkeit dar, die Eigenschaften von komplexen kolloidalen Lösungen reversibel und berührungslos zu schalten.

Schließlich wurden kationische Gold-Nanopartikel synthetisiert und an die anionischen Kern-Schale-Teilchen adsorbiert. Die Assozierung wurde mit Trübungstitration, UV-Vis-Spektroskopie, DLS und mikroskopischen Methoden detailliert untersucht, um ein umfassendes Bild über dieses komplexe dynamische System zu erhalten. Während mikroskopisch die Bildung von definierten und getrennten Dipolen beobachtet wurde, weisen die DLS-Experimente auf eine Neuorganisierung zu größeren Strukturen hin.

Die Arbeit geht im Detail auf neue Charakterisierungsmöglichkeiten von kolloidalen Kern-Schale-Teilchen durch Kryo-TEM ein. Im Mittelpunkt stehen rheologische Messungen dieser Kolloidlösungen. Die Ergebnisse werden durch eine vertiefte Anwendung und Verständnis theoretischer Modelle unterstützt und erklärt und liefern erweiterte fundamentale Erkenntnisse über das Verhalten kolloidaler Dispersionen. Die Untersuchung der Aggregationsphänomene in verschiedenen kolloidalen Systemen weist schließlich auf interessante Anwendungen hin.

7 Abbreviations

BIS	*N,N'*-Methylenbisacrylamide
Cryo-TEM	Cryogenic Transmission Electron Microscopy
DLS	Dynamic Light Scattering
KCl	Potassium chloride
KS	Core-Shell
KPS	Potassium Perodoxisulfate
LCST	Lower Critical Solution Temperature
NIPAM	*N*-Isopropylacrylamide
PAV	Piezoelectric Axial Vibrator
PNIPAM	Poly-*N*-isopropylacrylamide
PS	Polystyrene
SEM	Scanning Electron Microscopy
SFM	Scanning Force Microscopy
TR	Torsional resonator
UF	Ultrafiltration
V2	Polystyrene core

Bibliography

[1] M. Shibayama, T. Tanaka, and C. Han, *J. Chem Phys.*, 1992, **97**, 6829.

[2] M. Shibayama and T. Tanaka, *Adv. Polym. Sci.*, 1993, **109**, 1.

[3] M. Shibayama, *Macromol. Chem. Phys.*, 1998, **199**, 1.

[4] T. Tanaka, E. Sato, Y. Hirakawo, S. Hirotsu, and J. Peetermans, *Phys. Rev. Lett.*, 1985, **55**, 2455.

[5] M. J. Snowden and B. J. Vincent, *J. Chem. Soc., Chem. Commun.*, 1992, p. 1103.

[6] K. Kratz and W. Eimer, *Ber. Bunsenges. Phys. Chem.*, 1998, **102**, 848.

[7] H. Senff and W. Richtering, *J. Chem. Phys.*, 1999, **111**, 1705.

[8] E. Daly and B. R. Saunders, *Phys. Chem. Chem. Phys.*, 2000, **2**, 3187.

[9] J. Gao and Z. B. Hu, *Langmuir*, 2002, **18**, 1360.

[10] C. D. Jones and L. A. Lyon, *Macromolecules*, 2003, **36**, 1988.

[11] L. A. Lyon, J. D. Debord, S. B. Debord, C. D. Jones, J. G. McGrath, and M. J. Serpe, *J. Phys. Chem. B*, 2004, **108**, 19099.

[12] B. R. Saunders, *Langmuir*, 2004, **20**, 3925.

[13] K. Makino, S. Yamamoto, K. Fujimoto, H. Kawaguchi, and H. Oshima, *J. Colloid Interf. Sci.*, 1994, **166**, 251.

[14] M. Okubo and H. Ahmad, *Colloid Polym. Sci.*, 1996, **274**, 274.

[15] L. Nabzar, D. Duracher, A. Elaïssari, G. Chauveteau, and C. Pichot, *Langmuir*, 1998, **14**, 5062.

[16] D. Duracher, F. Sauzedde, A. Elaïssari, A. Perrin, and C. Pichot, *Colloid Polym. Sci.*, 1998, **276**, 920.

[17] N. Dingenouts, C. Norhausen, and M. Ballauff, *Macromolecules*, 1998, **31**, 8912.

[18] T. Hellweg, C. D. Dewhurst, E. Bruckner, K. Kratz, and W. Eimer, *Colloid Polym. Sci.*, 2000, **278**, 972.

[19] T. Taniguchi, D. Duracher, T. Delair, A. Elaïssari, and C. Pichot, *Colloid Surface B*, 2003, **29**, 53.

[20] D. Duracher, R. Veyret, and A. Elaïssari, *Polym. Int.*, 2004, **53**, 618.

[21] D. Suzuki and H. Kawaguchi, *Langmuir*, 2005, **21**, 8175.

[22] Y. Lu, Y. Mei, M. Drechsler, and M. Ballauff, *Angew. Chem. Int. Edit.*, 2006, **45**, 813.

[23] Y. Lu, Y. Mei, M. Drechsler, and M. Ballauff, *J. Phys. Chem. B*, 2006, **10**, 10.

[24] S. Nayak and L. A. Lyon, *Angew. Chem. Int. Edit.*, 2005, **44**, 7686.

[25] Z. B. Hu and X. H. Xia, *Adv. Mater.*, 2004, **16**, 305.

[26] A. M. Alsayed, M. F. Islam, J. Zhang, P. J. Collings, and A. G. Yodh, *Science*, 2005, **309**, 1207.

[27] Z. B. Hu and G. Huang, *Angew. Chem. Int. Ed.*, 2003, **42**, 4799.

[28] J. Wu, B. Zhou, and Z. B. Hu, *Phys. Rev. Lett.*, 2003, **90**, 048304.

[29] J. Wu, G. Huang, and Z. B. Hu, *Macromolecules*, 2003, **36**, 440.

[30] J. Zhou, G. N. Wang, L. Zou, L. P. Tang, M. Marquez, and Z. B. Hu, *Biomacromolecules*, 2008, **9**, 142.

[31] M. Karg, I. Pastoriza-Santos, J. Perez-Juste, T. Hellweg, L. M. Liz-Marzan, and M. Luis, *Small*, 2007, **3**, 1222.

[32] M. Das, N. Sanson, D. Fava, and E. Kumacheva, *Langmuir*, 2007, **23**, 196.

[33] W. B. Russel, D. A. Saville, and W. R. Schowalter, *Colloidal Dispersions*, Cambridge University Press, New York, 1989.

[34] H. Senff and W. Richtering, *Langmuir*, 1999, **15**, 102.

[35] I. Deike, M. Ballauff, N. Willenbacher, and A. Weiss, 2001, **45**, 709.

[36] M. Stieger, J. S. Pedersen, P. Lindner, and W. Richtering, *Langmuir*, 2004, **20**, 7283.

[37] M. Stieger, P. Lindner, and W. Richtering, *J. Phys.:Condens. Matter*, 2004, **16**, S3861.

[38] S. Pyett and W. Richtering, *J. Chem. Phys.*, 2005, **122**, 034709.

[39] M. Fuchs and M. Ballauff, *J. Chem. Phys.*, 2005, **122**, 094707.

[40] M. Fuchs and M. Ballauff, *Colloids Surf. A.*, 2005, **270-271**, 232.

[41] M. Fuchs and M. E. Cates, *J. Phys.: Condens. Matter*, 2005, **17**, S1681.

[42] S. P. Meeker, W. C. K. Poon, and P. N. Pusey, *Phys. Rev. E*, 1997, **55**, 5718.

[43] Z. Cheng, J. Zhu, P. M. Chaikin, S. E. Phan, and W. B. Russel, *Phys. Rev. E*, 2002, **65**, 041405.

[44] M. Fuchs and M. E. Cates, *Phys. Rev. Lett.*, 2002, **89**, 248304.

[45] M. Fuchs, *Faraday Disc.*, 2003, **123**, 267.

[46] A. Suzuki and T. Tanaka, *Nature*, 1990, **346**, 345.

[47] F. Ilmain, T. Tanaka, and E. Kokufuta, *Nature*, 1991, **349**, 400.

[48] S. Hirotsu, *Phase Transitions*, 1994, **47**, 183.

[49] A. Fernández-Barbero, A. Fernandez-Nieves, I. Grillo, and E. López-Cabarcos, *Phys. Rev. E*, 2002, **66**, 051803.

[50] P. J. Flory, *Principles of Polymer Chemistry*, University Press, Ithaca, Cornell, 1953.

[51] M. L. Huggins, *J. Am. Chem. Soc.*, 1964, **86**, 3535.

[52] P. J. Flory, *Discuss. Faraday Soc.*, 1970, **49**, 7.

[53] V. A. Baulin and A. Halperin, *Macromol. Theor. Simul.*, 2003, **12**, 549.

[54] H. G. Schild and D. A. Tirrell, *J. Phys. Chem.*, 1990, **94**, 4352.

[55] N. C. Woodward, B. Z. Chowdhry, M. J. Snowden, S. A. Leharne, P. C. Griffiths, and A. L. Winnington, *Langmuir*, 2003, **19**, 3202.

[56] M. Andersson, S. Hietala, H. Tenhu, and S. L. Maunu, *Colloid. Polym. Sci.*, 2006, **284**, 1255.

[57] T. Hoare and R. Pelton, *J. Phys. Chem. B*, 2007, **111**, 1334.

[58] B. Sierra-Martin, Y. Choi, M. S. Romero-Cano, T. Cosgrove, B. Vincent, and A. Fernandez-Barbero, *Macromolecules*, 2005, **38**, 10782.

[59] T. Hellweg, C. D. Dewhurst, W. Eimer, and K. Kratz, *Langmuir*, 2004, **20**, 4330.

[60] M. Stieger, W. Richtering, J. S. Pedersen, and P. Linder, *J. Chem. Phys.*, 2004, **120**, 6197.

[61] I. Berndt, J. S. Pedersen, and W. Richtering, *J. Am. Chem. Soc.*, 2005, **127**, 9372.

[62] I. Berndt, J. S. Pedersen, and W. Richtering, *Ang. Chem. Inter. Ed.*, 2006, **45**, 1737.

[63] S. Seelenmeyer, I. Deike, S. Rosenfeldt, C. Norhausen, N. Dingenouts, M. Ballauff, and T. Narayanan, *J. Chem. Phys.*, 2001, **114**, 10471.

[64] N. Dingenouts, S. Seelenmeyer, I. Deike, S. Rosenfeldt, M. Ballauff, P. Lindner, and T. Narayanan, *Phys. Chem. Chem. Phys.*, 2001, **3**, 1169.

[65] M. Ballauff and Y. Lu, *Polymer*, 2007, **48**, 1815.

[66] A. Wittemann, M. Drechsler, Y. Talmon, and M. Ballauff, *J. Am. Chem. Soc.*, 2005, **127**, 9688.

[67] N. Dingenouts, J. Bolze, D. Pötschke, and M. Ballauff, *Adv. Polym. Sci.*, 1999, **144**, 1.

[68] B. E. Eichinder and P. J. Flory, *Trans. Faraday Soc.*, 1968, **64**, 2275.

[69] A. Boudaoud and S. Chaïeb, *Phys. Rev. E*, 2003, **68**, 021801.

[70] A. Weiss, M. Hartenstein, and N. D. M. Ballauff, *Colloid Polym. Sci.*, 1998, **276**, 794.

[71] I. Berndt, J. S. Pedersen, P. Linder, and W. Richtering, *Langmuir*, 2006, **22**, 459.

[72] T. López-León, J. L. Ortega-Vinuesa, D. Bastos-Gonzalez, and A. Elaïssari, *J. Phys. Chem. B*, 2006, **110**, 4629.

[73] X. Wu, R. H. Pelton, A. E. Hamielec, D. R. Woods, and W. McPhee, *Colloid Polym. Sci.*, 1994, **272**, 467.

[74] M. Adrian, J. Dubochet, J. Lepault, and A. W. McDowall, 1984, **308**, 32–36.

[75] K. A. Dryden, D. L. Farsetta, G. J. Wang, J. M. Keegan, B. N. Fields, T. S. Baker, and M. L. Nibert, *Virology*, 1998, **245**, 33.

[76] R. Grimm, H. Singh, R. Rachel, D. Typke, W. Zillig, and W. Baumeister, *Biophysical Journal*, 1998, **74**, 1031.

[77] C. L. Hill, T. F. Booth, B. V. Prasad, J. M. G. adn P. P. Mertens, G. C. Sutton, and D. I. Stuart, *Nat. Struct. Biol.*, 1999, **6**, 565.

[78] C. Toyoshima and N. Unwin, *Ultramicroscopy*, 1988, **25**, 279.

[79] C. Toyoshima and N. Unwin, *J. Cell Biol.*, 1991, **111**, 2623.

[80] J. P. Langmore and M. F. Smith, *Ultramicroscopy*, 1992, **46**, 349.

[81] M. F. Smith and J. P. Langmore, *J. Mol. Biol.*, 1992, **226**, 763.

[82] Y. Zheng, Y. Y. Won, F. S. Bates, H. T. Davis, L. E. Scriven, and Y. Talmon, *J. Chem. Phys. B*, 1999, **103**, 10331.

[83] Z. Li, E. Kesselman, Y. Talmon, M. A. Hillmyer, and T. P. Lodge, *Science*, 98, **2004**, 306.

[84] D. J. Pochan, Z. Y. Chen, H. G. Cui, K. Hales, K. Qi, and K. L. Wooley, *Science*, 2004, **306**, 94.

[85] M. Klookenburg, R. P. A. Dullens, W. K. Kegel, B. H. Erne, and A. Philipse, *Phys. Rev. Lett.*, 2006, **96**, 037203.

[86] R. Erhardt, M. F. Zhang, A. Böker, H. Zettl, C. Abetz, P. Frederik, G. Krausch, V. Abetz, and A. H. E. Müller, *J. Am. Chem. Soc.*, 2003, **125**, 3260.

[87] H. Cui, T. K. Hodgon, E. W. Kaler, L. Abegauz, D. Danino, M. Lubovsky, Y. Talmon, and D. J. Pochan, *Soft Matter*, 2007, **3**, 945.

[88] J. Bang, S. M. Jain, Z. B. Li, T. P. Lodge, J. S. Pedersen, E. Kesselman, and Y. Talmon, *Macromolecules*, 2006, **39**, 1199.

[89] A. Guinier and G. Fournier, *Small-Angle Xray Scattering*, Wiley, New York, 1955.

[90] J. C. Higgins and H. C. Benoit, *Polymers and Neutron Scattering*, Oxford University Press, New York, 1994.

[91] G. Molière, *Z. Naturforsch.*, 1948, **3a**, 78.

[92] A. V. Crewe and T. Groves, *J. Appl. Phys.*, 1974, **45**, 3662.

[93] L. Reimer, *Transmission Electron Microscopy: Physics of Image Formation and Microanalysis, 4th ed.*, Springer series in optical sciences, Berlin, Heidelberg, New York, 1997.

[94] T. G. Mason and M. Y. Lin, *Phys. Rev. E*, 2005, **71**, 040801.

[95] H. Ericksonand and A. Klug, *Phil. Trans. Roy. Soc. (London)*, 1971, **261**, 105.

[96] J. Frank, *Optik*, 1973, **38**, 519.

[97] D. W. Walker, *Adv. Phys.*, 1971, **20**, 257.

[98] J. P. Desclaux, *Comput. Phys. Commun.*, 1977, **9**, 31.

[99] J. P. Desclaux, *Comput. Phys. Commun.*, 1977, **13**, 7.

[100] J. N. Furness and I. E. McCarthy, *J. Phys. B: At. Mol. Opt. Phys.*, 1973, **6**, 2280.

[101] F. Salvat and R. Mayol, *Comput. Phys. Commun.*, 1993, **74**, 358.

[102] A. Jablonski, F. Salvat, and C. J. Powell, *J. Phys. Chem. Ref. Data*, 2004, **33**, 409.

[103] A. Jablonski, F. Salvat, and C. J. Powell, *NIST Electron Elastic-Scattering Cross-Section Database, Version 3.1*, National Institute of Standards and Technology, Gaithersburg, 2003.

[104] J. Wall, M. Isaacson, and J. P. Langmore, *Optik*, 1974, **39**, 359.

[105] C. J. Powell, A. Jablonski, and F. Salvat, *Surf. Interface Anal.*, 2005, **37**, 1068.

[106] M. G. Sceats and S. A. Rice, *Water, Vol. 7*, Plenum Press, New York, 1982.

[107] F. Sciortino, P. H. Poole, U. Essmann, and H. E. Stanley, *Phys. Rev. E*, 1997, **55**, 727.

[108] R. Grimm, D. Typke, M. Barmann, and W. Baumeister, *Ultramicroscopy*, 1996, **63**, 169.

[109] T. Tanaka, S. T. Sun, Y. Hirokawa, S. Katayama, J. Kucera, Y. Hirose, and T. Amiya, *Nature*, 1987, **325**, 796.

[110] T. Hwa and M. Kardar, *Phys. Rev. Lett.*, 1988, **61**, 106.

[111] A. Onuki, *Phys. Rev. A*, 1989, **39**, 5932.

[112] N. Suematsu and K. S. K. Kawasaki, *Phys. Rev. A*, 1990, **41**, 5751.

[113] H. Tanaka, H. Tomita, A. Takatsu, T. Hayashi, and T. Nishi, *Phys. Rev. Lett.*, 1992, **68**, 2794.

[114] T. Moraa and A. Boudaoud, *Eur. Phys. J. E*, 2006, **20**, 119.

[115] S. Bolisetty, M. Hoffmann, S. Lekkala, T. Hellweg, M. Ballauff, and L. Harnau, *Macromolecules*, 2008, p. (submitted).

[116] P. N. Pusey, *In Liquid, Freezing, and the Glass Transition*, J. P. Hansen, D. Levesque and J. Zinn-Justin, North-Holland, Amsterdam, 1991.

[117] P. N. Pusey and W. van Megen, *Nature*, 1986, **320**, 340.

[118] V. J. Anderson and H. N. W. Lekkerkerker, *Nature*, 2002, **416**, 811.

[119] N. M. Dixit and C. F. Zukoski, *Phys. Rev. E*, 2002, **66**, 051602.

[120] U. Gasser, E. R. Weeks, A. Schofield, P. N. Pusey, and D. A. Weitz, *Science*, 2001, **292**, 258.

[121] W. van Megen and S. M. Underwood, *Nature*, 1993, **362**, 616.

[122] J. L. Harland, S. I. Henderson, S. M. Underwood, and W. van Megen, *Phys. Rev. Lett.*, 1995, **75**, 3572.

[123] J. L. Harland and W. van Megen, *Phys. Rev. E*, 1997, **55**, 3054.

[124] T. Palberg, *J. Phys.: Condens. Matter*, 1999, **11**, R233.

[125] T. Okubo, A. Tsuchida, and T. Kato, *Colloid Polym. Sci.*, 1999, **277**, 191.

[126] E. R. Weeks, J. C. Crocker, A. C. Levitt, A. Schofield, and D. A. Weitz, *Science*, **287**, 62.

[127] Z. Cheng, J. X. Zhu, W. B. Russel, and P. M. Chaikin, *Phys. Rev. Lett.*, 2000, **85**, 1460.

[128] J. Liu, D. A. Weitz, and B. J. Ackerson, *Phys. Rev. E*, 1993, **48**, 1106.

[129] W. B. Russel, *Phase Transit.*, 1990, **21**, 27.

[130] B. J. Ackerson and K. Schatzel, *Phys. Rev. E*, 1995, **52**, 6448.

[131] W. B. Russel, P. M. Chaikin, J. X. Zhu, W. V. Meyer, and R. B. Rogers, *Langmuir*, 1997, **13**, 3871.

[132] J. Zhu, M. Li, R. B. Rogers, W. V. Meyer, R. H. Ottewill, W. B. Russel, and P. M. Chaikin, *Nature*, 1997, **387**, 883.

[133] Z. Cheng, P. M. Chaikin, J. Zhu, W. B. Russel, and W. V. Meyer, *Phys. Rev. Lett.*, 2002, **88**, 015501.

[134] S. Tang, Z. Hu, Z. Cheng, and J. Wu, *Langmuir*, 2004, **20**, 8858.

[135] P. Wette, H. J. Schöpe, and T. Palberg, *J. Chem. Phys.*, 2005, **123**, 174902.

[136] Z. Cheng, J. Zhu, W. B. Russel, W. V. Meyer, and P. M. Chaikin, *Appl. Opt.*, 2001, **40**, 4148.

[137] Y. N. Xia, B. Gates, Y. Yin, and Y. Lu, *Adv. Mater.*, 2000, **12**, 693.

[138] Y. Chen, W. T. Ford, N. F. Materer, and D. Teeters, *Chem. Mater.*, 2001, **13**, 2697.

[139] Y. Takeoka and M. Watanabe, *Adv. Mater.*, 2003, **15**, 199.

[140] Y. J. Lee and P. V. Braun, *Adv. Mater.*, 2003, **15**, 563.

[141] J. M. Weissman, H. B. Sunkara, A. S. Tse, and S. A. Asher, *Science*, 1996, **274**, 959.

[142] J. H. Holtz and S. A. Asher, *Nature*, 1997, **389**, 829.

[143] C. E. Reese, A. V. Mikhonin, M. Kamenjicki, A. Tikhonov, and S. A. Asher, *J. Am. Chem. Soc.*, 2004, **126**, 1493.

[144] J. D. Debord and L. A. Lyon, *J. Phys. Chem. B*, 2000, **104**, 6327.

[145] L. A. L. S. B. Debord, *J. Phys. Chem. B*, 2003, **107**, 2927.

[146] Z. B. Hu, X. H. Lu, J. Gao, and C. J. Wang, *Adv. Mater.*, 2000, **12**, 1173.

[147] Z. B. Hu, X. H. Lu, and J. Gao, *Adv. Mater.*, 2001, **13**, 1708.

[148] J. Gao and Z. B. Hu, *Langmuir*, 2002, **18**, 1360.

[149] T. Okubo, H. Hase, H. Kimura, and E. Kokufuta, *Langmuir*, 2002, **18**, 6783.

[150] A. D. Bruce, N. B. Wilding, and G. J. Ackland, *Phys. Rev. Lett.*, 1997, **79**, 3002.

[151] A. Inhof, A. van Blaaderen, and J. K. G. Dhont, *Langmuir*, 1994, **10**, 3477.

[152] S. E. Paulin, B. J. Ackerson, and M. S. Wolfe, *J. Coll. Int. Sci.*, 1996, **178**, 251.

[153] W. G. Hoove, S. G. Gray, and K. W. Johnson, *J. Chem. Phys.*, 1971, **55**, 1128.

[154] S. E. Paulin and B. J. Ackerson, *Phys. Rev. Lett.*, 1990, **64**, 2663.

[155] P. N. Pusey and W. van Megen, *Phys. Rev. Lett.*, 1987, **59**, 2083.

[156] W. Megen and P. N. Pusey, *Phys. Rev. A*, 1991, **43**, 5429.

[157] J. D. Ferry, *Viscoelastic Properties of Polymers, 3rd ed.*, Wiley, New York, 1980.

[158] R. G. Larson, *The Structure and Rheology of Complex Fluids*, Oxford University Press, New York, 1999.

[159] G. W. Fritz, W. Pechhold, N. Willenbacher, and J. W. Norman, *J. Rheol.*, 2003, **47**, 303.

[160] T. G. Mason and D. A. Weitz, *Phys. Rev. Lett.*, 1995, **74**, 1250.

[161] G. M. T and D. A. Weitz, *Phys. Rev. Lett.*, 1995, **75**, 2770.

[162] W. Götze, *Liquids, Freezing and Glass Transition*, J. P. Hansen, D. Levesque, and J. Zinn-Justin, North-Holland, Amsterdam, 1991.

[163] W. Goetze and L. Sjoegren, *Phys. Rev. A*, 1991, **43**, 5442.

[164] W. Götze and L. Sjögren, *Rep. Prog. Phys.*, 1992, **55**, 241.

[165] W. J. Goetze, *J. Phys.: Condens. Matter*, 1999, **11**, A1.

[166] I. S. Sohn and R. Rajagopalan, *J. Rheol.*, 2004, **48**, 117.

[167] J. C. V. der Werff, C. G. D. Kruif, C. Blom, and J. Mellema, *Phys. Rev. A*, 1989, **39**, 795.

[168] A. I. Romoscanu, M. B. Sayir, K. Häusler, and C. Servais, *Meas. Sci. Technol.*, 2003, **14**, 451.

[169] T. Shikata and D. S. Pearson, *J. Rheol.*, 1994, **38**, 601.

[170] T. G. Mason, H. Gang, and D. A. Weitz, *J. Mol. Struct.*, 1996, **383**, 81.

[171] T. G. Mason, *Curr. Opin. Colloid Interface Sci.*, 1999, **4**, 231.

[172] G. H. Koenderink, H. Zhang, D. G. Aarts, M. Lettinga, P. Pavlik, P. Albert, and G. Naegele, *Faraday Discuss.*, 2003, **123**, 335.

[173] R. Bartolino and G. Durand, *Phys. Rev. Lett.*, **39**, 1346.

[174] M. Cagnon and G. Durand, *Phys. Rev. Lett.*, 1980, **45**, 1418.

[175] M. Cagnon and G. Durand, *J. Phys. Lett.(France)*, 1981, **42**, 451.

[176] L. Kirschenmann and W. Pechhold, *Rheol. Acta*, 2002, **41**, 362.

[177] L. Kirschenmann, *Ph.D. thesis, Institut für Dynamische Materialprüfung (IdM), University of Ulm*, 2003.

[178] R. B. Bird, R. C. Armstrong, and O. Hassager, *Dynamic of Polymeric Liquids, 2nd ed.*, Wiley, New York, 1987.

[179] H. M. Laun, M. Rady, and O. Hassager, *J. Non-Newtonian Fluid Mech.*, 1999, **81**, 1.

[180] J. D'Ans and J. E. Lax, *Taschenbuch für Chemiker und Physiker, Band 1*, Springer, Heidelberg, 1967.

[181] W. W. Graessley, *The Entanglement Concept in Polymer Rheology, Adv. in Polymer Science Vol. 16*, Springer, New York, 1974.

[182] M. Baumgärtel and N. Willenbacher, *Rheol. Acta*, 1996, **35**, 168.

[183] M. L. Williams, R. F. Landel, and J. D. Ferry, *J. Am. Chem. Soc.*, 1955, **77**, 3701.

[184] T. M. Stokich, D. R. Radtke, C. C. White, and J. L. Schrag, *J. Rheol.*, 1994, **38**, 1195.

[185] R. H. C. L. Leibler, M. Rubinstein, *Macromolecules*, 1991, **24**, 4701.

[186] J. Desbrières, M. Hirrien, and S. B. Ross-Murphy, *Polymer*, 1999, **41**, 2451.

[187] R. A. Lionberger and W. B. Russel, *J. Rheol.*, 1994, **38**, 1885.

[188] I. M. D. Schepper, H. E. Smorenburg, and E. G. D. Cohen, *Phys. Rev. Lett.*, 1993, **70**, 2178.

[189] N. Aksel and L. Heymann, *Springer Handbook of Experimental Fluid Mechanics, Chapter 9.3: Rheology of Suspensions and Emulsions*, Springer, 2007.

[190] W. van Megen and S. M. Underwood, *Phys. Rev. Lett.*, 1993, **70**, 2766.

[191] W. van Megen and S. M. Underwood, *Phys. Rev. E*, 1994, **49**, 4206.

[192] P. Hébraud, F. Lequeux, J. Munch, and D. Pine, *Phys. Rev. Lett.*, 1997, **78**, 4657.

[193] C. Beck, W. Härtl, and R. Hempelmann, *J. Chem. Phys.*, 1999, **111**, 8209.

[194] E. Bartsch, T. Eckert, C. Pies, and H. Sillescu, *J. Non-Cryst. Solids*, 2002, **802**, 307.

[195] T. Eckert and E. Bartsch, *Faraday Discuss.*, 2003, **123**, 51.

[196] M. Zackrisson, A. Stradner, P. Schurtenberger, and J. Bergenholtz, *Phys. Rev. E*, 2006, **73**, 011408.

[197] G. Petekidis, D. Vlassopoulos, and P. Pusey, *Faraday Discuss.*, 1999, **123**, 287.

[198] G. Petekidis, P. N. Pusey, A. Moussaïd, S. Egelhaaf, and W. C. K. Poon, *Physica A*, 2002, **306**, 334.

[199] G. Petekidis and P. Pusey, *Phys. Rev. E*, 2002, **66**, 051402.

[200] K. N. Pham, G. Petekidis, D. Vlassopoulos, S. U. Egelhaaf, P. N. Pusey, and W. C. K. Poon, *Europhys. Lett.*, 2006, **75**, 624.

[201] R. Besseling, E. R. Weeks, A. B. Schofield, and W. C. Poon, *Phys. Rev. Lett.*, 2007, **99**, 028301.

[202] T. Phung, J. Brady, and G. Bossis, *J. Fluid Mech.*, 1996, **313**, 181.

[203] P. Strating, *Phys. Rev. E*, 1999, **59**, 2175.

[204] B. Doliwa and A. Heuer, *Phys. Rev. E*, 2000, **61**, 6898.

[205] E. H. Purnomo, D. van den Ende, J. Mellema, and F. Mugele, *Europhys. Lett.*, 2006, **76**, 74.

[206] J. K. G. Dhont, *An introduction to dynamics of colloids*, Elsevier Science, Amsterdam, 1996.

[207] H. M. Laun, R. Bung, S. Hess, W. Loose, O. Hess, K. Hahn, E. Hädicke, R. Hingmann, F. Schmidt, and P. Lindner, *J. Rheology*, 1992, **36**, 743.

[208] H. M. Wyss, K. Miyazaki, J. Mattsson, Z. Hu, D. R. Reichman, and D. A. Weitz, *Phys. Rev. Lett.*, 2007, **98**, 238303.

[209] J. F. Brady, *J. Chem. Phys.*, 1993, **99**, 567.

[210] P. Sollich, F. Lequeux, P. Hébraud, and M. Cates, *Phys. Rev. Lett.*, 1997, **78**, 2020.

[211] P. Sollich, *Phys. Rev. E*, 1998, **58**, 738.

[212] S. Fielding, P. Sollich, and M. E. Cates, *J. Rheol.*, 2000, **44**, 323.

[213] L. Berthier, J.-L. Barrat, and J. Kurchan, *Phys. Rev. E*, 2000, **61**, 5464.

[214] L. Berthier and J.-L. Barrat, *J. Chem. Phys.*, 2002, **116**, 6228.

[215] K. Miyazaki and D. Reichman, *Phys. Rev. E*, 2002, **66**, 050501.

[216] K. Miyazaki, D. R. Reichman, and R. Yamamoto, *Phys. Rev. E*, 2004, **70**, 011501.

[217] V. Kobelev and K. S. Schweizer, *Phys. Rev. E*, 2005, **71**, 021401.

[218] F. Varnik and O. Henrich, *Phys. Rev. B*, 2006, **73**, 174209.

[219] L. Heymann, S. Peukert, and N. Aksel, *Rheol. Acta.*, 2002, **41**, 307.

[220] L. Heymann and N. Aksel, *Phys. Rev.E*, 2007, **75**, 021505.

[221] J. M. Brader, T. Voigtmann, M. E. Cates, and M. Fuchs, *Phys. Rev. Lett.*, 2007, **98**, 058301.

[222] J. Zausch, J. Horbach, M. Laurati, S. U. Egelhaaf, J. M. Brader, T. Voigtmann, and M. Fuchs, *J. Phys.: Condens. Matt.*, 2008, **20**, 404210.

[223] Note that this discussion neglects the subtleties of the limit of infinite Peclet number [278], which corresponds to the limit of non-Brownian particles under shear [279], and thus only provides insight into the limit of small to intermediate bare Peclet numbers.

[224] Equation (3.17) presents a slightly simplified version of the general expression in Ref. [44], restricting its use, so that only variables A, like the shear stress σ_{xy}, with $\langle A \rangle^{(\dot{\gamma}=0)} = 0$ and $\langle A \varrho_{\mathbf{q}} \rangle^{(\dot{\gamma}=0)} = 0$ can be considered in the following.

[225] G. Nägele and J. Bergenholtz, *J. Chem. Phys.*, 1998, **108**, 9893.

[226] K. Miyazaki, H. M. Wyss, D. R. Reichman, and D. A. Weitz, *Europhys. Lett.*, 2006, **75**, 915.

[227] Parameter $c^{(\dot{\gamma})}$ is not yet well known as it could only be estimated in the isotropically sheared hard sphere model (ISHSM), which underestimates the effect of shear [45, 221].

[228] W. Götze, *Z. Phys. B*, 1984, **56**, 139.

[229] The schematic $\mathrm{F}_{12}^{(\dot{\gamma})}$-model of Refs. [39] differs by setting $\gamma_c = 1$. This choice can be made by rescaling Γ and v_σ if only a single experiment is considered [232].

[230] For the numerical solution of the schematic model (Eqs. (3.31) to (3.35)) the algorithm of Ref. [280] was used, as has been done in previous studies [39]. The microscopic model (Eqs. (3.20) to (3.24)) was evaluated without shear for hard spheres with structure factor S_k taken from the Percus-Yevick approximation;[33] the wavevector integrals were discretized according to Ref. [281] with only difference that $M = 600$ wavevectors were chosen from $k_{\min} = 0.05/R_H$ up to $k_{\max} = 59.95/R_H$ with separation $\Delta k = 0.1/R_H$. Time was discretized with initial step-width $dt = 2\,10^{-7} R_H^2/D_s$, which was doubled each time after 400 steps. Note that the MCT shear modulus at short times depends sensitively on the large cut-off $k_{\max}$ [225]; for hard spheres, $g(t, \dot{\gamma} = 0) = (n^2 k_B T/60\pi^2) \int_{k_{\min}}^{k_{\max}} dk\, k^4 (c'_k)^2\, S_k^2\, \Phi_k^2(t)$ gives the correct short time or high frequency divergence $G'(\omega \gg D_0/R_H^2) \sim \sqrt{\omega}$ only for $k_{\max} \to \infty$.

[231] O. Henrich, F. Varnik, and M. Fuchs, *J. Phys.: Condens. Matter*, 2005, **17**, S3625.

[232] D. Hajnal and i. p. . M. Fuchs.

[233] E. H. Purnomo, D. van den Ende, S. A. Vanapalli, and F. Mugele, *Phys. Rev. Lett.*, 2008, **101**, 238301.

[234] X. H. Xia and Z. B. Hu, *Langmuir*, 2004, **20**, 2094.

[235] R. H. Pelton and P. Chibante, *Colloids Surf. A*, 1986, **20**, 247.

[236] M. Rasmusson, A. Routh, and B. Vincent, *Langmuir*, 2004, **20**, 3536.

[237] P. W. Zhu and D. H. Napper, *Phys. Rev. E*, 1994, **50**, 1360.

[238] P. W. Zhu and D. H. Napper, *Colloids Surf. A*, 1995, **98**, 93.

[239] D. Duracher, A. Elaïssari, and C. Pichot, *Colloid Polym. Sci.*, 1999, **277**, 905.

[240] M. Ishikawa, H. Misawa, and N. K. H. Masuhara, *Chem. Lett.*, 1993, p. 481.

[241] M. Ishikawa, H. Misawa, N. Kitamura, and H. Masuhara, *Bull. Chem. Soc. Jpn.*, 1996, **69**, 59.

[242] J. Hofkens, J. Hotta, K. Sasaki, H. Masuhara, and K. Iwai, *Langmuir*, 1997, **13**, 414.

[243] C. D. Jones and L. A. Lyon, *J. Am. Chem. Soc.*, 2003, **125**, 460.

[244] H. Holthoff, S. U. Egelhaaf, M. Borkovec, P. Schurtenberger, and H. Sticher, *Langmuir*, 1996, **12**, 5541.

[245] M. von Smoluchowski, *Phys. Z.*, 1916, **17**, 557.

[246] M. von Smoluchowski, *Z. Phys. Chem.*, 1917, **92**, 129.

[247] M. Kerker, *The Light Scattering of Light and Other Electromagnetic Radiation*, Academic Press, New York, 1969.

[248] G. Oster and D. P. Riley, *Acta Crystallogr.*, 1952, **5**, 1.

[249] J. Happel and H. Brenner, *Low Reynolds Number Hydrodynamics*, Martinus Nijhoff Publishers, The Hague, 1983.

[250] M. Born and E. Wolf, *Principles of Optics, Cambridge University Press, New York*, 1998.

[251] A. Voit, A. Krekhov, and W. Köhler, *Phys. Rev. E*, 2007, **76**, 011808.

[252] D. Asnaghi, M. Carpineti, M. Giglio, and M. Sozzi, *Phys. Rev. Lett.*, 1992, **45**, 1018.

[253] A. F. Routh and B. Vincent, *Langmuir*, 2002, **18**, 5366.

[254] A. Voit, A. Krekhov, W. Enge, L. Kramer, and W. Kohler, *Phys. Rev. Lett.*, 2005, **94**, 214501.

[255] A. Voit, A. Krekhov, and W. Köhler, *Phys. Rev. E*, 2007, **76**, 011808.

[256] A. Voit, A. Krekhov, and W. Köhler, *Macromolecules*, 2007, **40**, 9.

[257] V. N. Manoharan, M. T. Elsesser, and D. J. Pine, *Science*, 2003, **301**, 483.

[258] Y. S. Cho, G. R. Yi, J. M. Lim, S. H. Kim, V. N. Manoraharan, D. J. Pine, and S. M. Yang, *J. Am. Chem. Soc.*, 2005, **127**, 15968.

[259] Y. S. Cho, G. R. Yi, S. H. Kim, S. J. Jeon, M. T. Elsesser, H. K. Yu, S. M. Yang, and D. J. Pine, *Chem. Mater.*, 2007, **19**, 3183.

[260] C. N. Wagner and A. Wittemann, *Langmuir*, 2008, **4**, 12126.

[261] Y. Xia, Y. Yin, Y. Lu, and J. McLellan, *Adv. Funct. Mater.*, 2003, **13**, 907.

[262] S. Berger, A. Synytska, L. Ionov, K. J. Eichhorn, and M. Stamm, *Macromolecules*, 2008, **41**, 9669.

[263] W. Lu, M. Chen, and L. Wu, *J. Coll. Int. Sc.*, 2008, **328**, 98.

[264] T. Isojima, M. Lattuada, J. B. V. Sande, and T. A. Hatton, *ACS NANO*, 2008, **2**, 1799.

[265] J. W. Kim, D. Lee, H. C. Shum, and D. A. Weitz, *Adv. Mat.*, 2008, **20**, 3239.

[266] B. Wang, B. Li, B. Zhao, and C. Y. Li, *J. Am. Chem. Soc.*, 2008, **130**, 11594.

[267] A. Walther and A. H. E. Muller, *Soft Mat.*, 2008, **4**, 663.

[268] M. Hoffmann, Y. Lu, M. Schrinner, and M. Ballauff, *J. Phys. Chem. B*, 2008, **112**, 14843.

[269] W. Lin, M. Kobayashi, M. Skarba, C. Mu, P. Galletto, and M. Borkovec, *Langmuir*, 2006, **22**, 1038.

[270] T. Niidome, K. Nakashima, H. Takashi, and Y. Niidome, *Chem. Comm.*, 2004, **17**, 1978.

[271] C. Kneuer, M. Sameti, U. Bakowsky, T. Schiestel, H. Schirra, H. Schmidt, and C. M. Lehr, *Bioconjugate Chem.*, 2000, **11**, 926.

[272] K. K. Sandhu, C. M. McIntosh, J. M. Simard, S. W. Smith, and V. M. Rotello, *Bioconjugate Chem.*, 2002, **13**, 3.

[273] A. Shipway, E. Katz, and I. Willner, *Chemphyschem*, 2000, **1**, 18.

[274] J. M. Klostranec and W. C. W. Chan, *Adv. Mater.*, 2006, **18**, 1953.

[275] D. Pissuwan, S. M. Valenzuela, and M. B. Cortie, *Trends in Biotechnology*, 2006, **24**, 62.

[276] Q. Sun and Y. Deng, *Langmuir*, 2005, **21**, 5812.

[277] S. Link and M. A. El-Sayed, *J. Phys. Chem. B*, 1999, **103**, 4212.

[278] J. F. Brady and J. F. Morris, *J. Fluid Mech.*, 1997, **348**, 103.

[279] D. Drazer, J. Koplik, B. Khusid, and A. Acrivos, *J. Fluid Mech.*, 2002, **460**, 307.

[280] M. Fuchs, W. Götze, I. Hofacker, and A. Latz, *J. Phys.: Condens. Matter*, 1991, **3**, 5047.

[281] T. Franosch, M. Fuchs, W. Götze, M. R. Mayr, and A. P. Singh, *Phys. Rev. E*, 1997, **55**, 7153.

8 Publications

J. J. Crassous, R. Régisser, M. Ballauff, N. Willenbacher: *"Characterization of the viscoelastic behavior of complex fluids using the piezoelectric axial vibrator (PAV)"*, *J. Rheol.*, **49**, 851 (2005)

A. Kelarakis, J. J. Crassous, M. Ballauff: *"Micellar spheres in high-frequency oscillatory field"*, *Langmuir*, **22**, 6814 (2006)

J. Bosco Stanislaus, H. Zettl, J. J. Crassous, M. Ballauff, G. Krausch: *"Interactions between methyl cellulose and sodium dodecyl sulphate in aqueous solution studied by single molecule fluorescence correlation spectroscopy"*, *Macromolecules*, **39**, 8793-8798 (2006)

J. J. Crassous, M. Siebenbürger, M. Ballauff, M. Drechsler, O. Henrich, M. Fuchs: *"Thermosensitive core-shell particles as model systems for studying the flow behavior of concentrated colloidal dispersions"*, *J. Chem. Phys.*, **125**, 204906 (2006)

J. J. Crassous, M. Ballauff, M. Drechsler, J. Schmidt, Y. Talmon: *"Imaging the volume transition in thermosenstive core-shell particles by cryo-transmission electron microscopy"*, *Langmuir*, **22**, 2403 (2006)

J. J. Crassous, M. Siebenbürger, A. Wittemann, O. Henrich, M. Fuchs, M. Ballauff:"Rheology of concentrated suspension and the glass transition", *Proceedings PARTEC 2007, International Congress on Particle Technology Nuremberg, March 2007.*

J. J. Crassous, M. Siebenburger, M. Ballauff, M. Drechsler, D. Hajnal, O. Henrich, M. Fuchs: *"Shear stresses of colloidal dispersions at the glass transition in equilibrium and in flow"*, *J. Chem. Phys.*, **128**, 204902 (2008)

J. J. Crassous, A. Wittemann, M. Siebenburger, M. Schrinner, M. Drechsler, M. Ballauff: "Direct imaging of temperature-sensitive core-shell latexes by cryogenic transmission electron microscopy", *Colloid Polym. Sci.* **286**, 805, (2008).

D. Hajnal, O. Henrich, J. J. Crassous, M. Siebenbürger, M. Drechsler, M. Ballauff, M. Fuchs: "Theory of Thermodynamic Stresses in Colloidal Dispersions at the glass transition", *XVTH INTERNATIONAL CONGRESS ON RHEOLOGY - THE SOCIETY OF RHEOLOGY 80TH ANNUAL MEETING, PTS 1 AND 2 Book Series: AIP CONFERENCE PROCEEDINGS*, **1027**, 674 (2008).

J. J. Crassous, C. N. Rochette, A. Witttemann, M. Drechsler, M. Schrinner, M. Ballauff:

"Analysis of Polymer Colloids by Combining Cryo-Transmission Electron Microscopy with Small Angles X-Ray Scattering", *Langmuir* **25**, 7862, (2009).

9 Erklärung

Hiermit erkläre ich, dass ich die Arbeit selbständig verfasst und keine anderen als die angegebenen Quellen und Hilfsmittel benutzt habe. Ferner erkläre ich, dass ich nicht anderweitig mit oder ohne Erfolg versucht habe, eine Dissertation einzureichen oder mich einer Doktorprüfung zu unterziehen.

Bayreuth, den

Jérôme Crassous

Bayreuth, 04.05.2009

Jérôme Crassous